UNIVERSITY OF STRATHCLYDE
Department of Physics

Solution-processable, mechanically-flexible lasers

by
Caroline Foucher

A thesis presented in fulfilment of the requirements for the degree of Doctor of Philosophy in Physics at the University of Strathclyde in Glasgow (UK)

2015

Frontispiece

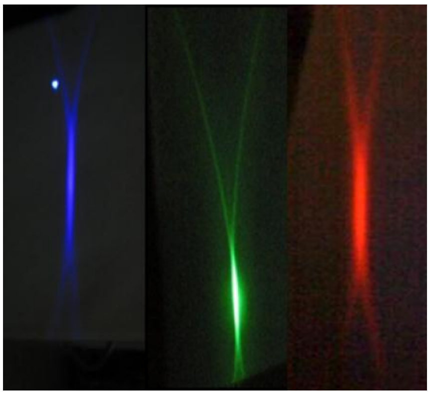

Typical fan-shaped emissions of organic and hybrid distributed-feedback lasers.

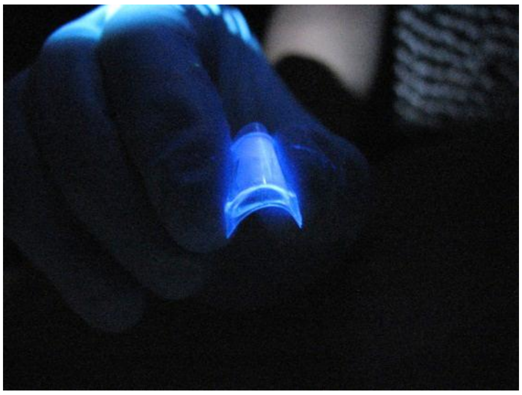

A mechanically-flexible all-organic blue emitting distributed feedback laser under UV exposure.

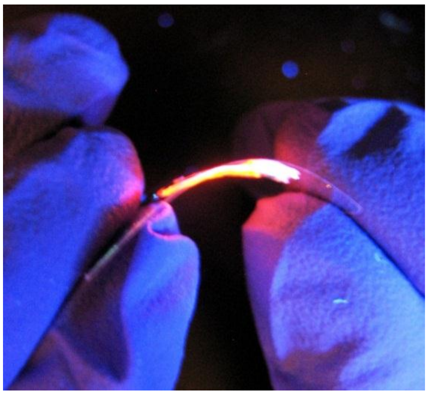

A mechanically-flexible hybrid organic-inorganic colloidal quantum dot laser made on flexible glass.

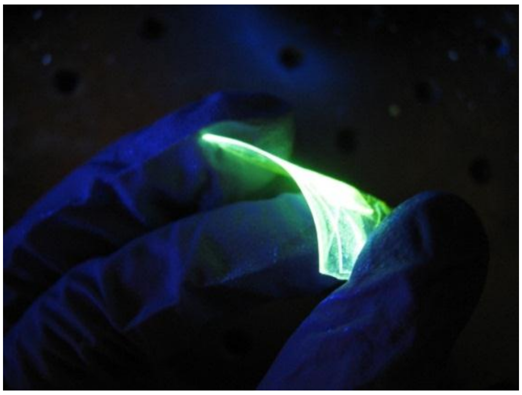

A mechanically-flexible green emitting organic distributed feedback laser encapsulated with flexible glass.

Copyright Statement

This thesis is the result of the author's original research. It has been composed by the author and has not been previously submitted for examination which has led to the award of a degree.

Signed:
Date:

Acknowledgments

I would like to acknowledge Martin Dawson for giving me the opportunity to join the Institute of Photonics. I wouldn’t have been able to complete this PhD without the help, advice and support of many people that I would like to thank here.

First of all I would like to thank Nicolas Laurand for always encouraging me, guiding me and being a great supervisor. I would also like to particularly thank Benoit Guilhabert for all his great ideas, advice and everything he taught me; my PhD would have never been as successful without him.

I would like to express my gratitude to all my collaborators, colleagues and friends at the IoP who made my PhD an amazing journey; every day I spent at the IoP was a joy thanks to all of them. So thank you Lynda McLaughlin for helping me so much during my first year. Thank you Sharon Kelly, Lisa Flanagan, Lorraine Annand and Ewan Mulhern for being so helpful. Thank you Johannes Herrnsdorf for his advice. Thank you to all the PhD students in my office who brought the best work atmosphere ever. A particular big thank you to Antonio Trindade for everything, from the start to the end of my PhD, Antonio you have been a number one friend.

Finally I would like to thank the closest people in my life who have always supported me and been there for me all the way here. Firstly I would like to thank my parents Bernard and Ghislaine Foucher who have pushed me studying and working so hard; I owe them everything. I’d like to thank my dad for always believing in me and giving me his taste for Physics. I’d like to thank my mum for supporting me and always helping me. Also thank you Françoise, Claudine, Lulu and Robert Picq for all the support.

The person I’d like to thank the most is my sister Géraldine Foucher who has always been there for me, every single day of my PhD and my life. Thank you to all my friends but particularly to Cécile Vallon (for texting me every day and I hope we will finally stop being stressed out and both do something we really like) and Sandrine Braud (for her support)! Finally I’d like to thank Robert Scharf for his patience and for always being there for me even when my PhD was driving me crazy!

So thank you to all the people who made my PhD a great accomplishment and experience!

Abstract

The aim of the work in this thesis is to push the technology of solution-processed semiconductor lasers beyond the state-of-the-art and bring it closer to real-world implementation. An emphasis is put on the demonstration of mechanically-flexible lasers having low thresholds, high photostability and potential for cost-effectiveness and compact integration.

Different gain materials, designs and pump sources are used to improve the performance and capabilities of these lasers. Distributed feedback resonators are chosen due to their planar fabrication and their potential for lower threshold than other cavities in the case of solution-processed lasers. Two types of gain materials are used: organic semiconductors and colloidal quantum dots. Encapsulation schemes compatible with the mechanical flexibility of the final devices, e.g. using transparent polymers or flexible glass membranes, are proposed and studied in order to extend the operational lifetime of the devices.

One highlight of this work is the development of, to our knowledge, the first diode-pumped, mechanically flexible organic lasers encapsulated with thin-glass for high photostability. Other important outcomes include mechanical wavelength tuning of lasers, record performance for colloidal quantum dot lasers optically-pumped in the nanosecond regime and the demonstration of a red/green/blue laser. The capability for sensing applications of some reported formats of lasers are also shown.

Content

List of figures

Abbreviations

ACQ	Aggregation-Caused Quenching
AIE	Aggregation-Induced Emission
ACQ	Aggregation-Caused Quenching
ASE	Amplified Spontaneous Emission
BBEHP-PPV	Poly[2,5-bis(2',5'-bis(2''-ethylhexyloxy)phenyl)-p-phenylenevinylene]
CQDs	Colloidal Quantum Dots
DBR	Distributed Bragg Reflector
DFB	Distributed Feedback
FWHM	Full Width Half Maximum
LED	Light Emitting Diode
LD	Laser Diode
NOA	Norland Optical Adhesive
PFC	Piezofluorochromic or Mechanofluorochromic
PL	Photoluminescence
PLQY	Photoluminescence Quantum Yield
PMMA	Poly(methyl methacrylate)
PVA	Poly (vinyl alcohol)
OS	Organic Semiconductor
T3	Tris(triuorene)truxene
TE	Transverse Electric
TM	Transverse Magnetic
THF	Tetrahydrofuran
UV	Ultraviolet
VECSOL	Vertical External Cavity Surface Emitting Organic Laser
VCSEL	Vertical Cavity Surface Emitting Laser
YAG	Yttrium Aluminium Garnet

Part I

Introduction

Chapter 1

Solution-processed gain materials for lasers

In this chapter, the background and motivations of the thesis are initially presented. This is followed by information on the basic principles of lasers and discussions of solution-processed organic semiconductors and colloidal quantum dot materials for lasers.

1.1. Introduction

1.1.1. Background

The invention of the laser has dramatically revolutionised technology and, while not always noticed or acknowledged, it has impacted our everyday life [1]. Lasers are nowadays commonly used in a wide range of fields, e.g. medicine, national security and defence, telecommunications, lighting displays, law enforcement, manufacturing industry equipment, consumer electronics etc. Different types of devices, such as dye lasers, gas lasers, solid-state lasers, semiconductor lasers and fibre lasers have been developed over the years and put into practice for these applications [2–4]. However, new laser technologies are constantly emerging, particularly thanks to advances in material science.

Among these, solution-processed semiconductors have recently attracted great interest in the photonic research community because they possess many potential advantages such as (i) their suitability for attractive fabrication processes – e.g. materials can be accurately deposited by ink-jet printing, spray and spin-coating or doctor blading and they can be patterned using simple soft lithography techniques; (ii) their compatibility with a wide range of material systems, including plastics, enabling for example composite and mechanically-flexible laser cavities; and (iii) the possibility to chemically alter the structure of the semiconductors at the nanoscale in order to tune the desired wavelength of operation. These are in turn opening up a wide range of possibilities for optoelectronic applications [5–11], (bio)-sensing [12] and data communications [13,14].

Solution-processable semiconductors for lasers can take the form of organic materials, such as luminescent conjugated macromolecules or polymers, but also of colloidal quantum dots, which are basically nanocrystals of inorganic semiconductor alloys. These are both promising gain materials as they can be tailored to emit through the whole visible spectrum, have high photoluminescence quantum yields and large absorption cross-sections [5]. This thesis focuses on the development of lasers made from such solution-processed semiconductor laser gain media.

1.1.2. Motivations and Thesis outline

The main aim of the work developed in this thesis was to push the technology of solution-processed lasers and its applicability beyond the state-of-the-art. In particular, the emphasis was on the demonstration of the wavelength versatility of such lasers in mechanically-flexible formats and on exploring ways to improve the photostability without trade-off in performance.

As said before, solution-processed lasers are attractive and are undergoing research for various applications. Some of these devices can be in mechanically flexible formats, which promises to unlock novel applications, e.g. in the field of large-area flexible photonics. However, there exist challenges before such lasers can be implemented in 'real world' application settings. Electrical injection has proven elusive for organic semiconductor lasers (OSLs) although efforts are still being made in that direction. On the other hand, optical pumping with compact blue emitting InGaN light sources such as laser diodes and light-emitting diodes (LEDs) is possible for high performance OSLs and this looks like the most likely near-term route for taking these lasers 'out of the laboratory'. Other challenges for OSLs are photostability and continuous wave (CW) operation. Organic laser materials operate in pulsed mode, because of inter-system crossing and triplet accumulation hinders oscillation in the CW regime. Pulsed operation is acceptable for some applications, however, increasing the photostability of solution-processed lasers though is crucial. Encapsulating the gain material as is done for organic LED (OLED) technology is required but doing this without compromising the other laser characteristics, such as threshold and/or mechanical flexibility, is not straightforward. Alternative solution-processable laser materials such as colloidal quantum dots might be the answer to the above challenges, but this material technology is not as mature for lasers and performance still lags that of organic semiconductors.

As a result of these considerations, the research of this thesis focused on the demonstration and study of high-performance (low threshold and high photostability) mechanically-flexible, solution-processed lasers suitable for pumping with InGaN light sources. It involves the use of novel encapsulation approaches and laser materials, including organic semiconductors but also colloidal quantum dots. One highlight result is the development of diode-pumped, mechanically flexible organic lasers encapsulated with thin glass. Other important outcomes include mechanical wavelength tuning of lasers, record performance for colloidal quantum dot lasers optically-pumped in the nanosecond regime and the demonstration of a red/green/blue laser. The capability for sensing applications of some reported formats of lasers are also shown.

The thesis is divided into three broad parts comprising a total of 7 chapters: (I) Introduction (chapters 1 and 2), (II) Experiments and Results (chapters 3, 4, 5 and 6) and (III) Conclusion and Outlook (chapter 7).

The rest of this chapter describes in more detail the laser technology studied in this thesis. The basic principles of a laser are first introduced followed by a description of organic semiconductor and colloidal quantum dot lasers. The state-of-the-art for these lasers is also presented.

Chapter 2 looks into the fundamentals of distributed feedback (DFB) lasers and lists the properties of the different materials (including gain materials) used in the fabrication of the DFB lasers studied here. It also explains the fabrication steps for these lasers and describes how they were optically excited and characterised. Finally, it details an analytical model that is used to calculate the modes and related characteristics of the DFB laser structures. This model is used throughout part II to discuss the experimental results.

Chapter 3 reports the study of different formats of highly-photostable, mechanically-flexible, all-organic semiconductor lasers. The gain material used in this chapter is based on blue-emitting semiconducting macromolecules.

Chapter 4 extends the work of chapter 3 to another gain material, this time a green-emitting pi-conjugated polymer with high absorption in the blue. A hybrid encapsulation geometry based on flexible glass membranes is introduced and InGaN laser diode pumping is demonstrated paving the way for a highly photostable and compact system with potential for bio-sensing applications.

Chapter 5 presents red-emitting flexible hybrid lasers made with CdSe/ZnS colloidal quantum dots as the gain medium. The capability to assemble these lasers on different substrates, including silicon, is established. Wavelength tunability of lasers on thin-glass by mechanical bending is shown, as is the capability for bulk-refractive index sensing (a first step towards biosensing).

In chapter 6, a slightly different type of organic gain material, whose characteristics change with pressure, is reported. Following this, solution-processed lasers emitting at different wavelengths are assembled onto a common substrate in order to demonstrate a red/green/blue laser excited by a single UV pump.

Finally, chapter 7 gives a summary of the achievements presented in the thesis and the corresponding outlook for future work.

1.2. Basic principles of lasers

1.2.1. Basic concept

To make a laser, three components are needed: a pump to inject energy into the system, a gain medium that receives that energy and uses it to emit and amplify light and an optical cavity forming a resonator in the latter recirculates the light back and forth through the gain medium so stimulated emission builds up to the point of oscillation (when the overall losses of the system are compensated by the optical gain).

There are several alternative schemes to pump a gain medium, the two main ones being electrical pumping (energy is injected from an external source in the form of an electric current) and optical pumping (a pump source injects energy in the form of light). Here, we will focus on optical pumping as electrical pumping of organic semiconductor lasers remains an unresolved challenge, mainly due to the low carrier mobility of organic semiconductors [5,11,15]. We also note that advances in high power blue lasers and LEDs are enabling the development of potentially small-form factor optically-pumped organic semiconductor lasers [16].

There exist a variety of laser gain media, such as doped crystals and glasses, dyes in liquid or solid matrices, gases in sealed tubes, epitaxially-grown semiconductor crystals and solution-processable semiconductors. The latter in the form of organic semiconducting polymers, macromolecules and colloidal quantum dots are used in this work.

There is alsoa multitude of possible laser resonators: Fabry-Perot cavities, including vertical cavities for surface emitting lasers (e.g. VCSELs) and planar distributed Bragg reflector (DBR) lasers, whispering gallery mode (WGM) cavities, etc. In this work, the DFB resonator geometry was chosen as it has been shown to lead to the lowest thresholds for OS lasers, as highlighted later in this chapter (section 1.4), but also because of the planar geometry, which is well suited to solution-processed fabrication. Details on the design and operation of DFB lasers are given in chapter 2.

1.2.2. Absorption, spontaneous and stimulated emission

Laser action rests upon three basic light-matter processes: absorption, spontaneous emission and stimulated emission, as illustrated in Figure 1.1 a), Figure 1.1 b) and Figure 1.1 c), respectively [3,17]. To describe these phenomena, we consider an active medium made of molecules, with a molecule having two possible energy levels, 1 and 2, at energies E_1 and E_2 with $E_1 < E_2$. It is assumed that 1 represents the ground energy level and 2 the excited level. The energy difference between these two states is expressed by:

$$h\nu = (E_2 - E_1) \qquad \textbf{Eq. 1.1}$$

With h the Planck's constant and v the frequency corresponding to the transition 1 to 2 or 2 to 1.

At thermodynamic equilibrium, all molecules are in the ground state (if E_2-E_1 greater than the thermal energy). If a monochromatic electromagnetic wave with corresponding photon energy $h\nu$ equal to E_2-E_1 is incident on a molecule, then a photon has a certain probability to be absorbed by the molecule, raising the latter to the energy level E_2. This is the absorption process.

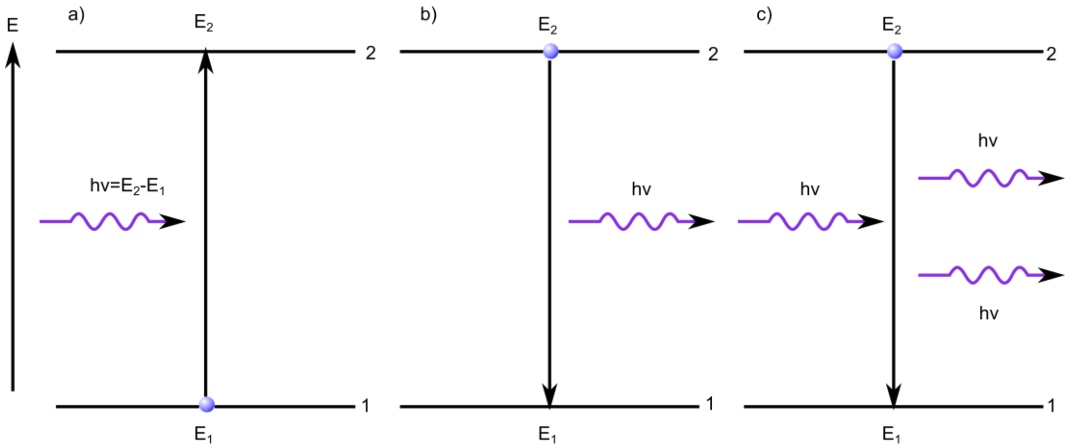

Figure 1.1: Schematic of a) absorption, b) spontaneous emission and c) stimulated emission.

Now, we consider that a molecule is in the excited state, level 2. As level 2 is unstable, the electron will tend to decay to a stable state, level 1, after a lapse of time called the decay lifetime or the excited state lifetime. One possible way for the molecule to relax to the ground state is by releasing the difference of energy between the two levels as a photon of energy E_2-E_1. This process is called spontaneous emission. Spontaneous emission can be described using the Einstein coefficient A_{21}:

$$\left(\frac{dN_2}{dt}\right)_{sp} = -A_{21}N_2 \tag*{Eq. 1.2}$$

$$A_{21} = \frac{1}{\tau_{sp}} \tag*{Eq. 1.3}$$

Eq. 1.2 describes the rate of decay of the population of excited molecules per unit volume, N_2. A_{21} is the reciprocal of the spontaneous radiative lifetime τ_{sp} as expressed in Eq. 1.3. We note that the decay lifetime is equal to τ_{sp} if there are no decay processes other than spontaneous emission. However, usually non-radiative recombination also occurs, which adds a contribution to the total decay lifetime.

Finally, if we still consider that the molecule is in the excited state but that now an electromagnetic wave with an energy matching E_2-E_1 is incident onto it, then the incident photon can force (stimulate) the electron to decay from level 2 to level 1. Such a stimulated photon has the same energy, phase and direction as the incident photon: they are coherent. This process is called stimulated emission (see section 1.2.4 for the equations describing the rates of absorption and stimulated emission).

The crucial difference between spontaneous and simulated emission is that in the first case the photon emitted has no definite phase or direction but in the second case, the phase and direction of the photon are determined by the incident photon [3,17–19].

1.2.3. Pumping scheme and population inversion

The condition for amplification of light waves is that the gain medium has to be kept in a state of population inversion. This state is obtained when the number of molecules in the upper level of energy is higher than in the lower level, i.e. if N_1 and N_2 are the numbers of molecules per unit volume present in the energy levels E_1 and $E_{2,}$ respectively, then $N_1<N_2$. This does not happen spontaneously but can occur when pumping the material.

Population inversion is impossible for the ideal two-level energy system described above, as pumping will at best bring an equal population $N_1=N_2$ at which point transparency is reached. When this is the case, then a photon incident on the medium has, an equal chance to either be absorbed or to stimulate emission, with both processes cancelling each other.

To obtain population inversion, it is necessary to populate level 2 through higher lying electronic levels (i.e. non resonant pumping). Two simple but effective models can be used to explain such laser materials: the three-level laser and the four-level laser schemes, illustrated respectively in Figure 1.2 a) and Figure 1.2 b).

In a three-level laser, pumping of the gain materials engenders excitation from the ground state to level 3. For a laser medium to be effective the population of E_3 needs to relax rapidly to level 2 and population inversion can then be obtained between level 2 and the ground state (level 1). For a four-level scheme, electrons are excited from level 1 to level 4 under pumping. They relax rapidly from level 4 to level 3 and population inversion is obtained between level 3 and 2 (the laser transition). The advantage of a four-level system is that population inversion is reached faster, in principle almost immediately on absorption if the decay from level 2 to level 1 is really rapid. Hence, this leads to a lower lasing threshold in theory compared to a three-level scheme. The gain materials used in this work can be considered as quasi three-level (intermediate situation, where the lower laser level is close enough to the ground state so a certain population occurs in that level at the operating temperature) [3,17–19].

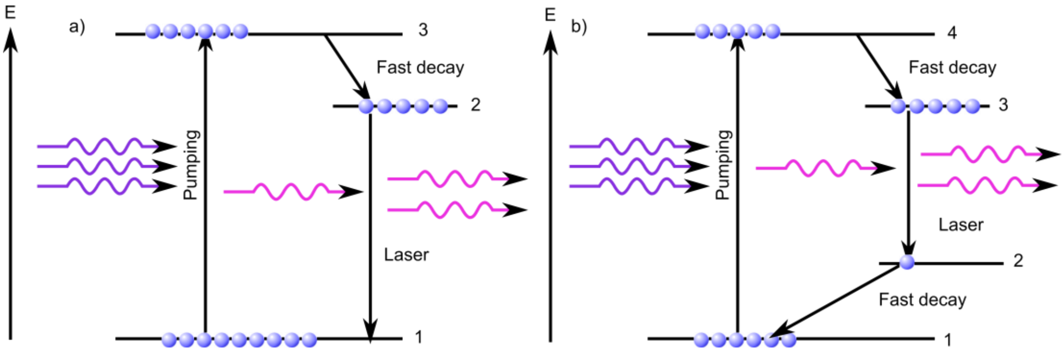

Figure 1.2: Schematics of a) three-level laser scheme and b) four-level laser scheme.

1.2.4. Absorption and emission cross section

The rate of absorption and stimulated emission can be expressed as a function of the absorption and emission cross sections of the laser transition, which qualify the likelihood that an absorption or a stimulated emission event will be triggered for a given density of molecules in the upper state and a given flux of photons. The absorption and emission cross sections depend on the particular transition of the molecules, the wavelength of the photons and, for some materials, the polarisation of the photons.

The rate of absorption R_{abs} can be described as [17]:

$$\left(\frac{dN_l}{dt}\right)_{abs} = -R_{abs}N_l \qquad \textbf{Eq. 1.4}$$

$$R_{abs} = u_p\sigma_{abs} \qquad \textbf{Eq. 1.5}$$

Where $\left(\frac{dN_l}{dt}\right)_{abs}$ is the rate of the transition due to absorption, σ_{abs} the absorption cross section, u_p the photon flux (number of photons crossing a unit area per unit time) and N_l the lower level population density (number of molecules in the lower state of energy per unit volume).

The photon flux can be related to the intensity, I, of the light wave as:

$$u_p = \frac{I}{h\nu} \qquad \textbf{Eq. 1.6}$$

The absorption cross section is defined as [17]:

$$\sigma_{abs} = \frac{2\pi^2}{3n\epsilon_0 ch} |\pi|^2 \nu g(\nu) \qquad \textbf{Eq. 1.7}$$

With n the refractive index of the gain medium, ε_0 the permittivity of free space, c the velocity of light in free space and $g(\nu)$ the lineshape function, a function describing the frequency dependence of the transition.

Similarly, the rate of stimulated emission R_{em} is expressed as:

$$\left(\frac{dN_u}{dt}\right)_{em} = -R_{em}N_u$$

$$R_{em} = \sigma_{em}U_p \qquad \textbf{Eq. 1.8}$$

Where $\left(\frac{dN_u}{dt}\right)_{em}$ is the rate at which the transition occurred due to stimulated emission, σ_{em} the stimulated emission cross-section and N_u the upper laser level population density, i.e. the number of molecules in the excited state per unit volume.

For a transition involving two non-degenerate levels, the rate of absorption and stimulated emission are equal and then the absorption and emission cross sections are equal. However, for organic semiconductors and for colloidal quantum dots the absorption peak and emission peak are at different wavelengths and, as the absorption and emission cross section depend on the wavelength, it means that the absorption and emission cross sections can be expected to be different [3,17–19].

1.2.5. Rate Equations

The interaction between light and a laser material can be summarised by the so-called rate equations. For information, the rate equations for a four-level laser medium are given here. As seen previously, for this kind of system, the population density N_1 of the ground state E_1 decreases under pumping and the molecules get excited to the level E_4. N_1 also increases by fast relaxation from the level E_2. N_2 decreases by the relaxation process but increases by spontaneous and stimulated emission. Then the population density N_3 of the higher laser level E_3 decreases by spontaneous and stimulated emission and increases by a very fast relaxation process from E_4. The rate equations for the 4-level system are:

$$\frac{dN_1}{dt} = -u_p\sigma_{24}N_1 + R_{21}N_2 \tag{Eq. 1.9}$$

$$\frac{dN_2}{dt} = \frac{N_3}{\tau_{sp}} + B_{32}S(N_3 - N_2) - R_{21}N_2 \tag{Eq. 1.10}$$

$$\frac{dN_3}{dt} = R_{43}N_4 - \frac{N_3}{\tau_{sp}} - B_{31}S(N_3 - N_1) \tag{Eq. 1.11}$$

$$\frac{dN_4}{dt} = u_p\sigma_{14}N_1 - R_{43}N_4 \tag{Eq. 1.12}$$

With u_p the photon energy density at the pump wavelength, σ_{ij} the absorption cross section corresponding the i^{th} to j^{th} transition, R_{ij} the relaxation rate from the energy level i to the energy level j, τ_{sp} is the spontaneous emission lifetime of the energy level E_3, B_{32} is the second Einstein coefficient for the laser transition and S the photon density at the laser transition wavelength. B_{32} is equal to the emission and absorption cross-sections when taken at the wavelength of the laser transition. Note that non-radiative relaxation processes from level 3 to level 2 have been ignored.

1.2.6. Amplified spontaneous emission

Amplified spontaneous emission (ASE) is the physical phenomenon of amplification of spontaneously emitted light by stimulated emission as the light travels in a gain medium. It can lead to a spectral distortion and narrowing of the emission (compared to the intrinsic luminescence) as the photons with energy close to the maximum of the gain are preferentially amplified and come to dominate this emission. ASE was first observed in organic semiconductors by Hide *et al.* using an MEH-PPV film containing TiO_2 nanoparticles [20].

Two equations need to be considered to explain ASE [21,22]. Here, for simplicity, we consider a transition between a level 2 and a level 1. The transition probability W_{12} of a molecule to undergo a transition from the level of energy E_2 to the level E_1 during a period dt is the sum of the contributions from spontaneous emission and stimulated emission. The transition probability due to spontaneous emission, considering the Einstein coefficient A_{21}, is [17]:

$$dW_{21} = A_{21}dt \qquad \textbf{Eq. 1.13}$$

In the case of stimulated emission, the probability of a downward transition of an electron from the level E_2 to the level E_1 W_{21} is equal to:

$$dW_{21} = u_i B_{12} dt \qquad \textbf{Eq. 1.14}$$

With B_{21} the Einstein coefficient for stimulated emission and u_i the photon energy density of the incident radiation.

The equations Eq. 1.13 and Eq. 1.14 show that the transition probability of stimulated emission, but not of spontaneous emission, is determined by the photon energy density. A point can be reached where, if the photon density is high enough, stimulated emission dominates over spontaneous emission. One can picture spontaneously emitted photons being amplified by stimulated emission as they travel in a medium that has an inversion of population for the active transition. This amplification process in turn increases the photon density, then again increasing the likelihood of stimulated emission. However, the optical gain (or amplification) is function of the wavelength so photons of different energies will be amplified differently. It means that the spectrum around the gain peak experiences the highest amplification, possibly leading to significant narrowing of the emission.

This effect can be further understood by considering a photon flux u_p travelling along a direction z in an inverted, i.e. amplifying material. We still consider that the active transition is between a level 2 and a level 1. The change of flux du_p as light travels through an elemental length dz is the sum of the amplified light and of the spontaneous emission in that direction. The change of flux du_p due to amplification (difference between stimulated emission and absorption) is given by:

$$du_p = \sigma_{em} F(N_2 - N_1)dz$$ **Eq. 1.15**

With *F* the electrons flux (number of electrons per unit area per unit time).
This can be expressed as a function of the light intensity *I* using Eq. 1.15:

$$dI = \sigma_{em} I(N_2 - N_1)dz$$ **Eq. 1.16**

Or

$$\frac{dI(\lambda)}{dz} = g_{net}(\lambda)I(\lambda)$$ **Eq. 1.17**

With g_{net} the net gain per length. Eq. 1.17 is written to take into account the wavelength dependence of the transition.
The light intensity increases due to spontaneous emission coupled in the *z* direction is [17]:

$$\frac{dI(\lambda)}{dz} = \frac{A_{21}N_2hc}{\lambda}\frac{A}{4\pi L^2}$$ **Eq. 1.18**

With *L* the length of the gain material, *A* the cross-sectional area of the gain medium, N_2 the population density in the excited state, *h* the Planck's constant and *c* the speed of light.

Considering both spontaneous and stimulated emission, the following equation is obtained:

$$\frac{dI(\lambda)}{dz} = g_{net}(\lambda)I(\lambda) + \frac{A_{21}N_2hc}{\lambda}\frac{A}{4\pi L^2}$$ **Eq. 1.19**

The solution of Eq. 1.19 is:

$$I(\lambda, z) = \frac{A_{21} N_2 hc}{\lambda g_{net}(\lambda)} \frac{A}{4\pi L^2} \left(e^{g_{net}(\lambda)z} - 1\right)$$ **Eq. 1.20**

This equation shows that ASE depends on the population inversion (i.e. on the gain) and on the length of the amplifying medium. Spectral narrowing will therefore be more significant for longer lengths.

We will see in chapter 2 that to assess the capability of solution-processed semiconductors to sustain optical gain, we often look for the tell-tale sign of ASE (spectral narrowing of the emission) by exciting the material in a configuration where the detected intensity can be expressed by Eq. 1.20 (stripe excitation and edge detection).

1.2.7. Gain and threshold

As seen previously, the gain medium amplifies incident waves because of population inversion. But to obtain laser oscillation, the optical gain of the active material must overcome the overall losses of the laser system. The minimum population inversion density necessary to compensate the losses is called the ‘threshold’. As an example a Fabry-Perot cavity is considered to calculate the threshold condition. The cavity has two mirrors of reflectivity R_1 and R_2, respectively, and the radiation is amplified by being bounced back and forth between the mirrors and passing through the gain medium of length L. We denote as α the average loss per unit length (that could be due to diffraction or scattering loss) and g the optical gain coefficient necessary to compensate the losses [3,17–19].

Ignoring losses, after one pass in the gain medium (and the cavity) the intensity of the light is amplified by G:

$$G = \frac{I_{out}}{I_{in}} = e^{gL}$$ **Eq. 1.21**

Where:

$$g = \sigma_{em}(N_u - N_l) \qquad \textbf{Eq. 1.22}$$

I_{out} is the intensity exiting the gain medium and I_{in} the intensity entering it.

The radiation also experiences a loss of $e^{-\alpha L}$ as it propagates in the medium. If the initial intensity of the radiation at the position of the first mirror, R_1, is I_0 then the intensity of the radiation after hitting the second mirror is $I_0 R_2 e^{(g-\alpha)L}$. After a complete round trip in the cavity, the intensity is $I_0 R_1 R_2 e^{2(g-\alpha)L}$. In the case of an amplifying medium in the form of a waveguide (like a layer of OS), then a factor, Γ, describing the overlap of the laser mode with the gain region needs to be added: $I_0 \Gamma R_1 R_2 e^{2(g-\alpha)L}$. This overlap will be detailed in chapter 2, section 2.6. Here, we consider that $\Gamma = 1$, so we can ignore it.

The lasing threshold is reached when the round-trip amplification overcomes the overall losses, i.e.:

$$R_1 R_2 e^{2(g-\alpha)L} \geq 1 \qquad \textbf{Eq. 1.23}$$

So the gain coefficient at threshold can be written:

$$g \geq \alpha - \frac{\ln(R_1 R_2)}{2L} \qquad \textbf{Eq. 1.24}$$

And the population inversion density necessary to reach threshold is then:

$$N_u - N_l \geq \frac{1}{\sigma}[\alpha - \frac{\ln(R_1 R_2)}{2L}] \qquad \textbf{Eq. 1.25}$$

Equations Eq. 1.24 and Eq. 1.25 show that threshold is reached when the gain of the laser is exactly balanced by the sum of all the losses in one round trip of light in the laser cavity. The inversion of population is linked to the absorbed pump power through the rate equations.

1.3. Organic semiconductors

1.3.1. Different types of organic gain media

There is a variety of organic gain media and more particularly organic semiconductors that has been developed over the years. They can be categorised according to their molecular structure and their fabrication process. The main categories are: dyes, small-molecule organic semiconductors, oligomers and conjugated polymers. All of these gain materials, except from dyes, are organic semiconductors, organic materials with semiconducting properties. Some inorganic emitters also utilise organics: for example colloidal quantum dots (see further section 1.5), having organic ligands.

1.3.1.1. Dyes

The first organic laser was demonstrated with a dye gain medium by Sorokin *et al.* in 1966 [23]. Dyes are now widely used for organic solid state lasers. The most common dyes for laser fabrication are Perylene, Coumarin, 4-(dicyanomethylene)-2-methyl-6-(4-dimethylaminostyryl)-4H-pyran (DCM), 4-(dicyanomethylene)-2-methyl-6-(julolidin-4-yl-vinyl)-4H-pyran (DCM2), Pyrromethane and Rhodamine 6G [24–27]. They are very small solution processable conjugated molecules having a conjugation of about 10 carbon atoms. They need to be dissolved in a polymer matrix as their photoluminescence quenches when the molecules are closely packed. Their proximity engenders non-radiative relaxation pathways [5].

1.3.1.2. Small-molecule organic semiconductors

In contrast to dyes, small-molecule organic semiconductors (also called molecular solids) do not need to be embedded in a polymer matrix to emit. Carriers can hop from a molecule to another and create charge transport and delocalisation [28]. However, molecular solids present a disadvantage: they are not solution processable. This means that the use of several attractive fabrication techniques, such as spin-coating or printing methods, is not possible. The most common molecular solids are anthracene and aluminium tris(quinolate) [5].

1.3.1.3. Conjugated polymers

In contrast to small-molecules organic semiconductors, conjugated polymers are solution processable, which allows much simpler fabrication processes for photonic devices. Conjugated polymers are very big molecules that have a long backbone of repeated units (monomers). Each of these monomers has a size comparable to a dye molecule and can be functionalised with side groups conferring additional properties to the molecules, such as solubility. The first conjugated polymer was fabricated in the 1970's: polyacetylene; however it did not have good electronic properties and forming films with good semiconducting properties was difficult. Advances in organic chemistry in the following decades allowed, for example, the addition of ring structures (like benzene or thiophene) and enabled stable molecular conformations [28,29]. The properties of conjugated polymers can be adjusted by tailoring the conjugation length or by adding specific monomer units to the molecule. The main conjugated polymers used as laser gain materials to date are derivatives of poly(phenylene vinylene) (PPV) [30] and polyfluorene (PF) [31].

1.3.1.4. Conjugated oligomers

The main difference between conjugated polymers and oligomers that conjugated oligomers have a much smaller number of monomers, usually below 10, meaning that they can be made monodisperse, i.e. the number of units is constant from one molecule to another. They are also solution processable. Oligomers are the most recent category of semiconducting gain material and are attractive for physical studies and as laser materials in their own right. Complex oligomers have been developed recently: as for example star-shaped molecules, highly branched structures or spiro-linked cyclopentadiene groups allowing adjustment of the electronic and optical properties. These properties can also be tuned by varying the conjugation length or introducing single monomers in the molecule [32].

1.3.1.5. Inorganic gain materials utilising organics

Solution processable inorganic nanocrystals have been developed that incorporate organic molecules or organic ligands. Colloidal quantum dots (CQDs) fall within this category. Further explanation of CQDs is given in section 1.5.

1.3.2. Electronic properties

Organic molecules are mainly formed by carbon and hydrogen atoms. More particularly, backbones of polymers are made of long chains of carbon-carbon bonds. The electronic and photophysical properties of organic semiconductors can be understood by looking at how the atoms forming these molecules are bound together. An isolated carbon atom has six electrons in the configuration $1s^2 2s^2 2p^2$. The orbital 1s represents the core electrons; they do not participate in bonds. The four valence electrons, in the orbital 2s and 2p, are the ones participating in the bonds with other atoms. The spatial distribution of the corresponding orbitals is shown in Figure 1.3. This configuration would normally allow two bonds, via the unpaired electrons of the orbital 2p. However, when actually forming bonds, the electronic configuration of carbon atoms can hybridise, mixing the orbitals 2s and 2p and leading, for example, to a $1s^2 2s^1 2p^3$ (sp^3 hybridisation). This configuration enables the formation of four bonds rather than two, which is a more stable configuration [30,33]. A schematic of the sp^2 and sp^3 hybridisations is shown in Figure 1.4.

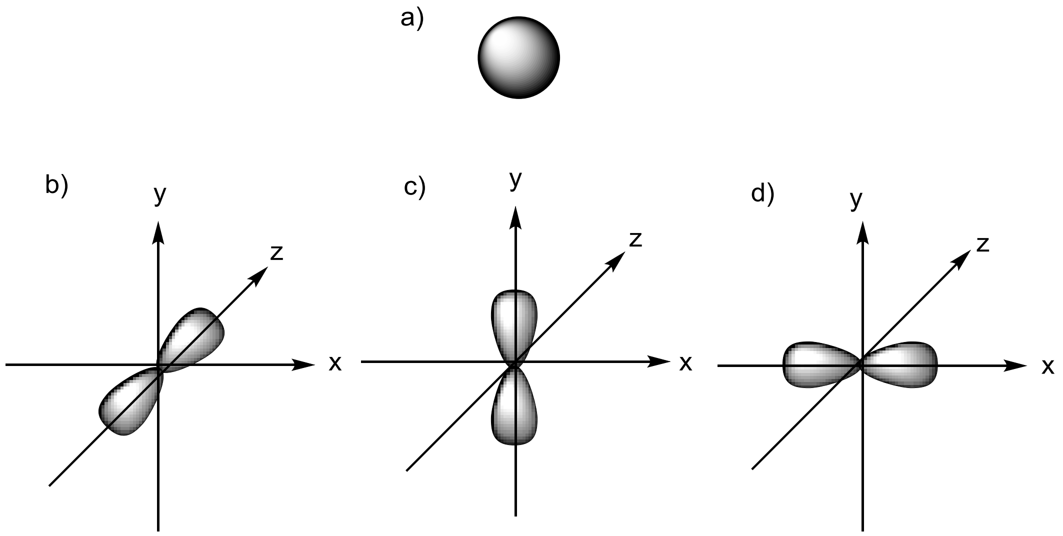

Figure 1.3: a) orbital 2s and b), c) and d) three orbitals 2p.

Bonding in organic molecules can be deduced from the hybridisation geometry. In the case of a double bond between two carbon atoms, three half-filled sp^2 orbitals and an unhybridized 2p orbital are obtained (from the 2s orbital and two half-filled 2p orbitals). Two types of bond are then obtained: a σ bond, which is formed by two sp^2 orbitals from two atoms facing each other and a π bond, which is formed by the two parallel and overlapping 2p orbitals [30,33].

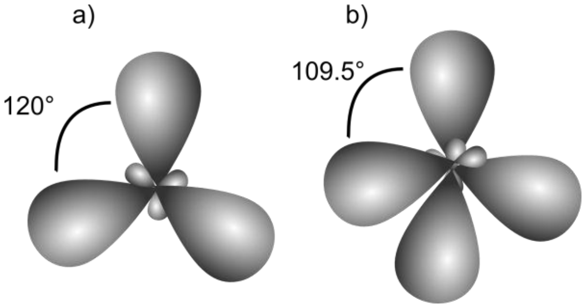

Figure 1.4: a) sp^2 and b) sp^3 hybridisation.

The σ bonds are strong and stable, but the π bonds are weaker. A single bond corresponds to a σ bond and a double bond to a σ+π bond. In a simple representation, this system of connected p-orbitals, a conjugated system, leads to alternating single and double bonds between C atoms. In fact, this picture of alternating bonds is not correct. The π bonds allow electron delocalisation along entire overlapping p-orbitals and the π-orbitals are shared by a group of atoms – the backbone in the case of a conjugated polymer. In principle, therefore, in a conjugated molecule the π electrons are delocalised across the whole molecule. An illustration of π bonds and σ bonds is given in Figure 1.5 in the case of the molecule of ethylene as an example [30,33,34].

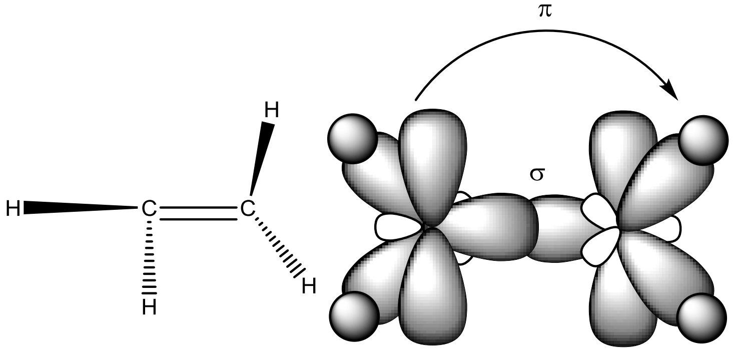

Figure 1.5: π bond and σ bond illustrated in an ethylene molecule.

Furthermore, when a π bond is formed, the wavefunctions of electrons of the p-orbitals forming the bond can be either in phase or out of phase, as shown in Figure 1.6. When they are out of phase, an "antibonding" orbital called π* is formed, having a higher energy than a π bonding orbital that is obtained when they are in phase. π* is called the lowest unoccupied molecular orbital (LUMO) and π is the highest occupied molecular orbital (HOMO). These HOMO and LUMO orbitals are the analogues of the valence and conduction bands in inorganic semiconductors. Under excitation the electrons can move within the whole π* orbital because it is partially empty, producing conductivity (directional conductivity if the molecule is linear). The transition between HOMO and LUMO is the active laser transition for light-emitting organic semiconductors [30,33].

Each π and π* energy level can have two electrons, with four possible combinations of spin (↓↓,↑↑,↓↑,↑↓). A singlet state is obtained when the total spin is 0, i.e. when all the electron spins are paired. A triplet state is when the total spin is 1, i.e. when there are two unpaired electrons. Transitions are possible between singlets and between triplets, but forbidden between a singlet and a triplet. Triplet excited states are called metastable and have a lifetime ranging from microseconds to seconds. Singlet excited states have a lifetime of the order of nanoseconds [30,33,35].

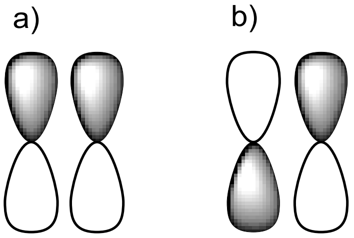

Figure 1.6: a) π orbital and b) π* orbital.

1.3.3. Optical properties

As seen in the previous section, the absorption and emission of photons in conjugated organic molecules is caused by transitions of electrons between π and π* orbitals. The energy gap between π and π* orbitals is determined to a certain extent by the conjugation length. The smaller the conjugation length, the higher the energy required for electronic transitions, hence the shorter the absorption wavelength. As an example Table 1.1 gives the absorption wavelength as a function of the number of benzene rings [36].

Molecule	Number of benzene rings	Absorption λ (nm)
Benzene	1	255
Naphthalene	2	315
Anthracene	3	380
Tetracene	4	480

Table 1.1: Absorption wavelength as a function of the number of benzene rings.

The Franck-Condon principle explains the emission of photons, as illustrated in Figure 1.7 [37]. As the triplet-singlet transitions are forbidden, pump light will excite only singlets from their ground state S_0 to their excited stated S_1. S_0 and S_1 are divided in different vibronic states, having different levels of energy. Excited singlets can relax to the ground state or cross into the triplet state, and singlets and triplets decay radiatively or non-radiatively. This results in two types of luminescence: the luminescence from triplets (long lifetime) is called phosphorescence and the luminescence from singlets (shorter lifetime) is called fluorescence [38,39].

As seen in Figure 1.7, fluorescence and absorption spectra are separated. This separation is called the Stokes' shift. This can be caused by different factors leading to energy loss like molecule dispersity, or for an isolated molecule, vibration transitions (phonons), called the Franck-Condon effect. When the molecule is at an excited state, a rearrangement of the molecular structure engenders a shift in wavelength. The bigger the Stokes shift, the smaller the re-absorption of the luminescence, i.e. the more the material approaches a 4-level system. This can lead to a higher photoluminescence quantum yield and to lower lasing thresholds [40,41].

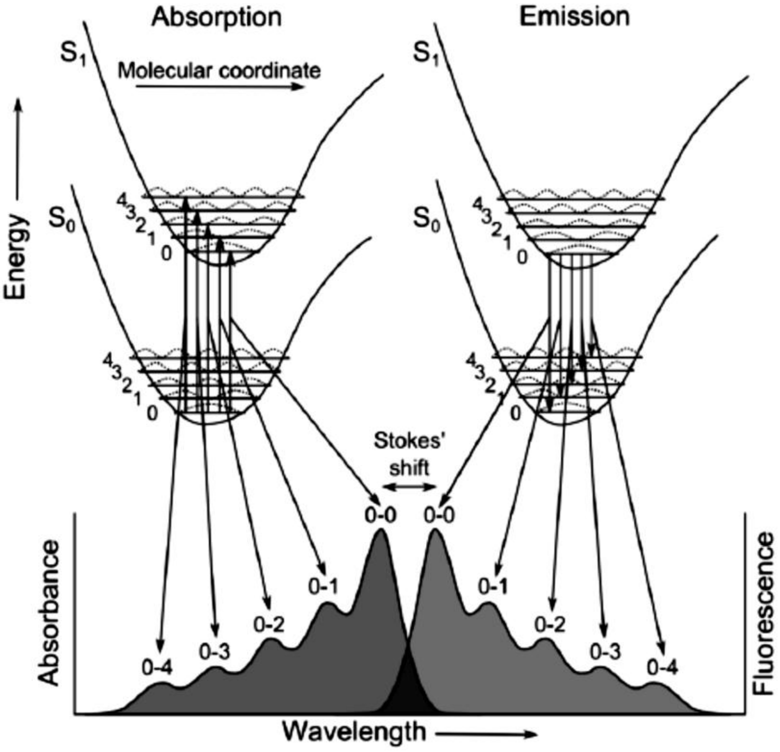

Figure 1.7: Absorption and emission of photons with corresponding absorbance and fluorescence [42]**.**

1.4. Organic laser: background and state-of the-art

The first organic solid-state lasers were demonstrated in 1971 by Kaminow *et al*. and Kogelnik *et al*. who managed to obtain lasing action from, respectively, a DBR resonator and a DFB resonator [43,44]. Both used dye-doped host polymers as gain material. The first laser made with a conjugated polymer in solution was reported in 1992 [45] and, in 1996, the first organic laser made with a solid-state film of π-conjugated polymer was demonstrated by Tessler *et al.* [46]. Since then, organic semiconductor lasers have been developed in many different formats and in a wide range of gain materials due to improvements in material synthesis and processing.

1.4.1. Resonators for organic lasers

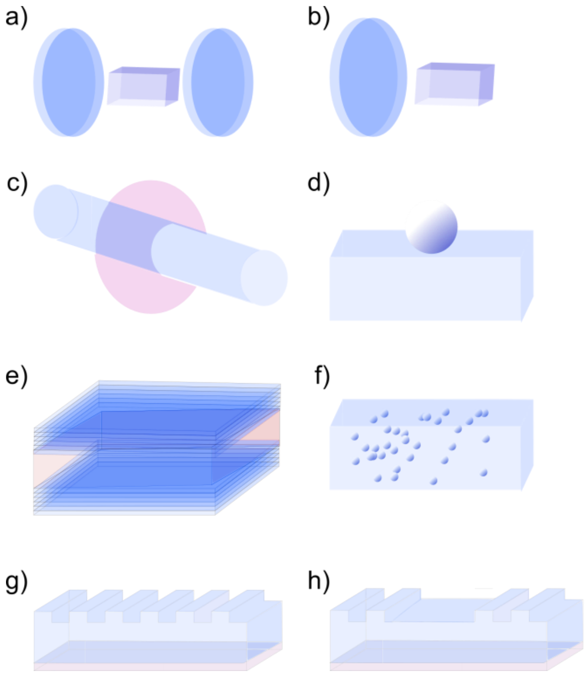

Figure 1.8: Examples of different resonators that have been used for organic lasers: a) 'classic' Fabry-Perot cavity, b) variation of Fabry-Perot cavity using only one mirror and a polished facet, c) micro-ring resonator, d) microsphere resonator, e) VCSEL, f) random laser, g) one dimensional DFB laser and h) DBR laser.

As mentioned previously, a laser is made of three elements: a gain material, a pump source and a resonator (an optical cavity that amplifies the light by creating feedback through the gain medium). Various types of organic laser resonators have been demonstrated [5]. The simplest case consists in two mirrors placed in parallel, with a rod of gain material placed in between, as seen in Figure 1.8 a). This configuration, called a Fabry-Perot, is the classic laser cavity and it has been used for organic lasers [47,48]. A variation of this cavity has only a mirror on one side while the opposite facet of the rod is polished in order to get Fresnel reflection, as shown in Figure 1.8 b) [49,50]. As illustrated in Figure 1.8, other types of resonators are used for OS lasers, for example, micro-resonators in the form of an optical fibre coated with polymer [51,52] or of a microsphere resonator fabricated by lithographic patterning where the organic semiconductor film is etched to form a sphere [53]. The two latter types are whispering gallery mode cavities and have non-directional outputs. Other OS lasers that have been demonstrated include random lasers (Figure 1.8 f)) (a type of laser that does not have a cavity per se but is made of a highly disordered gain medium with light confined by random scattering) [54,55], vertical cavity surface emitting lasers (VCSELs) (Figure 1.8 e)) (a type of Fabry-Perot laser with a thin gain region “sandwiched” between two DBR mirrors) [46,56], vertical external cavity surface emitting organic laser (VECSOL) (a half VCSEL structure with the second mirror separated from the structure by an air gap) [57], DBR lasers (Figure 1.8 h) [43,58] and DFB lasers (Figure 1.8 g)) [8,59–61]. The DFB resonator is basically a photonic crystal structure in one or two-dimensions. The laser output characteristics are dominated by scattering at the periodic structure. Details of the principles of DFB lasers will be given in chapter 2.

1.4.2. State-of-the-art

In this section, a review of different characteristics (wavelength, threshold and photostability) of organic lasers reported in the literature is compiled. The data collected is for lasers with different cavity formats: DFB lasers, facetted waveguide lasers, DBR lasers, VCSEL, VECSOL, micro-ring lasers, droplet lasers, doped fibre lasers, random lasers and Fabry-Perot lasers.

1.4.2.1. Wavelength

An overview of the wavelengths of the different types of organic lasers is given in Figure 1.9. As stated earlier, one of the major advantages of organic gain media is the availability of chromophores emitting through the entire visible spectrum. The shortest wavelength was obtained for spiro-terphenly emitting at 361.9 nm and the longest for IR-140 dye emitting at 930 nm [62,63]. This wide range of wavelengths was obtained from many different organic materials such as dyes (DCM, coumarin, PM-597 etc.), conjugated polymers (BBEHP-PPV, MEH-PPV, DOO-PPV, etc.), and macromolecules (oligofluorene truxene, perylene, etc.). More than 350 organic lasers have been reported in the past 20 years, and *more than two thirds of these lasers are DFB lasers* [8,24–27,36,41,43,47,49,50,52,54,56–58,60–153].

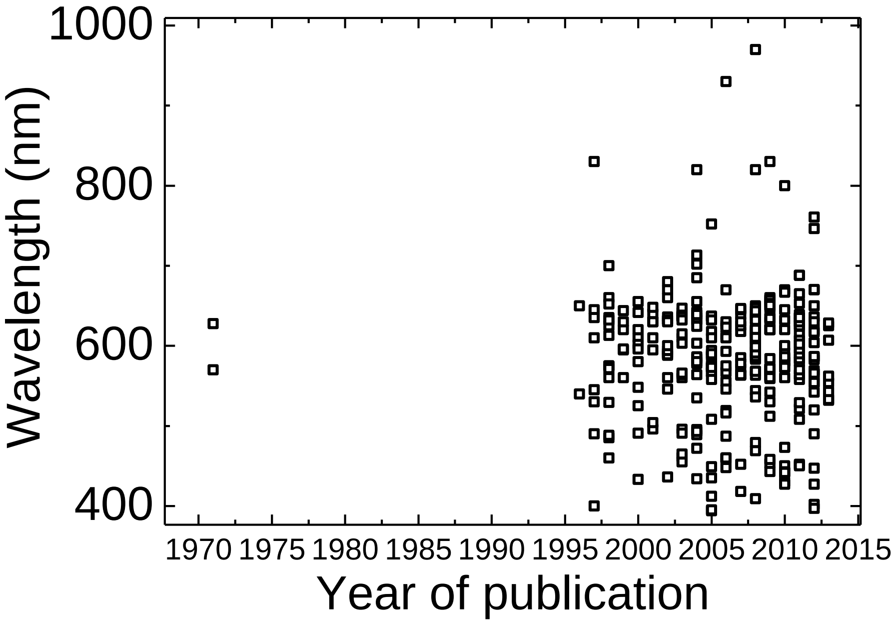

Figure 1.9: Summary of reported wavelengths of organic lasers.

1.4.2.2. Threshold

Thresholds are usually measured in terms of pump energy fluence, F_{th} in µJ/cm^2, or in pump power density in kW/cm^2. When the pulse width of the laser emission is much longer than the singlet state lifetime, the threshold should be given in kW/cm^2 and when the pulse width is much shorter than the singlet state lifetime, the threshold should be given in µJ/cm^2. Figure 1.10 gives the pump energy fluence threshold F_{th} reported in the literature as function of the pulse duration of the pump source for different types of organic lasers. Most of these reported values used solid-state lasers or gas lasers as pump sources but, some of them, having a low threshold, were pumped by laser diodes or light emitting diodes (LEDs). All the pump sources were pulsed, having pulse durations from 150 fs to 50 ns. The lowest threshold was obtained by Karnutsch *et al.* [120] for a pulse duration of 10 ns, for a DFB laser. As seen on Figure 1.10, the lowest thresholds are obtained for DFB lasers [8,24–27,36,41,43,47,49,50,52,54,56–58,60–153].

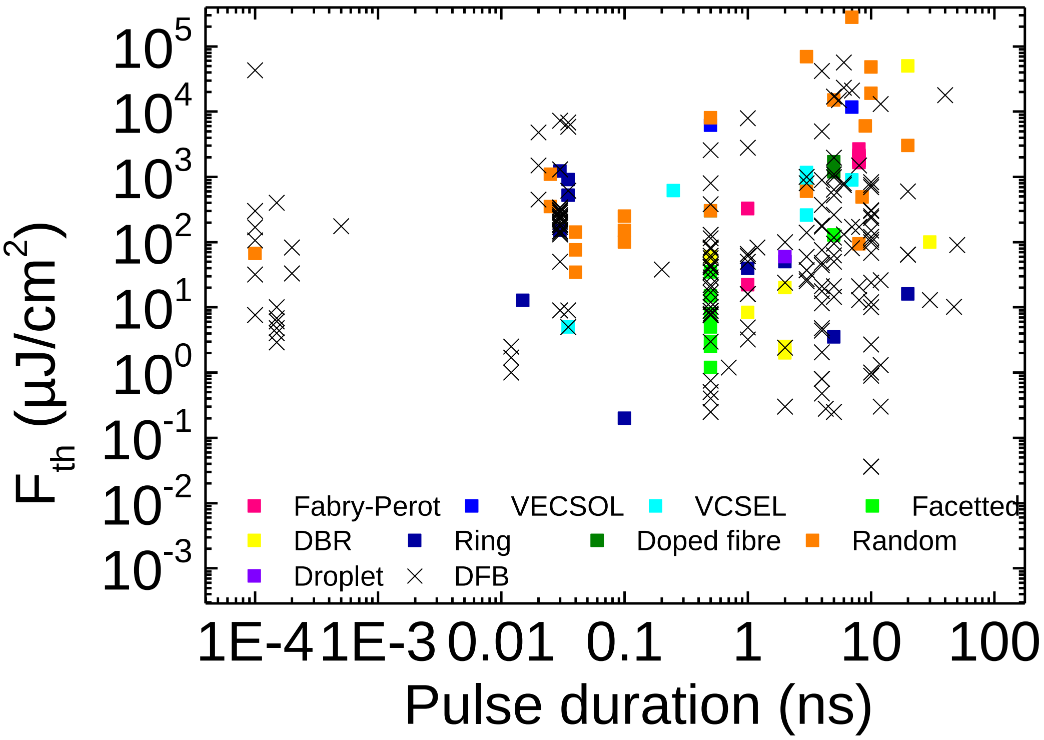

Figure 1.10: Summary of reported thresholds of organic lasers.

1.4.2.3. Photostability

It will be explained in the next section that organic gain media tend to degrade under operation, mainly due to photo-oxidation. A few studies have reported on the photostability of OS lasers. Figure 1.11 shows these reported photostability values, F_{deg}, expressed in J/cm^2 [8,24–27,43,54,56,57,63,94–109]. F_{deg} usually represents the total exposure dose the laser has been exposed to when its intensity has fallen to 1/e of its initial value. However, these values are taken from the literature and sometimes F_{deg} was defined for an intensity drop of 50% or 10% from its initial value, while sometimes it was not even specified. Therefore, values plotted in Figure 1.11 only give an order of magnitude for the photostability of OS lasers. It has been stated that F_{deg} does not depend on the pump source fluence [96,103]. But it can be dependent on the repetition rate as explained in section 1.4.3.2.2. The longest operating lifetime (highest photostability) was obtained for a DFB laser encapsulated with thick glass by Richardson *et al.* [96].

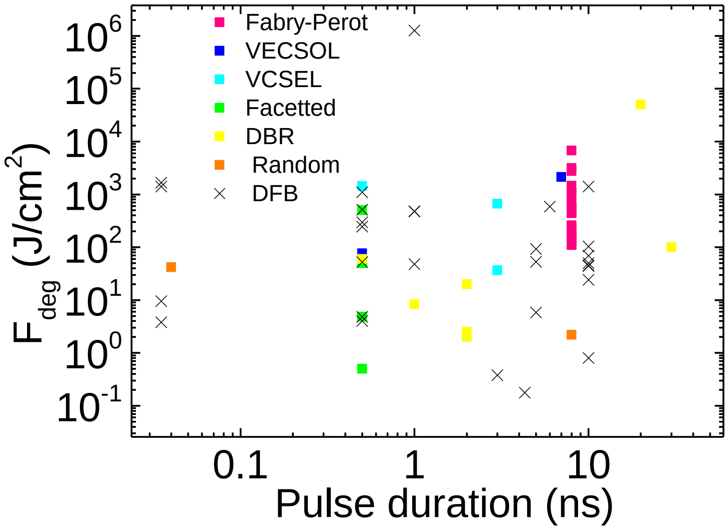

Figure 1.11: Summary of reported photostability of organics lasers.

1.4.3. Challenges

1.4.3.1. Photodegradation

One of the main issues which has limited the application of OS lasers in ‘real-world’ settings so far is that OS degrade under operation in an uncontrolled environment [154–156]. The main mechanisms responsible for such degradation are heat, which can engender thermal decomposition; high energy decomposition, causing photolysis of the molecules; and photo-oxidation [157].

Thermal degradation of organic compounds affects carbon-carbon bonds of the main chain of molecules or bonds between the main chain and side chains. In general the first step of thermal degradation is the separation of the side groups attached to the backbone, forming unstable molecules further reacting and in general forming aromatic molecules (like benzene). Then the second step is the scission of covalent bonds of the backbone, forming oligomers. The last step is called depolymerisation: the backbone is split off forming free radicals (molecules having unpaired valence electrons). These free radicals can then combine and form stable small inert molecules. The polymer then loses its monomers one by one and all its properties. Depolymerisation is an irreversible phenomenon [154,157–160].

In an environment containing oxygen, organic compounds can oxidise. In general, this phenomenon results in the formation of oxygen groups like carbonyl, hydroxyl, peroxide etc., along the backbone of the molecules or at their extremities. This changes significantly the mechanical, physical and chemical properties of the molecules. The oxidation process has two different phases: a first period of initiation of the oxidation starting slowly with oxygen atoms bonding to the molecule and a second phase corresponding to a fast auto-oxidation. This second phase could in certain cases be recognised by an apparent degradation such as a change in colour or texture or even odour [154,155,157,161,162]. Oxidation is facilitated by exposure of radiation, such as light (photooxidation) and more particularly UV light. This phenomenon is called photo-oxidatio. It can engender single oxygen atoms to react with excited electrons in the molecule. It can also cause bond scission of the organic material due to the provision of energy to the molecule by light, engendering the formation of free radicals that bind easily with oxygen. Taking the light coming from the Sun on Earth as an example, and considering photons of wavelength of 400 and 300 nm, the respective corresponding energies are 300 and 390 kJ/mol. However the energy of a C-H bond is 340 kJ/mol. It means that a photon having a wavelength of 300 nm has a sufficient energy to break this bond and a shorter wavelength could be even more effective (to break for example a C-C bond having an energy of 420 kJ/mol) [154].

Photo-oxidation and thermal degradation can happen simultaneously when pumping organic gain materials. For practical applications, it is critical to mitigate these issues by (i) minimising heat build-up in OS through an increase in thermal conductivity and/or possibly low-repetition rate operation and by (ii) preventing photo-oxidation through isolation of the OS gain materials from the environment, using encapsulation or embedding the organic molecules in a host matrix.

To date, encapsulation using an inorganic (glass) layer as oxygen-barrier represents the best method. This is in fact the approach taken for commercial OLEDs. However, such encapsulation, before the work of this thesis, was not compatible with mechanical flexibility. We wanted to find geometries for flexible lasers with improved photostability and with a fabrication as simple as possible. Consequently, all the devices fabricated in this thesis were entirely made in air, although the systems can be extended to fabrication in an oxygen-free environment (e.g. in a glove-box).

1.4.3.2. Pump sources

1.4.3.2.1. Electrical pumping

The second main hurdle to application for plastic-like lasers is their pumping scheme. Direct electrical injection has not been demonstrated yet, due to a combination of unresolved technical issues. The high current density necessary for laser oscillation engenders a poor thermal stability of OS. Metal contacts cause electron trapping at the interface with OS that limits the actual carrier injection. Moreover, other losses are created by the annihilation of singlet-polarons when the excitation strength increases. Finally, another key problem with electrical pumping of OS is the low carrier mobility. To reduce the effect of singlet-triplet/polaron annihilations and induced absorption losses (for example polaron and triplet absorption) a gain medium should have high-carrier mobility. However, the typical charge-carrier mobility for an OS is ~10^{-4} cm^2/Vs and the mobility necessary to obtain electrical pumping should be greater than 5 x 10^{-2} cm^2/Vs [5,11,15,163–165]. For these reasons, all OS lasers are currently optically pumped.

The majority of OS lasers studied in the research environment are optically-pumped with solid-state lasers (but also nitrogen lasers, optical parametric oscillators, etc…). These systems are bulky and can be expensive, which basically prevents applications out of the lab.

Recently, advances in low-threshold OS laser and InGaN semiconductor technologies have been combined for the demonstration of OS lasers pumped by laser diodes (LDs) in 2006 [24,118,124] and by LED in 2008 [118]. Even more recently, InGaN micro-LED pumped lasers have been demonstrated [16]. Indirect electrically-pumped OS lasers can be obtained this way, by pumping the OS laser with an electrically driven inorganic semiconductor device, opening possibilities for fully integrated systems. This paves the way for compact and integrated OS laser systems, thereby greatly enhancing their applicability.

1.4.3.2.2. Pulse pumping

No OS lasers to date are pumped by CW sources but rather require pulsed sources because of the build-up of triplet-state excitons. The associated excited state absorption of triplets at the laser wavelength prevents population inversion. It is therefore necessary to limit triplet formation by using excitation shorter than the triplet lifetime and to leave sufficient time for any triplets to relax between two excitation pulses. Consequently, pulses should ideally be in the range of nanoseconds (or shorter) and the repetition rate should be low [166].

Despite these limitations, schemes are being explored to obtain CW emission. OSL operation at 5 MHz repetition rate has been demonstrated, showing that quasi-CW pumping can be possible [119]. This result was only possible as the material used for the experiment had low triplet state absorption [167].

1.5. Colloidal quantum dots

1.5.1. Quantum size effect

CQDs are nanometre-sized semiconductor crystals with typical size between 2 nm and 10 nm. The size of these nanocrystals is chosen to be comparable to, or smaller than, the bulk material exciton Bohr radius a_0. The electron-hole (e-h) Coulomb interaction determines a_0. Hence, the size of the CQDs will have an influence on the e-h pair state and the electronic energies. This spatial confinement of excitons induces a quantum-size effect, which discretizes the electronic levels.

The resulting energy level separation can reach hundreds of meV. Figure 1.12 a) shows that the radius of the dot determines the band gap of the CQDs. Therefore, their colour can be tuned by changing the radius of the dot even though the material system is the same. Figure 1.12 b) indicates that reducing the size of the CQDs blue-shifts the emission wavelength. Changing the material system is also possible. Consequently, emission from the ultraviolet to the near-infrared can be obtained by modifying the size and/or the material alloy of CQDs [168,169].

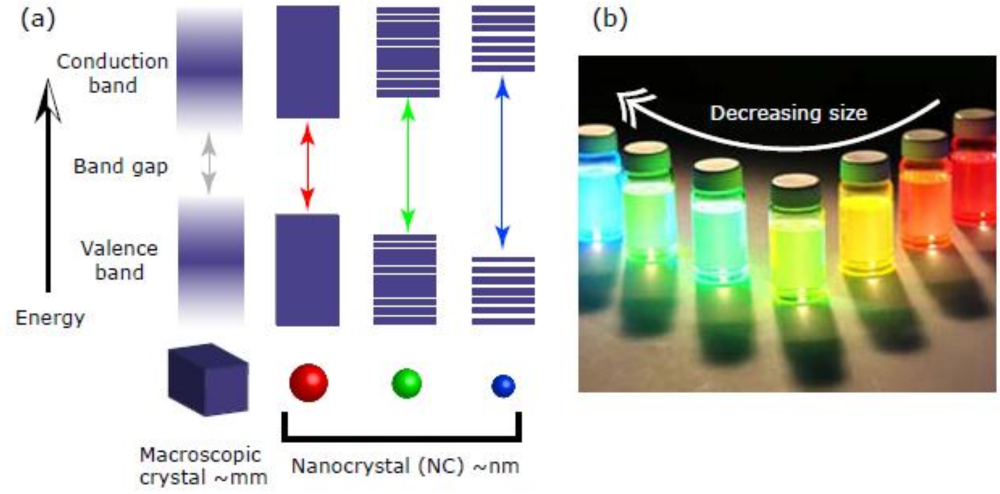

Figure 1.12: a) Band gap of CQDs determined by their radius b) Solutions of CQDs having different diameters [169].

1.5.2. Synthesis and structure

CQDs are synthesised in a variety of material alloys (III-V, II-VI), shapes (spheres, single, twin- and tetra-rods) and compositions. The most developed CQDs for visible emission are spherical and based on cadmium selenide based materials (CdSe). Monodisperse CdSe can be obtained by wet chemistry fabrication. Figure 1.13 illustrates the standard fabrication process where CQDs result from the decomposition of chalcogenides and metal-organics in a high-temperature organic solvent [168,170]. The photoluminescence quantum yield can be improved by adding a zinc sulphide (ZnS) shell around the CdSe core as it passivates dangling bonds, reducing carrier trapping [171,172]. This design geometry is called core/shell. Organic ligands surround the CQDs making them solution processable in the same way as OS [170]. Different ligands can be used depending on the desired solvent.

Two types of core-shell CQDs can be fabricated: “type-I” and “type-II”. The bandgap configuration of type-I confines electron and hole wavefunctions in the core of the CQD thus the radiative combination probability is enhanced and the CQDs produce band-edge emission. Type-II separate the wavefunctions, reducing the probability of a radiative recombination and the emitted photon energy is the difference between conduction (valence) of the core and valence (conduction) band of the shell, respectively [173,174]. Type-I and type-II band gap configurations are illustrated in Figure 1.14.

In this thesis, the CQDs used for the fabrication of lasers are type-I CdSe/ZnS core-shell CQDs.

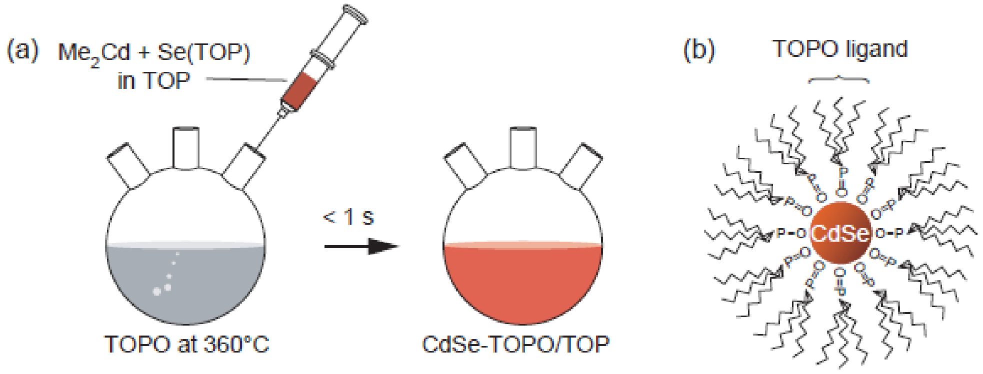

Figure 1.13: Fabrication process of CQDs: a) chemical reaction used for the synthesis of CdSe CQDs and b) CdSe CQD surrounded by organic ligands. Adapted from [169], with TOPO: trioctylphosphine oxide and TOP: trioctylphosphine.

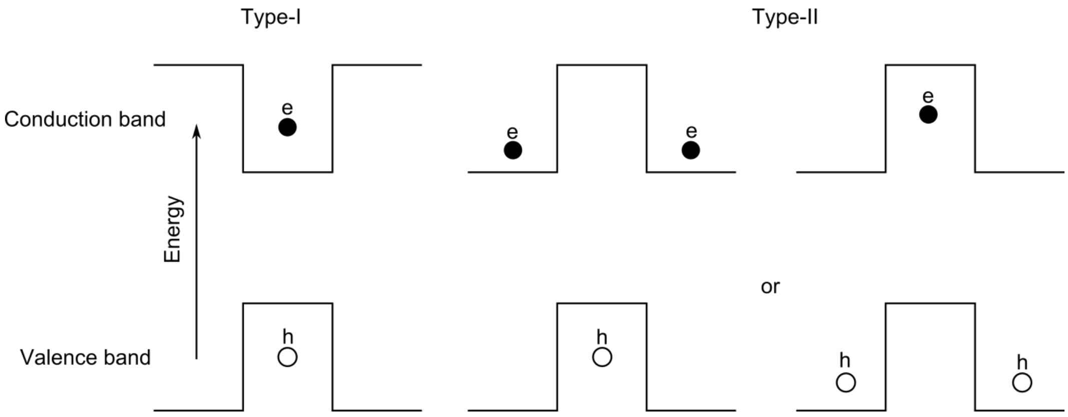

Figure 1.14: Band gap configuration of type I and II CQDs.

1.5.3. CQDs as a laser material

Nowadays, CQDs are applied as biological fluorescent labels, within devices such as light-emitting diodes [175,176], photovoltaic cells [177,178], photodetectors [179,180] and displays [181]. The use of CQDs as laser materials became an active field of research 15 years ago following the first report of optical gain in neat CQDs.

The quantum size effect of CQDs is advantageous for laser applications as it could potentially offer lower threshold, narrower linewidth and higher temperature stability compared to gain media having a lower level of confinement [169]. As stated before, one other advantage of CQDs is that they are solution-processable, making them compatible with a wide range of substrates. In that sense, they are the inorganic counterparts of OS.

Small CQDs can be simply understood with a (quasi) two-level laser scheme. If two electrons in the ground state are considered, one with spin up and one with spin down, then to reach population inversion, one has to excite them both to the excited state, resulting in two e-h pairs (biexciton).

However, the quantum confinement present in CQDs engenders mixing between different valence subbands. This leads to a subband structure with various possible interband optical transition, as shown is Figure 1.15 a). As seen in Figure 1.15 b), the linear absorption spectrum of a CQD involves corresponding transistions to these subbands. For this example, there are four resolved transitions corresponding to 1S and 1P electron states [182].

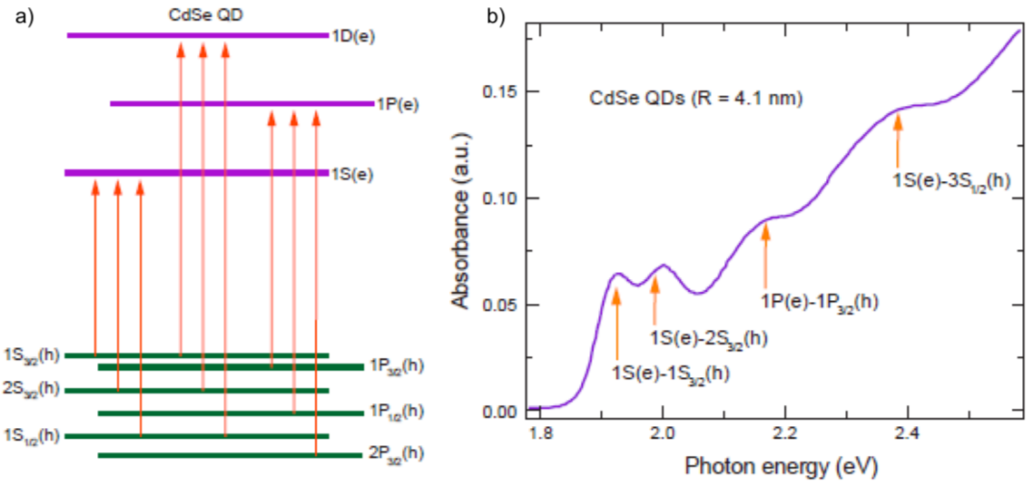

Figure 1.15: a) Subband structure of a CdSe CQD and b) corresponding linear absorption spectrum [182]**.**

The first demonstration of gain in neat solid-state CQDs was demonstrated by Klimov *et al.* [183]. However, it was identified early that one of the main challenges of CQDs for lasers is the fast Auger recombination rate, which reduces the gain lifetime. Auger recombination engenders nonradiation transfer of energy of an exciton (e-h) to either an electron or a hole [169]. It is possible however to alleviate this issue through careful design of the CQDs and this is an active field of investigations [184]. Since the initial demonstration of optical gain, there have been a number of device demonstrations, including, reports of whispering gallery mode lasers [185–187], vertical cavity surface emitting lasers [188,189] and DFB lasers [190–192]. However, except in a limited number of cases such laser demonstrations have used ultrafast (10s of fs to a few ps) optical pulse excitation with bulky and expensive pump lasers. To enable practical implementation of CQD lasers, operation with nanosecond or longer pulse duration is necessary. If low-threshold operation in such a regime can be achieved, it will then be possible to envisage pumping CQD laser systems with compact Q-switched solid-state lasers and possibly, for sufficiently low threshold, with laser diodes. As for OS lasers, the result will be a reduction in the footprint and cost of the CQD laser technology, bringing it closer to applications.

1.6. Conclusion

Organic semiconductor lasers open the door to simple, compact and possibly low-cost visible lasers suitable for applications like bio-sensing, medical diagnostics, spectroscopy, lab-on-chip, etc. Their solution-processability and resulting mechanical properties makes them attractive as sources for flexible photonics. However, OS lasers present several challenges, including their photostability, which currently limits their deployment. One particular difficulty is to ensure high performance in terms of threshold and photostability in a mechanically-flexible format.

An alternative to organic semiconductors is CQDs. However, despite recent developments, research into CQD lasers is not as mature. In particular, performance of optically-pumped CQD lasers in the nanosecond regime of operation is still limited.

Our work targets both OS and CQD materials to advance the technology of solution-processable mechanically-flexible lasers. The lowest thresholds ever reported for OS lasers have been obtained for DFB cavities. This is why in this thesis all the devices were made with DFB resonators.

Chapter 2

DFB lasers: design, materials and modelling

2.1. Introduction

The first section of this chapter explains the design and principle of operation of a second-order DFB laser – this is the type of laser studied throughout the thesis. The second section lists all the materials that enter into the fabrication of the different lasers studied and give their principal characteristics. The main steps of the fabrication of a solution-processed DFB laser are explained in the third section. The optical pumping set-up implemented for the characterisation of these lasers is described in the fourth section. The last section details the theoretical model of the lasers that is used in the following chapters to discuss and optimise their performance.

2.2. Distributed feedback laser

In its simplest form, a DFB laser consists of a thin film of gain medium and a periodic structure (grating) whose role is to diffract the light back and forth in the thin film through Bragg scattering. As is explained further, in this thesis the thin film of gain material sits directly on top of a substrate that incorporates the grating on its surface. Three main conditions are necessary: (i) the refractive index of the gain material must be higher than that of the substrate and of the superstrate media to obtain a planar waveguide (Figure 2.1); (ii) the gain film thickness must ensure the propagation of at least one transverse mode – ideally this would be the fundamental transverse electric (TE_0) mode (TE, electric field parallel to the plane of the waveguide interface); and (iii) the period of the grating must be chosen so that optical feedback is obtained for the desired mode, at the desired wavelength, to trigger laser oscillation [5].

First of all, the periodic structure is not considered in order to explain how the light is confined within the thin film. A schematic illustration of a slab waveguide made of gain material is drawn in Figure 2.1. This structure can allow light to travel in the z direction without diverging in the x direction. In the representation of geometrical optics, a guided mode is confined in the gain medium by total internal reflection (TIR), following a repetitive path as it travels in the z direction. To have TIR, the refractive index of the organic gain medium must be higher than the refractive index of the substrate and of the superstrate, i.e.: $n_p > n_{sub}$, $n_p > n_{sup}$ and - [193]. More specifically, the modes of a waveguide structure are the solutions of Maxwell's equations, satisfying the boundary conditions of the system. The transverse profile of a mode remains unchanged as it travels in the z direction with a propagation constant that depends on an effective refractive index n_{eff}. In fact, the mode can be pictured as propagating in the *z* direction only within an equivalent medium of refractive index n_{eff}.

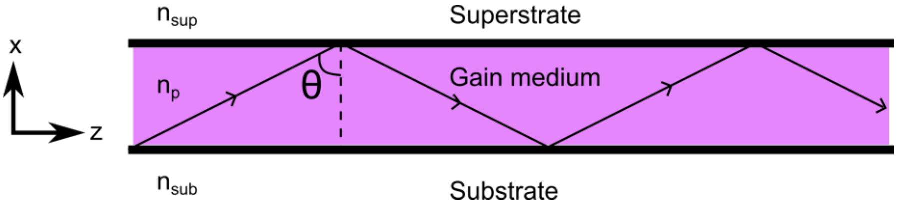

Figure 2.1: A three layer slab waveguide.

It is possible to calculate the effective refractive index of a waveguide mode by solving the so-called dispersion equation. The effective refractive index is important because it affects the laser cavity resonance as we will see later. The dispersion relation can be simply obtained by considering the interference condition in the transverse direction (*x*):

$$\frac{4\pi d}{\lambda}\sqrt{n_p^2 - n_{eff}^2} = \phi_{sub} + \phi_{sup} + 2m\pi \qquad \textbf{Eq. 2.1}$$

With *d* the organic film thickness, λ the wavelength of the light in vacuum, m an integer, n_p the gain material refractive index and Φ_{sub} and Φ_{sup} the phase shift upon total internal reflection at the gain medium/superstrate interface and at the gain medium/substrate interface respectively [193].

Φ_{sub} and Φ_{sup} depend on the polarization of the electromagnetic wave. Two cases need to be considered: when the electric field *E* is along the y-direction (TE) and when the magnetic field *M* is along the y-direction (TM). Φ_{sub} and Φ_{sup} are given for these two cases by:

$$\phi_{sub} = 2tan^{-1}\sqrt{\frac{n_{eff}^2 - n_{sub}^2}{n_p^2 - n_{eff}^2}}\ ; \qquad \textbf{Eq. 2.2}$$

$$\phi_{sup} = 2tan^{-1}\sqrt{\frac{n_{eff}^2 - n_{sup}^2}{n_p^2 - n_{eff}^2}} \text{ for TE mode} \qquad \textbf{Eq. 2.3}$$

$$\phi_{sub} = 2tan^{-1}\frac{n_p^2}{n_{sub}^2}\sqrt{\frac{n_{eff}^2 - n_{sub}^2}{n_p^2 - n_{eff}^2}}\ ; \qquad \textbf{Eq. 2.4}$$

$$\phi_{sup} = 2tan^{-1}\frac{n_p^2}{n_{sup}^2}\sqrt{\frac{n_{eff}^2 - n_{sup}^2}{n_p^2 - n_{eff}^2}} \text{ for TM mode} \qquad \textbf{Eq. 2.5}$$

The thickness of the waveguide, d, determines the number of possible waveguided modes. For a planar waveguide having $n_{sup}=n_{sub}$, TE_0 and TM_0 have no cut-off. However, if $n_{sup} \neq n_{sub}$, there is then a cut-off thickness for each mode. This means that there is a thickness d_0 under which the TE_0 mode is not guided – and below this thickness there are no guided modes at all. For thicker waveguides, there can be several modes. For example, above a thickness d_1 ($>d_0$) both TE_1 and TE_0 can propagate, and so on. This is the same for TM modes but the cut-off thicknesses are usually different.

The dispersions of a few transverse modes are plotted in Figure 2.2 for $n_{sub} =1.526$, $n_{sup}=1$ and $n_p=1.996$ for a wavelength of 530 nm [193]. The thickness of the gain material is chosen to limit the number of transverse modes, i.e. to operate in a single-transverse mode regime for the laser.

For a thin enough film, the effective refractive index of the TE polarization is higher than for TM of the same order. This means that the optical confinement of a TE mode is stronger than for a TM mode of the same order, i.e. it interacts more with the gain material. Hence a lower lasing threshold is typically obtained from a TE mode than a TM mode of the same order. For this reason, in this thesis lasers were designed to oscillate on the TE_0 mode.

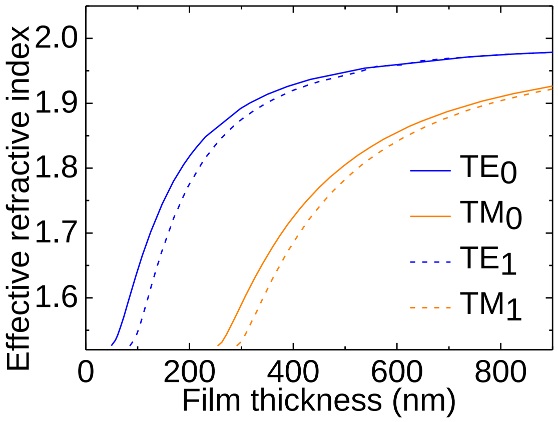

Figure 2.2: Example of TE and TM mode effective refractive index as a function of the film thickness.

Let us now take the full resonator into account and use coupled-wave theory to understand how optical feedback is obtained (Figure 2.3). For this, we consider only one transverse mode (e.g. TE_0) but recognise the possibility for the light to travel in the positive z direction (forward guided wave) and in the negative z-direction (backward guided wave). Note that as an approximation, the equivalent thickness for the gain region can be taken as an averaged thickness considering the grating depth. The diffractive grating structure couples these two counter-propagating waves. This diffractive structure can be a one-dimensional grating [194] but can also be made of two-dimensional and three-dimensional corrugations. In this thesis, the DFB lasers use 1-dimensional gratings, so 2D [8,195] and 3D structures will not be detailed.

The refractive index modulation caused by the grating couples the waves propagating back and forth within the gain medium through Bragg diffraction. The resulting total intra-cavity electric field of the mode can be written as a sum of the forward and backward guided waves:

$$E(z) = \phi(x)\,[A(z)\exp(-ik_b z) + B(z)\exp(ik_b z)]] \quad \textbf{Eq. 2.6}$$

With $\Phi(x)$ the transverse amplitude of the ‘uncorrugated’ guided mode, A the amplitude of the forward wave, B the amplitude of the backward wave and k_b the wave-vector, which for a DFB laser corresponds to the Bragg vector. k_b is defined by the Bragg equation:

$$k_b = \frac{2\pi n_{eff}}{\lambda_b} = \frac{m\pi}{\Lambda} \qquad \textbf{Eq. 2.7}$$

with n_{eff} the effective refractive index of the mode, λ_b the Bragg wavelength, m the diffraction order and Λ the grating period [5,196] and where m determines the emission mode of the laser. In a DFB grating of order m, in-plane feedback is provided by the m^{th} scattering order and all other orders couple light out of the waveguide.

For a first order DFB laser, $m=1$, there is only one diffraction order, which is in the plane of the film and gives the feedback. In this case, the laser emission is obtained from the edge of the gain film. The equation Eq. 2.7 becomes:

$$\frac{2n_{eff}}{\lambda_b} = \frac{1}{\Lambda} \qquad \textbf{Eq. 2.8}$$

A first order DFB laser is illustrated in Figure 2.3 a).

For a second order DFB laser, $m=2$, then laser emission is perpendicular to the plane as the first diffraction order is scattered out of the waveguide at 90° and the second order of diffraction is in the plane giving the optical feedback. In this thesis second order DFB lasers are used. In this case, the equation Eq. 2.7 reduces to:

$$\frac{n_{eff}}{\lambda_b} = \frac{1}{\Lambda} \qquad \textbf{Eq. 2.9}$$

A second order DFB laser is illustrated in Figure 2.3 b).

One can see from equation Eq. 2.9 that n_{eff} is critical for the choice of the grating periodicity. In practice, this means having a combination n_{eff} and Λ that aligns the Bragg resonance to the desired emission wavelength. For a given periodicity, tuning slightly the thickness of the film provides some flexibility for setting the emission wavelength.

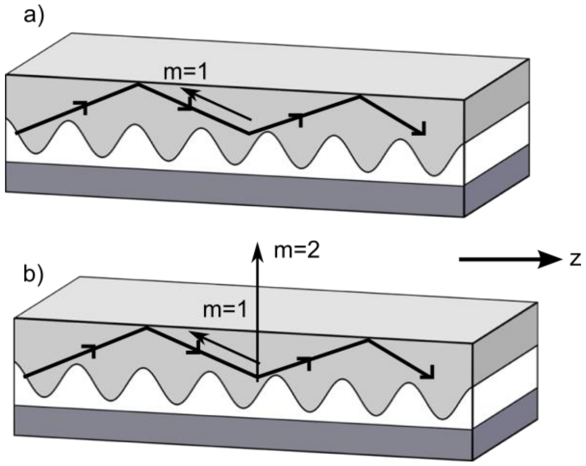

Figure 2.3: a) First order DFB laser and b) second order DFB laser

The field inside the waveguide of the DFB consists of the two waves *A(z)* and *B(z)* amplified as they propagate through the *z* direction because of the gain and Bragg scattering and was described in Eq. 2.6. From equation Eq. 2.6 and the wave theory for the Bragg wavelength region, it is possible to find the wave propagation of the coupled waves *A(z)* and *B(z)*:

$$\frac{\partial}{\partial z}A - \left({}^{g}/_{2} - i\delta\right)A = -i\kappa B \quad \textbf{Eq. 2.10}$$

$$\frac{\partial}{\partial z}B + \left({}^{g}/_{2} - i\delta\right)B = i\kappa A \quad \textbf{Eq. 2.11}$$

With g the gain coefficient for the mode, $\delta \approx \beta - \beta_{Bragg}$, ($\beta$ being the modal propagation constant), κ the coupling coefficient, depending on the laser structure, grating height, index contrast, mode overlap with the grating and possibly on the gain.

The solution of these coupled wave equations is:

$$A = a_1 e^{\gamma z} + a_2 e^{-\gamma z} \quad \textbf{Eq. 2.12}$$

$$B = b_1 e^{\gamma z} + b_2 e^{-\gamma z} \quad \textbf{Eq. 2.13}$$

With γ the complex propagation constant defined as:

$$\gamma^2 = \kappa^2 + \left({}^{g}\!/_{2} - i\delta\right)^2 \qquad \textbf{Eq. 2.14}$$

Depending on g and κ, there are three possible regimes for the propagation constant γ: *index coupling* ($g = 0$ and κ is real), *gain coupling* ($g = 0$ and κ is imaginary) and *complex coupling* (κ is complex). In the first case, pure index coupling, a spectral region is present close to the Bragg wavelength where γ has real values. No waves can propagate in this region, called the photonic bandgap. The laser does not emit at the Bragg wavelength in that case but emits at wavelengths at the edge of the photonic bandgap. This happens for deep gratings.

In our case (see later), the grating is relatively shallow and we have a complex coupling. Gain-coupled DFB lasing can occur in the bandgap, close to the Bragg wavelength. For design purposes, considering only the Bragg wavelength is therefore sufficient.

2.3. Materials

2.3.1. Laser materials

2.3.1.1. T3 hexyl – blue emitters

One of the OS gain materials used in this work (chapter 3) are star-shaped macromolecules consisting of π-conjugated oligofluorene arms around a truxene core and called 'T3' (due to the three fluorene units on each arm). The chemical structure of T3, where n=3, is shown in Figure 2.4 a) [197]. Different types of T3 can be synthesised: butyl, hexyl and octyl, referring to the side chains on the fluorene units. All the experiments presented in this work were done with T3 hexyl. One of the main advantages of T3 as opposed to polymers is that it is a macromolecule and as such has a 100% synthetic reproducibility with high monodispersity and purity. It possesses an excellent solubility in most organic solvents. Conjugated star-shaped molecules are particularly attractive as they bring interesting morphological, optical and electrical properties, making them good candidates for optoelectronic applications (transistors, photovoltaic, light-emitting diodes, lasers, etc.) [197,198].

T3 fluoresces in the blue with a photoluminescence spectrum spanning the 410-450nm region, as shown in Figure 2.4 c) along with its absorption which peaks in the UV at ~375nm. The main emission peaks corresponding to the two first excitonic transitions of the material are at about 410 nm and 434 nm. The refractive index is shown in Figure 2.4 as measured by variable angle spectroscopic ellipsometry [5]. At 430 nm, the refractive index of a typical spin-coated film is about 1.82, which ensures a good confinement of the propagating mode within a waveguide structure. Note, however, that T3 is not ideal for diode pumping as InGaN laser diode emitting in the UV are still rare and show relatively poor performance [36].

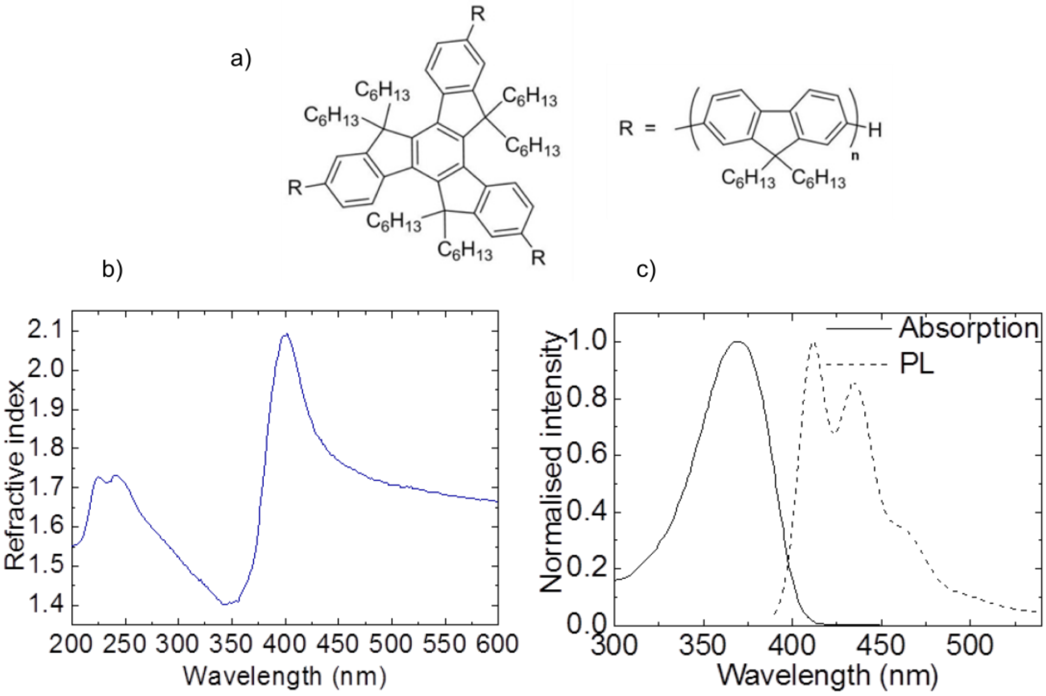

Figure 2.4: a) Chemical structure of T3, b) refractive index of T3 and c) transmission and absorption of T3 in toluene.

2.3.1.2. BBEHP-PPV – green emitter

Another organic semiconductor used as a gain material for the fabrication of the lasers in this study (Chapter 4) is a π–conjugated polymer poly[2,5-bis(2’,5’-bis(2”-ethylhexyloxy)phenyl)-*p*-phenylene vinylene] (BBEHP-PPV), whose main luminescence is in the green region of the visible spectrum. The molecular structure of BBEHP-PPV is shown in Figure 2.5 a). Originally this polymer was synthesised for chemosensing applications by Swager’s group at the Massachusetts Institute of Technology [199]. This material was then reproduced by Skabara’s group at the University of Strathclyde. The gain spectrum of BBEHP-PPV spans the 490-540nm region while the absorption peaks at 431 nm as seen in Figure 2.5 b) [111,199]. This semiconducting polymer is also soluble in toluene, chloroform, tetrahydrofuran (THF), etc., i.e. most of the common organic solvents. However, contrary to T3, BBEHP-PPV is not 100% reproducible and is multidisperse. The length of the molecular chain varies and therefore the molecular weight is not constant from one batch to another of the same synthetic polymer. Consequently, there can be some small differences when using a new batch of BBEHP-PPV, engendering variations in photophysical (photoluminescence and absorption) and lasing properties.

Its absorption peaks being in the blue, BBEHP-PPV is a good candidate for diode pumping as high-power blue InGaN laser diodes are widely available commercially (and can be low cost).

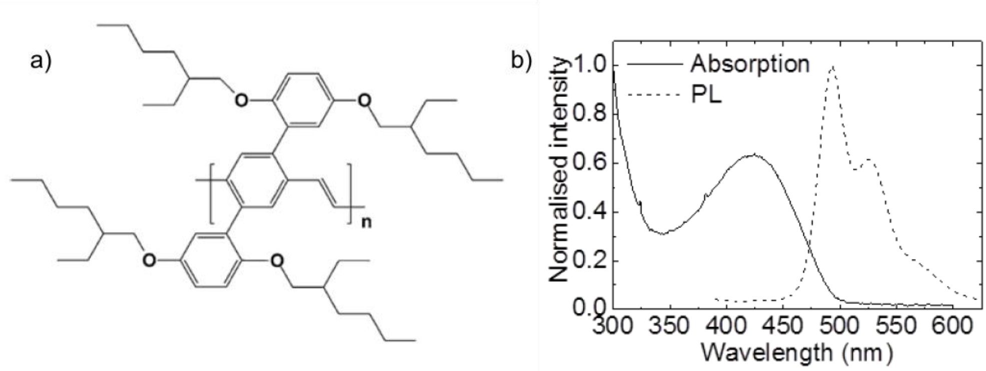

Figure 2.5: a) Molecular structure of BBEHP-PPV and b) Absorption and Photoluminescence.

2.3.1.3. Cadmium selenide colloidal quantum dots – red emitters

CQDs are used in chapter 5. As seen in chapter 1 section 1.5, CQDs are nanometre-sized semiconductor materials (typical diameter of 2-10 nm). Their emission can be tuned from blue to red by increasing the dot diameter from 2.5 nm to 6.3 nm for CdSe CQDs [200]. CQDs also benefit from a high photoluminescence quantum efficiency in solution, broad absorption and narrow bandwidth emission in combination with solution process compatibility [201].

In this work, type-I discrete CdSe core and ZnS shell CQDs (see in Figure 2.6 a)) were chosen. These CQDs are widely available commercially such as the Lumidots™ series from Nanoco with emission ranging from 480 nm to 630 nm with PLQY of 30 to 50% in liquid phase [200]. Only red-emitting Lumidots were studied here. The emission and absorbance spectra of four types of Lumidots are displayed in Figure 2.6 c).

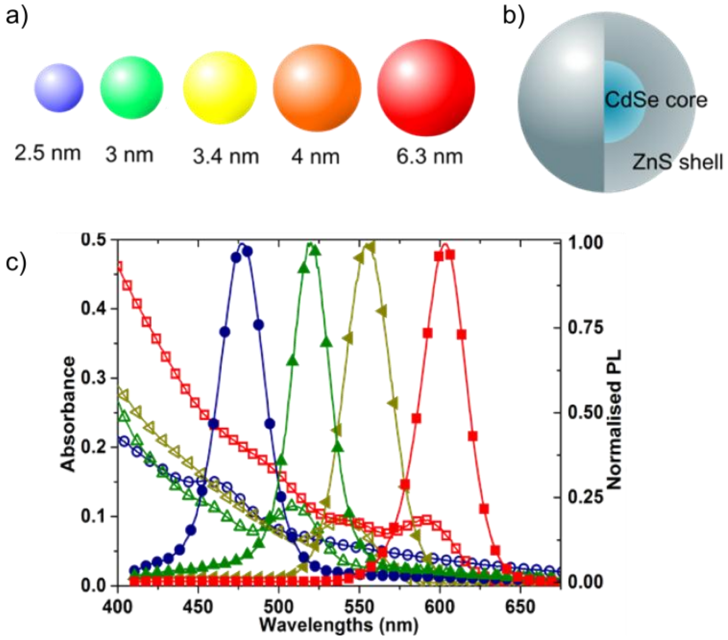

Figure 2.6: a) Schematic illustration of the change in colour of Lumidots^{TM} when increasing the diameter, b) schematic of the CdSe/ZnS CQD structure and c) emission and absorbance of Lumidots^{TM} of different sizes.

2.3.1.4. TPE1 – aggregation-induced green emitter

Another organic gain medium we worked with is called TPE1 (chapter 6). It consists of a tetraphenylethene (TPE) core surrounded by monofluorene arms, as seen in its molecular structure the Figure 2.7 a). This material was synthesised and characterised by Clara Orofino Peña (University of Strathclyde, Glasgow). Figure 2.7 b) shows the absorption and photoluminescence of TPE1 in a solution of dichloromethane. The absorption is broad and peaks at 329 nm. The emission presents two bands: one at ~408 nm and the other one is observed around 530 nm. The refractive index was found to be 1.407 for a 5x10^{-7} M solution of TPE1 in THF at 330 nm.

This material is peculiar in that, in contrast to usual organic emitters, it has high fluorescence efficiency in the solid state but is a poor emitter when in solution – basically it has the particularity of enhanced fluorescence when aggregated. This effect is called aggregation induced emission (AIE) and was discovered by Tang's group in 2001 [202]. Aggregation increases the fluorescence efficiency due to the shape of the molecules, which cannot pack through a π-π stacking process and because the intramolecular rotations are highly restricted due to physical constraints [203,204]. When these molecules are free to rotate and twist non-radiative relaxation pathways are obtained for the decay of the excited stated, quenching the luminescence, but when the rotations are restricted (in the condensed state) these non-radiative pathways are blocked. TPE is an active AIE core due to its four phenyl groups forming a "propeller" that prevents π-stacking in the solid state [205]. The AIE effect of TPE is already used for various applications, like DNA probes [206], cell imaging [207], explosive detection [208] and organic light emitting diodes (OLEDs) [209].

The AIE property of TPE1 can be demonstrated trivially by adding water to a solution of TPE1. Water engenders the formation of nano-aggregates of material [202]. Seven solutions of TPE1 were prepared, with a constant concentration of 30 mg/mL in THF and water, with different percentage of water: 0%, 10%, 20%, 30%, 40%, 50% and 60%. The AIE can be observed in Figure 2.7 c). It is clearly seen that the two first solutions, with 0% and 10% of water have weak fluorescence but when the amount of water was increased, the emission of TPE1 was strongly enhanced. However, for a much higher amount of water added (60%) of water the fluorescence starts decreasing. To confirm these observations, a spectrum of the emission as a function of the wavelength was taken for solutions having a 10^{-5} M concentration in different THF:H_20 ratio (from 0% to 90%) (Figure 2.7 d)), where the same phenomenon was observed. The fluorescence is highly boosted when water is added, to a certain point (here up to 90%, due to a different concentration of TPE1 in THF/H_2O). This lowering of intensity is due to the intramolecular restrictions, responsible for the AIE, when too many nano-aggregates are formed, forcing them to be too close to each other. Figure 2.7 d) also shows that the emission presents a blue shift when adding water. The increase of water forms some crystals changing the geometry of the molecule, due to a lack of space.

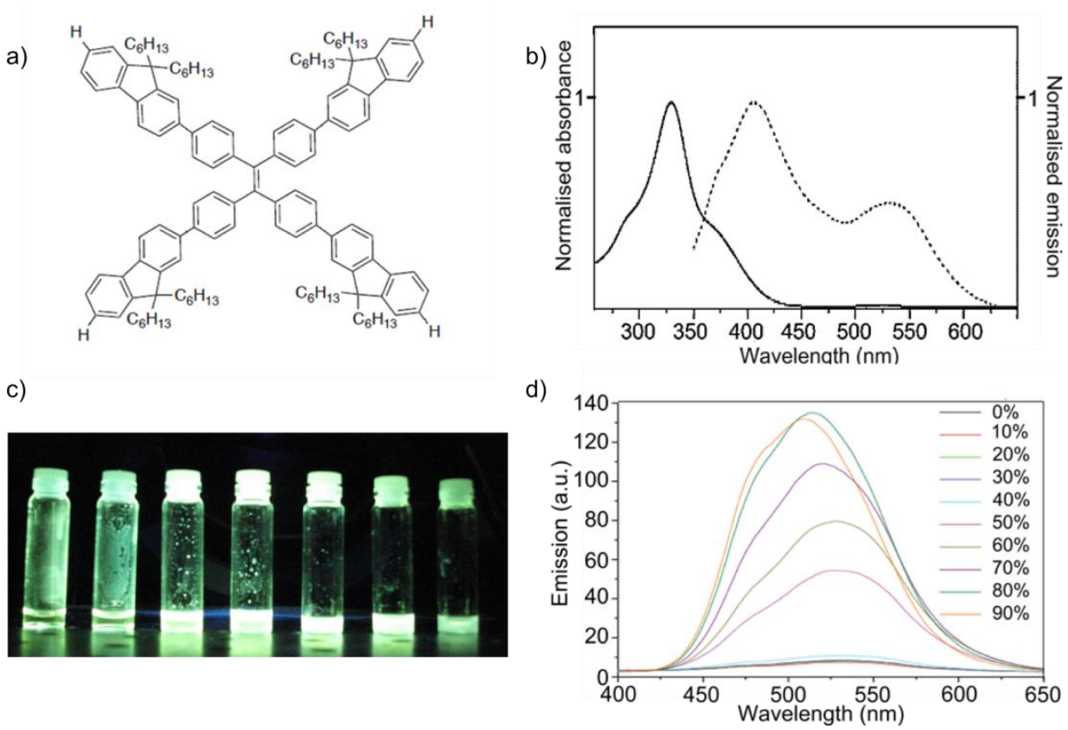

Figure 2.7: a) Molecular structure of TPE1, b) absorption (solid line) and emission (dashed line) of TPE1 in solution, c) 30mg/mL solution solutions of TPE1 in THF:H_2O mixtures with increasing water ratio, under UV light. From left to right 0%, 10%, 20%, 30%, 40%, 50% and 60% of water in THF and d) emission spectrum of TPE1 solutions in THF:H_2O for varying percentage of water.

2.3.1.5. Linear-c DPP – orange emitter

Another oligofluorene organic macromolecule for the gain medium is used in this thesis (chapter 6): linear-c DPP. It is made of a 1,4-diketo-2,3,5,6-tetraphenyl-pyrrolo[3,4-c]pyrrole (DPP) core surrounded by two oligofluorene arms (see Figure 2.8 a) for the molecular structure). Like T3, linear-c DPP is a π-conjugated oligomer, monodisperse, 100% reproducible, soluble in most of the organic solvents and has a high purity. Linear-c DPP fluoresces in the orange with a photoluminescence spectrum spanning the 530-600nm region, as shown in Figure 2.8 b) along with its absorption, which peaks in the UV at ~366nm. The refractive index of linear-c DPP is 1.69 at 633 nm [210]. However, contrary to T3, it aggregates in the solid state due to very strong interactions between molecules. The π-π stacking of the aromatic groups rings of these molecules changes their shape to a propeller-like conformation instead of being planar. This twisted conformation engenders energy losses between the core and the arms of the molecules and prevents the chromophores from emitting efficiently, reducing the lasing capabilities. Thresholds of the lasers having linear-c DPP as gain medium are then higher than for a laser using T3 as gain emitter [210].

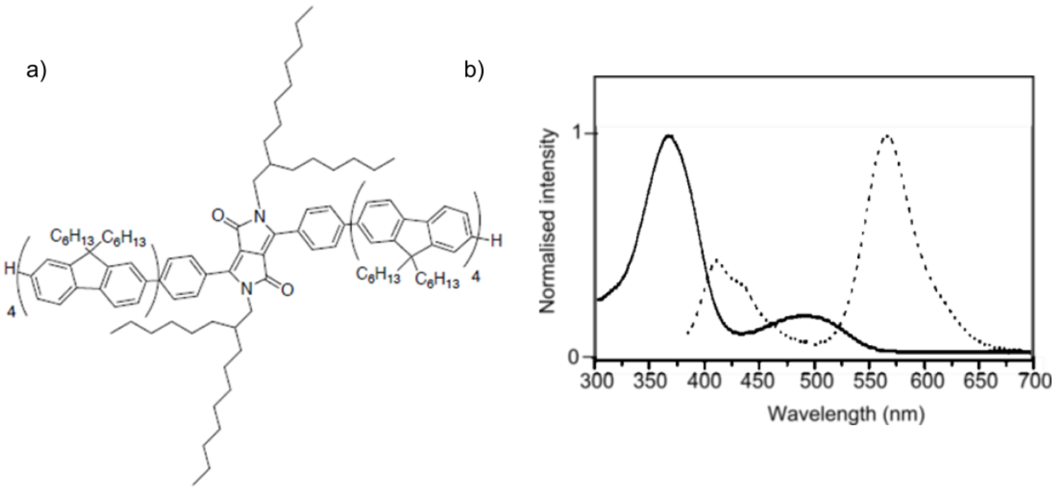

Figure 2.8: a) Molecular structure of linear-c DPP and b) absorption (solid line) and emission (dashed line) of linear-c DPP in solution,

2.3.2. Host matrices and encapsulants

2.3.2.1. CP1

For the nanocomposite lasers studied in chapters 3 and 4 the emitters are incorporated into a host material or matrix. This helps protect the gain material from the environment. The choice of the matrix material is evidently important. Polyimides form a family of polymers that has some attractive attributes for playing that role (high glass temperature transition, TG, and resistance to harsh environmental conditions) but their lack of transparency in the visible had up to now prevented their use in lasers. However, polyimides with improved transparency have recently been developed, making them relevant for photonics [156,211,212]. The CP1 chosen in this thesis for the nanocomposite matrix is a fluorinated polyimide (manufacturer: ManTech), which is highly transparent and very resistant to a harsh environment [211]. It offers high durability against oxygen and has a TG of 263˚C. However, it has a 50% transparency cut-off at 390 nm for a 12µm thick film, from data given in the material datasheet. To form the nanocomposite, CP1 powder was dissolved in tetrahydrofuran (THF) and gain materials were directly added and dispersed inside the liquid matrix to the desired load (weight ratio between solid CP1 amount and gain material) of 4% weight ratio (wr) CP1/gain material without addition of extra solvent. To choose this optimum concentration of CP1, the onset of ASE in films of different concentrations of CP1/gain material was measured.

2.3.2.2. Polyvinyl alcohol

Polyvinyl alcohol (PVA) is a water-soluble polymer. It is a good candidate for encapsulation and it is already used to protect some organic solar cells from oxidation [213,214]. Its molecular structure is given in Figure 2.9 a). It is a highly transparent polymer that has many industrial applications, not only in photonics: for example PVA films are used in food packaging and fishing nets and some sail cloth are made of PVA fibres [215]. For all these applications, the advantage of PVA is that it has a very low oxygen permeability. At 23°C PVA has an oxygen permeability coefficient P of 5.0 x 10^{-17} cm^3 cm/(cm^2 s Pa). In comparison, PET (Polyethylene terephthalate), which is also used for food packaging, has a coefficient P of 3.1 x 10^{-15} cm^2/(s Pa) [214,216]. Figure 2.9 b) shows the barrier property to oxygen of the PVA compared to common polymers.

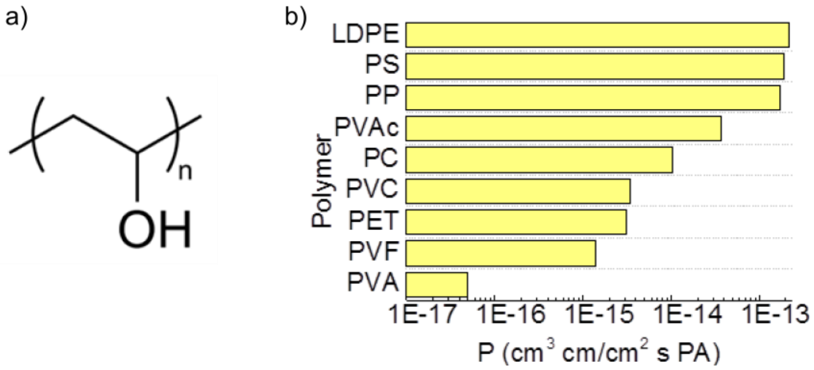

Figure 2.9: a) Molecular structure of PVA and b) Oxygen barrier coefficient of common polymers (with LDPE low-density polyethylene, PS polystyrene, PP polypropylene, PVAc polyvinyl acetate, , PC polycarbonate, PVC polyvinyl chloride, PET Polyethylene terephthalate and PVF polyvinyl fluoride) [216]**.**

Photolysis affects the properties of PVA. Sunlight is one of the main factors of degradation of polymers over time. It causes bond scission of the organic material due to the provision of energy to the molecule (see chapter 1, section 1.4.3.1, for more details on the cause of deterioration of polymers) [154]. In general, photolysis engenders the formation of free radicals that bind easily with oxygen. Then exposure of polymers to harsh UV light is a factor to photo-oxidation [154]. Photo-oxidation of PVA is at the origin of the formation of other products, like acetone, formic acid but also esters, lactones, oxalic and succinic acids, but the main compounds formed are the carboxyl end group (-RCOOH) and carbonyl group (-RCO) [214,215,217]. The reaction which occurs is shown in Figure 2.10. However, due to the low oxygen permeability of PVA the oxidation occurs only on surface of the film. The products of the photo-oxidation stay on the top layer (within 5 µm) and do not affect the deeper layers of the material [214]. We will see that even in thin-films (<1 µm) PVA is effective at protecting the laser gain region. The PVA used in this study has a refractive index of ~1.55, is 89% hydrolysed and has a molecular weight in the range of 85,000-124,000 g/mol.

2.3.2.3. Ultra-thin flexible glass

Another way to encapsulate organic materials is to use glass. In fact, this is what is typically done with OLEDs, but, thick glass does not permit the mechanical flexibility of the resulting device. However even solid, inorganic materials like glass can bend if they are made thin enough. Recently, glass manufacturers including Corning and Schott have released high quality ultra-thin glass, mainly for the display market. In our work, ultra-thin glass is used to encapsulate a mechanically-flexible organic laser (chapter 4). For this, we utilised 30µm-thick glass membranes (Schott, AF 32) [218]. The main advantages of using these glass membranes compared to a polymer for encapsulation is that the glass has the same coefficient of thermal expansion as silicon, making it suitable for optical packaging material in the semiconductor industry, a high temperature resistance of up to ~ 600 °C, high transmittance, low roughness and it has an extremely low gas permeability. AF 32 has a refractive index of 1.51 and a roughness <1 nm RMS. The flexibility of the glass membranes is demonstrated in Figure 2.11 a) and b). Figure 2.11 b) shows that even after dicing the glass sheet (with a diamond pen) to obtain a ~2x2 cm glass square, the flexibility remains.

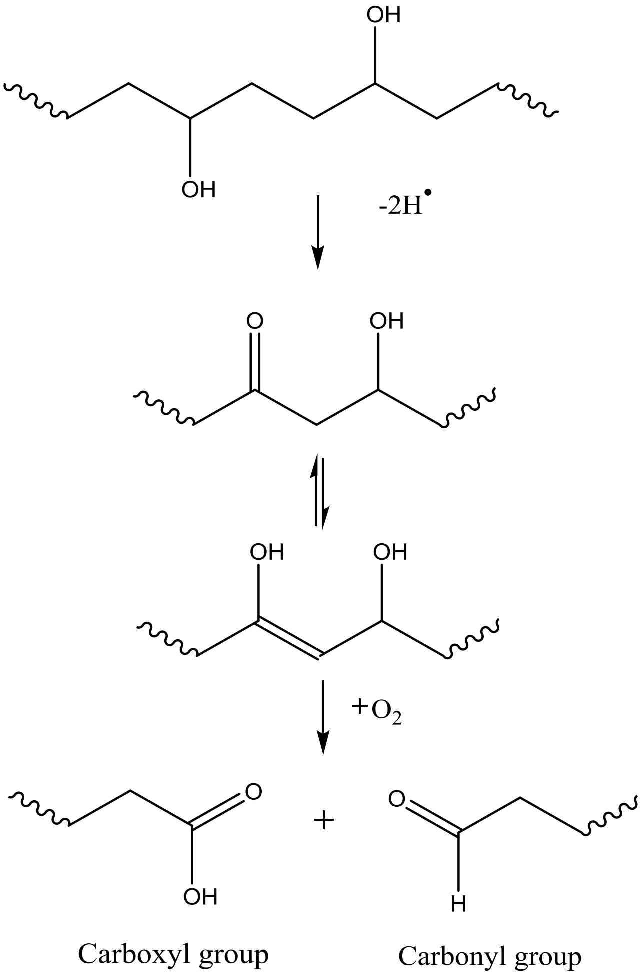

Figure 2.10: Chemical reaction occurring in photo-oxidation of PVA [215]**.**

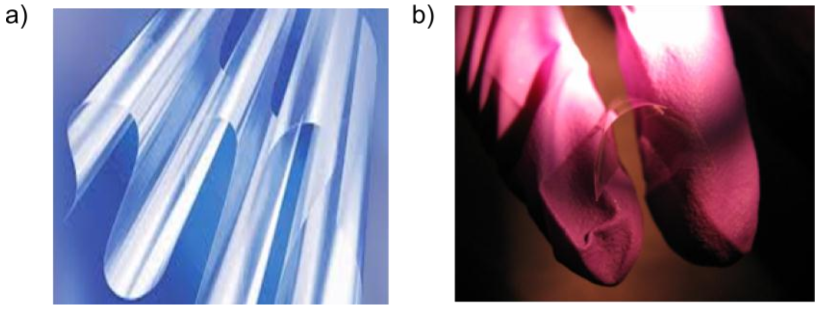

Figure 2.11: a) Photo of flexible glass membranes from Schott website [218] **and b) flexible glass membrane bended after dicing a sheet.**

2.3.3. Inert materials

2.3.3.1. Solvents

Depending on the type of gain materials, different solvents were needed to form thin films by spin-coating. Three organic solvents were used: toluene, THF and chloroform. Each of these solvents has a different boiling point that gives an additional degree of freedom for controlling the thickness of spin-coated films of gain emitters. A higher boiling point solvent typically engenders a thicker film for a same spin-coating-speed, while higher spin-coating speeds are preferable for uniformity of the film. The boiling point of toluene is ~110°C, ~60°C for THF and ~61°C for chloroform [219–221]. So depending on the desired thickness of the gain film to ensure sufficient confinement and promote oscillation on the fundamental TE-polarised mode (see section 2.2), the appropriate solvent and spin-coating recipe was chosen. Another criterion for choosing the solvent is the solubility of the organic semiconductor (or quantum dots) in that particular solvent.

2.3.3.2. Epoxies and transparent polymers

To fabricate the cavities of the DFB lasers studied in this thesis (see section 2.4.1), two commercial polymers were used: NOA65 and NOA85. They are both UV curable transparent, colourless liquid polymers. NOA65 is an epoxy having a refractive index of 1.524 at 589 nm when cured. A UV exposure dose of 4.5 J/cm^2 in air is needed to fully cure the polymer. NOA85 is an acrylate having a refractive index of 1.46 at 589 nm once cured and needs an exposure dose of 3.5 J/cm^2 to be cured. Both materials are flexible with a modulus of elasticity of 20,000 psi and 9,340 psi respectively for NOA65 and NOA85 [222,223] – hence their choice for mechanically flexible lasers. Depending on the gain medium of the laser, either polymer was chosen, according to their refractive index, as the refractive index of the laser cavity must be lower than the refractive index of the gain material to obtain a waveguide (see section 2.2). Another criterion to choose was that it is possible to spin-coat NOA85 but not NOA65, so the choice also depended on the thickness desired.

2.3.3.3. Poly(methyl methacrylate)

Poly(methyl methacrylate) (PMMA) is commonly used as a host matrix for CQDs [224,225]. Even in small quantity, PMMA helps the uniform dispersion of CQDs, yielding films of higher quality than when using neat CQDs. The PMMA used in this work has a molecular weight of 120,000 g/mol. It dissolves in most of the organic solvents (toluene, chloroform, etc.) and has a refractive index of 1.49 [226]. The molecular structure of PMMA is shown in Figure 2.12.

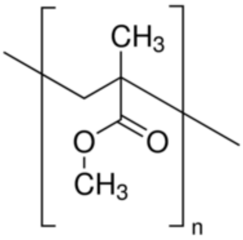

Figure 2.12: Molecular structure of PMMA.

2.4. Fabrication of DFB lasers

The basic fabrication steps of the solution-processed DFB lasers studied in this work are explained here. When extra steps specific to a laser structure are required these are given in the relevant sections of the corresponding chapters.

All lasers studied in this thesis are formed by at least a gain layer deposited on top of a one-dimensional, mechanically-flexible grating acting as the DFB reflector. Deposition is done by spin-coating. A drop of solution is placed on the surface of the polymer grating (usually between 20 and 30 µL) and spin-coated at speeds between 1000 and 8000 rpm, depending on the thickness desired [8]. All processes described below are performed in air.

2.4.1. DFB grating substrate

The mechanically flexible grating is made by soft lithography using a glass master grating, fabricated by electron beam lithography. The latter has a typical modulation depth of 50 nm and a period, Λ, which is chosen depending on the emission wavelength of the gain material (see chapter 2, section 2.2). An SEM picture of a glass master grating having a period of 350 nm is given in Figure 2.13. The master grating features are reproduced into an ultraviolet-transparent and photo-curable epoxy material, Norland NOA65, or an acrylate material, Norland NOA85. They are chosen according to their refractive index, noting that the refractive index of the grating must be lower than the refractive index of the gain layer and that the higher this index contrast, the more efficient the DFB effect.

For the replication process, a drop of NOA65 or NOA85 is either drop coated or spin coated on the master grating. A 0.1-mm-thick sheet of acetate is used as an underlying substrate and pressed onto the epoxy or acrylate that covers the master grating. After photocuring under a UV (370 nm) dose of 300 mJ/cm^2 when using NOA65 and 100 mJ/cm^2 when using NOA85, the flexible grating is peeled off the master and then further post-cured under UV light for about an hour for NOA65 (~1.8 J/cm^2) and half an hour for NOA85 (~0.9 J/cm^2). A flexible grating replicating the features of the master is then obtained. An atomic force microscopy (AFM) image and a profile scan of a typical grating fabricated this way can be found in Figure 2.13 b) and c). These measurements were made on an epoxy grating with a period of 350 nm.

In some instances, other holding substrates are used, such as flexible glass membranes or silicon (see chapters 4, 5 and 6). For these cases, the replicated grating is then removed from the acetate substrate and a free-standing flexible film replicating the features of the master is thus obtained. This free-standing film is then transferred onto the desired substrate. A drop of NOA85 or NOA65 is spin-coated at 8000 rpm on top of the receiving substrate prior to the transfer. The latter is followed by the final photocuring step under a UV flooding for a total exposure dose of ~1.8 J/cm^2 or ~0.9 J/cm^2.

2.4.2. Neat lasers

When the gain material is deposited from solution onto the grating substrate with no additional encapsulation layers or no host matrix the lasers are referred to simply as “neat lasers”. In this case, the gain layer is made of pure organic semiconductor (or colloidal quantum dots, see chapter 5) dissolved in a solvent and then spin-coated on top of the mechanically-flexible grating. Details on the different solution-processable semiconductors were given in section 2.3.1. Solvents are chosen according to their boiling point (a higher boiling point gives a thinner film for a given deposition recipe) and the compatibility with the OS to yield uniform films. Information on the concentration of gain material in solvent is given in the relevant chapters. As stated before, the thickness of the gain layer has to ensure the propagation of a single transverse electric (TE) mode. The thickness of the layer is determined by controlling the spinning speed at deposition. This thickness is different for each gain medium and will be specified in the relevant chapters.

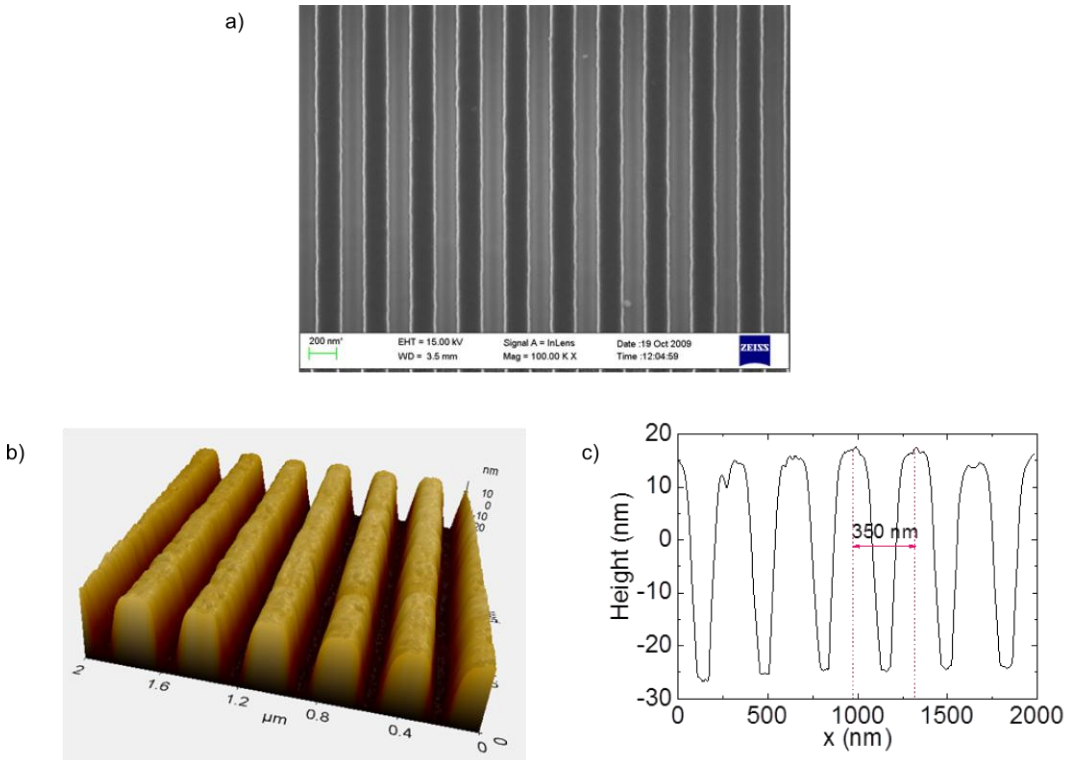

Figure 2.13: a) SEM image of the master grating, b) AFM image of an epoxy grating and c) its profile scan.

2.4.3. Nanocomposite lasers

To form nanocomposite lasers, the gain material is embedded in a polymer matrix. The fabrication process is the same as for a neat laser except that the gain layer corresponds to a mixed matrix/gain material chosen according to the desired properties. The matrix used is the polyimide CP1 detailed in section 2.3.2.1. The ratio of CP1 to gain material will be defined in the corresponding sections.

2.4.4. Encapsulated lasers

An encapsulated laser follows the same fabrication process as a neat laser except that the gain layer is further overcoated with an encapsulant. PVA was used as the polymer encapsulant in chapters 3, 4 and 6. The film of PVA was prepared by mixing an 89% hydrolysed PVA powder, having a molecular weight in the range of 85,000-124,000 g/mol, with deionised (DI) water to obtain a concentration of 50 mg/ml. The solution was stirred for an hour at a temperature of 80°C. After being completely dissolved, the resulting solution was spin-coated on top of the gain layer to form a film 180 ± 20-nm thick, as measured by AFM. While a sub-micron PVA film might not totally suppress photo-oxidation of OS, it is still expected to slow down the process. The device was then annealed in air for three days at 35°C in order to totally evaporate the solvent and obtain a good crystalline cohesion [69]. Encapsulated lasers were also made using the same fabrication process but with a higher concentration (70 mg/mL) of PVA in order to achieve a thicker film (580 ± 70 nm).

In order to determine the thicknesses of PVA, the two solutions were prepared as described in the previous paragraph and spin-coated on glass covers. They were then annealed for three days. A scratch was then made on the PVA layer and the height difference between the scratch and the surface of the layer was measured by AFM. This method was used to determine all thicknesses of thin films in this thesis.

Ultra-thin flexible glass membranes were also used for encapsulation (chapter 4). The initial encapsulation steps differ slightly from the previous method. Once post-cured, a replicated grating (fabricated by spin-coating the polymer on the master grating) is removed from the acetate substrate. The resulting 43µm-thick free-standing epoxy grating is then transferred onto a 30µm thin-glass membrane (AF 32 thin glass from Schott) [218,227]. A drop of NOA65 is spin-coated at 8000 rpm on top of the 30µm-thick flexible glass substrate prior to the transfer. The latter is followed by a photocuring step under a UV flooding for a total exposure dose of 300 mJ/cm^2. BBEHP-PPV is then spin-coated on the grating and overcoated with

PVA (again 180nm thick or 580nm thick) as per the description above. Finally, a second ultra-thin glass membrane is deposited on top of the devices to ‘close’ the encapsulated structure. NOA65 is used to seal the edges of the two glass membranes together. A final photocuring step is applied (UV dose of 300 mJ/cm^2). The device is finally annealed in air for three days at 35°C.

2.5. Photo-pumping characterisation set-up

2.5.1. Laser characterisation

Most of the DFB lasers studied in this work were optically pumped for characterisation by a Q-switched, frequency-tripled Nd:YAG laser emitting 5ns pulses at a wavelength of 355 nm and with a 10Hz repetition rate. The emission of a device was detected by a 50µm-core optical fibre, connected to a CCD-spectrometer with a maximum spectral resolution of 0.13 nm [8]. The samples were placed at an angle with respect to the beam axis to prevent collection of pump photons through the optical fibre. The full width at half maximum (FWHM) pump spot size on the device was measured by knife edge. The pump spot size varied from one experiment to another so it will be defined in each chapter. For each laser, the power transfer function and spectra were measured and in some cases the operation lifetime or photosatbility as well (by monitoring the laser intensity above threshold as a function of pulses). Figure 2.14 shows a detailed schematic of the optical characterisation set-up. The pump energy can be varied (from 6 nJ to 3 mJ) using a quarter-wavelength plate followed by a polariser and a neutral attenuator wheel. A dichroic mirror filters any green components from the laser emission. The various lenses are used to shape the pump spot.

In chapter 4, a laser diode is used to optically pump an OS DFB laser. The specific characterisation set-up will be explained in that chapter.

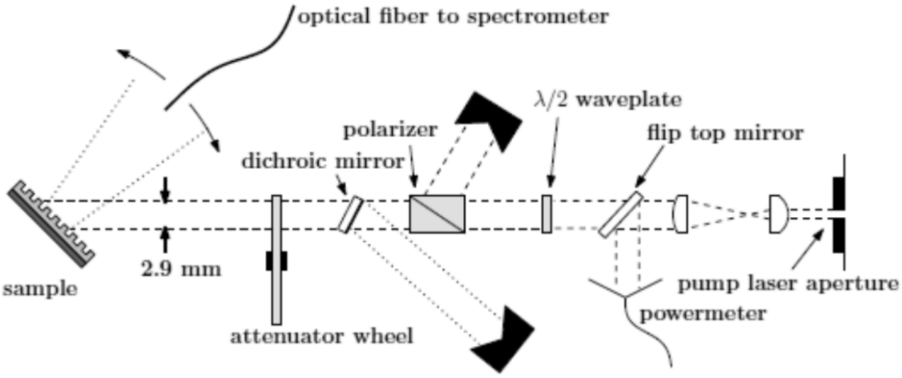

Figure 2.14: Optical characterisation set-up.

2.5.2. Amplified spontaneous emission

In most cases, the potential of the laser materials was tested before making a laser by measuring if a thin film could sustain ASE. The same pump source as for laser characterisation was used. However, instead of a spot, the pump was shaped as a stripe, as shown in Figure 2.15. The typical size of stipe used was ~2.8 x 0.3 mm^2. The gain materials were simply spin-coated into a film on a smooth glass substrate and placed perpendicularly in front of the pump source. The pump stripe excited the gain material from the top. The amplified intensity was then collected at the edge of the sample through an optical fibre going to a spectrometer.

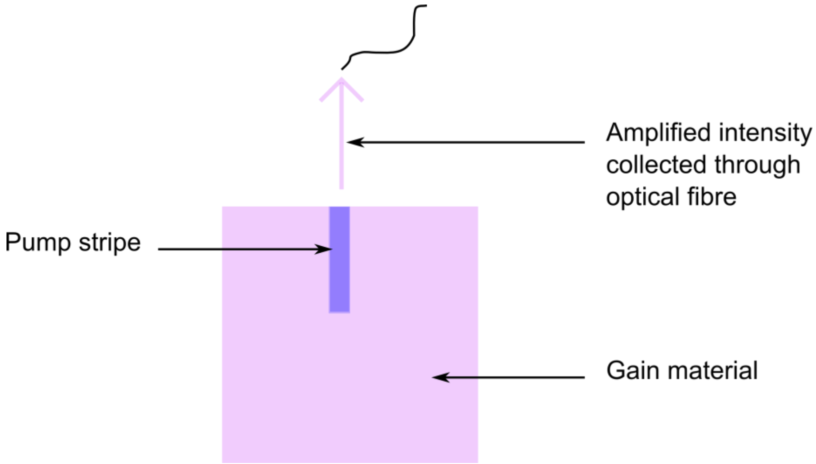

Figure 2.15: Method used to carry out an ASE measurement (plan view schematic).

In such a configuration, a sign of ASE is spectral narrowing (see chapter 1, section 1.2.6). So it possible to determine if a gain material presents ASE, if after reaching a certain pump energy threshold the photoluminescence spectrum shows a spectral redistribution and narrowing peak (see Figure 2.16 as an example). Integrating the spectrum around this 'ASE peak' wavelength and plotting the result as a function of the pump level also gives a function with a threshold-like behaviour above which the slope increases.

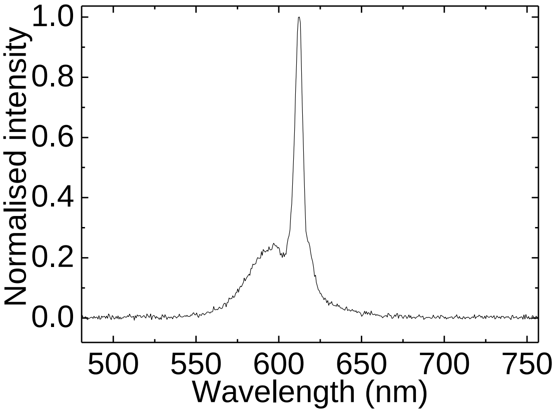

Figure 2.16: Example of spectral narrowing obtained for a gain material presenting ASE (CQDs).

2.6. Modelling

For the discussion on the threshold performance of the devices in part II of this thesis, the laser mode transverse intensity profile and its overlap with the gain region were calculated for the different structures. This overlap, characterised by the overlap factor as defined further below, is important because it influences the modal gain and hence the laser threshold as it can be understood in section 2.6.3 (a higher overlap factor leading to a lower threshold in principle). The calculations were made by considering slab waveguides equivalent to the laser structures, i.e. with the appropriate refractive indices and thicknesses, and using a multilayer matrix model in order to determine the TE_0 intensity profile across the whole laser structure. The principles of this method are explained in [228,229]. The model was adapted and written in Mathcad by **Dr Nicolas Laurand**. An explanation of the model is given below.

2.6.1. Transfer matrix

In order to find the mode profile of a DFB laser, the effective refractive index of the laser mode needs to be calculated. To do this, a matrix describing the boundary conditions at each layer composing the DFB laser is used. The structure of the laser taken into account for the calculation of the transfer matrix is described in Figure 2.17. This figure shows that the laser consists of a multilayer stack of N thin films between semi-infinite substrate and superstrate. The boundaries between the N layers are numbered from 1 to N-1, the layer 0 being the superstrate and N the substrate. To derive the matrix, a plane wave is considered to be incident on the structure with an angle θ. The direction cosines are given by $\alpha = ncos\theta = \sqrt{n^2 - \beta^2}$ with $\beta = nsin\theta$ – β is constant in all the layers and is in fact the propagation constant of the mode.

The transfer matrix allows calculation of the mode profile of the lasers for any layers added on top of the gain medium. This will be useful further on in this thesis when several layers of encapsulation are used (see chapters 3 and 4). While any mode can be calculated, only the mode TE_0 will be considered here.

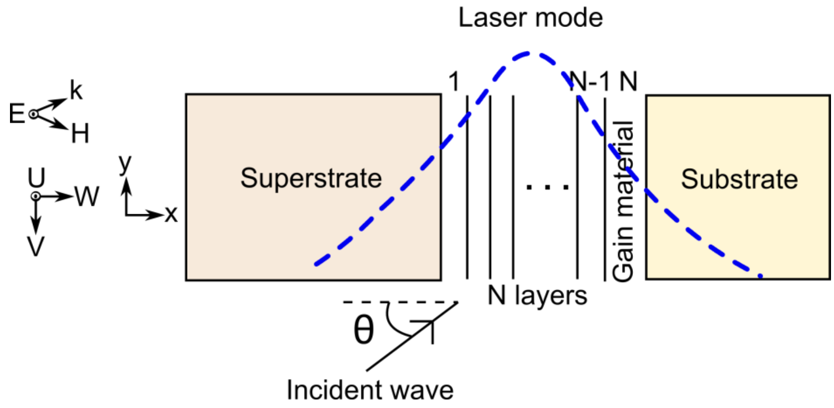

Figure 2.17: Multilayer stack of N thin films bounded by semi-infinite substrate and superstrate layers.

Equation Eq. 2.15 represents the transfer matrix for one layer of the stack, i.e. it links the amplitude of the field at the two boundaries of the layer.

$$M_n = \begin{bmatrix} cos\Phi_n & \frac{-i}{\gamma_n} sin\Phi_n \\ -i\gamma_n sin\Phi_n & cos\Phi_n \end{bmatrix} \quad \textbf{Eq. 2.15}$$

Here Φ_n represents the phase thickness, $\phi_n = k\alpha_n(x_n - x_{n-1})$ and γ is α/z_0 (z_0 being the impedance of free space). This matrix can be derived from the Maxwell's equations applied to a stratified medium and the details of the calculations is reported in the literature [229].

Once M_n is known for each layer of the DFB laser structure, the overall matrix of the structure that links the field amplitude at the substrate and superstrate boundaries can be obtained by the product of all the M_n (equation Eq. 2.15). The result of the calculation (done with Mathcad®) gives:

$$M = \prod_{n=1}^{N} M_n = \begin{pmatrix} m_{11} & m_{12} \\ m_{21} & m_{22} \end{pmatrix}$$ **Eq. 2.16**

2.6.2. Effective refractive index

As discussed, the transfer matrix of the equation Eq. 2.16 links the field amplitude between the interfaces of the substrate and the superstrate. The field satisfies equation Eq. 2.17 (where "*sup*" means superstrate and "*sub*" means substrate and *U* and *V* are the amplitude of the field components, see Figure 2.17).

$$\begin{pmatrix} U_{sup} \\ V_{sup} \end{pmatrix} = M \begin{pmatrix} U_{sub} \\ V_{sub} \end{pmatrix}$$ **Eq. 2.17**

With *U*, depending on *E*, and *V*, depending on *H*, for TE modes, according to Maxwell's equations:

$$U = \frac{1}{ik\gamma\alpha}\frac{dV}{dx}$$ **Eq. 2.18**

$$V = \frac{\gamma}{ik\alpha}\frac{dU}{dx}$$ **Eq. 2.19**

In a perfect system, for a guided mode, the energy would be confined in the stack of thin films by total internal reflections and the amplitudes of the field would be independent of *y* and *z*. According to the radiation condition, the waves are negative going in the substrate so $U = U_{sup}\exp(-ik\alpha_{sup}x)$ and positive-going in the superstrate so $U = U_{sub}\exp(ik\alpha_{sub}(x - x_{sub}))$. For a waveguided mode (for us the laser mode) the field is evanescent in the substrate and the supertsrate and α_{sub} and α_{sup} are imaginary. The equation Eq. 2.17 then becomes:

$$\begin{pmatrix} 1 \\ -\gamma_{sup} \end{pmatrix} U_{sup} = M \begin{pmatrix} 1 \\ \gamma_{sub} \end{pmatrix} U_{sub}$$ **Eq. 2.20**

Eq. 2.20 can be solved to find the modal-dispersion function for bound modes which is given by equation Eq. 2.21:

$$\chi(\beta) = \gamma_{sup}m_{11} + \gamma_{sup}\gamma_{sub}m_{12} + m_{21} + \gamma_{sub}m_{22} = 0$$ **Eq. 2.21**

The solutions (if any) of this equation Eq. 2.21 represent the effective refractive indices of the modes TE_0, TE_1, TE_2, etc.The highest value is for the lowest waveguided mode (TE_0).

2.6.3. Mode profile

Once the refractive index of the TE mode is found, the field distribution between the boundaries of the N layers can be plotted. To do this, one of the values of the field amplitudes is arbitrarily chosen and Eq. 2.22 is used to calculate the field amplitudes at the other points of the laser structure. In our case, the amplitude U was chosen to be 1 at the boundary between the gain layer and the substrate.

$$\begin{pmatrix} U_{n-1} \\ V_{n-1} \end{pmatrix} = M \begin{pmatrix} U_n \\ V_n \end{pmatrix}$$ **Eq. 2.22**

To plot the mode profile of the whole laser structure, equation Eq. 2.23 was used. The mode profile can then be plotted against the refractive index of the laser structure.

$$E(x) = U_n \cos[k\alpha_n(x - x_n)] + \frac{i}{\gamma_n} \sin[k\alpha_n(x - x_n)] \qquad \textbf{Eq. 2.23}$$

The intensity profile of the mode is simply $|E(x)|^2$. The overlap of the modal intensity with the gain region is then given by Eq. 2.24.

$$\Gamma = \frac{\int_0^t |E(x)|^2 dx}{\int_{-\infty}^{+\infty} |E(x)|^2 dx} \qquad \textbf{Eq. 2.24}$$

t represents the thickness of the gain region. The higher this overlap, the lower the threshold of the laser (see chapter 1).

2.7. Conclusion

The principle of operation and the design of DFB lasers were explained. The main elements and the fabrication steps for these DFB lasers were described. The different materials including gain, encapsulation and substrate materials, were listed and their main characteristics given. The principal characterisation approaches and corresponding experimental set-ups were discussed – although more details are given in later chapters. The theoretical model, whose outputs are sometimes used in the discussion of experimental results, was also explained.

The experimental results of this thesis and the related discussions are given next. A fundamental problem for the application of organic semiconductor lasers is the photo-oxidation. The first investigation of this thesis is toward to improving the operational lifetime of mechanically-flexible organic lasers by studying different encapsulation approaches.

Part II
Experiments and results

Chapter 3

Highly-photostable all-organic semiconductor lasers

3.1. Introduction

The overall aim of this chapter is to explore approaches for obtaining low-threshold, highly photostable mechanically-flexible OS lasers. In the first section of the chapter, two formats of all-organic distributed-feedback lasers with improved photostability, respectively called nanocomposite and encapsulated lasers are proposed, demonstrated and studied. These lasers are compatible with mechanically-flexible platforms. The gain elements in both types of these lasers are monodisperse π-conjugated star-shaped macromolecules (oligofluorene truxene, T3). For the nanocomposites lasers, these elements are incorporated into a transparent polyimide matrix, while in the encapsulated devices a neat layer of T3 is overcoated with PVA. These choices of materials for incorporating the gain material and for encapsulation are justified in chapter 2, sections 2.3.2.1 and 2.3.2.2. The T3-nanocomposite devices show a 3-fold improvement in operation lifetime under ambient conditions (photostability) compared to the equivalent non-encapsulated laser, albeit with a 1.6-times increase in threshold. The PVA-encapsulated lasers have the best overall performance: a 40-times improvement in the operation lifetime and crucially no-trade-off on the threshold, with respectively a degradation energy dosage of ~280 ± 20 J/cm^2 and a threshold fluence of 36 ± 8 µJ/cm^2.

Results of this chapter were published in Optics Materials Express (C. Foucher, B. Guilhabert, A. L. Kanibolotsky, P. J. Skabara, N. Laurand, and M. D. Dawson, “Highly-photostable and mechanically flexible all-organic semiconductor lasers,” Opt. Mater. Express, vol. 3, no. 5, p. 584, 2013).

3.2. T3 Lasers

As described in chapter 1, one of the main challenges for application of organic semiconductor lasers is their short photostability under ambient conditions. For practical applications, it is critical to mitigate this issue by (i) minimising heat build-up in the OS through an increase in thermal conductivity and/or possibly low-repetition rate operation and by (ii) preventing or slowing the photo-oxidation process through isolation of the OS gain materials from the environment. One possible way to achieve this is to embed the OS emitters within an appropriate polymeric host matrix, creating (when the OS gain molecules are of appropriate size) a nanocomposite. OS lasers have been reported using such an approach, showing extended photostability but to the detriment of the laser threshold performance [96,152]. Another way to improve the lifetime of an organic laser is to 'encapsulate', i.e. to overcoat, the neat gain region with another material acting as a protective oxygen barrier. However, for mechanically-flexible lasers it is also necessary to maintain the overall mechanical properties of the device. Therefore, standard encapsulation techniques making use of thick inorganic materials (like glass) such as are often used in OLED technology are not directly applicable here [230].

In the following, we demonstrate all-organic, one dimensional, second-order DFB lasers with improved photo-stability based on, respectively, a nanocomposite and an encapsulated gain region, that are both compatible with the fabrication of mechanically-flexible devices. Section 3.3 explains the design and fabrication of these flexible lasers including a reminder of the relevant characteristics of the different materials composing the devices. In section 3.4, the optical set-up used for the characterisation of the lasers is detailed and the laser mode transverse intensity profiles and their overlap with the gain regions are calculated with the multilayer slab waveguide model (see chapter 2, section 2.6). The latter are used in the discussion of the experimental results of section 3.5. The photostability in air of each type of lasers is measured and compared with reference lasers made with neat OS (based on a pure film of OS, i.e. not incorporated in a matrix nor encapsulated) in order to identify the best performing structure with both low lasing threshold and high photostability. In addition, as one of the possible applications of the neat and nanocomposite OS lasers is bio-sensing, which typically necessitates operation in polar solvents, e.g. biological buffers, the photostability of these devices when immersed in deionised water is also highlighted.

3.3. Design and fabrication

3.3.1. Structure of the mechanically-flexible lasers

Figure 3.1 (a), (b) and (c) show the structures of the three types of lasers studied in this section, namely neat, nanocomposite and encapsulated lasers. They are all formed by a gain layer deposited on top of a one-dimensional, mechanically-flexible grating acting as a DFB reflector (see Chapter 2, section 2.4). NOA65 is used here to reproduce the features of a master grating having period of 276 nm (the epoxy is deposited on top of the master grating). The gain layer of both neat and encapsulated lasers is made of pure OS whereas, as stated before, the OS is incorporated into a transparent polyimide matrix in the case of the nanocomposite lasers. Encapsulated lasers use neat OS but are further overcoated with a protective layer of PVA. Common to all these lasers, the active elements of the gain layer are star-shaped tris(terfluorenyl) based on a truxene core (T3) macromolecules that luminesce in the blue region of the visible spectrum (see Chapter 2, section 2.3.1.1). We remind the reader here that the synthesis of these monodispersed macromolecules is 100% reproducible [198] and that they can form amorphous films with low-optical loss that are ideal for laser applications [36]. The gain spectrum of T3 spans the 410-450nm region while the absorption peaks at 375 nm (see Figure 2.4 in chapter 2).

The fabrication of the laser cavity is explained in chapter 2, section 2.4.1, as well as the principal fabrication steps of a neat, nanocomposite and an encapsulated laser. Only the fabrication steps specific to this chapter are given in the following sub-sections.

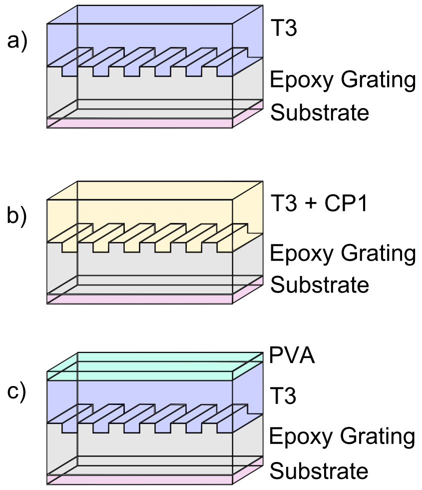

Figure 3.1: Schematics of the device structures are shown: a) neat T3 laser, b) nanocomposite laser and c) encapsulated laser.

3.3.2. Neat T3 lasers

For neat lasers, T3 in solid phase (powder) is dissolved in toluene, at a concentration of 20 mg/mL. To form OS lasers, the dispersed T3 is then spin-coated to form a film of 75 ± 5 nm (as measured by AFM) onto a mechanically-flexible grating and left to dry for a few minutes in air. Such a thickness, determined by controlling the spinning speed at deposition, ensures laser oscillation on a single TE-polarised mode.

A device was also made using tetrahydrofuran (THF) instead of toluene in order to verify the effect of the solvent on the operation lifetime of neat lasers and also because THF was utilised in the fabrication of the nanocomposites lasers.

3.3.3. Nanocomposite lasers

CP1 powder was dissolved in THF and T3 was directly added and dispersed in the liquid matrix to the desired load of 4% wr CP1/T3 without addition of extra solvent.

The nanocomposite was spin-coated to form a 75 ± 10nm-thick film onto the mechanically-flexible grating. Again this thickness and the relevant refractive index values ensure that sufficient confinement is achieved to promote oscillation on the fundamental TE-polarised mode.

3.3.4. Encapsulated laser

The encapsulation was obtained by overcoating a neat T3 layer with a layer of PVA. Similarly to the neat laser, T3 was dissolved in toluene at a concentration of 20 mg/mL and spin-coated on the grating to form a 75 ± 5 nm thick gain material layer. Two encapsulated lasers were fabricated, with a concentration of PVA of 50 mg/mL and of 70 mg/mL respectively. This was in order to check the influence the thickness of PVA has on the photostability of the lasers. The respective PVA film thicknesses obtained with such concentration were, respectively, 180 ± 20 nm and 580 ± 70 nm (evaluated by AFM on a films prepared with the same recipes and spin-coated on glass).

3.4. Photo-pumping experiments and model for mode profile calculations

3.4.1. Optical pumping

The DFB lasers were optically pumped as described in chapter 2, section 2.5. We remind the reader that the pump source emits at 355 nm and has 5ns pulse duration. Moreover, the optimum spectral resolution of the spectrometer is 0.13 nm. The full width at half maximum (FWHM) pump spot size on the sample was 70,000 μm^2 ± 5% for the nanocomposites lasers and 145,000 μm^2 ± 5% for the encapsulated lasers. The differing sizes of the pump spot are due to changes in the configuration of the system between both sets of measurements. However, it was verified that this difference had no significant effect on our lasers in terms of performance by measuring neat T3 lasers in both configurations. Consequently, in the following, all experimental results are discussed in terms of the pump fluence (energy density).

For each laser, the power transfer function and spectra were measured. The threshold given in the text for each laser is obtained by averaging measurements taken at different closely-spaced positions on a device. In order to determine the operating lifetime, the intensity of each laser was monitored and recorded every thirty seconds (i.e. every ~300 pulses) while operated above threshold at a pump fluence of 3.5 mJ/cm^2 unless stated otherwise in the text. This represents a fluence 30 to 100 times the threshold depending on the particular type of laser. Results were then plotted versus the number of pulses. The resulting operation lifetimes are given in terms of the pump energy fluence (F_{deg}) a device has been exposed to when its output intensity falls to 1/e of its initial value. Lasers were characterised in air and ambient conditions except in a few instances, specified in the text, when the lasers were immersed in DI water.

3.4.2. Mode profile

For the discussion on the threshold performance in section 3.4, the laser mode transverse intensity profile and its overlap with the gain region were calculated for the different types of lasers using the model described in Chapter 2, section 2.6. In the case of neat and nanocomposite lasers there is only one layer to be considered, the gain material T3 or the polyimide nanocomposite, enclosed between a semi-infinite epoxy substrate (NOA65) and air or water. For encapsulated devices an additional layer representing the PVA (refractive index~1.55) was taken into account. The mode and refractive index profiles of a neat laser, a nanocomposite laser and an encapsulated laser having an 180nm-thick PVA and a 580nm-thick PVA are plotted in respectively Figure 3.2 a), b), c) and d). Table 3.1 summarises the values of the overlap and the effective refractive index for each of these T3 laser.

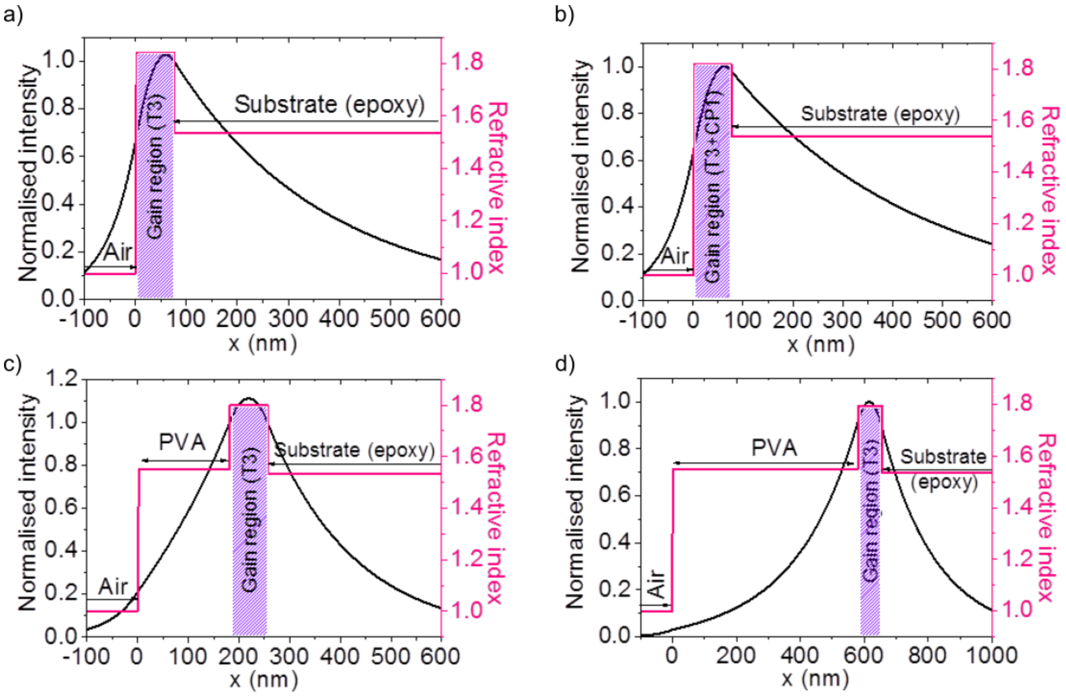

Figure 3.2: Mode and refractive index profile of a) a neat laser and b) a nanocomposite laser, c) a laser encapsulated with a 180nm-thick PVA layer and d) a laser encapsulated with a 580nm-thick PVA layer.

Laser	Overlap (%)	n_{eff}
Neat	16.7	1.55
Nanocomposite	13.4	1.54
180nm thick PVA	23.6	1.58
580nm thick PVA	20.4	1.59

Table 3.1: Values of the overlap and effective refractive index for each T3 laser.

3.5. Experimental results and discussion

3.5.1. Neat T3 lasers

Neat T3 lasers were made and their characteristics measured in order to use them as references for the nanocomposite and encapsulated lasers. Two reference lasers were fabricated using solutions of T3 dissolved, respectively, in THF and in toluene to verify the effect of the nature of the solvent on the laser operation lifetime. These two solvents enter into the fabrication of the nanocomposite and encapsulated lasers, respectively (see section 2.4.3 and 2.4.4).

The power transfer functions and the spectra of both lasers are plotted in Figure 3.3 a) and b). The T3/THF laser emits at 440.6 nm, with a linewidth of 0.32 nm and the T3/toluene laser emits at 426.3 nm, with a linewidth of 0.26 nm. The wavelength difference is simply attributed to the thickness of the gain region, which is around ~130 nm for the T3/THF sample while it is ~75 nm for the T3/toluene device. A thinner gain region leads to a lower n_{eff} and hence to a shorter wavelength (see equation Eq. 2.9 in chapter 2). The emission wavelength obtained for the T3/toluene laser is close to the expected value from the calculated n_{eff} in Table 3.1 (427.8 nm). Average threshold energy fluence, F_{th}, is found to be 30 ± 3 µJ/cm^2 per pulse for the T3/THF laser, whereas it is 70 ± 7 µJ/cm^2 for the T3/toluene laser. The difference in threshold is again an effect of the thicker T3 layer thickness for the T3/THF laser. The 440.6 nm emission wavelength is better aligned with the T3 spectral gain maximum, which peaks around 435-440 nm [228]. Furthermore, the thicker gain region of the T3/THF device leads to a higher spatial overlap factor and hence a higher modal gain. Using the model as described in section 3, the calculated overlap factor for the T3/THF laser and T3/toluene laser are found to be, respectively, 16.7% and 12.5%. Such values are consistent with the lower threshold for the laser having the thicker gain region. The fan-shaped emission of a T3 laser is shown in Figure 3.3. The intensity decay of the neat T3/THF device under constant pulse pumping was measured for 15 minutes (9000 pulses) and the intensity plotted against the number of pulses (Figure 3.3 c)). A mono-exponential decay is fitted to the curve, giving a 1/e degradation dosage, F_{deg}, of 9.4 ± 2.5 J/cm^2. Neat T3/toluene lasers have a similar F_{deg} (11.5 ± 5.8 J/cm^2) [8]. This means that the use of either THF or toluene as solvent has no significant effect on the degradation dosage of T3 and therefore the degradation characteristics of devices fabricated with these solvents can be directly compared.

The intensity decay of the neat laser was also measured in water (Figure 3.3 c)). This was done for two reasons: (i) to study the operation of the organic laser when immersed in a polar solvent, which is relevant for example to biosensing applications [231,232] and (ii) to measure the degradation of the laser when placed in an oxygen-poor environment, i.e. not in air. The intensity was still recorded every 300 pulses but the device was exposed to a higher pump intensity of 13.8 µJ per pulse (7.6 mJ/cm^2, 250 times the threshold). A two-fold improvement in F_{deg} is obtained, with 19.5 ± 5.0 J/cm^2, compared to operation in air. This improvement is attributed to the fact that less free oxygen molecules are present in water than in air, so the device does not photo-oxidize as fast. It is interesting to note that the emitted wavelength stays constant on the timescale of the measurement even as the laser intensity degrades. This indicates that such lasers can be used for refractive index sensing in solution [12,233,234].

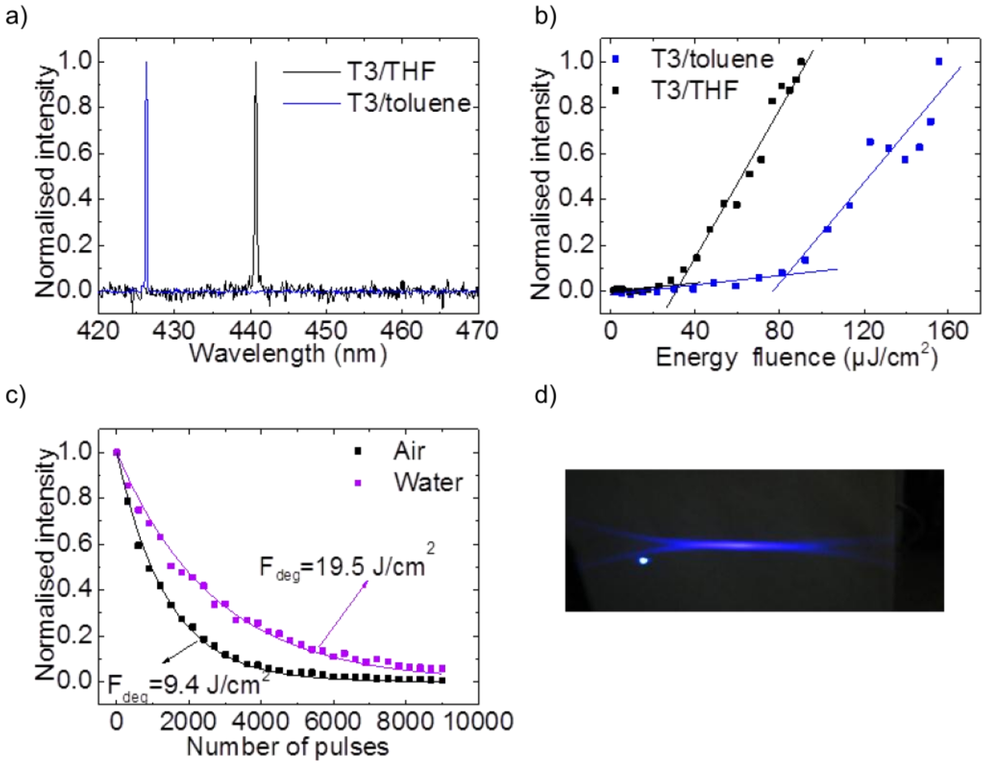

Figure 3.3: a) and b) Respective spectra and power transfer functions of a neat T3/THF and a T3/toluene laser, c) comparison of the intensity decay of a T3/THF laser in air and water and d) fan-shaped emission of a T3 laser.

3.5.2. Nanocomposite lasers

The characteristics of a typical nanocomposite laser are shown in Figure 3.4. It emits at 428.6 nm (Figure 3.4 a)), has a linewidth of 0.20 nm and has a threshold of 115 ±10 µJ/cm^2 (Figure 3.4 b)), which is about 1.6 times the value found for the neat T3/toluene laser emitting close to this wavelength and 3.7 times higher than the T3/THF laser emitting at 440.6 nm (see section 3.5.1)). The increase in threshold is mainly attributed to residual pump absorption by the matrix at 355 nm and to the slightly lower density of T3 molecules leading to a lower modal gain. The expected emission wavelength from the calculation of n_{eff} in Table 3.1 is slightly different from the experimental value. This difference is attributed to the repeatability of the experiment (small changes in the thickness due to the repeatability of the spin-coating, roughness of the gain material, etc.).

Figure 3.4 c) shows a comparison of the photostability in air of the nanocomposite laser with the neat OS laser. The polyimide nanocomposite brings a ~3-fold improvement in terms of photostability with a F_{deg} of 27.0 ± 6.5 J/cm^2. The operational lifetime of another nanocomposite laser was measured both in air and water at a pump energy of 13.8 µJ per pulse (7.6 mJ/cm^2, about 70 times threshold). Results are plotted in Figure 3.4 d). The intensity decay is found to be the same in both media with a F_{deg} of 22.0 ± 4.5 µJ/cm^2, whereas it was twice as long in water for the neat T3 laser. This result shows that the CP1-nanocomposite approach slows-down the degradation of the organic semiconductor and that the intensity decay is probably caused by the oxygen already present in the material after the fabrication process (the lasers being made in air). It also indicates that the benefit brought by the nanocomposite in terms of photostability for biosensing applications requiring immersion of the laser in water/solution is only marginal. Nevertheless, it may bring other potential advantages, e.g. for surface functionalization, and is still advantageous for operation in air.

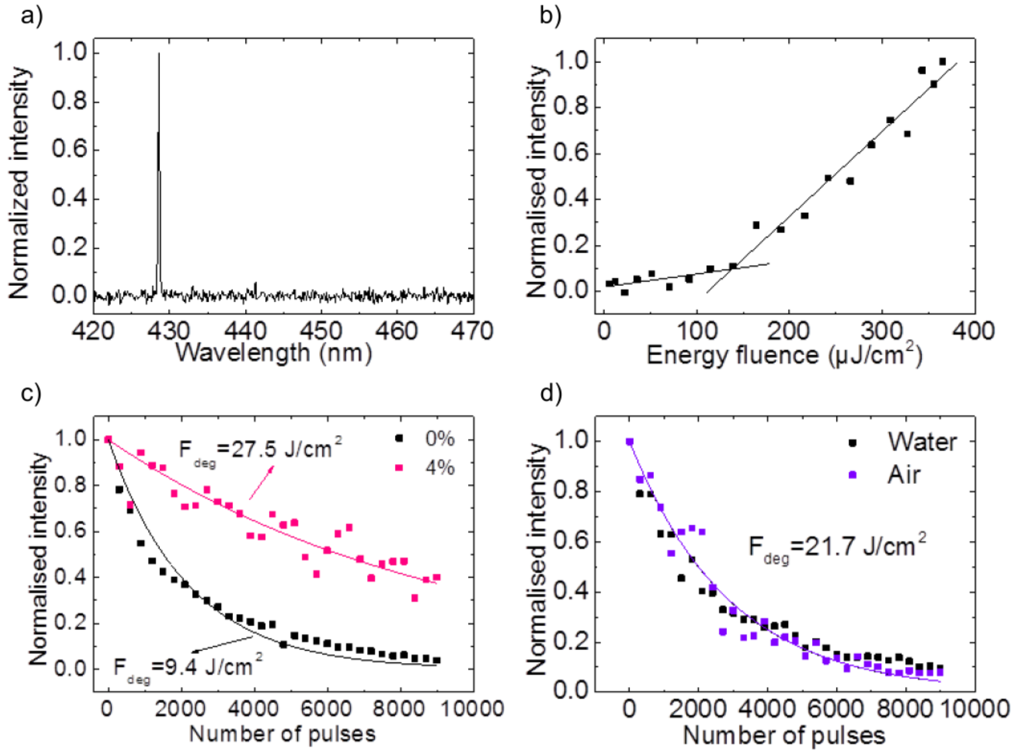

Figure 3.4: a) Emission spectrum and b) power transfer function of a nanocomposite laser, c) comparison of the intensity decay of the nanocomposite and neat laser and d) intensity decay of the nanocomposite laser in air and in water.

3.5.3. Encapsulated laser

3.5.3.1. Laser with a 180nm thick PVA film

The emission wavelength of an encapsulated laser with a 180nm-thick PVA layer is shown in Figure 3.5 a) and is 438.9 nm. The linewidth of the peak emission is 0.29 nm. This emission wavelength is slightly higher than the expected value from the calculated n_{eff}, due to the repeatability of the experiment; however this value follows the expected trend as a red shift was anticipated. The average threshold is measured as 25 ± 6 μJ/cm^2 (Figure 3.5 b)). These values show that the encapsulating layer both redshifts the oscillation wavelength and lowers the threshold when comparing to the equivalent neat laser (F_{th}~70 ± 7 μJ/cm^2 for a 426.3 nm emission). These effects are mainly due to changes in the refractive index profile of the laser structure as shown in Figure 3.2. As a result of the PVA layer addition, the laser mode is pulled away from the substrate and overlaps more with the gain region leading to an increase in the effective refractive index of the mode. To verify this point the modal effective index and the corresponding overlap factor were calculated and found to be 1.543 and 12.5% for the neat laser and 1.5906 and 15.9% for the laser encapsulated with 180 nm of PVA. This is consistent with the emission of a red-shifted wavelength and lower threshold observed experimentally.

The lifetime of the T3/PVA laser was measured and compared to the previous lifetimes obtained for the neat and the nanocomposite devices (see Figure 3.5 c) and d)). The intensity of this OS laser stays stable for ~13,000 pulses and then starts to decrease slowly. We attribute the initial, stable phase to the time it takes to photooxidise the PVA film when photopumped in air and for the oxygen to migrate to the active region. The second phase characterised by an exponential drop in intensity corresponds to the photodegradation of the organic semiconductor. The 1/e degradation dosage, F_{deg}, is here 44.0 ± 1.5 J/cm^2, i.e. 1.6 times longer than for the nanocomposite laser and 6.2 times longer than for the neat laser. Crucially, and unlike the nanocomposite lasers, this increase in lifetime is accompanied by a reduction in the threshold fluence.

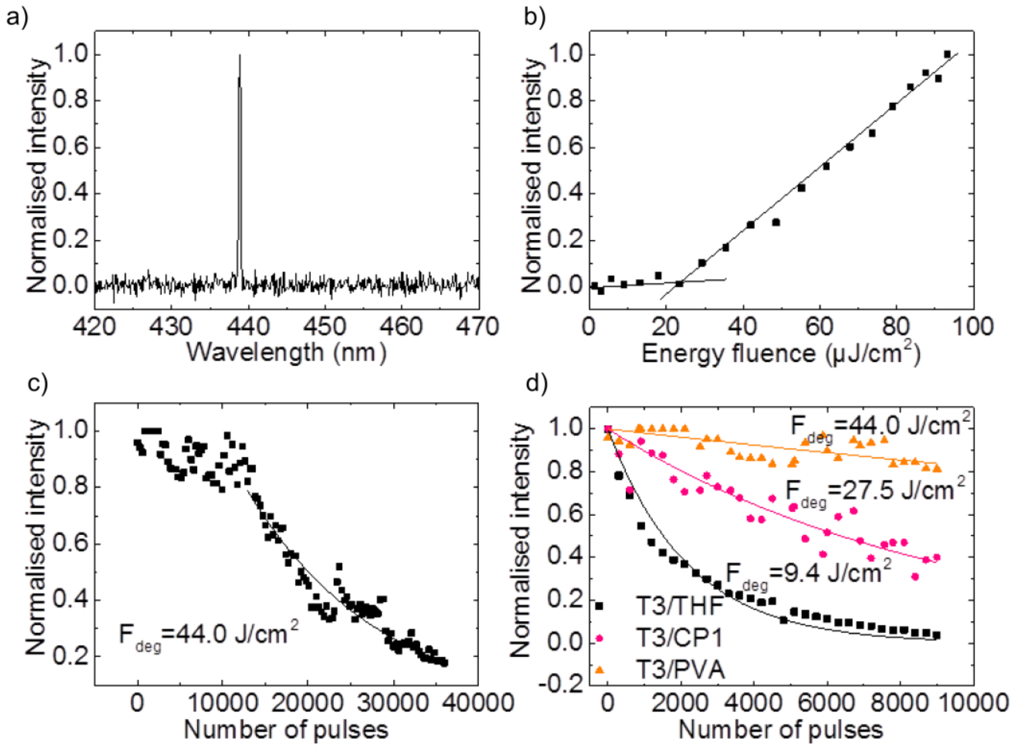

Figure 3.5: a) Spectrum and b) power transfer function of an encapsulated laser with a 180nm PVA layer, c) intensity decay of the encapsulated laser, d) comparison of intensity decay of the encapsulated laser with the nanocomposite laser and the neat laser.

3.5.3.2. Laser with a 580nm thick PVA film

The thickness of the encapsulating film was increased to 580 ± 70 nm in order to study the influence on the laser photostability.

The emission wavelength of the device shown in Figure 3.6 a) is at 440.9 nm and the peak emission has a linewidth of 0.21 nm. The further 2nm red-shifted emission with respect to the previous device mainly results from the higher effective index of the laser mode induced by the thicker PVA film (1.587 versus 1.583 as determined with the multilayer model). As previously, this emission wavelength value follows the expected trend as a 2nm red shift was predicted from the calculated value of n_{eff}. The average threshold fluence is measured to be 36 ± 8 μJ/cm^2, i.e. not significantly higher (Figure 3.6 b)).

A hundred times above threshold the laser intensity of the sample was stable for 79,400 pulses (equivalent to 132 minutes at 10Hz operation). To accelerate the degradation the frequency of the pulses was increased to 14 Hz after 50,700 pulses. After the 79,400-pulse-long plateau, the laser intensity started to decay. The pump energy fluence for degradation F_{deg} is found to be 280 ± 20 J/cm^2, which is ~6.5 times higher than for the thinner encapsulated laser (Figure 3.6 c)) and 40 times higher than for the neat T3 laser. The dominant degradation is assumed here to come from molecular oxygen diffusing from the environment into the gain layer. The improvement in operation lifetime is attributed to the thicker PVA film offering a better oxygen barrier. Basically, it takes longer for the PVA to degrade and for oxygen to reach the gain material. Results also indicate that the amount of molecular oxygen trapped in the OS after fabrication is lower than in the case of the nanocomposite lasers. This could possibly be possible due to the annealing step of the fabrication process. To the best of our knowledge, this value of F_{deg} was the highest reported for a mechanically-flexible organic laser at the time of the demonstration [8,24,100], prior to our further work on ultra-thin glass encapsulation (see chapter 4). Importantly, it is achieved with no trade-off in the threshold performance.

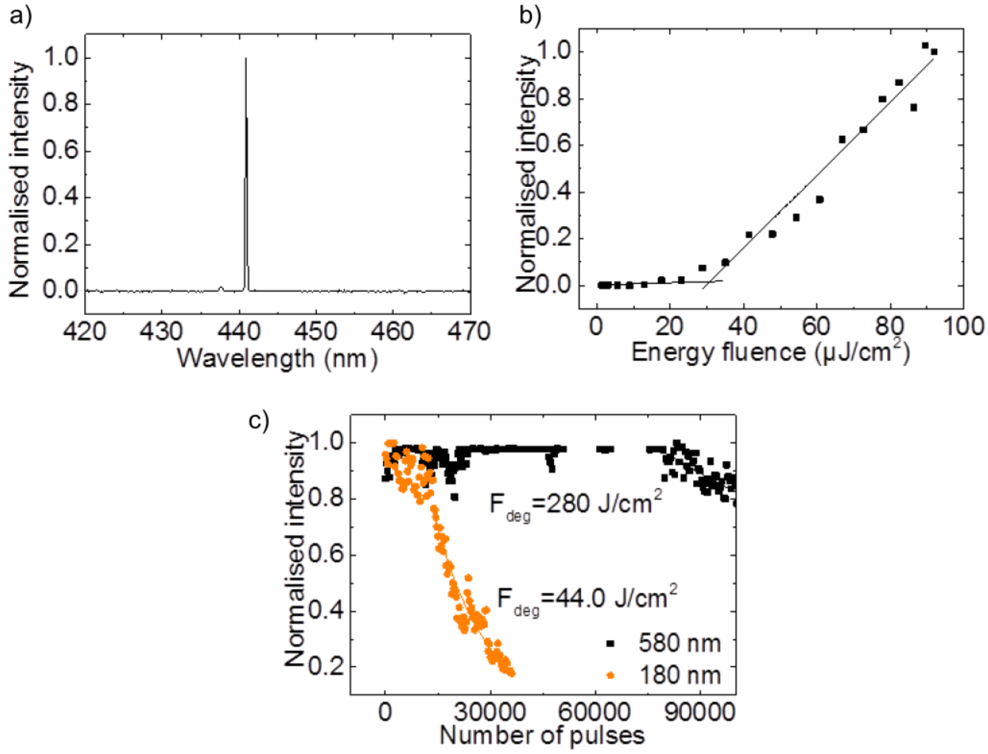

Figure 3.6: a) Emission spectrum and b) power transfer function of the encapsulated laser with a 580nm-thick PVA layer and c) comparison of the energy decay of both encapsulated lasers.

3.5.3.3. Importance of the annealing

To see the importance of the annealing step, a sample was made with a 180nm overlayer of PVA as previously, but without being annealed for 3 days. It was tested right after the PVA deposition. The emission wavelength of the non-annealed encapsulated T3 laser was 432 nm and the average threshold energy was 394.6 µJ/cm^2 (Figure 3.7 a) and b)). This threshold value is 4.7 times higher than for the neat laser.

The lifetime of the encapsulated laser is longer than for the neat laser but shorter than for the T3/CP1 laser (Figure 3.7 c)). Indeed the value of F_{deg} is 12.4 J/cm^2 for this T3/PVA device (7.1 J/cm^2 for the T3/THF laser and 27.5 J/cm^2 for the nanocomposite laser). Then annealing increases the photostability by ~3.5 as the lifetime of the same sample annealed for 3 days was found to be 44 J/cm^2.

The annealing step therefore improves the PVA properties for encapsulation and lowers the threshold. This is attributed to a lower density and a higher porosity of PVA before annealing. These characteristics lower the overlap with the gain region and possibly engender higher scattering losses in the PVA layer and an increase in oxygen diffusion. Consequently, a higher threshold and a lower operation lifetime are obtained when the sample is not annealed [215].

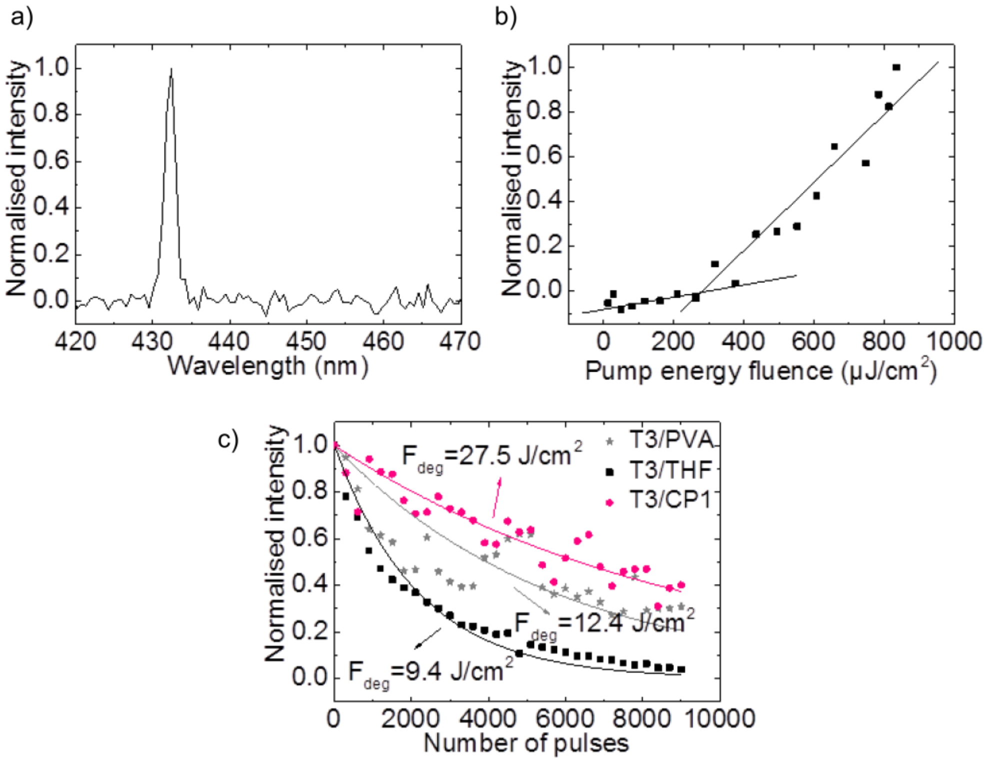

Figure 3.7: a) Emission spectrum, b) power transfer function of the encapsulated laser with a 180nm-thick PVA layer without annealing and c) comparison of the intensity decay of the neat, the nanocomposite and the encapsulated lasers with 180 nm of PVA without annealing.

3.6. Conclusion

Type of OS laser		Air			Water
		Threshold µJ/cm^2	Degradation fluence J/cm^2	Wavelength (nm)	Degradation fluence J/cm^2
Neat	T3/toluene	70 ± 7	11.5 ± 5.8 [8]	440.6	x
	T3/THF	30 ± 3	9.4 ± 2.5	426.3	19.5
Nanocomposite	T3/CP1 (4%)	115 ± 10	22.0 ± 4.5-27.0 ±6.5	428.6	22.0-27.5
Encapsulated	180nm-thick PVA	25 ± 6	44 ± 1.5	438.9	x
	580nm-thick PVA	36 ± 8	280 ± 20	440.9	x

Table 3.2: Summary of the results on neat, nanocomposite and encapsulated T3 lasers.

The operating lifetime under ambient conditions of mechanically-flexible organic semiconductor lasers based on monodisperse star-shaped oligofluorenes has been improved by using two approaches. A flexible organic laser comprising a T3-polyimide nanocomposite shown a ~3-fold photostability improvement in air over an equivalent neat OS laser, albeit with an increase in threshold up to 115 ± 10 µJ/cm^2. A flexible OS laser encapsulated with an oxygen barrier polymer (PVA) shown a photostability improvement of ~40 combined with an improvement in the threshold performance.

In conclusion, we have managed to encapsulate a mechanically flexible OS laser with a thin polymeric film and demonstrated improved operation stability in air for a total degradation dosage of 280.0 ± 20 J/cm^2. The latter was, to our knowledge, the highest reported for a mechanically-flexible organic laser at the time of the experiment. This degradation dosage corresponds to a working lifetime of about 7 hours under 10Hz pulse pumping before the intensity falls to 1/e of its initial value. The structure has also the benefit of lowering the device threshold to 36 ± 8 µJ/cm^2 by rendering the laser refractive index profile more symmetric. Table 3.2 summarises the main results of this study and can be ‘calibrated’ with reference to Figure 1.10 and Figure 1.11. Further work on ultra-thin glass encapsulation has shown longer operation lifetime (see chapter 4).

Chapter 4

Diode-pumped, mechanically flexible encapsulated DFB laser

4.1. Introduction

Following the work of the previous chapter, this chapter reproduces the same experiments but here using the green emitting π-conjugated polymer, BBEHP-PPV. However, the encapsulation method is pushed one step further by using ultra-thin glass membranes and laser-diode pumping is made possible due to the low-threshold. First, two formats of green emitting, flexible encapsulated distributed-feedback lasers with highly improved photostability and reduced threshold are demonstrated. The gain material is overcoated with PVA and fully encapsulated with two ultra-thin flexible glass membranes. An improvement in operation lifetime up to 120 times and high threshold reduction (up to 22 times) over an equivalent non-encapsulated device is obtained. The last section reports a diode-pumped, mechanically-flexible organic distributed-feedback laser that is fully encapsulated with ultra-thin glass. The organic laser is excited with a 450nm laser diode and emits at 537.1 nm with an oscillation threshold of 290 W/cm^2. The encapsulation format of the device results in a photostability that is improved by two orders of magnitude compared to a non-encapsulated device while maintaining mechanical flexibility thanks to an overall device thickness below 105 µm. The laser is also wavelength-tunable between 535 nm and 545 nm by mechanically bending the ultra-thin glass.

Results of this chapter were published in Optics Express (C. Foucher, B. Guilhabert, J. Herrnsdorf, N. Laurand, and M. D. Dawson, “Diode-pumped, mechanically-flexible polymer DFB laser encapsulated by glass membranes,” Opt. Express., vol. 22, no. 20, p. 584, 2014).

4.2.BBEHP-PPV lasers

As seen previously, OS lasers face a hurdle to applications: photodegradation. It has been shown in the previous chapter that photostability can be improved by embedding the gain material in a polymer matrix or by encapsulating the gain layer. In this chapter, we try to improve the operation lifetime of OS lasers further by looking at another OS material and another type of encapsulation. Glass is the ideal encapsulation material but resulting OS lasers so far have been rigid [96]. Glass is the material of choice for many technological solutions, often providing the interface between the ‘outside world’ and an underlying electronic/photonic core device. It offers advantageous characteristics compared to polymers such as high thermal stability, high chemical resistance, excellent barrier properties and high transmission of visible light [218]. At the same time, mechanical-flexibility in glass sheets can still be obtained if they are made thin enough (<100 µm) [153]. Such thin-glass sheets with high optical quality are being developed for the display market, which in turn is opening up opportunities for other photonic devices. A limited number of optical structures made on 75-µm or 100-µm thick glass substrates have been demonstrated recently (e.g. AM-LCDs, ChLC e-paper and electrophoretic displays [235–237]). Here we used an ultra-thin glass membrane to encapsulate OSLs that allows keeping the advantages of glass whilst also being flexible.

T3 is replaced by the green emitting π-conjugated polymer BBEHP-PPV, the absorption of which peaks in the blue region, meaning that it is the perfect candidate for diode-pumping; blue emitting laser-diodes are low-cost and easy to produce compared to UV emitting laser diodes. The ultimate aim of the work described in this chapter is to finally obtain a low-cost, compact, highly photostable and mechanically flexible OS laser system.

In the following, section 4.3 explains the design and fabrication of these flexible lasers. Some specific details of the optical set-ups are also given. Finally, section 4.4 demonstrates the substantial improvement in threshold and operation lifetime engendered by the different encapsulations, in comparison to an unencapsulated laser, and the first flexible OS lasers pumped with a laser diode is reported. We demonstrate laser diode pumping of mechanically-flexible BBEHP-PPV lasers and report improved performance in terms of threshold and photostability in section 4.4.2. These lasers are based on two encapsulation formats that were studied in the previous sections. The fabrication of the two OS lasers is the same as in section 4.3.2. The optical set-up for optical pumping as well as the properties of the pump laser diode are detailed first in section 4.4.2.1. Performance results including optical spectra, oscillation threshold and photostability are then presented, discussed and compared to device performance under 355nm Q-switched laser pumping (studied in section 4.4.1) in section 4.4.2.2. In particular, the substantial improvements in threshold and operation lifetime when pumping at 450 nm are highlighted. Finally, the effect of the pulse repetition rate on the OS laser characteristics is studied.

4.3. Design, fabrication and characterisation

4.3.1. Design of the flexible/glass DFB laser and of comparative laser structures

The design of the flexible glass/DFB lasers is detailed in this section. Descriptions of other laser structures that are also studied in order to benchmark the encapsulation performance of these flexible glass/DFB lasers are given as well. Figure 4.1 c) represents the structure of the ultrathin glass laser with a 180nm PVA overcoat. It is formed by a 130nm-thick gain layer deposited on top of a one-dimensional grating acting as a DFB reflector. The gain layer is made of pure OS, a π–conjugated poly[2,5-bis(2',5'-bis(2''-ethylhexyloxy)phenyl)-*p*-phenylene vinylene] (BBEHP-PPV). The gain spectrum of BBEHP-PPV spans the 490-540nm region while the absorption peaks at 431 nm [111,199]. More details on BBEHP-PPV are given in chapter 2, section 2.3.1.2. Encapsulation is obtained by overcoating with a protective layer of PVA and by "sandwiching" the whole structure between two thin glass sheets.

In order to compare the properties of this laser to a neat laser and other forms of encapsulation, four other devices were made and are represented in Figure 4.1. As shown in Figure 4.1 a), the neat laser is simply made of a layer of BBEHP-PPV deposited on top of the epoxy grating. A nanocomposite laser was made by embedding BBEHP-PPV in a CP1 matrix. Two other lasers were encapsulated with only PVA (a 180nm layer and a 580nm layer). Finally, another ultrathin glass laser with PVA overcoat was fabricated, but the thickness of the PVA layer was increased to 580 nm.

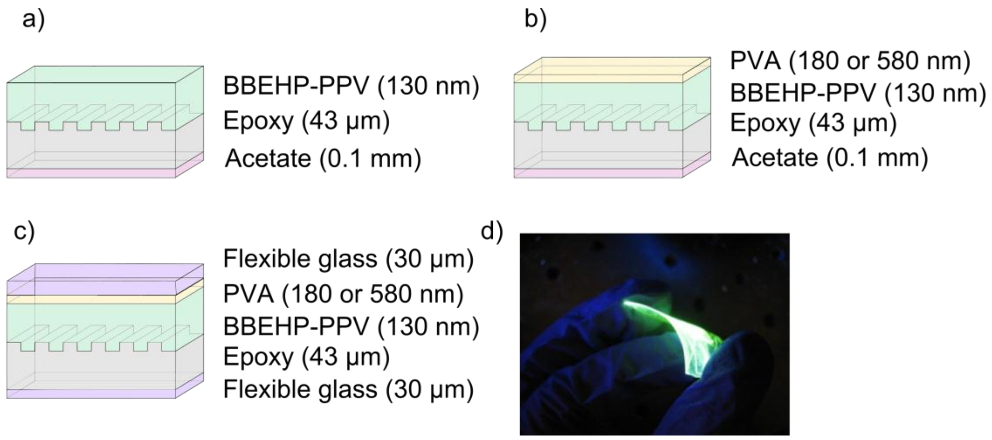

Figure 4.1: Schematics of the device structures: a) neat BBEHP-PPV laser, b) encapsulated laser with a layer of PVA layer (180nm or 580nm thick) and c) encapsulated laser overcoated with a 180nm or 580nm thick layer of PVA and sandwiched between two ultra-thin flexible glass membranes. d) Photo of a BBEHP-PPV laser encapsulated with flexible glass and PVA under UV exposure – the laser can bend.

4.3.2. Fabrication steps

The grating is identical for all 6 types of laser. It is made by soft lithography as described in chapter 2, section 2.4.1. NOA65 is spin-coated on top of a master grating having a period of 350 nm. An epoxy layer of thickness 43µm is obtained (measured with a microscope). The neat laser, the nanocomposite laser, the PVA-encapsulated lasers and the ultra-thin glass lasers also follow the same fabrication method as detailed in chapter 2, section 2.4.4, with BBEHP-PPV as the gain medium. A concentration of BBEHP-PPV in toluene of 20 mg/mL is spin-coated on top of the epoxy grating, forming a gain layer of thickness 130 nm. For the nanocomposite laser, CP1 powder was dissolved in toluene and BBEHP-PPV was directly added and dispersed inside the liquid matrix to the desired load of 4% wr CP1/BBEHP-PPV [153]. The solution was then spin-coated at 5000 rpm on top of the grating forming the 130nm-thick gain layer.

As shown in Figure 4.1 d), the glass-encapsulated lasers are still mechanically flexible thanks to a total device thickness below 110 µm.

4.3.3. Laser characterisation set-ups

All the DFB lasers are first optically pumped and characterised using the method described in chapter 2, section 2.5.1. The full width at half maximum (FWHM) pump stripe size on the sample under test is 1.789 x 0.329 mm^2. For each laser, the power transfer function, spectra and photostability are measured. For the latter, in order to determine the operating lifetime, the intensity of each laser is monitored and recorded every thirty seconds (i.e. every ~300 pulses) when operated above threshold, at a pump fluence of 0.59 mJ/cm^2. The degradation dosage F_{deg} is defined as the total pumping dosage for which the laser intensity has dropped to 1/e of its initial value.

The effect of mechanical bending on the emission wavelength of a laser encapsulated with flexible glass is studied here, as we presented in [227]. The laser is mounted in a slightly different set-up (see Figure 4.7 a)). The laser was fixed on each end of the mechanical stage and the distance was reduced using the micrometre screw. Depending on the position of the laser on the stage, the radius of curvature could either be negative of positive (see Figure 4.7 b) and c)), increasing or decreasing the grating period and therefore inducing a red shift or a blue shift.

4.3.4. Mode profile

For the discussion on the threshold performance in section 4.4, the laser mode transverse intensity profile and its overlap with the gain region are calculated for the different types of laser structures. The details of the overlap calculations are given in chapter 2, section 2.6.

In the case of the neat laser, there is only one layer to be considered, the gain material BBEHP-PPV, of refractive index n~1.7, enclosed between the (considered semi-infinite) epoxy substrate (NOA65), n~1.52, and air media. For the nanocomposite laser the refractive index of the gain material incorporated in the matrix was estimated to be ~1.69 [238]. For the PVA encapsulated devices, the additional PVA layer, n~1.55, has to be taken into account [153]. For devices encapsulated with PVA and flexible glass, the different sections include the ultra-thin glass substrate (n~1.51), the epoxy layer, the BBEHP-PPV layer, the PVA thin film and the top thin glass membrane. The calculated mode and refractive index profiles of a neat laser, a nanocomposite laser, an encapsulated laser with 180 nm of PVA, an encapsulated laser with 580 nm of PVA, an encapsulated laser with 180 nm of PVA and ultra-thin glass and an encapsulated laser with 580 nm of PVA and ultra-thin glass are plotted respectively, in Figure 4.2 a), b), c), d), e), f) and the calculated overlaps and effective refractive indexes are given in Table 4.1.

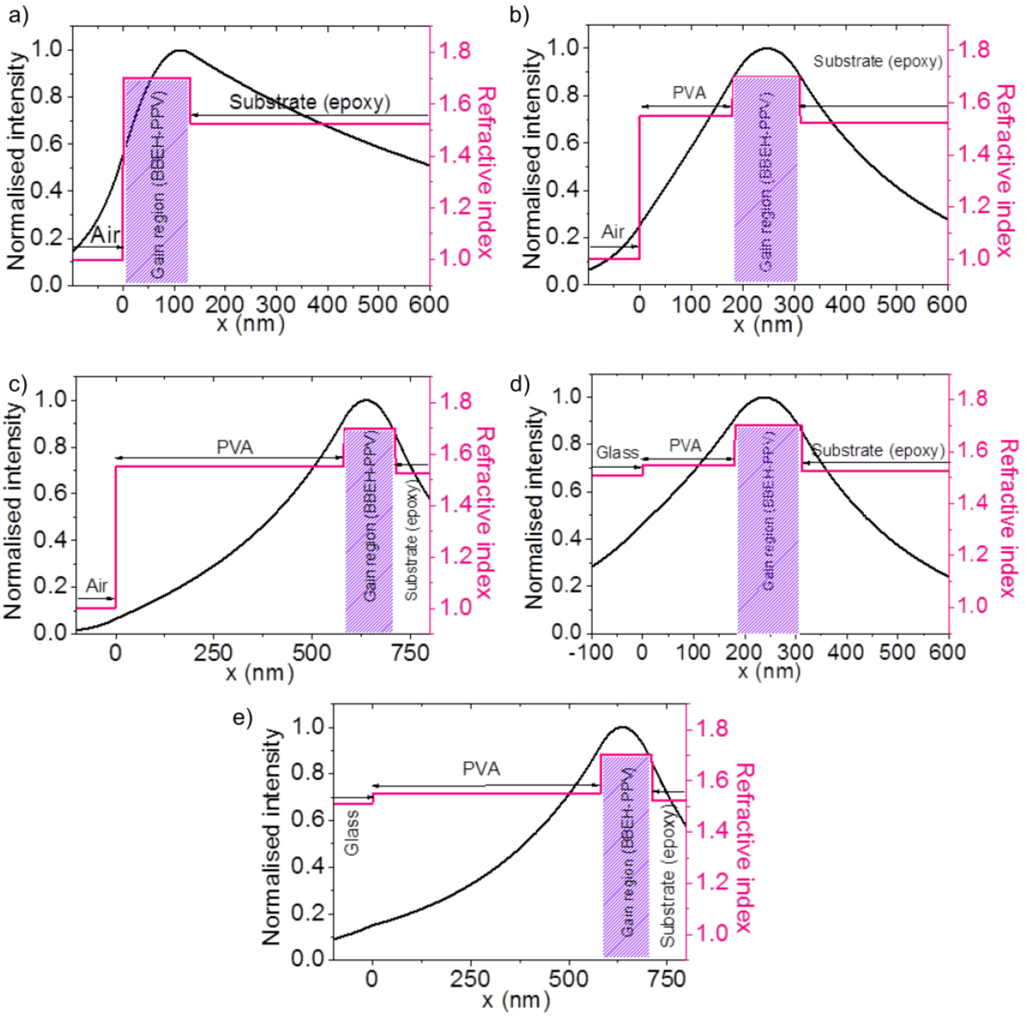

Figure 4.2: Mode profile superposed onto the refractive index profile of the multilayer structure for a) a neat laser, b) a laser encapsulated with a 180nm PVA layer, c) a laser encapsulated with a 580nm PVA layer, d) a laser encapsulated with a 180nm PVA layer and flexible glass and e) a laser encapsulated with a 180nm PVA layer and flexible glass.

Laser	Overlap (%)	n_{eff}
Neat	12.0	1.53
Nanocomposite	8.7	1.53
180nm thick PVA	29.5	1.56
580nm thick PVA	26.0	1.57
Glass + 180nm thick PVA	26.5	1.57
Glass + 580nm thick PVA	24.1	1.57

Table 4.1: Values of the overlap and effective refractive index for each BBEHP-PPV laser.

4.4. Experimental results and discussion

4.4.1. 355nm pumping

4.4.1.1. Neat laser

A neat BBEHP-PPV laser was made and its characteristics measured in order to use them as references for the encapsulated lasers. The power transfer function and the spectrum of the device are plotted in Figure 4.3 a) and b). The emission wavelength is at 536.9 nm. The average threshold energy fluence, F_{th}, is found to be 239.5 µJ/cm^2 per pulse (corresponding to a power density threshold of 47.9 kW/cm^2). The intensity decay of the neat BBEHP-PPV device was measured for 12,300 pulses at 0.59 mJ/cm^2 and the intensity is plotted against the number of pulses in Figure 4.3 c). A mono-exponential decay is fitted to the curve, giving a 1/e degradation dosage, F_{deg}, of 5.8 J/cm^2. However it is seen that the fit does not go through zero as the degradation presents a first phase corresponding to a fast decay. This could be due to a higher presence of oxygen on the surface of the laser than inside the layer.

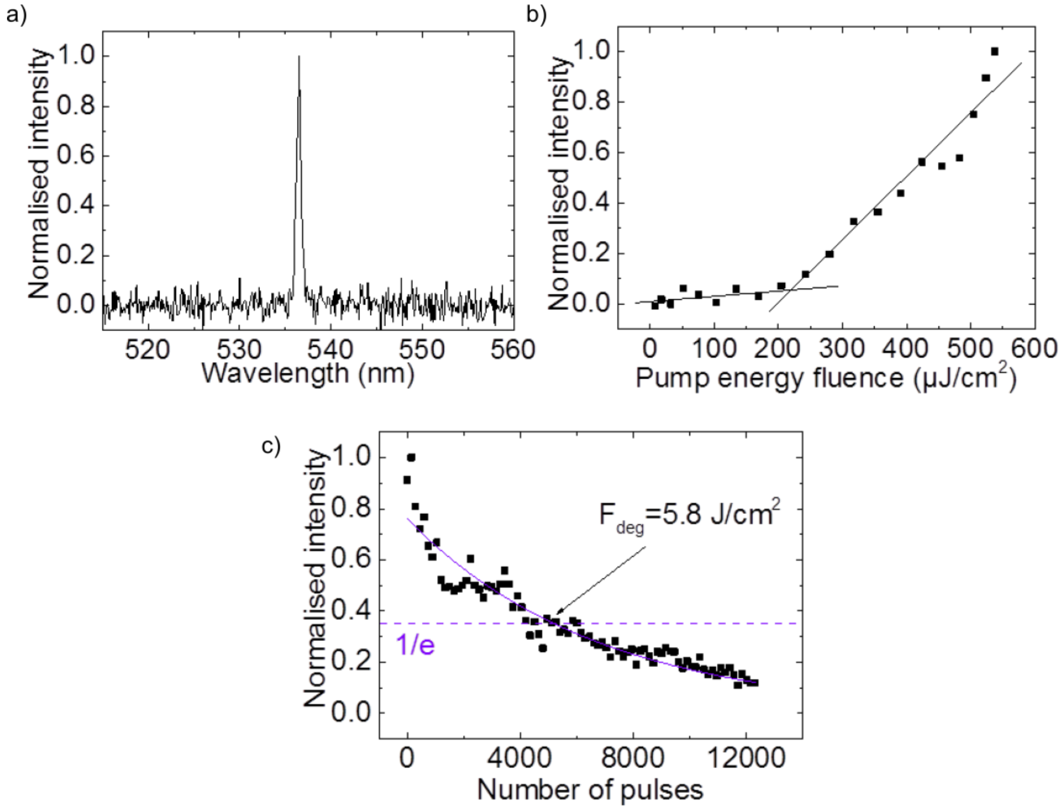

Figure 4.3: a) Spectrum, b) power transfer functions of a neat BBEHP-PPV laser and c) its intensity decay.

4.4.1.2. Nanocomposite laser

The characteristics of the BBEHP-PPV/CP1 nanocomposite laser are shown in Figure 4.4. The spectrum in Figure 4.4 a) shows an emission wavelength of 529.1 nm and Figure 4.4 b) an average threshold of 772.6 μJ/cm^2, which is about 3.2 times the value found for the neat BBEHP-PPV laser (see Figure 4.4 a)). The increase in threshold is mainly attributed to residual pump absorption by the matrix at 355 nm and to the slightly lower density of BBEHP-PPV molecules.

The nanocomposite laser brings a ~7.5-fold improvement in terms of photostability with a F_{deg} of 43.1 J/cm^2 showing that the polyimide matrix helps protects BBEHP-PPV from degradation, but with an increase in threshold.

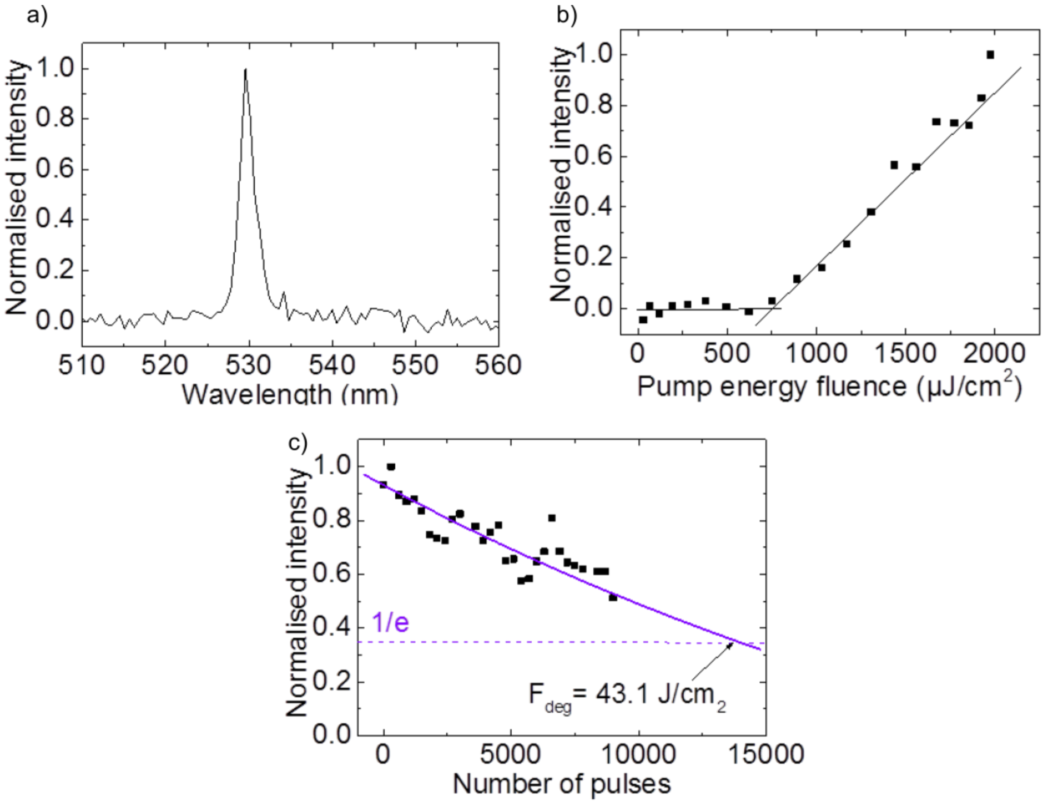

Figure 4.4: Characteristics of the nanocomposite laser with a) the spectrum, b) the power transfer function and c) the photostability.

4.4.1.3. Laser encapsulated with a 180nm and a 580nm PVA layer

The emission wavelengths of both encapsulated lasers with an 180nm-thick and a 580nm-thick PVA layer are shown in the inset of Figure 4.5 a) and are respectively 537.8 nm and 540.2 nm. The average threshold is measured at 8.0 µJ/cm^2 (1600 W/cm^2) for the thin layer of PVA and 13.0 µJ/cm^2 (2600 W/cm^2) for the thicker layer (Figure 4.5 a)). These values indicate that the encapsulating layer both redshifts the oscillation wavelength and lowers the threshold when compared to the equivalent neat laser; a 30-times improvement in threshold is obtained after encapsulation with a thin layer and an 18-times improvement for the thicker layer. These effects are mainly due to changes in the refractive index profile of the laser structure as shown in Figure 4.2. As a result of the PVA layer addition, the laser mode is pulled away from the substrate and overlaps more with the gain region leading to an increase in the effective refractive index of the mode. As shown in section 4.3.4, the overlap factor was calculated and found to be 12.0% for the neat laser and 29.5% for the laser encapsulated with 180 nm of PVA This is consistent with the trend in threshold observed experimentally. We note that there is an optimum PVA thickness (close to 190 nm) however. For example, if the PVA thickness is increased to 580 nm, the overlap factor decreases to 26% and the threshold increases to 13.0 μJ/cm^2 (2600 W/cm^2). The lifetime of the BBEHP-PPV/PVA lasers were measured and compared to the previous lifetime obtained for the neat devices (Figure 4.5 b)) and c)). The intensity of the OS laser having a small layer of PVA stays stable for 24,000 pulses and then starts to decrease slowly (Figure 4.5 c)). We attribute the initial, stable phase to the time it takes to photo-oxidise the PVA film when photo-pumped in air and for the oxygen to migrate to the active region. The second phase characterised by an exponential drop in intensity corresponds to the photodegradation of the organic semiconductor. The 1/e degradation dosage, F_{deg}, is here 46.6 J/cm^2, i.e. 8 times larger than for the neat laser. When the thickness of the encapsulating film was increased, the laser intensity of the sample was stable for ~330,000 pulses (Figure 4.5 c)). To accelerate the degradation the frequency of the pulses was increased to 15 Hz after 115,500 pulses. After the 330,000-pulse-long plateau, the laser intensity started to decay. The pump energy fluence for degradation F_{deg} is found to be 390 J/cm^2, which is ~8.4 times higher than for the thinner encapsulated laser and 68 times higher than for the neat BBEHP-PPV laser. The dominant degradation is assumed here to come from molecular oxygen diffusing from the environment into the gain layer. The improvement in operation lifetime is attributed to the thicker PVA film offering a better oxygen barrier. Basically, it takes longer for the PVA to degrade and for oxygen to reach the gain material.

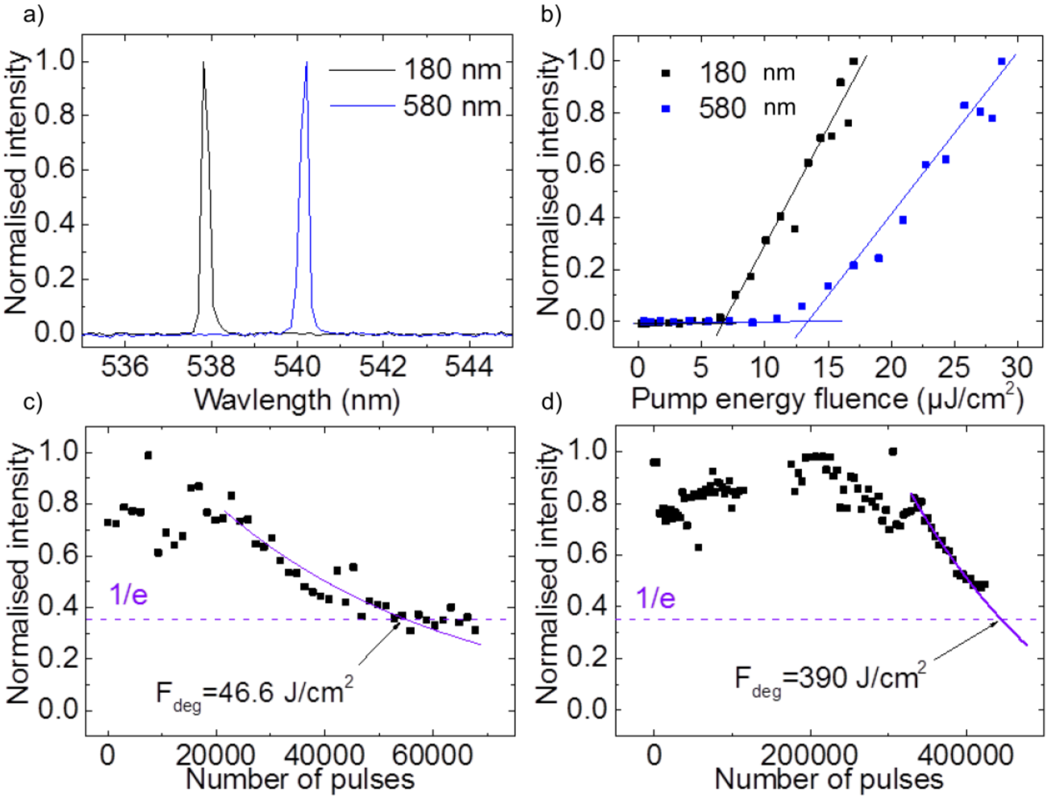

Figure 4.5: a) Spectrum and b) power transfer functions of an encapsulated BBEHP-PPV laser with a layer of PVA, c) the intensity decay of the laser encapsulated with a thin layer of PVA and d) the intensity decay of the laser encapsulated with a thick layer of PVA.

4.4.1.4. Laser encapsulated with a 180nm or a 580nm PVA layer and flexible glass

The emission wavelengths of the two devices, shown in Figure 4.6 a), are at 537.1 nm for the laser having the thin layer of PVA and 534.1 nm when the PVA is thicker. The average threshold fluences are measured to be, respectively, 10.8 µJ/cm^2 and 25.7 µJ/cm^2 (Figure 4.6 b)). The encapsulation with glass and a small layer of PVA shows a 22-fold improvement in threshold compared to the equivalent neat laser and the encapsulation with glass and a small layer of PVA shows a 10-fold improvement in threshold. However, it represents a small increase compared to the same lasers made with PVA encapsulation but without glass encapsulation. This change is due to the glass refractive index being higher than the air, changing the overlap of the laser mode with the gain region. It has been seen in Table 4.1 that the overlap is higher when the laser is not encapsulated with glass than when encapsulated only with PVA. The threshold is higher for the thick layer of PVA than for the thin one for the same reason (see Table 4.1).

The intensity of the sample having the thinner layer of PVA was stable for ~449,000 pulses, as shown in Figure 4.6 b). For a thicker layer of PVA, the intensity was constant for 480,000 pulses. To accelerate the degradation the frequency of the pulses was increased to 15 Hz after 129,300 pulses for the first sample and 173,700 pulses for the second one. For the laser encapsulated with glass and the thinner layer of PVA, the pump energy fluence for degradation F_{deg} is found to be 681 J/cm^2, which is ~14.6 times higher than for the encapsulated laser made with the same layer of PVA but no glass and 118 times higher than for the neat BBEHP-PPV laser. This results shows that the glass encapsulation inhibits oxygen affecting the gain material.

The 1/e degradation dosage, F_{deg} of the device encapsulated with glass and a thicker layer of PVA is found to be 701 J/cm^2 (see Figure 4.6 c)), which is ~1.8 times higher than for the encapsulated laser made with the same layer of PVA but no glass and 122 times higher than for the neat BBEHP-PPV laser. The degradation results are similar for both glass encapsulated lasers, showing that the glass is mostly responsible for the long photostability of the devices.

4.4.1.5. Wavelength tunability by bending

The behaviour of the laser encapsulated with a thin layer of PVA and flexible glass under bending was studied. The emission wavelength above threshold for different bending radii of curvature is shown in Figure 4.7 c). For these measurements, the pump energy is kept constant at 1.68 µJ. Reducing the radii of curvature to -1.9 and -1.7 cm induces a blue shift of the wavelength by 2.2 nm and 4.8 nm, respectively. For radii of curvature of 1.8 and 1.0 cm, the wavelength red-shifts by 2.1 nm and 4.6 nm, respectively. The total tuning of 9.4 nm is limited by a maximum radius of curvature before fracture of the device and is not limited by the gain bandwidth of the gain material.

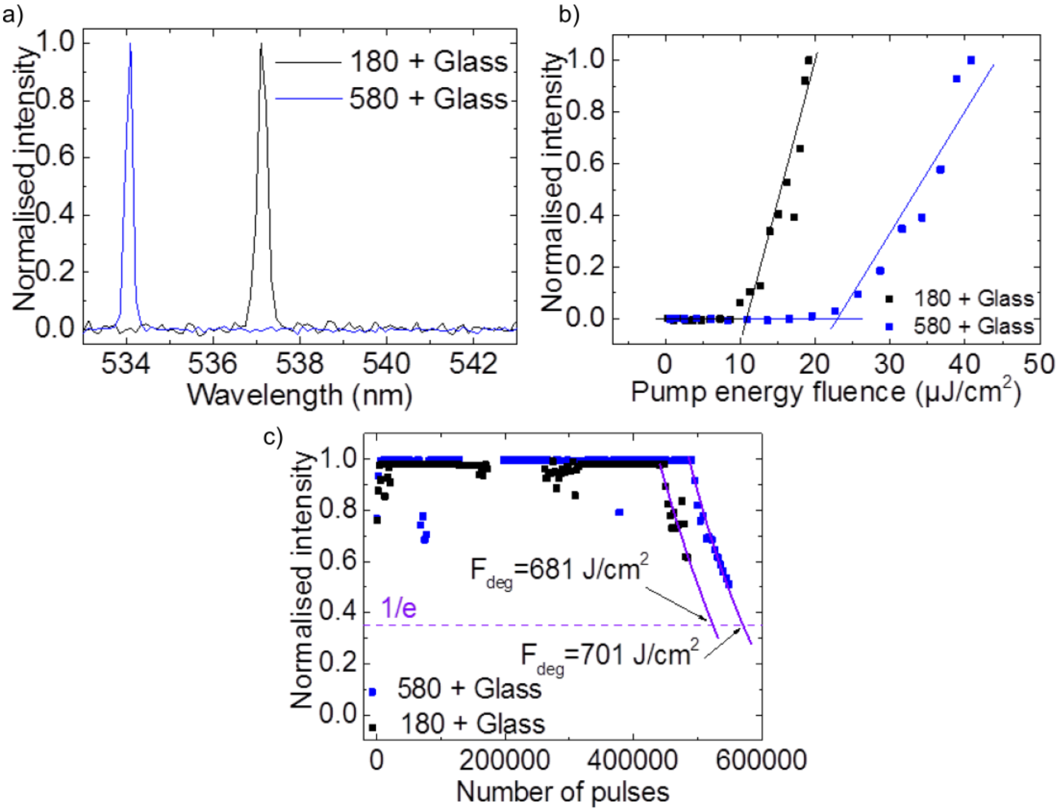

Figure 4.6: a) Spectrum and b) power transfer functions of the encapsulated BBEHP-PPV lasers with a layer of PVA of 180 nm and 580 nm and glass and c) its intensity decay.

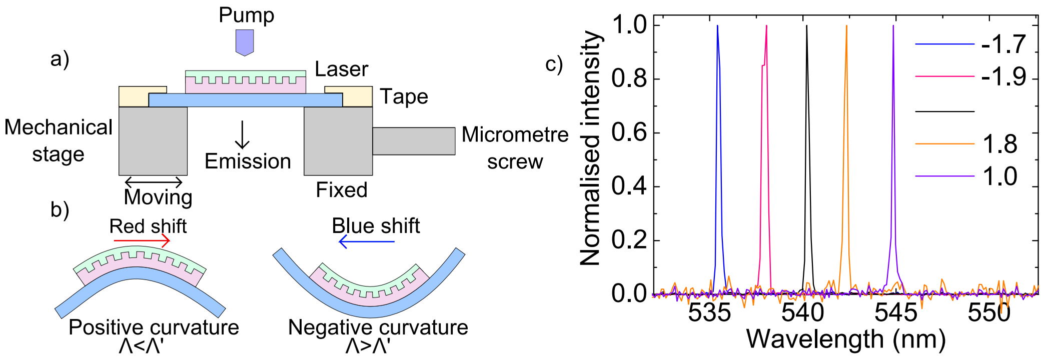

Figure 4.7: a) Schematics of the set-up for testing mechanical bending of the ultrathin glass laser with 180nm PVA overcoat, b) the two ways the laser can be bent and c) shift in the emission wavelength of the flexible encapsulated DFB laser with glass for different radii of curvature.

It was verified that the emission wavelength does not change significantly as a function of the pump fluence, providing assurance that the tuning comes from the bending of the device. These shifts of the emission wavelength are attributed to corresponding changes in the period of the grating as the glass substrate is bent. The change in period can be approximated from these wavelength measurements by using the Bragg equation (see chapter 2, section 2.2) and assuming that the effective refractive index is constant for the considered bending radii. Knowing that for a period of 350 nm (flat substrate) the emission wavelength is 540.21 nm, the effective refractive index for the guided mode can be deduced (~ 1.543). Then, for all the other emission wavelengths obtained when bending the laser, the corresponding 'altered' period, *Λ'*, is calculated. The corresponding radius of curvature of the laser is determined geometrically using Eq. 4.1. It is assumed here that the thickness of the gain material stays constant upon bending. Knowing the total thickness of the laser (BBEHP-PPV layer, PVA layer, epoxy grating and glass membranes), the period of the grating with (*Λ'*) and without (*Λ*) bending, the radius of curvature is given by:

$$\Lambda' = \frac{R+h}{R}\Lambda \;\Rightarrow R = \frac{h\Lambda}{\Lambda' - \Lambda} \qquad \textbf{Eq. 4.1}$$

Here, *R* is the radius of curvature, *h* the thickness of the laser structure, *Λ* the initial period of the grating and *Λ'* is the period of the grating under bending. The values of the grating period and radius of curvature thus calculated are plotted as a function of the wavelength in Figure 4.8 (open triangles).

Theoretical values for the radii of curvature and the grating periods can be calculated and then compared to the values deduced previously from the experimental data. From buckling theory and Euler's column formula, the radius of curvature can be calculated as follows [239]:

$$R = \pm e[1 - \cos\sqrt{\frac{P}{EI}}x] \qquad \textbf{Eq. 4.2}$$

In Eq. 4.2, *e* is the distance separating the sample from the neutral axis, *P* is the allowable load, *E* is the modulus of elasticity, *I* is the moment of inertia and *x* is the horizontal displacement applied on the micrometre screw of the mechanical stage (see Figure 4.7 a)). The sign of the equation changes according to a negative or positive bending (see Figure 5.3 b)). Euler's equation states that [240]:

$$P = \frac{\pi^2 EIn}{L^2} \qquad \textbf{Eq. 4.3}$$

In Eq. 4.3 *L* is the initial length of the sample and *n* is a coefficient for end conditions. In our case, *n=0.5* as the sample behaves as a fixed-fixed column [241,242]. Therefore Eq. 4.3 becomes:

$$\frac{P}{EI} = \frac{0.5\pi^2}{L^2} \qquad \textbf{Eq. 4.4}$$

Using Eq. 4.2 and Eq. 4.4 leads to:

$$R = \pm e[1 - cos(\frac{\pi}{L}\sqrt{0.5x}]) \qquad \textbf{Eq. 4.5}$$

Knowing the displacement applied from the micrometre screw, the radius of curvature is calculated for each measurement using Eq. 4.5. Finally, using those values of radii of curvature, the grating period is deduced with Eq. 4.1 as previously. These theoretical results are plotted (open squares) as a function of the emission wavelength in Figure 4.8 for comparison with the values obtained directly from the experimental data, showing good agreement. In Figure 4.9, the evolution of the wavelength as a function of the horizontal displacement *x* is displayed. The ascending part of the plot represents the red shift of the wavelength (positive curvature of the laser) and the descending line represents the blue shift or negative curvature, both having a slope of ± 11.1 nm/cm.

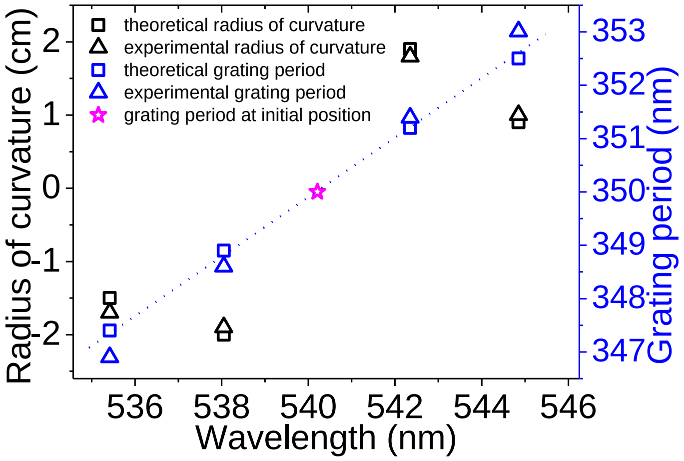

Figure 4.8: Comparison of theoretical and experimental values of the grating period and radius of curvature for each emission wavelength obtained after bending the laser encapsulated with ultra-thin glass.

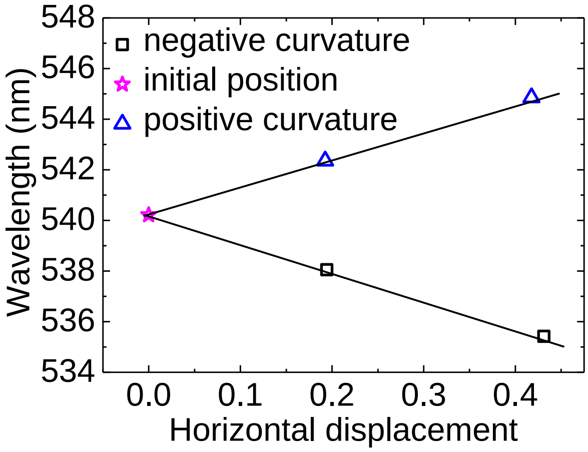

Figure 4.9: Evolution of the emission wavelength of the laser as a function of the horizontal displacement of the micrometre. Lines: theory; Open points: data points.

4.4.2. Laser diode pumped laser

4.4.2.1. Optical pumping set-up

Diode pumping experiments were undertaken with an InGaN laser diode LD emitting at 450 nm. The set-up used for LD pumping is shown in Figure 4.10 a). The LD was placed in a tin oxide (TO) can. An aspheric lens with a focal length of 4.51 mm was then placed in the TO can to reduce the divergence of the LD and collimate the beam. A second lens with a focal length of 10 cm was placed after the first lens in order to focus the beam on the DFB laser to a spot of size 390 x 220 µm^2. The DFB laser was placed at an angle of ~45° compared to the main axis to avoid collecting the pump when measuring the emission of the laser.

The LD delivers nanosecond pulses with energies up to 150 nJ at a repetition rate that can be varied. However, to compare the measurements with the previous results, spectra, power transfer functions and photostabilities were measured at 10 Hz, except when specified in the text. The LD was driven by a high voltage power supply coupled to a PCB driving board (PCO-7110). This board was driven by a high voltage power supply and a signal generator controlling the repetition rate. The optical characteristics of the LD are plotted in Figure 4.10 b), showing the pulse width and the fluence as a function of the driving peak current. The pulse width increases when the peak current is increased, meaning that when the pump energy fluence of the LD is increased, the pulse width increases as well.

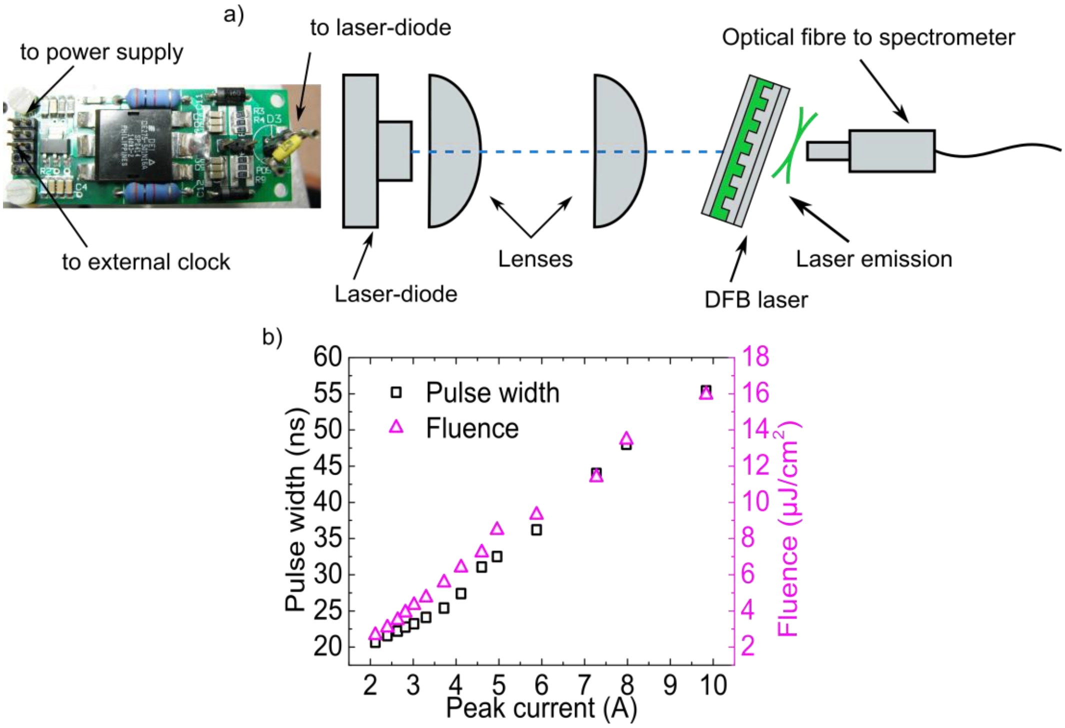

Figure 4.10: a) Schematic of the optical pumping set-up by the LD, b) LD optical pulse energy and duration plotted against driving peak current and c) fan-shaped emission of the laser.

In order to measure spectra and transfer functions, the emission of a device was detected by a 50µm-core optical fibre, connected to a CCD-spectrometer with a maximum spectral resolution of 0.13 nm. The energy of the LD was measured by an energy sensor from Coherent having a resolution from 100 pJ to 1 µJ connected to an energy meter (Coherent Labmax-top) [243]. The pulse width of the LD was measured with a photodetector connected to the oscilloscope. The operating lifetime under LD pumping was measured at a pump energy fluence of 27 µJ/cm^2 and at a frequency of 10 Hz.

4.4.2.2. Results and discussion

4.4.2.2.1. Laser encapsulated with a 180nm-thick layer of PVA

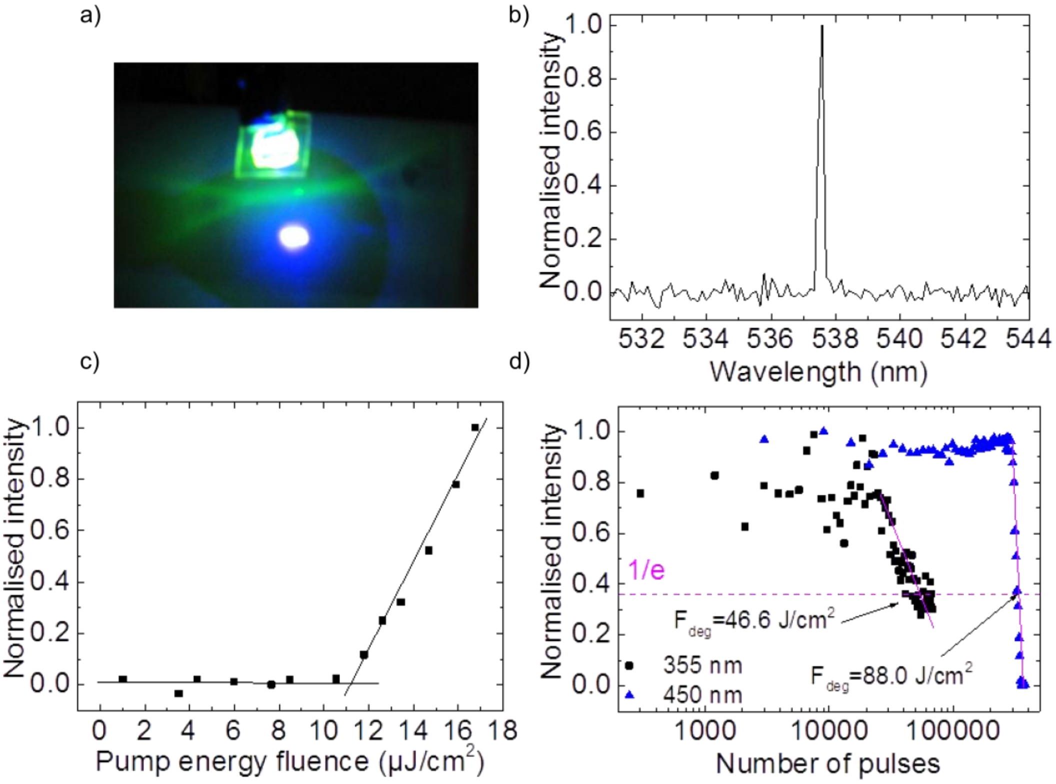

Figure 4.11: a) Typical fan-shaped emission of the DFB laser being pumped, b) spectrum, c) power transfer function of the 180nm PVA encapsulated BBEHP-PPV laser, d) its intensity decay caused by photodegradation when pumped at 355 nm (black squares) and at 450 nm (blue triangles).

Figure 4.11 shows the characteristics of the laser encapsulated with a thin layer of PVA when pumped with a 450nm LD. The typical fan-shaped emission of the laser is shown in Figure 4.11 a). The laser emits at 537.6 nm wavelength (inset of Figure 4.11 b)) with a <0.20nm linewidth. This is similar to results under 355nm pumping indicating that the pump wavelength has no significant effect on the oscillating wavelength of the OS laser. The pump average threshold of the device when pumped with the LD is 11.1 µJ/cm^2, corresponding to a LD power density at threshold of

~269 W/cm^2 (Figure 4.11 c)). This corresponds to a power density reduction of about 6 times compared to the power density obtained when pumped at 355 nm. This is attributed to the higher absorption (about 2.5 times higher) of BBEHP-PPV at 450 nm [111] (see Figure 2.5 in chapter 2).

The intensity decays of the device due to photodegradation when pumped by the LD at 450 nm and by the solid-state laser at 355 nm are plotted in Figure 4.11 d). A pump energy fluence for degradation F_{deg} of 88.0 J/cm^2 is found when pumping at 450 nm, representing an operating lifetime ~2-times longer than for the equivalent laser pumped at 355 nm. This increase in lifetime could be explained by the replacement of the UV pump photons by a blue pump photons, as UV radiation is known to damage organic molecules by breaking covalent bonds [244].

4.4.2.2.2. Ultrathin glass laser with 180nm PVA overcoat

The spectrum and power transfer function above threshold of the LD-pumped ultra-thin glass laser with a 180nm layer of PVA are plotted in Figure 4.12 a) and b). The laser emits at 540.4 nm wavelength with a <0.16nm linewidth and a LD power density at threshold of ~290 W/cm^2 (14 μJ/cm^2), corresponding to a 7-times improvement in threshold compared to the device pumped at 355 nm. Again, we attribute this to the higher absorption of BBEHP-PPV at 450 nm.

Figure 4.12 b) shows the photostability of the laser encapsulated with PVA and flexible glass when pumped with the LD at 450 nm and with the solid-state laser at 355 nm. As seen in the previous section, F_{deg} presents a ~2-fold improvement compared to a similar device pumped in the UV, *i.e*. F_{deg} of 1440 J/cm^2 compared to 681 J/cm^2 when pumping at 355 nm. This confirms the influence of UV radiations on the stability of BBEHP-PPV.

We note that the 450nm 10Hz pumping result corresponds to stable operation of the laser for more than 10 hours.

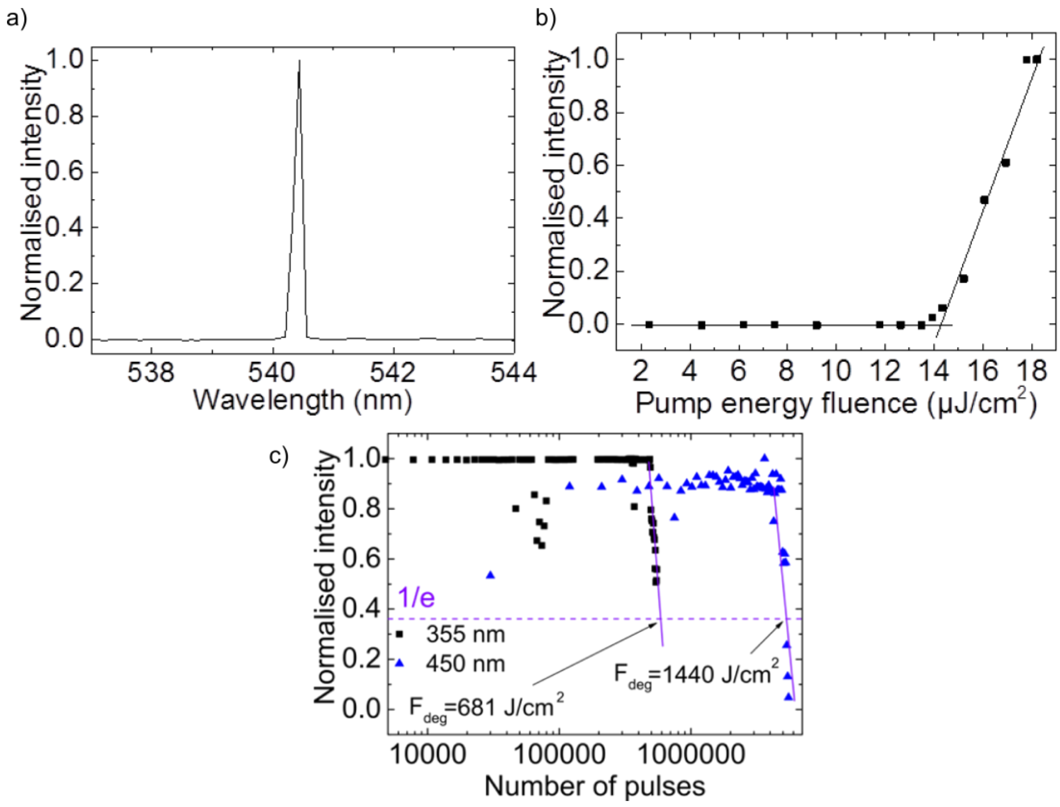

Figure 4.12: a) Spectrum and b) power transfer functions of the encapsulated BBEHP-PPV lasers with a layer of PVA of 180 nm and glass, c) its intensity decay when pumped at 355 nm (black squares) and at 450 nm (blue triangles).

4.4.2.2.3. Effect of the repetition rate

Given the stability above and in order to see the effect of the repetition rate on organic semiconductor lasers, spectrum, threshold and photostability of an encapsulated BBEHP-PPV laser encapsulated by 180 nm of PVA and an ultra-thin membrane of glass were studied at different repetition rates.

The spectrum of a laser was measured at a constant energy fluence of 27 μJ/cm^2 without changing position on the sample. The repetition rate was raised from 10 Hz to 100 Hz and then to 1000 Hz. The respective spectra are shown in Figure 4.13 a). It is seen that the repetition rate has no influence on the emission wavelength when increased from 10 Hz to 100 Hz. However, when increased to 1000 Hz, the laser emission is multimode and has a lower intensity; a multimode emission is detected, with a lower intensity. It was noticed that this emission disappears in a few seconds whereas the when pumped at 10 Hz and 100 Hz the intensity stays constant during the measurement. In order to explain this change in appearance of spectrum, the photostability of the laser was measured at 100 Hz, studying the evolution of the spectrum during the measurement. The evolution of the laser emission peak is plotted in Figure 4.13. No degradation of the spectrum is seen. This means that the degradation of the spectrum happens between 100 Hz and 1000 Hz. The threshold and photostability at 100 Hz are shown in Figure 4.13 c) and Figure 4.13 d), respectively. The threshold value increases from 14 µJ/cm^2 at 10 Hz to 17.3 µJ/cm^2 at 100 Hz. F_{deg} becomes only 1.4 J/cm^2, which is a 1000 times shorter than when pumped at 10 Hz.

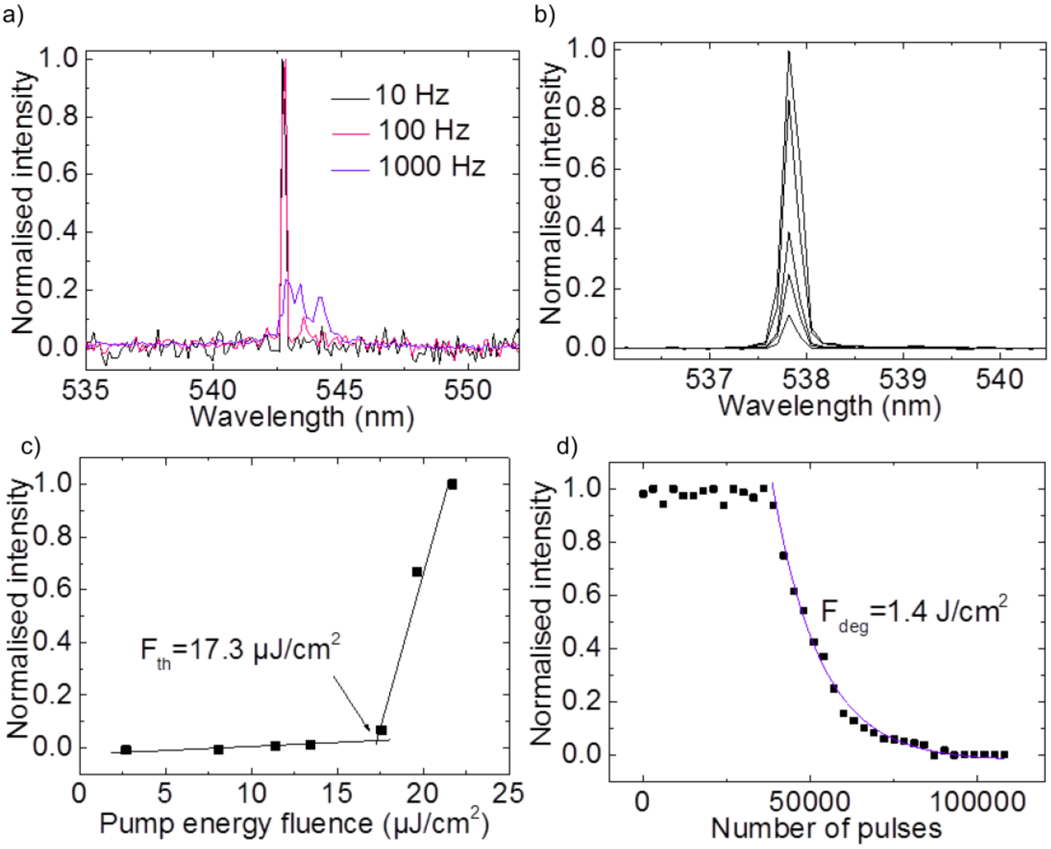

Figure 4.13: a) Spectrum of a PVA/glass encapsulated BBEHP-PPV laser pumped at 10 Hz, 100 Hz and 1000 Hz, b) evolution of spectrum at 100 Hz, c) threshold at 100 Hz and d) photostability at 100 Hz.

These results can be explained by the short lifetime of the excitons of organic semiconductors. This means that they need high excitation densities in order to keep the population inversion. An increase in repetition rate engenders high cavity losses and then diminishes the gain. It is necessary that the electrons at the excited state have time to relax between two pulses to avoid triplet excited-state absorption [166]. The pulse of the laser diode is compared to the output pulse of the organic laser in Figure 4.14. Both are measured at 10 Hz and 100 Hz. It is seen that the laser pulse is shorter than the laser diode pulse as the excited state lifetime of the organic semiconductor is shorter than the pump than the pump lifetime. However the repetition rate does not change the duration of the pulse.

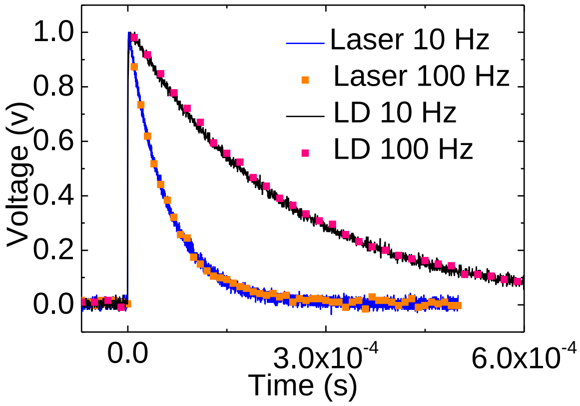

Figure 4.14: Laser pulse and laser diode pulse at 10 Hz and 100 Hz.

4.5. Conclusion

		Laser					
Characteristic		**Neat**	**Nano-composite**	**180nm thick PVA**	**580nm thick PVA**	**Glass + 180nm thick PVA**	**Glass + 580nm thick PVA**
Wavelength (nm)		536.9	529.1	537.8	540.2	537.1	534.1
Fluence Threshold (μJ/cm^2)	**355 nm**	239.5	772.0	8	13	10.8	27.5
	450 nm	x	X	11	x	14	X
Power density threshold (W/cm^2)	**355 nm**	47900	154400	1600	2600	2160	5149
	450 nm	x	X	269	x	290	x
F_{deg} (J/cm^2)	**355 nm**	5.8	43.1	46.6	390	681	701
	450 nm	x	X	88.0	x	1440	x

Table 4.2: Summary of the results on neat and encapsulated BBEHP-PPV lasers

In this chapter, a flexible organic laser comprising a BBEHP-PPV-polyimide nanocomposite shown a ~7.5-fold photostability improvement over an equivalent neat OS laser, albeit with an increase in threshold (~3.2-times). Moreover, OS lasers fully encapsulated with PVA or with ultra-thin glass membranes show high improvement in operation lifetime (up to 250 times) and high threshold reduction (up to 22 times smaller) over an equivalent non-encapsulated device.

In the second part of this section, LD pumped mechanically-flexible OS lasers fully encapsulated with PVA and ultra-thin glass membranes were demonstrated. They showed high improvement in operation lifetime (up to 250 times) and high power density threshold reduction (up to 265 times smaller) over an equivalent non-encapsulated device. This demonstration brings OS lasers closer to applications. The integration of a polymer laser with a laser-diode and the achievement of a high photostability offers a potential low-cost and compact system suitable for (bio)-sensing, medical diagnostics and spectroscopy.

The main results in threshold and photostability of the OS lasers obtained in this chapter are summarised in Table 4.2.

Chapter 5

Colloidal semiconductor nanocrystal lasers

5.1. Introduction

The motivations of this chapter are (i) to show the integration compatibility of solution-processed lasers with different substrate materials (initiated in the previous chapter with thin-glass) and (ii) to explore another promising type of solution-processed gain material: colloidal quantum dots. The first section reports a mechanically-flexible and wavelength-tunable laser with an ultra-thin glass membrane as substrate. The optically-pumped hybrid device has a distributed-feedback cavity that combines a colloidal quantum dot gain film with a grating-patterned polymeric underlayer, all on a 30-µm thick glass sheet. The total thickness of the structure is only 75 µm. The hybrid laser has an average threshold fluence of 450 ± 80 µJ/cm^2 (for 5-ns excitation pulses) at an emitting wavelength of 607 nm. This result is to our knowledge the lowest threshold for colloidal quantum dot lasers in this temporal regime (>1ns) at the time of writing. Mechanically bending the thin-glass substrate enables continuous tuning of the laser emission wavelength from 600 nm to 618 nm. The correlation between the wavelength tunability and the mechanical properties of the thin laser structure is verified theoretically and experimentally. The second section demonstrates that solution-processable lasers can be integrated onto different types of substrates. The same fabrication process as for the CQD lasers on flexible glass is employed with semi-flexible silicon substrates. Two lasers are obtained respectively made to emit at two different wavelengths, 613 nm and 608 nm, by tailoring the laser cavity. The devices have a threshold fluence of 420 ± 70 µJ/cm^2 per pulse at 613 nm and 1400 ± 360 µJ/cm^2 at 608 nm. Finally, in the last section of the chapter, a CQD laser is tested for refractive index sensing in solution by immersion in water. A 4nm red-shift of the laser emission is detected when the DFB laser is operated in deionised water compared to air. This is a first step towards biosensing with CQD DFB lasers.

Results of this chapter were published in Applied Physics Letters (C. Foucher, B. Guilhabert, N. Laurand, and M. D. Dawson, “Wavelength-tunable colloidal quantum dot laser on ultra-thin flexible glass,” Appl. Phys. Lett., vol. 104, no. 14, p. 141108, 2014) and in Optics Express (B. Guilhabert, C. Foucher, A.-M. Haughey, E. Mutlugun, J. Herrnsdorf, H. D. Sun, H. V Demir, and M. D. Dawson, “Nanosecond colloidal quantum dot lasers for sensing," Opt. Express, vol. 22, no. 6, pp. 7308–7319, 2014).

5.2. Colloidal quantum dot lasers

Colloidal quantum dots (CQDs) are attractive nanomaterials for the fabrication of photonic devices, as explained in chapter 1, section 1.5. They have high photoluminescence efficiency, are compatible with solution–processing techniques and their emission wavelength can be tuned over a wide range by changing their size and/or composition. Consequently, CQDs are being developed for devices and applications that include displays, LEDs, lasers, bio-imaging and bio-sensing [169,181,186,245,246]. Furthermore, because CQDs can be deposited onto a variety of materials, they also have a role to play in devices for flexible photonics [247,248]. Usually, thin-films of light-emitting materials, e.g. CQDs, are combined with entirely polymeric substrates and structures to enable such devices. Polymers are used because of their high mechanical flexibility [249].

As seen in chapter 4, glass is the material of choice for many technological solutions. Our report focuses here on the first demonstration of a CQD laser on flexible glass.

Mechanically-flexible lasers are also attractive for transfer and integration onto different substrate materials and this potential has been used in previous chapter to a certain extent. Additional things we have not explored yet is the possibly for post-assembly of lasers on a common substrate. This is looked at in this chapter using CQD lasers.

We foresee that the laser technology reported here will provide opportunities for, amongst others, bio-sensing and/or mechanical sensing applications.

Section 5.3 presents a mechanically-flexible and wavelength-tunable laser with an ultra-thin glass membrane as substrate with colloidal quantum dots as gain material. We start by explaining the design and fabrication of the CQD flexible lasers on glass in section 5.3. We give details on the optical and mechanical set-ups that were used for the characterisation of the devices. Then, we present and discuss the experimental results, including spectra, power transfer functions and mechanical-tunability characteristics of the lasers. In particular, we show that the magnitude of the wavelength shift upon bending results from the interplay between the radius of curvature of the glass substrate and the overall mechanical properties of the 'layered' laser structure. Section 5.4 is about assembly of CQD lasers onto a common thin silicon substrate. Finally in section 5.5, we explore the potential of CQD lasers for refractive index sensing in solution.

5.3. Wavelength-tunable colloidal quantum dot laser on ultra-thin flexible glass

In this section, we propose a flexible laser based on CQDs and ultra-thin glass. The mechanical properties of the overall structure are such that the laser can be continuously tuned in wavelength by bending the glass membrane, as was done in chapter 4, section 4.4.1.5.

5.3.1. Design and fabrication

The schematic in Figure 5.1 a) represents the structure of the CQD laser with the thin glass membrane acting as substrate. It is composed of a CQD gain layer (commercial core-shell CdSe/ZnS CQDs from Sigma-Aldrich), ~160-nm-thick, deposited on top of a one-dimensional grating, which is imprinted into the surface of a 43-µm-thick polymer film (NOA85), having a period of Λ = 390 nm. NOA65 was spin-coated on top of the master grating. The resulting DFB resonator sits on top of a 30-µm-thick glass membrane. The details of the fabrication steps are given in chapter 2, section 2.4. The only difference is that the gain layer here is a solid film of CQDs in poly(methyl methacrylate) (PMMA) [250]. The CQDs are dispersed in a PMMA solution at 1.6 mg/mL in 50% of chloroform and 50% of toluene with a concentration of 50 mg/mL. The device is finally annealed for 5 minutes at 35°C on a hot plate.

Pictures of the fabricated flexible device are shown under white and ultraviolet light illumination, in Figure 5.1 b) and Figure 5.1 c) respectively.

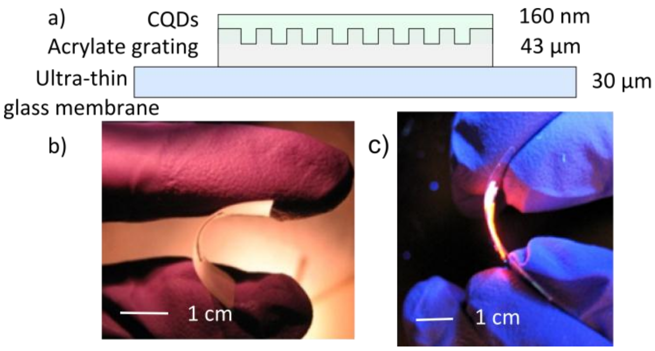

Figure 5.1: a) Schematic structure of the laser on a flexible glass substrate. Photos of the mechanically flexible device b) under white and c) UV light illumination.

Figure 5.2 summarizes the full fabrication process of these CQD DFB lasers.

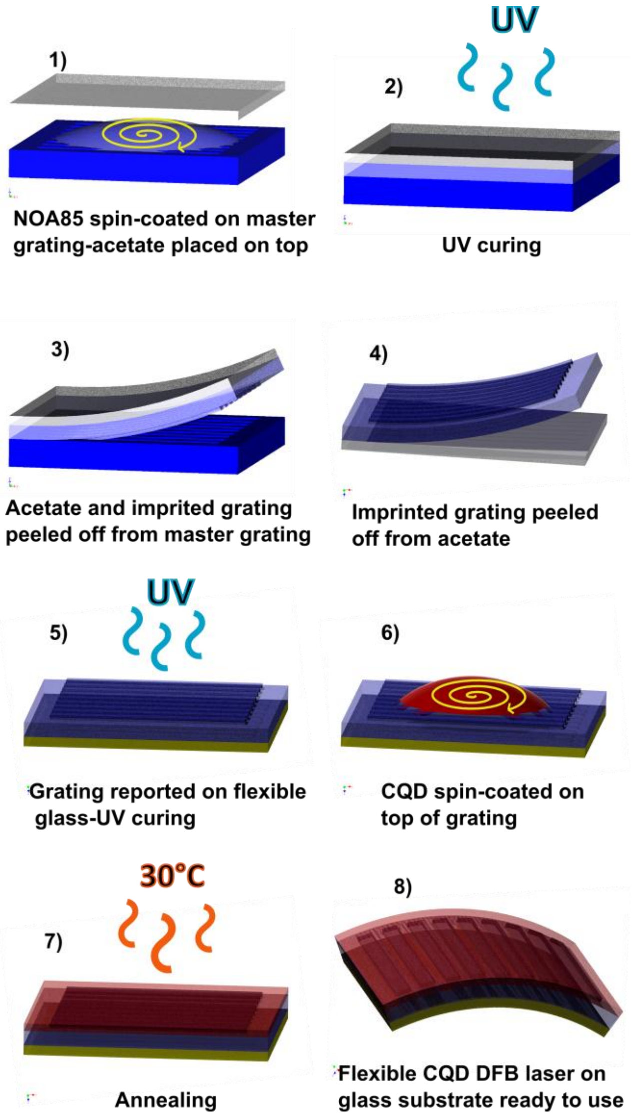

Figure 5.2: Fabrication steps of the CQD DFB laser on an ultra-thin flexible glass membrane.

5.3.2. Laser characterisation set-up

Prior to laser demonstration, thin films of CQD/PMMA on flat substrates were characterized in terms of photoluminescence (PL) and were assessed for their capabilities to sustain stimulated emission (through detection of amplified spontaneous emission, ASE). The PL spectra were recorded using a Jobin-Yvon TRIAX spectrometer under continuous wave excitation with a 374-nm-emitting laser diode either focused on the sample with a 60× magnification microscope objective for top emission PL (spot size of about ∼2 mm) or focused in a stripe on the side of the sample for edge emission PL (stripe size about 3.5 mm × 0.2 mm). The collection was realised through the same microscope objective. The amplified simulated emission was measured using the same optical set-up as described in chapter 2, section 2.5.2. The optical beam was shaped into a collimated stripe of 2.9 mm × 0.3 mm FWHM.

The DFB lasers were optically pumped as described in chapter 2, section 2.5.1. The FWHM pump spot size on the sample was 57.2 ± 0.8 µm x 35.0 ± 0.6 µm as verified by knife-edge measurement. The power transfer function and spectra of the laser were measured. The average threshold quoted in the experimental results section is obtained by averaging several measurements taken at different closely spaced positions (within an area of 2 x 2 mm^2) on the surface of the device.

To study the effect of mechanical bending on the emission wavelength of a laser encapsulated with flexible glass, the same method as in section 4.4.1.5 was used. The laser was mounted on a slightly different set-up (see Figure 5.3 a)). The laser was fixed on each end of the mechanical stage and the distance was reduced using the micrometre screw. Depending on the position of the laser on the stage, the radius of curvature could either be negative or positive (see Figure 5.3 b) and c)), increasing or decreasing the grating period and therefore inducing a red shift or a blue shift.

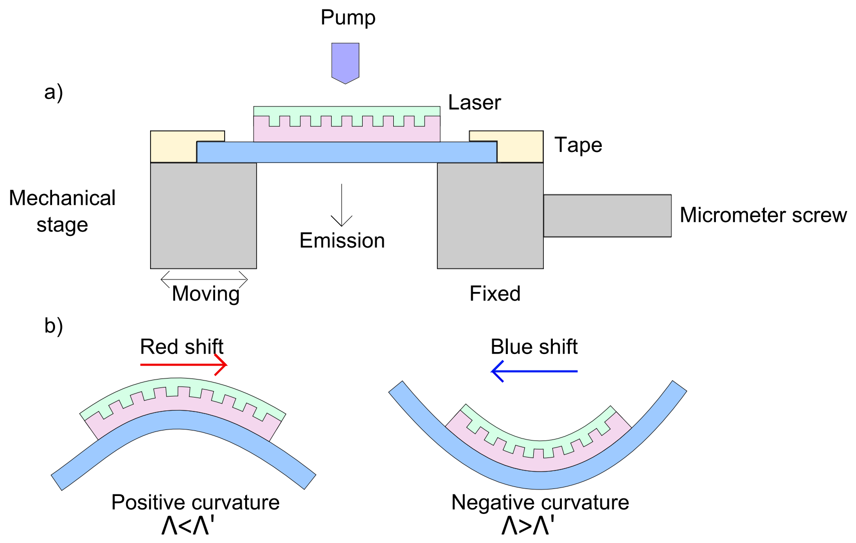

Figure 5.3: a) Schematics of the set-up for testing the DFB laser on glass under mechanical bending and b) the two ways the laser can be bent, increasing or reducing the grating period for, respectively, red shifting or blue shifting the laser emission wavelength.

5.3.3. Experimental results and discussion

5.3.3.1. Photoluminescence and amplified spontaneous emission

The data in this section were recorded by **Dr Benoît Guilhabert.** The top and edge PL spectra of CQD films excited in the UV at 371 nm were first measured. The CQDs were at a concentration of 50 mg/mL dispersed in PMMA solution at 1.6 mg/mL (50/1.6 w/r) and spin-coated on a glass substrate. The top emission PL of the film was recorded first and shows that the emission of core/shell CQDs within a PMMA matrix peaks at a wavelength of 590 nm in accordance with the stated value in the data sheet (Figure 5.4 a)). The edge PL of the sample is red-shifted by 7 nm (to 597 nm) with respect to the top PL. This is caused by re-absorption of the intrinsic emission as it propagates in the film due to the limited Stokes shift (~20 nm) of the CQDs. In addition, PL quantum yield (PLQY) was measured using an 8inch integrating sphere and a continuous wave pump source emitting at 450 nm. The resulting PLQY for the aforementioned film of spin-coated CQD/PMMA nanocomposite is 15%.

The evolution of the edge emission from a film under nanosecond optical excitation was investigated using the setup explained previously in section 5.3.2. The spectral shape is seen to significantly change above a certain excitation value (ASE threshold) with a narrower peak developing and dominating the PL as the excitation is further increased. Figure 5.4 b) shows such an ASE spectrum of the core/shell CQDs as recorded in an established regime, e.g., at a pumping fluence several times higher than the transparency value. The ASE peak develops around 611 nm with a FWHM of ~4.4 nm as fitted with a Gaussian curve (fit details not given). The peak value of the ASE is red-shifted compared to the edge PL peak as measured in the edge configuration PL (597 nm, Figure 5.4 a)). This behaviour is typical from core/shell CQDs systems and is attributed to photo-induced absorption phenomena within the CQDs and/or the bi-exciton binding energy [251]. These results indicate that the CQD/PMMA film can sustain stimulated emission. Hence, it can be used as a laser material.

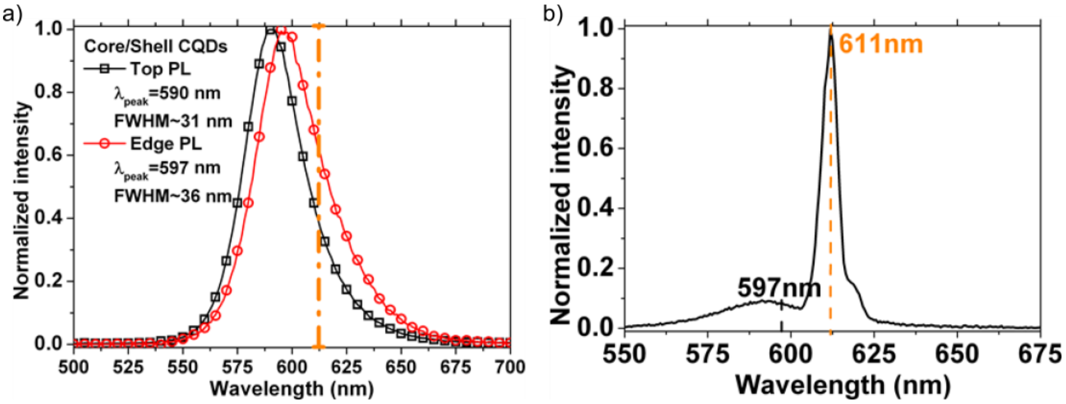

Figure 5.4: a) Top and edge micro-photoluminescence spectra under 371 nm optical excitation of core/shell CQDs dispersed at a concentration of 50 mg/mL in a PMMA solution at 1.6 mg/mL. The sample was processed by spin-coating on a silica substrate. b) Stimulated emission spectrum of the previous film under nanosecond optical pumping. The dash line in both figures represents the peak wavelength of the stimulated emission spectrum.

Interestingly, a variation in the composition of the CQD/PMMA composite is reflected in the ASE behaviour of similarly processed films and on similar substrates (e.g., amorphous glass in this case). As shown in Figure 5.5 a), the ASE for a composite with a lower load of PMMA (1.6 mg/mL, 50/1.6 w/r) has a threshold about 3-fold smaller at 1 mJ/cm^2 in comparison to nanocomposite with 16.6 mg/mL PMMA (50/16.6 w/r). In parallel, the stimulated emission peaks at different wavelengths for these two composites are shown in Figure 5.5 b). The most red-shifted ASE peak (611 nm) corresponds to the sample with the highest load of CQDs. The difference in the stimulated emission spectra is attributed to a higher volume fraction of active material in the spin-coated films with a low PMMA amount. Re-absorption phenomena are then more prominent and affect the ASE development. However, there are also more CQDs participating in the amplification process, thus leading to lower thresholds.

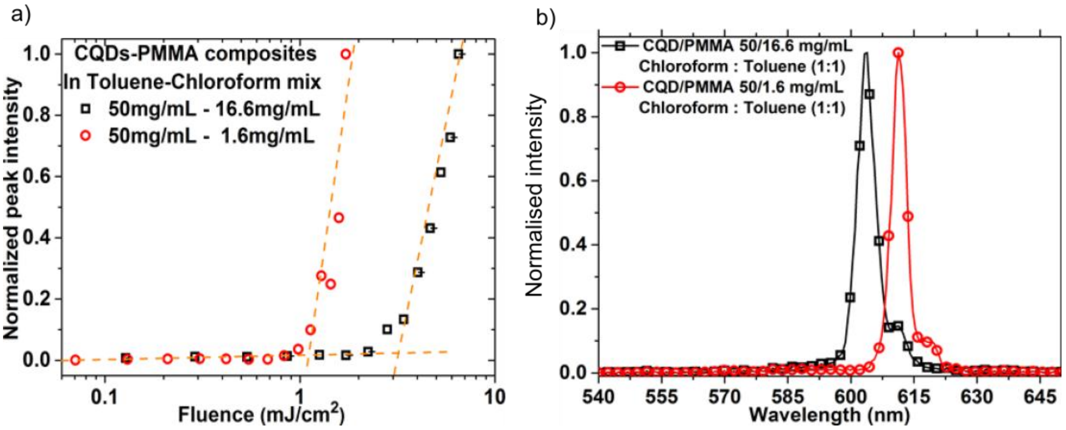

Figure 5.5: a) Transfer function of the ASE from CQDs/PMMA composite samples spin-coated on glass. These data show different CQD/PMMA w/r combination and how it affects their thresholds. b) Further details on the spectra emission of the ASE peaks for different composition of materials.

5.3.3.2. Laser demonstration

A typical spectrum and the power transfer function for a 'flat' DFB laser are plotted in Figure 5.6 a) and b), respectively. The oscillation threshold is 375 µJ/cm^2. This result is the lowest threshold obtained for a CQD laser in a temporal regime >1ns. The optical pulses of the pump source and of the CQD laser are plotted in Figure 5.6 c) and were measured by **Dr Benoit Guilhabert**. The spectrum of the CQD laser 2-times above threshold shows a single peak emission wavelength centred at 607.35 nm and with a FWHM of 0.6 nm, determined by Gaussian fit of the spectrum, as detailed in Figure 5.6 a). The equation of the Gaussian fit is:

$$y = l \times \exp(-4\ln(2)\,\frac{(\lambda - \lambda_0)^2}{fwhm^2} \qquad \textbf{Eq. 5.1}$$

With, l a constant, λ the wavelength, λ_0 the peak wavelength and *fwhm* the full width half maximum.

The inset of Figure 5.6 b) shows more details about the spectral evolution of the laser emission close to the threshold transition. The FWHM of the laser linewidth was between 0.3 nm and 0.6 nm across the whole range of operation studied. These linewidths are limited by the reproducibility of the gain layer. The optical pulse of the pump source and the laser are shown in Figure 5.6 c).

Two other representative transfer functions measured at different positions on the same sample are plotted in Figure 5.7. The overall average threshold for this laser is 450 ± 80 μJ/cm^2. The variation in threshold with position is attributed to possible defects and scattering centres within the film or on the grating surface at particular spatial positions and is not due to a change of the CQD film thickness, as the wavelength is constant within 1.1 nm over the whole surface of the laser. Other laser devices were fabricated and measured as well and shown similar characteristics with average threshold below 450 μJ/cm^2. This state-of-the-art threshold performance shows that a concentration of 50 mg/mL is sufficient to obtain laser oscillation with our approach whereas the literature often stresses the need for highly concentrated CQD solution (100 to 200 mg/mL) to obtain a dense, i.e. close packed, film after spin-coating [189]. This low threshold obtained for a CQD laser is influenced by the thickness of the film obtained by combining the right concentration and the right spin-coating speed.

Spectra and thresholds at three different positions are measured on the CQD DFB laser on an ultra-thin glass membrane. Figure 5.7 represents the power transfer functions at these different points with the corresponding values of threshold (595 μJ/cm^2, 375 μJ/cm^2, 372 μJ/cm^2). The spectrum at each point is plotted in the inset of Figure 5.7, showing that the wavelength does not vary significantly on the surface of the sample.

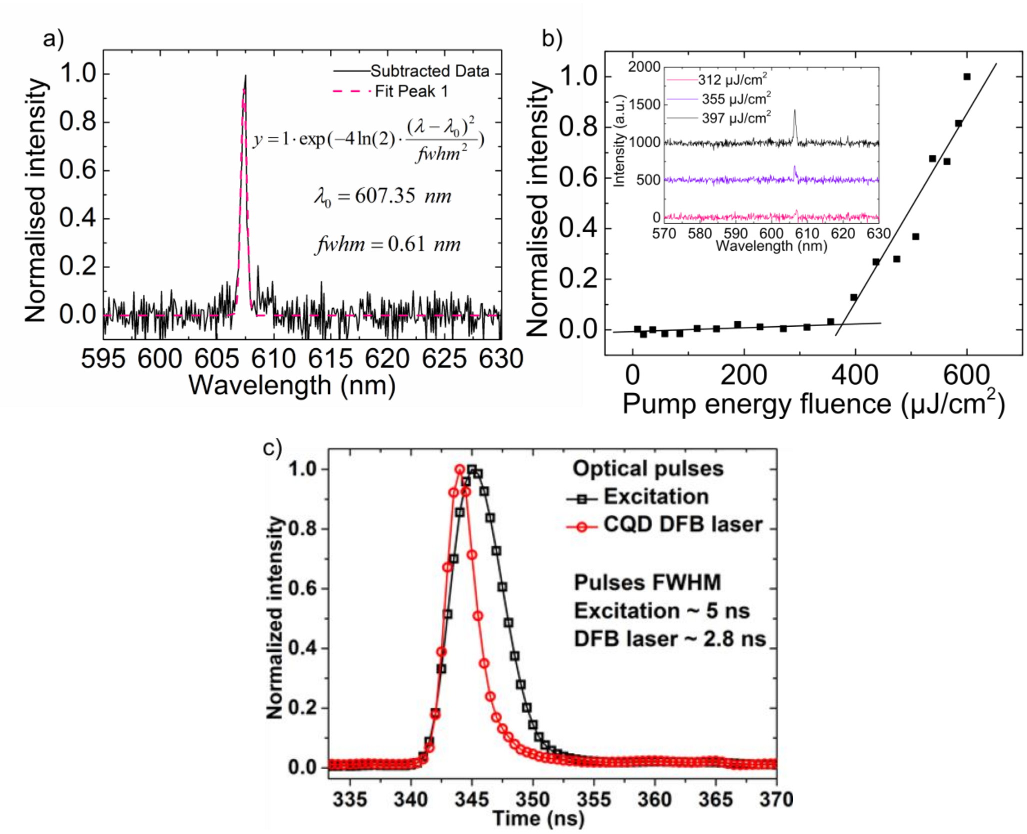

Figure 5.6: a) and b) represent respectively the spectrum and the power transfer function of the CQDs DFB laser on a flexible glass substrate. Inset of b) gives details of the spectrum around the threshold region. c) Represents the optical pulse of the pump source and the CQD laser.

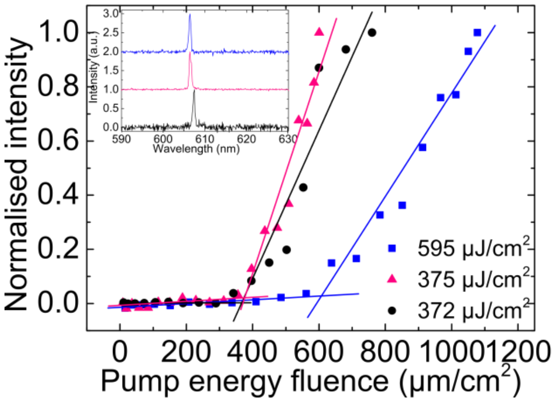

Figure 5.7: Detail of the threshold measured at different positions on the laser.

5.3.3.3. Demonstration of mechanical flexibility

The behaviour of the hybrid CQD DFB lasers when bending the flexible glass substrate was studied. The emission wavelength above threshold for different bending radii of curvature is shown in Figure 5.8. For these measurements, the pump energy was kept constant at 1.80 µJ. When the radii of curvature are reduced to -0.7 and -0.5 cm a blue shift of the wavelength by 5 nm and 8 nm is induced, respectively. For radii of curvature of 0.6 cm and 0.4 cm, the wavelength red-shifts by 6 nm and 10 nm, respectively. The total tuning of 18 nm is limited by a maximum radius of curvature before fracture of the device and is not limited by the gain bandwidth of the CQDs.

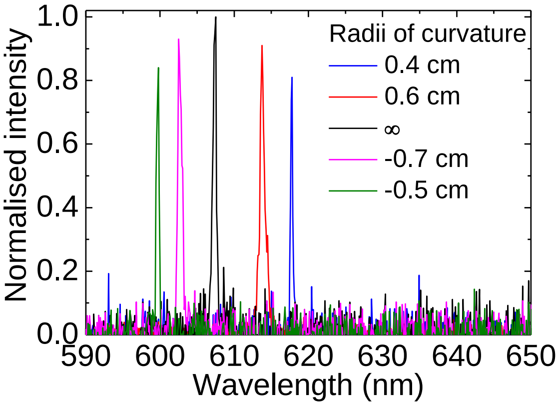

Figure 5.8: Shift in the emission wavelength of the flexible hybrid DFB laser on glass.

It was verified that the emission wavelength does not change significantly as a function of the pump fluence, providing assurance that the tuning comes from the bending of the device. These shifts of the emission wavelength are attributed to corresponding changes in the period of the grating as the glass substrate is bent. As detailed in chapter 4, section 4.4.1.5, the experimental changes in period of the grating and of the radius of curvature of the bending can be approximated and their theoretical values can be calculated. The results are plotted in Figure 5.9, showing good agreement between experimental and expected values.

In Figure 5.10, the evolution of the wavelength as a function of the horizontal displacement x of the translation is displayed. The ascending part of the plot represents the red shift of the wavelength (positive curvature of the laser) and the descending line represents the blue shift or negative curvature, both having a slope of ± 19 nm/cm.

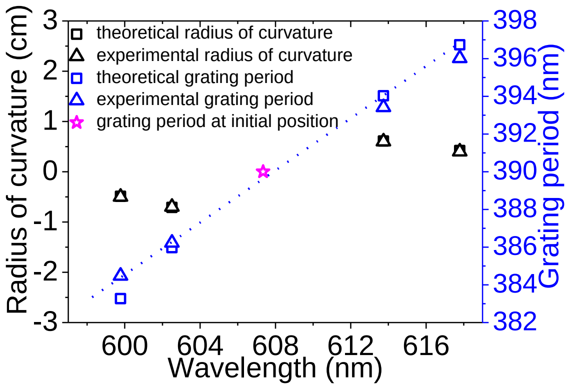

Figure 5.9: Comparison of theoretical and experimental values of the grating period and radius of curvature for each emission wavelength obtained after bending the CQD laser.

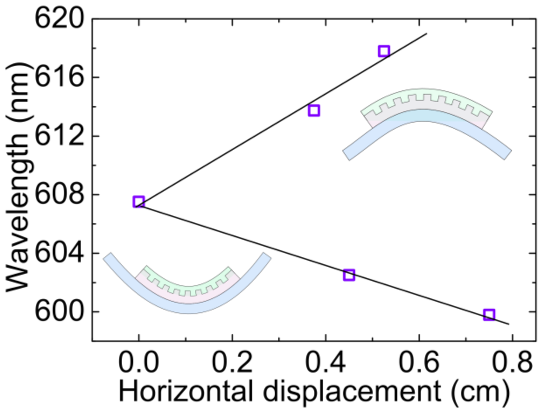

Figure 5.10: Evolution of the emission wavelength of the laser as a function of the horizontal displacement of the micrometre. Lines: theory; Open squares: data points.

In summary, a CQD laser on an ultra-thin glass membrane was demonstrated. The device is a mechanically-flexible, second-order DFB laser that combines colloidal quantum dots, a surface-patterned polymeric film and an ultra-thin glass substrate. It operates in a single transverse mode, with an average threshold fluence of 450 ± 80 µJ/cm^2 (90 ± 16 kW/cm^2) for an emission close to 607.5 nm. The emission wavelength of the device is continuously-tunable over 18 nm by mechanically flexing the thin-glass substrate. The confirmed correlation between the curvature of the glass substrate and the emission wavelength can serve as a guideline for the future design of such tunable lasers. These lasers could find applications in areas including (bio-) sensing thanks to the nature of their substrate and their overall mechanical and optical properties. The values of thresholds found for CQD lasers are nonetheless higher than for organic semiconductors (as demonstrated in chapter 3 and 4). However, future work on encapsulation and different CQD designs may help reduce the thresholds.

5.4. Quantum dot laser on a flexible silicon substrate

Silicon photonics combines photonic devices (emitters, waveguides and detectors) on a single silicon platform [122]. It allows hybridisation of photonics with electronics, as for example the CMOS technology, offering a route to dense, high-performance and reproducible systems [252,253]. The major issue of silicon for use in the visible is that silicon absorbs light in that spectral region and related platforms are therefore not suited for guiding light. A possibility, if one still wants to utilise silicon as the base platform, is to form waveguides (for example made of polymers) onto the Si but with the guiding section at a sufficient optical distance from the Si substrate (a few microns). Moreover, there are no emitters made directly in silicon. The main cause of this poor light emission efficiency of silicon is due to a low carrier mobility and an indirect band gap. This necessitates hybridisation of the source as well. There are different possibilities for such hybrid sources, one of them being solution-processed lasers – although there will still need to be an InGaN source for excitation somewhere. This hybrid integration is cheap and has a simple fabrication process [122,253–255].

Here, we show the possibility to integrate CQD lasers on silicon. We demonstrate two, one-dimensional, second-order DFB ‘semi-flexible’ (the overall device is flexible but without involving a change in wavelength) red emitting laser platforms. Each laser of the platforms is hybridised on a thin Si substrate element. The elements are then assembled onto an acetate sheet. The geometry is therefore suitable for applications in flexible photonics. One of the devices is made by assembling 3 lasers emitting at the same wavelength. The second device has 5 lasers and emits at two different wavelengths. The lasers are made with colloidal quantum dots as gain medium and follow the same fabrication process as the previous devices described in section 5.3.1. In the following, section 5.4.1 explains the design and fabrication of these integrated hybrid lasers. Section 5.4.2 presents the discussion of the experimental results (spectra and thresholds).

5.4.1. Design and fabrication

Figure 5.11 a) and b) show the two laser platforms studied in this work. The laser elements are formed by a gain layer deposited on top of one-dimensional, acrylate gratings acting as the DFB resonator. The gain medium of both devices is made the same CQDs as in section 5.3. The first platform is made of three individual lasers emitting at the same wavelength (Figure 5.11 a)). Each of those lasers is made on a small silicon substrate; this device will be called device 1 in the text. The second device consists of five independent lasers, again each on a silicon substrate, emitting at two different wavelengths (Figure 5.11 b)); this device will be called device 2 in this text.

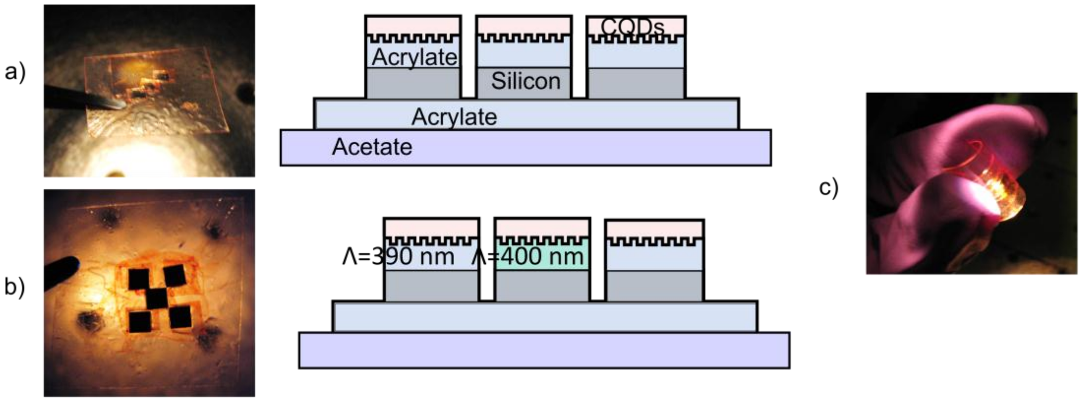

Figure 5.11: Schematics and photos of the two laser structures are shown: (a) silicon-based CQD laser emitting at one wavelength and (b) silicon-based CQD laser emitting at two wavelengths and c) proof of flexibility.

For device 1, the laser gratings all have a period of 390 nm, as for the CQD lasers on ultra-thin glass. For device 2, three gratings having a period of 390 nm and two having a period 380 nm are used to obtain the two different wavelengths. The thickness of the film of the gain material stays unchanged so the different periodicity leads to the different emission wavelengths, which can be determined with the Bragg equation. The solution of CQDs in a PMMA matrix was prepared as previously and spin-coated on top of each grating with the same spin-coating speed as the previous devices. The gratings are then removed from the acetate substrate and cut with a scalpel in order to obtain ~3 x 3 mm free-standing flexible lasers. A drop of NOA85 is spin-coated on top of another acetate sheet at 8 000 rpm. Silicon substrates measuring 2 x 2 mm and having a thickness of 500 µm are placed on the acetate sheet. Another layer of acrylate NOA85 is spin-coated on top of the silicon substrates at 8 000 rpm in order to stick the grating to the silicon substrate. The individual free-standing gratings are placed on top of each silicon substrate. Finally the device is photo-cured under a UV dose of 100 mJ/cm^2 and annealed at for 5 minutes at 35°C on a hot plate.

The advantage of this method is that individual lasers can be arranged freely and according to the number or position required by the applications. Device 1 and 2 only represent examples of what can thus be achieved.

Figure 5.11 c) shows that the overall devices are flexible, however the wavelength does not vary when bending as each individual silicon substrate is not flexible.

The pumping set-up and method are the same as in the previous section.

5.4.2. Experimental results and discussion

5.4.2.1. Device 1

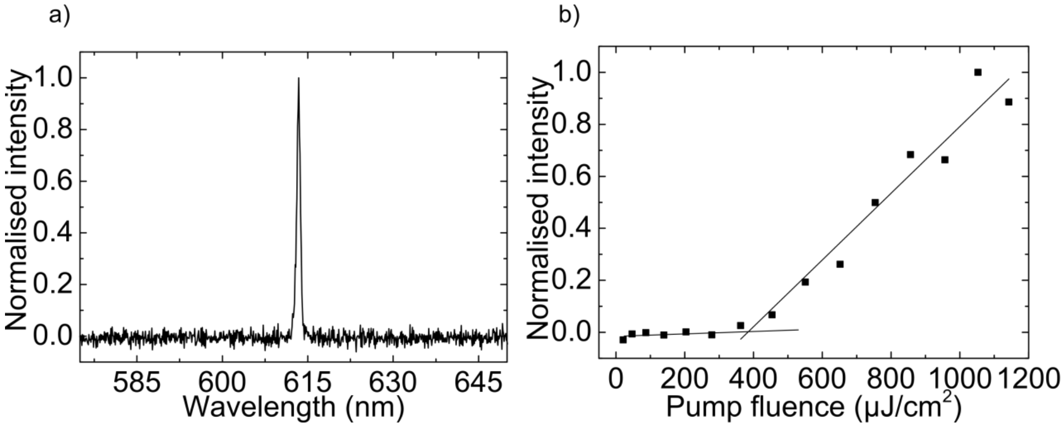

Figure 5.12: a) and b) ,respectively, spectra and power transfer functions of a silicon-integrated CQD laser.

The characteristics of device 1 were measured first. The power transfer functions and the spectra of the laser are plotted in Figure 5.12 a) and b). The spectrum of the CQD lasers shows a single emission wavelength at 613 nm. The threshold is measured on each individual laser at different positions and averaged. Average threshold energy fluence, F_{th}, is found to be 420 ± 70 µJ/cm^2 per pulse for the complete device. This threshold is the same as found previously for CQD lasers made on a flexible glass substrate. It shows that the nature of the substrate has no influence on the threshold of the laser and that the lasers can be integrated on any type of substrate without affecting their performance.

5.4.2.2. Device 2

The emission spectra of the silicon-based laser array emitting at two different wavelengths are shown in Figure 5.13 a) and are 608 nm on the 380nm-period grating and 613 nm on the 390nm-period grating. The wavelength difference is due to the change of grating period. However, by considering Bragg's law, a higher shift in wavelength should be obtained for the same film thickness. The variation could be attributed to a variation of the film thickness formed on the surface of the laser. Average threshold energy fluence, F_{th}, is found to be 420 ± 70 μJ/cm^2 per pulse for the 390nm grating period, as obtained previously, whereas it is 1400 ± 360 μJ/cm^2 for the 380nm grating period. The difference in threshold is due to the laser is operating on the TM mode when the period of the grating is changed to 380 nm.

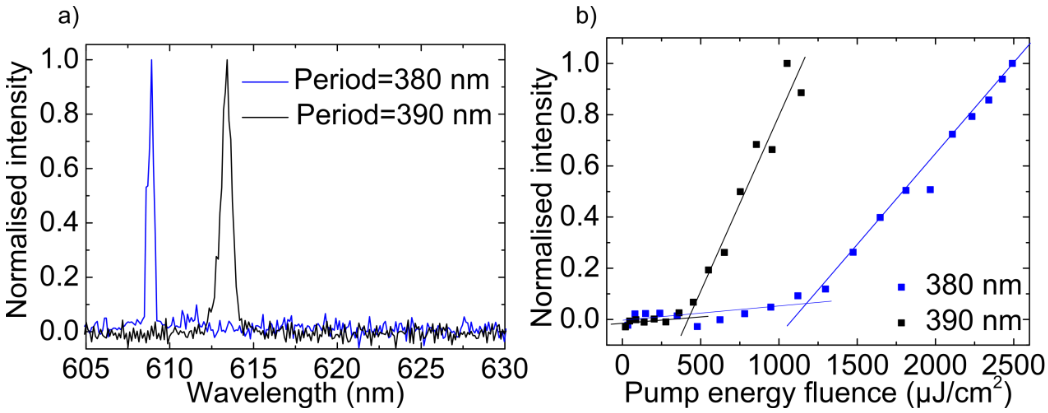

Figure 5.13: a) and b) Respectively spectra and power transfer functions of a based -silicon CQD laser emitting at two different wavelengths.

In summary, silicon-based second order DFB lasers with spin-coated CQDs have been obtained, using commercial core-shell CQDs. Two types of devices were fabricated. Device 1 was a system of three lasers on silicon substrates, each emitting at the same wavelength of 613 nm. All individual lasers of this device were single-mode and demonstrated a threshold fluence of 420 ± 70 μJ/cm^2. Device 2 was a combination of 5 lasers emitting at two different wavelengths. The lasers emitting at

613 nm showed a threshold fluence of 420 ± 70 µJ/cm^2 per pulse and the lasers emitting at 608 nm demonstrated a threshold fluence of 1400 ± 360 µJ/cm^2. Both devices were compatible with mechanically-flexible platforms but without involving a shift in wavelength, as the silicon substrates themselves were not flexible. The flexibility was due to the small size of the lasers on the acetate underlayer film.

5.5. Quantum dot laser as a sensor

Solution-processed lasers are attractive for sensing applications because their characteristics (e.g. flexibility or bendability) can be chosen to facilitate system integration. For example, they can be incorporated into compact lab-on-chip systems and provide non-disruptive and non-contact sensitive platforms that can detect multiple analytes [256–260]. This is why recent research on organic DFB lasers has targeted explosive detection [199,261] and biomarker protein detection in biological solutions for medical sciences application [262]. However, one problem with organic dyes and organic semiconductors for such applications is that their absorption bandwidth is to a certain limited, making the development of systems at multiple wavelengths using a single optical pump laser difficult. It necessitates the development of different materials emitting at different wavelengths but having a common absorption wavelength. Multiple-wavelength lasers with a single optical pump laser would certainly be useful for sensing as it would enable multiplexing, i.e. interrogation and analysis of different laser sensors at the same time with differentiation of the sensors done by the wavelength.

CQDs are suitable for multi-wavelength emission with optical pumping by a single pump source as photons with energies higher than the bandgap are absorbed, which relaxes the tolerances on the pump wavelength. In common with organic gain materials, CQDs are solution-processed and thus compatible with both organic and inorganic materials. This makes CQD a good candidate for optically-pumped hybrid laser sensors [225].

In the following, we demonstrate that colloidal quantum dot DFB lasers are indeed candidates for sensing applications. The potential of these CQD lasers for refractive index sensing in liquid phase is proven by immersion in water. The same lasers as in section 5.3 are used here, following the same fabrication steps and having the same characteristics. The only difference is that the substrate is an acetate sheet instead of an ultra-thin glass membrane. The basic principle of refractive index sensing is described in section 5.5.1. The set-up used to test the potential of these lasers for sensing applications is then presented in section 5.5.2. Finally the experimental demonstration of bulk refractive index sensing is demonstrated in section 5.5.3 by studying the effect of immersion of these lasers in water on the emission wavelength.

5.5.1. Basic principle of refractive index sensing

The potential for sensing applications of CQD lasers are tested in this chapter by sensing a change in refractive index when a laser is immersed in a liquid environment.

For sensing, the gain layer is put into contact with the biological environment (e.g. a drop of fluid to be tested can simply be deposited or flowed over the laser surface). The laser mode oscillates in the plane of the gain layer and interacts with the biological environment at its interface. For biosensing, the sensor needs to be able to detect analytes specifically. Therefore, the surface of the laser is functionalised with molecular probes whose role is to capture and immobilise the molecules to be detected that might be present in the biological medium (see Figure 5.14). Once captured, these immobilised analytes form a layer on the laser surface. As seen in chapter 2, the laser wavelength is given by the product of the period of the grating of the cavity with the mode effective refractive index. The formation of a biolayer on the surface of the laser modifies the effective index and hence changes the laser emission wavelength. The magnitude of this change depends on the mode overlap with the biolayer and its refractive index. Therefore it depends on the amount of analyte and monitoring the wavelength enables the sensing function.

One way to demonstrate this is to use a concept we have already employed for testing the capability of dye-doped and organic semiconductor DFB lasers for sensing applications [12,231,233]. Here as a preliminary demonstration, we show in this section the capability of our CQD lasers to operate in a liquid environment and to sense changes in bulk refractive index (there is no surface molecular probe on the surface). Water is used in this initial demonstration because i) it is a solvent in which many biological species are dissolved and ii) it is a solvent these CQDs will not disperse in. In addition, PMMA by its hydrophobic nature should help in making the sensor robust by ensuring that water does not swell the gain layer.

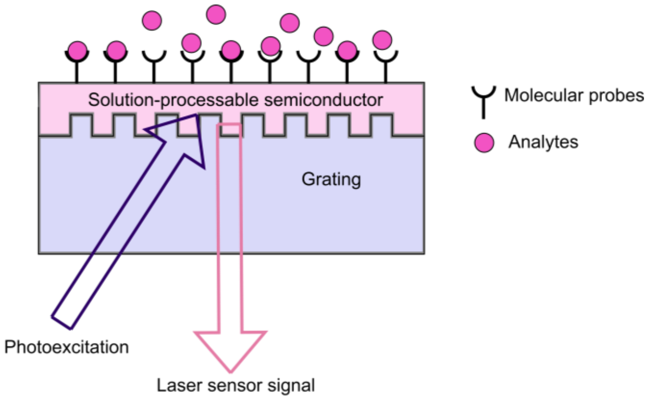

Figure 5.14: Schematic representing the implementation of the organic laser sensor.

5.5.2. Optical set-up used for refractive index sensing

Figure 5.15 shows the experimental set-up used to test the sensing capabilities of CQD lasers. A CQD laser was placed inside a glass cuvette with tweezers and taped on one of the side so that the gain layer faces into the cuvette. The laser was pumped through the back (i.e. through the substrate) and the lasing emission is also collected through the back and collected through an optical fibre. The pump source characteristics are the same as previously. Firstly, the laser emission was measured in air. Then deionised water was added to the cuvette and the laser emission was measured again. The energy of the pump source is kept constant during the experiment, to make sure that no shift is engendered by a change in pump energy. It has been noticed that the emission wavelength shifts slightly (~between 0.1 nm and 0.4 nm) when a laser is pumped under different pump energy fluences (between 450 µJ/cm^2 to 600 µJ/cm^2).

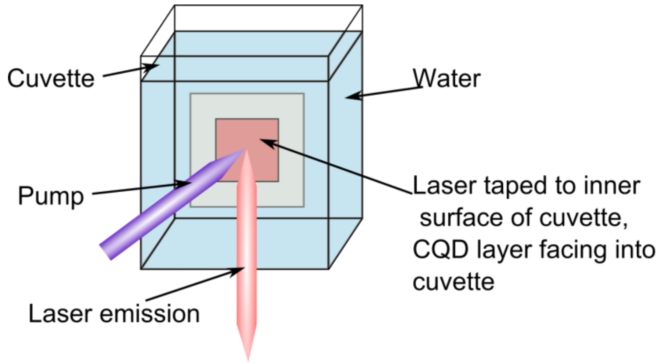

Figure 5.15: Schematic of the set-up used for refractive index sensing.

5.5.3. Demonstration of refractive index sensing

The measurements in this section were made by **Dr Benoît Guilhabert**. Figure 5.16 represents the spectrum of the CQD laser in air and then in water. The emission wavelength of the laser in air (n=1) is 610 nm. Once immersed in water, the refractive index of the superstrate is increased to ~1.33 and an emission wavelength of 614 nm is obtained, i.e. a red-shift of 4 nm.

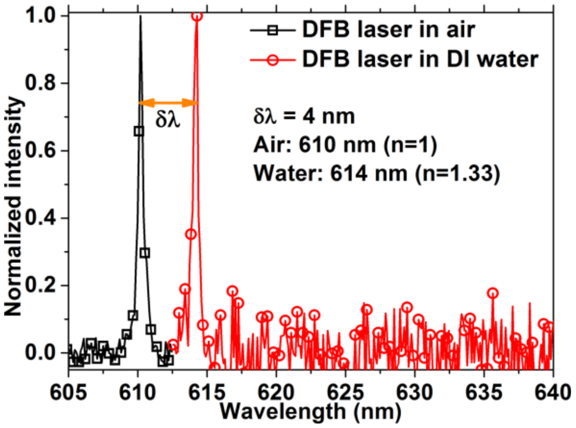

Figure 5.16: Spectrum of the CQD laser in air and in water.

At the same time, there is a drop in intensity by approximately 70% when the laser is immersed in water as shown by the level of noise in the spectrum. The drop is attributed to an increase of the threshold. Possible reasons for this are still to be determined. Nevertheless, it was verified that this lowered intensity is not detrimental to the sensing function. Figure 5.17 shows 2 cycles of water refractive index sensing with the same CQD DFB device probed at two different locations in sequence. Cycle 1 is done at position 1, cycle 2 at position 2. For each cycle, the water is placed and removed from the cuvette several times. Initially in air for cycle 1, the DFB emits at 610 nm with an intensity of ~1000 counts. In water, the emitted wavelength shifts to 614 nm. Alternation of air and water confirms that the shift is constant throughout the cycle without variations between each measurement (spaced in time by about 1 min). Each time the water is removed, the wavelength goes back to 610 nm. This shows that despite the variation of intensity, the DFB laser wavelength shift is not affected when pumped at a constant fluence. For cycle 2, the shift in wavelength also goes back to its initial value. The intensity drops when the laser is placed in water but increases when the water is removed. This proves that the shift in wavelength is reversible. These important results demonstrate that the CQD lasers can operate in a polar solvent and are suitable for sensing.

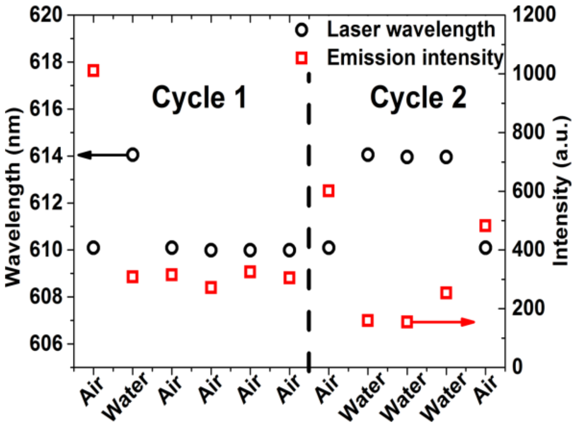

Figure 5.17: Emission wavelength and intensity of the CQD laser in air and water.

It has been shown that CQD DFB lasers are suitable for bulk refractive index sensing. A red shift in emission wavelength of 4 nm has been detected upon immersion in water. It has also been demonstrated that this change in wavelength is reversible. This study shows that CQD lasers have potential for sensing applications.

5.6. Conclusion

In conclusion we have reported new formats of distributed feedback lasers made with colloidal quantum dots as gain material dispersed in a PMMA matrix, with low operating thresholds. The overall aim of this chapter was to demonstrate that these lasers can be integrated on different kind of substrates and that their flexible nature allows arranging them in different shapes and sizes. Two materials were used as laser substrates: a new format of ultra-thin flexible glass membrane and 500µm-thick silicon squares. The nature of the substrate does not modify the performance of the lasers as the threshold did not vary according to the substrate. The devices made in this chapter were only examples of possible devices that could be fabricated based on CQD lasers but it shows the many possibilities; CQD lasers can be tuned to different wavelengths, integrated onto different substrate and assembled as desired.

It was also proven that CQD DFB lasers are potentially good candidates for refractive index sensing applications as it was found that the emission wavelength presents a shift when measured in a different media.

Chapter 6

Mechanically-responsive plastic lasers and multicolour lasers

6.1. Introduction

In the first part of this chapter, the suitability for lasers of a novel type of piezofluorochromic material presenting aggregation induced emission (called TPE1) is tested. A mechanically-flexible all-organic second order DFB laser is made using TPE1 as the gain material. An average threshold fluence of 60 ± 6 µJ/cm^2 (12 ± 1 kW/cm^2) for an emission close to 517.9 nm is reported. This is to our knowledge the first demonstration of a laser made with such a material. The piezofluorochromic properties of TPE1 are also studied by looking at the influence of pressure on the ASE in a thin film. A variation of the emission wavelength of TPE1 with pressure is found, opening up opportunities for the development of lasing-based pressure sensors.

The second part of the chapter demonstrates two formats of multiwavelength red, green blue (RGB) lasers on a mechanically-flexible platform. The devices were fabricated by combining three all-organic DFB lasers entirely made by soft lithography. The complete devices were encapsulated with polymer and a 50µm-thick glass membrane in order to improve the lasing threshold and the photosatbility. The first device consists in three lasers assembled next to each other on a flexible glass substrate. Each laser can be optically-pumped individually or simultaneously, giving multicolour red, green and blue laser output with individual threshold of, respectively, 28.2 µJ/cm^2, 11 µJ/cm^2 and 31.6 µJ/cm^2. The second device is obtained by stacking the three lasers, respectively the red, green and blue laser. The device emits simultaneously at the three wavelengths, giving a quasi-white laser output with a lasing threshold of 42.1 µJ/cm^2.

6.2. Mechanically induced luminescence changes, TPE1: a mechafluorochromic material

Interest in piezofluorochromic (PFC), or mechanofluorochromic, materials has grown in the past few years due to their potential applications in sensors [263,264], security inks [265] and memory chips [266]. The fluorescence of these materials changes when they are submitted to external force stimuli. Their behaviour can be changed either chemically or physically. The chemical method uses chemical reactions to modify the molecular structure by breaking bonds. Chemical structural changes are often accompanied by an alteration of the properties of the material, such as the fluorescence, and these reactions are in most cases irreversible [267]. The physical method on the other hand is based on the modification of the molecular packing density, not of the molecular structure, and this is in general reversible [268]. This method is really attractive as it allows tuning (switching) of the colour (luminescence) by simply changing the arrangement of the molecules, providing great opportunities for sensing [269]. Having a laser made from such a material would open doors for the development of new types of sensors. However, to our knowledge, no such laser has previously been demonstrated as organic semiconductors presenting PFC characteristics are still rare and suffer from an aggregation-cause quenching (ACQ) effect. This effect happens when chromophores aggregate via π-π stacking in the condensed phase, which leads to a fluorescence in concentrated solution and in the solid state that is weaker than in dilute solutions [270,271].

In 2001 an OS material presenting anti-ACQ characteristics was discovered by Ben Zhong Tang's group [202]. This chromophore is quenched in solution but shows luminescence in the solid-state. The aggregation increases the fluorescence efficiency due to the shape of the molecules that cannot pack through a π-π stacking process and because intramolecular rotations are highly restricted due to physical constraints [203,204]. When molecules are free to rotate a non-radiative relaxation pathway is obtained for the decay of the excited stated, quenching the luminescence. But when the rotations are restricted (in the condensed state) the non-radiative pathways are blocked. This phenomenon is called aggregation-induced emission (AIE) and is illustrated in Figure 6.1. The arrows on the figure represent the possible intramolecular rotations that are possible in solution, but blocked when the molecules are condensed.

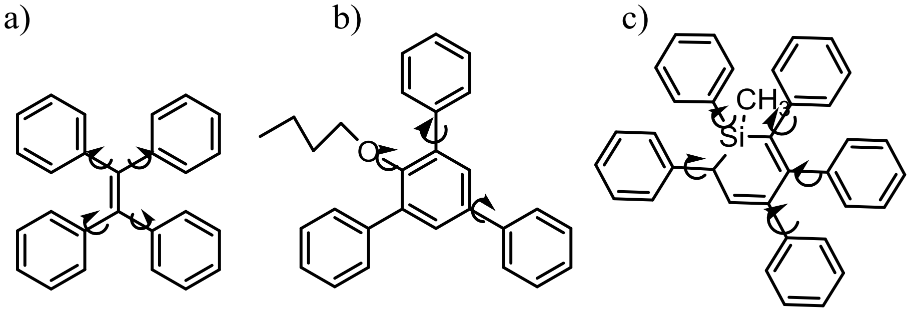

Figure 6.1: Examples of AIE active cores with a) tetraphenylethene, b) 2-butoxy-1,3,5-triphenylbenzene and c) 1-methylphenyl-2,3,4,5-tetraphenylsilole.

A novel PCF star-shaped oligofluorene tetraphenylethene material called TPE1 presenting AIE characteristics was synthesised by Clara Orofino Peña (WestChem). TPE1 is formed by a tetraphenylethene core (Figure 6.1 a)) surrounded by monofluorene arms. This material exhibits fluorescence quenching in solution but shows higher emission efficiency when aggregated. The AIE effect also induces a blue shift of the emission wavelength. TPE1 has a large absorption cross section and a large Stokes shift that could make it an attractive candidate for lasing applications. It is used here as an active element in order to test its suitability as an organic semiconductor lasing material and also to test its PFC properties. Details on TPE1 structure and characteristics are given in chapter 2, section 2.3.1.4.

In this study, we start by testing the suitability of TPE1 for lasers by characterising the ASE of thin films. Then, a laser is fabricated and demonstrated. Finally, the PCF properties of TPE1 are determined by looking at the influence of pressure on the emission wavelength of the material in the ASE regime.

6.2.1. Design and fabrication

To test the suitability of TPE1 as a gain material for lasing application, the ASE of the material was measured. To do this, different concentrations of TPE1 in different solvents were tested. Solutions of TPE1 were spin-coated onto smooth substrates. The substrates were 0.1mm-thick acetate sheets covered with epoxy (NOA65). The epoxy was spin-coated at 1000 rpm and cured under a UV dose of about 1.8 J/cm^2. Samples were left at room temperature overnight to dry.

Table 6.1 describes all the steps done in order to find the right concentration, spin-coating speed and solvent. In order to obtain gain, TPE1 needs to be aggregated and the film needs to be sufficiently thick. The solvent was changed from toluene to THF as THF has a lower boiling point, allowing a higher thickness of film. When the concentration increases, the aggregation is stronger as the molecules are closer to each other. However, when the aggregation is too high (high concentration or water added to solution), clusters are formed. This engenders an increase in threshold, sometimes killing any gain, as the crystals change the geometry of the molecule, due to a lack of space.

Solvent	**Spin-coating speed (rpm)**	**Concentration (mg/mL)**	**ASE result**
Toluene	3200	20	No gain
Toluene	3200	30	No gain
THF	3200	30	**Gain**
THF	1000	30	**Gain**
THF	1000	50	**Gain**
THF 10%/ water 90%	1000	20	No gain
THF 90%/ water 10%	1000	30	No gain

Table 6.1: Different recipes used to fabricate ASE samples in order to find gain.

From Table 6.1 it is seen that the only samples showing gain are made from 30 mg/mL of TPE1 in THF spin-coated at 3200 rpm, 30 mg/mL of TPE1 in THF spin-coated at 1000 rpm and 50 mg/mL of TPE1 in THF spin-coated at 1000 rpm. The optimum recipe is 30 mg/mL of TPE1 in THF spin-coated at 1000 rpm as it presents the better ASE property (lower threshold than the two others, see section 6.2.3.1). This recipe was chosen for fabricating thin-film samples used in the study of the influence of the pressure on the emission wavelength (section 6.2.3.2).

Figure 6.2 shows the structure of the lasers, formed by TPE1 deposited on top of a mechanically-flexible grating. The grating is made as described in chapter 2, section 2.4.1 and has a period of 330 nm. For processing, TPE1 in solid phase (powder) is dissolved in THF, at a concentration of 30 mg/mL, as found previously.

The dispersed TPE1 is then spin-coated at 4000 rpm to form a film of ~110 ± 10 nm and left to dry overnight.

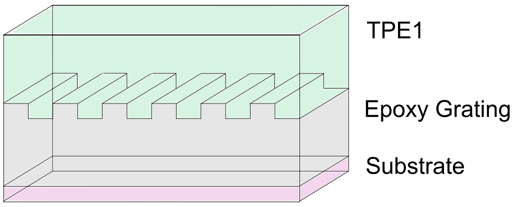

Figure 6.2: Schematic of the TPE1 laser structure.

6.2.2. Laser characterisation and pressure sensor set-ups

The DFB lasers were optically pumped by a Q-switched, frequency-tripled Nd:YAG laser and the emission was detected trough an optical fibre connected to a spectrometer as described in chapter 2, section 2.5.1. The full width at half maximum (FWHM) pump stripe size on the sample was 0.29 mm x 2.79 mm. The transfer functions and spectra of the lasers were measured. The average threshold quoted in the experimental results section was obtained by averaging several measurements taken at different positions on the surface of the device.

To measure the influence of the pressure on emission of TPE1 films, an hydraulic press was initially used. However, this did not allow knowing precisely the value of the pressured applied on the samples and therefore the set-up described in Figure 6.3 was built. It consists of a torque press. The sample is placed in a cylindrical container and a large screw is employed to apply pressure on the sample. To apply this pressure, a torque wrench is used (the corresponding pressure applied on the sample is deduced from the torque). The pressure is applied on the sample for one minute before the latter is characterised.

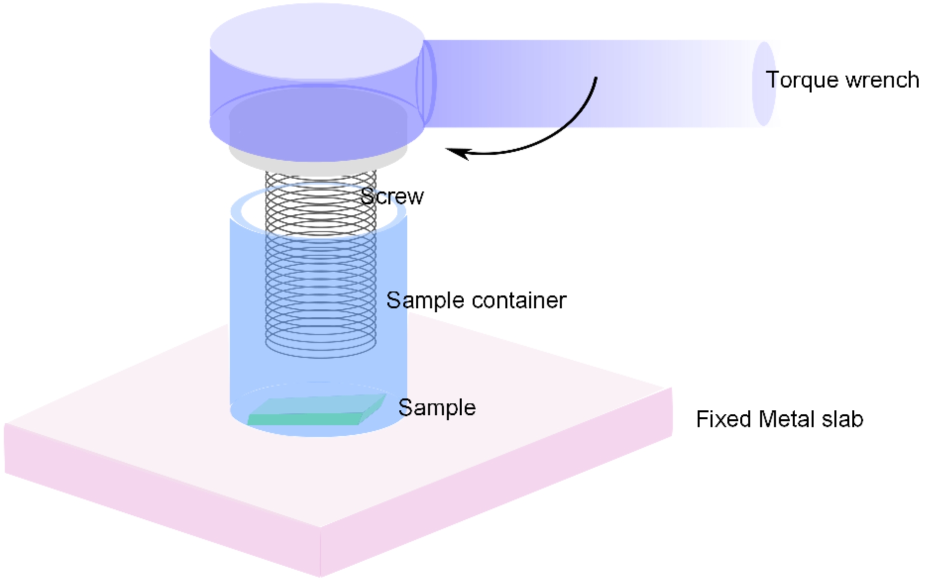

Figure 6.3: Set-up used to determine the influence of pressure on TPE1.

6.2.3. Experimental results and discussion

6.2.3.1. Lasing performance

ASE of different TPE1 films was measured in order to choose the best recipe suitable to make lasers. The spectra and power transfer functions of films showing gain are represented in Figure 6.4: the samples made with a concentration of 30 mg/mL of TPE1 in THF spin-coated at 3200 rpm, a concentration of 30 mg/mL of TPE1 in THF spin-coated at 1000 rpm and a concentration of 50 mg/mL of TPE1 in THF spin-coated at 1000 rpm are plotted respectively in Figure 6.4 a), b) and c). The first recipe gives an ASE peak centred at 503 nm, the second one at 505 nm and the third one at 509 nm. The change in wavelength is due to a different film thickness (caused by different spin-coating speed and concentration). Thresholds for the onset of ASE of 39 µJ/cm^2, 137 µJ/cm^2 and 540 µJ/cm^2 are found for respectively the first, the second and the third recipe. The concentration of 30 mg/mL was therefore chosen to make lasers. The increase in threshold between the different recipes is due to different thicknesses of the gain layer when changing the spin-coating speed and/or the concentration. The sample made with the concentration of 50 mg/mL probably has too high absorption of the pump, engendering an increase in threshold.

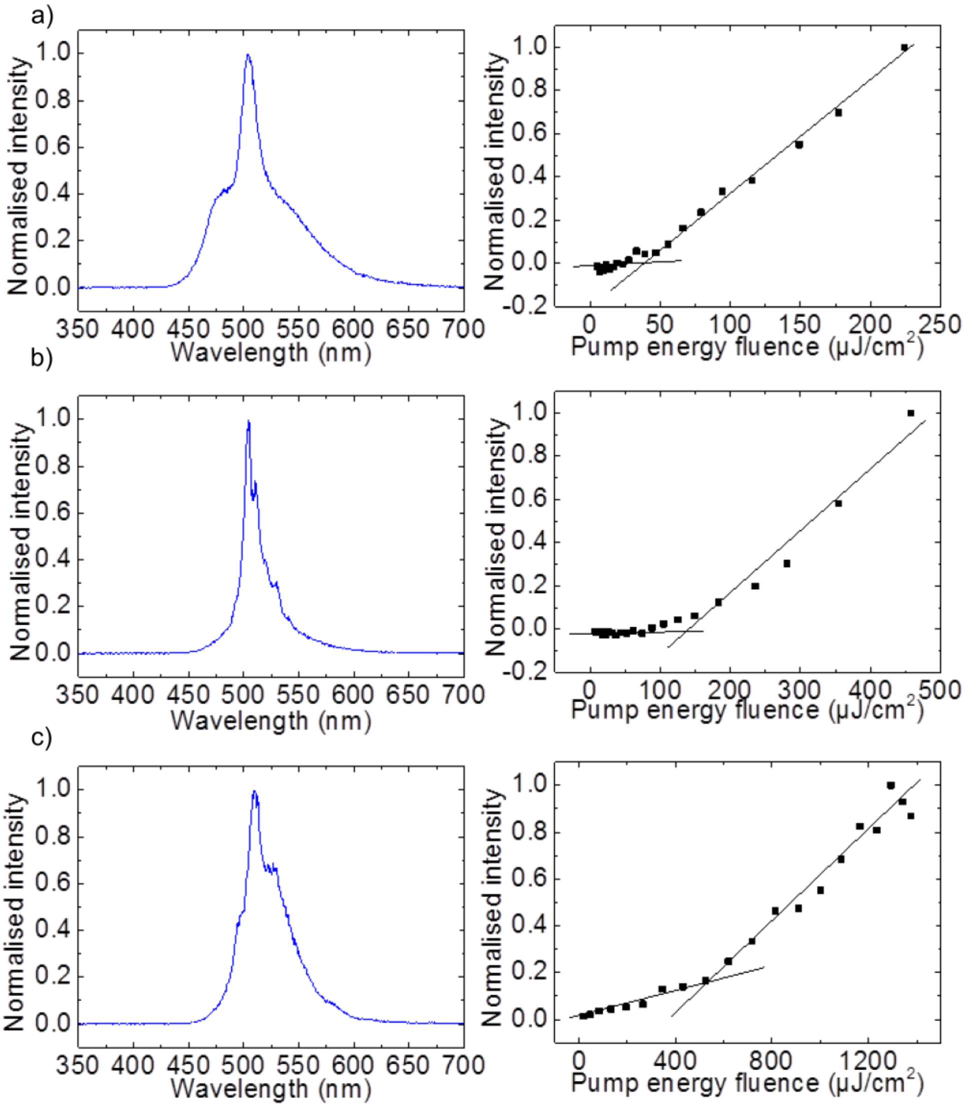

Figure 6.4: Spectra and power transfer function for ASE of samples made with a) a concentration of 30 mg/mL of TPE1 in THF spin-coated at 3200 rpm, b) a concentration of 30 mg/mL of TPE1 in THF spin-coated at 1000 rpm and c) a concentration of 50 mg/mL of TPE1 in THF spin-coated at 1000 rpm.

The concentration of 30 mg/mL of TPE1 in THF spin-coated at 3200 rpm gives the thinner layer and the concentration of 50 mg/mL of TPE1 in THF spin-coated at 1000 rpm gives the thicker layer. It is seen that the wavelength red-shifts when the thickness increases. This is due to the film being too thick: the pump then is absorbed too much and the film is not homogeneously excited. This means that some sections of the film, on the side of the pump, are amplifying while on the other side it may be absorbing and reabsorption leads to a redshift. However, for the laser fabrication, the spin-coating speed needs to be adjusted to ensure only a single TE-polarised mode.

A single transverse mode laser was obtained using a spin-coating speed of 4000 rpm. The spectrum of the TPE1 laser 3-times above threshold is shown in Figure 6.5. It displays a single peak emission wavelength at 517.9 nm with a FWHM of 0.26 nm determined by a Gaussian fit of the spectrum. The overall average threshold for this laser is 60 ± 6 µJ/cm^2. This threshold value is the average of three measurements taken on a same laser, within an area of 3 x 3 mm.

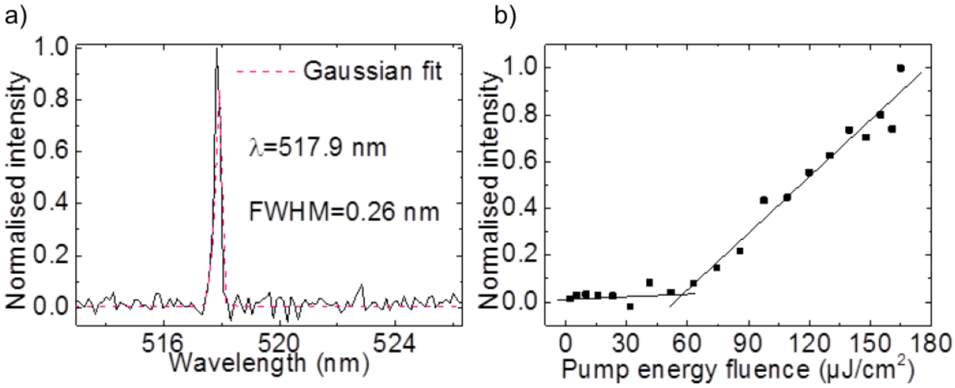

Figure 6.5: a) Spectrum and b) power transfer function of the TPE1 laser.

Figure 6.6 shows the spectra and transfer functions for each measurement. The threshold varies from 54 µJ/cm^2 to 66 µJ/cm^2, as shown in Figure 6.6 b). However Figure 6.6 a) indicates that the emission wavelength stays constant over the surface studied. The change in threshold is then not due to a change in TPE1 film thickness but attributed to possible defects within the film or on the grating surface. The FWHM of the laser linewidth at these three positions was also calculated by Gaussian fit. Values between 0.25 nm and 0.26 nm were found across the whole range of pumping level studied. Other laser devices were fabricated and measured as well and had similar characteristics with an average threshold around 60 µJ/cm^2.

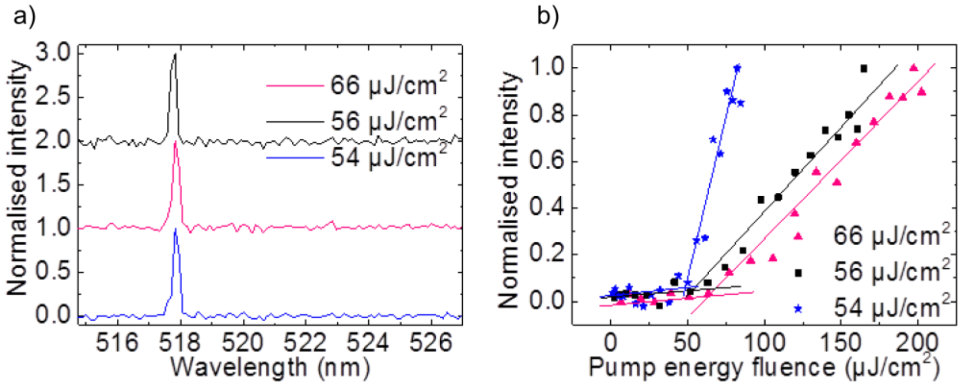

Figure 6.6: Details of a) spectra and b) threshold at different positions on the laser.

For additional characterisation, the photostability of TPE1 in air was measured (Figure 6.7). The intensity was monitored for about 30 minutes (17,400 pulses) with a pump fluence of 330 μJ/cm^2 (about 5.5 times above threshold). A mono-exponential decay is fitted to the curve intensity vs. the number of pulses, giving a 1/e degradation dosage, F_{deg}, of 4.5 J/cm^2. This value shows that the photostability of TPE1 is comparable to the photostability of T3 (see chapter 3 section 3.5.1). As for all organic gain materials the main mechanism responsible for such degradation is photo-oxidation. Possible ways to improve the lifetime of TPE1 would be to embed it within an appropriate polymeric host matrix or to use encapsulating layers (see chapter 3). Figure 6.7 also shows the evolution of the emission wavelength as a function of the number of pulses. It is seen that the wavelength decreases slightly when TPE1 is degrading, possibly due to a loss of conjugation.

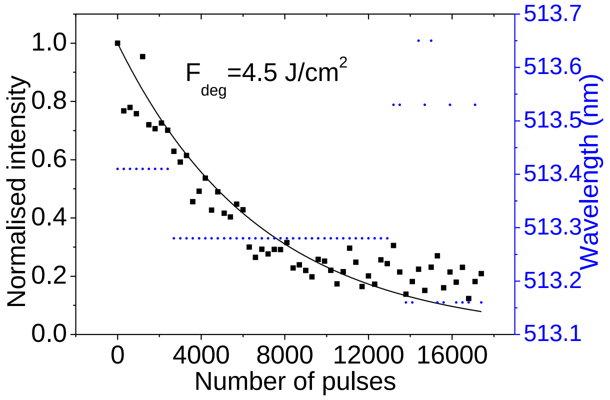

Figure 6.7: Photodegradation of TPE1.

6.2.3.2. Pressure study

TPE1 being an AIE material, a series of studies were carried out to check its piezofluorochromic behaviour. The effect of pressure on the ASE of films of TPE1 was first studied using a hydraulic press. Different pressures were applied on TPE1 films spin-coated on NOA65 substrates and the ASE was measured before and after applying the pressured as shown in Figure 6.8. The pressure was applied on a 1 cm^2 TPE1 film. A blue shift in wavelength was obtained for each pressure applied, as the AIE engenders a blue shift in wavelength. Shifts of 15.7 nm, 19.1 nm, 20.9 nm and 28.5 nm were obtained when applying respectively 2 tons/cm^2, 2.5 tons/cm^2, 3 tons/cm^2 and 5 tons/cm^2. This blue shift might be due to the greater constraint of the molecules of TPE1 under pressure, causing a reduction of the planar conformation, leading to an increase in the energy of emission.

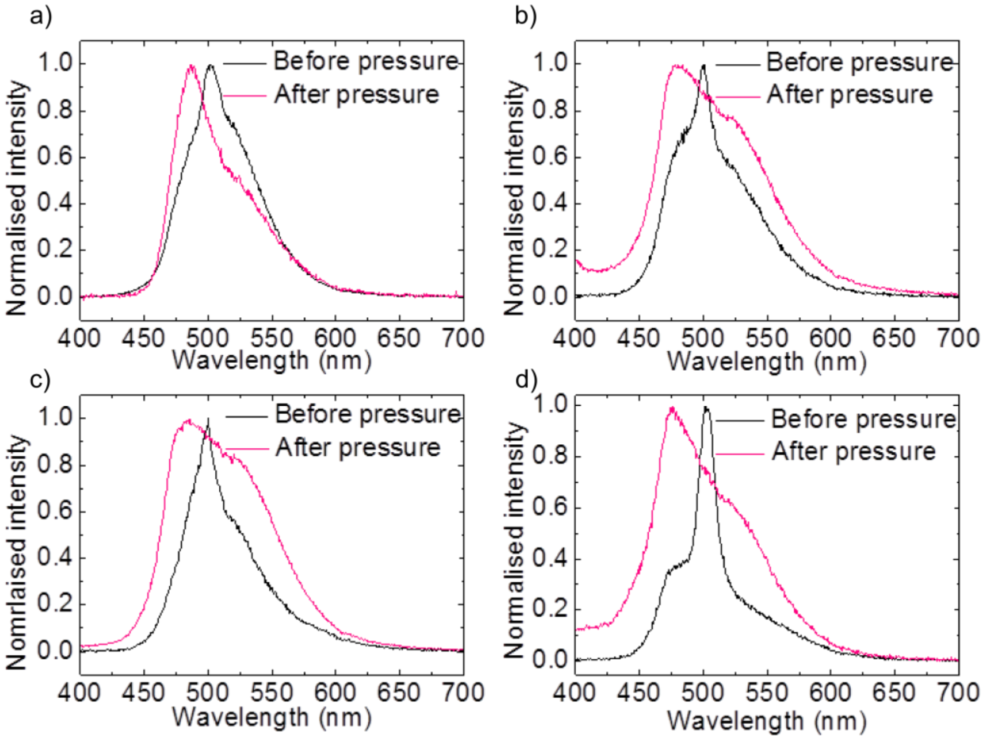

Figure 6.8: Pressure study on TPE1 films using a hydraulic press applying a) 2 tons/cm^2, b) 2.5 tons/cm^2, c) 3 tons/cm^2 and d) 5 tons/cm^2.

The relationship between the emission wavelength shift and the pressure applied on the TPE1 film is plotted in Figure 6.9. The weights applied in tons/cm^2 on the samples, as given on the hydraulic press, are converted to N/m^2 [272]. The values of the pressure in N/cm^2 are given in Table 6.2. The relationship is linear in that range, showing that TPE1 should be a promising material for pressure sensing devices based on the ASE of the material. However the hydraulic press did not give a precise value of the pressure applied.

Weight applied (ton/cm^2)	**Pressure (N/cm^2)**
2	18000
2.5	22000
3	27000
5	44000

Table 6.2: Conversion of weight applied on TPE1 films to N/cm^2.

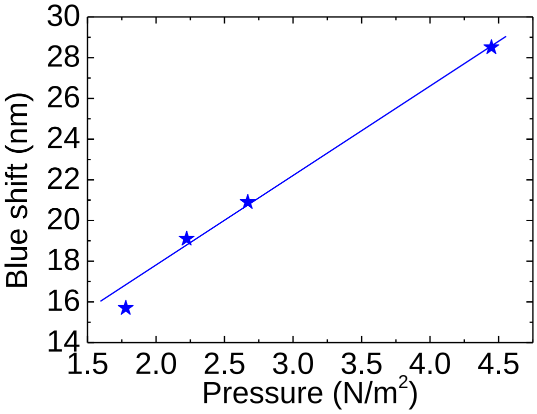

Figure 6.9: Blue shifts in wavelength obtained after applying different pressures on TPE1 films with the hydraulic press.

The effect of the pressure was reversible (Figure 6.10). The sample that received a pressure of 2 tons/cm^2 was left overnight and pumped the day after. The ASE wavelength returned to its initial value (i.e. before application of pressure). This means that the molecules of TPE1 relax to their initial planar conformation after a suitable lapse of time.

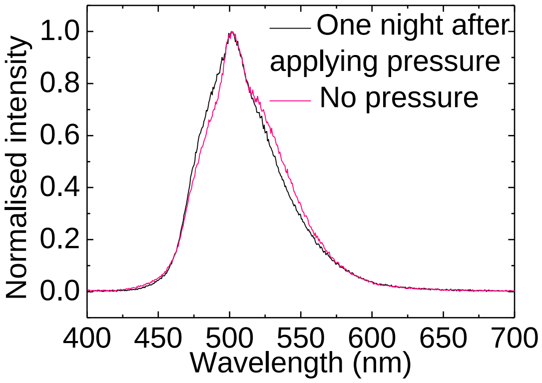

Figure 6.10: Reversible pressure effect.

To make sure that TPE1 was responsible for the spectral shift obtained after the application of pressure and that this effect did not occur with other non-aggregation induced emission gain material, the same test was done with T3. A pressure of 1.8 N/m^2 was applied on a film of T3 spin-coated on NOA65. Figure 6.11 shows the ASE of T3 before and after the application of pressure. A blue shift of only 1 nm was found, probably due to small defects on the surface of the sample or variation of the thickness of the T3 film. For the same pressure applied on TPE1, a shift in wavelength of 15 nm was found. This result confirms that the shifts obtained for TPE1 were due to the arrangement of the molecules after applying a pressure and not to a film effect (change in thickness or in refractive index for example).

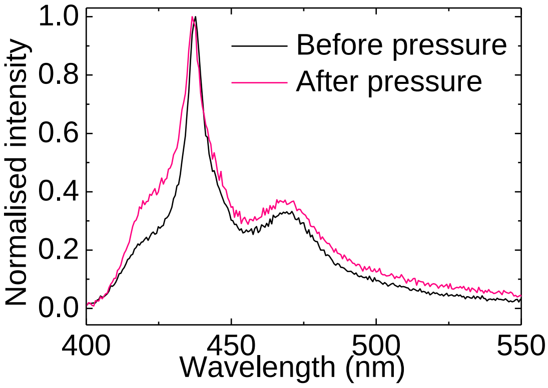

Figure 6.11: Comparison Pressure experiment done with T3.

In order to obtain more accurate measurements of the influence of the pressure on the emission of TPE1 film, the torque press was used. A torque value was set on the wrench allowing deduction the pressure applied on the sample. To calculate the pressure on the sample, the following formula was used [273]:

$$T = kdF \qquad \textbf{Eq. 6.1}$$

With T the torque (N·m), k the torque coefficient (0.36 for steel), d the diameter of the top of the screw (1.6 cm) and F the force applied on the sample.

The pressure can be deduced from the force applied by dividing the force by the area where the force is applied. This area is equal to 2.3 cm x 4.2 cm.

The torque values used were 10, 20, 30 and 40 ft.lbs. Table 6.3 shows the corresponding pressure values.

Torque (ft.lbs)	Pressure (N/cm^2)
10	274
20	549
30	823
40	1097

Table 6.3: Values of pressure applied on sample calculated for torque applied.

The emission wavelength of TPE1 was measured before and after applying the pressures listed in Table 6.3. Those values of pressure were a lot smaller than the ones applied with the hydraulic press, consequently the shift in wavelength was a lot smaller. Figure 6.12 shows the spectra of TPE1 after applying the different pressures. Pressures of 274 N/cm^2, 549 N/cm^2, 823 N/cm^2 and 1097 N/cm^2 respectively give shifts in wavelength of 4.1 nm, 4.6 nm, 5.2 nm and 5.8 nm. The shifts are plotted as a function of the pressures in Figure 6.13. In that range of pressure, the relationship is linear. This shift in wavelength is continuous and reproducible. It should be noted that the slope of the line relating the shift in wavelength to the pressure is five times bigger for small pressure than for high pressures (Figures 6.13 and 6.9). This could come from the fact that the response to pressure is much greater for low pressures as the molecules have more space within the film to rearrange than at high pressures.

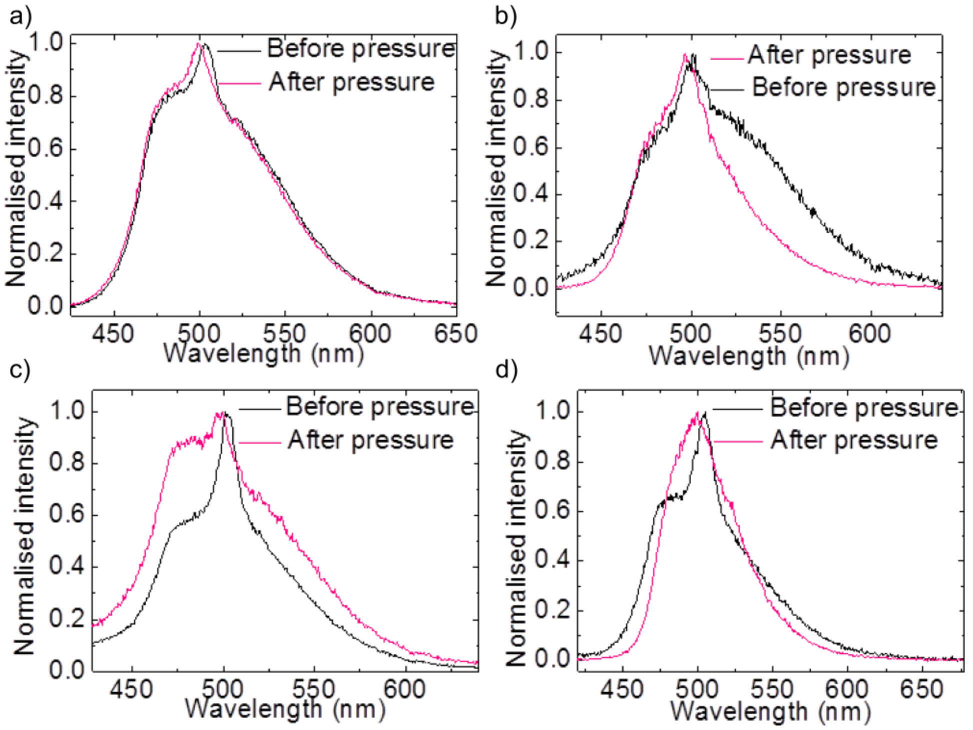

Figure 6.12: ASE spectra of TPE1 after applying a pressure of a) 274 N/cm^2, b) 549 N/cm^2, c) 823 N/cm^2 and d) 1097 N/cm^2.

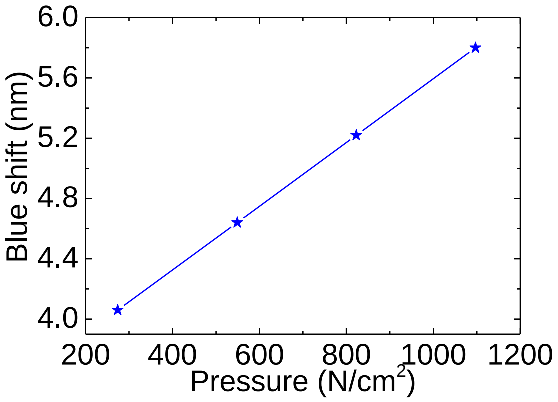

Figure 6.13: Shifts in wavelength obtained for different pressures applied on TPE1 films with the torque press.

The ASE threshold was measured before and after the pressure was applied. The average threshold before applying the pressure corresponded to a pump energy fluence of 719.5 µJ/cm^2. This value is higher than the value found previously for the same recipe and could be due to the reproducibility of the film. After pressing the film with different pressures, the threshold varied between 467 µJ/cm^2 and

684 µJ/cm^2. There was no trend following the threshold values but only random variations. These variations could come from irregularities in the film thickness due to a low speed spin-coating. It could also be due to the effect of the pressure on the film. However, these threshold values were smaller than for a non-pressed sample. This could indicate that applying a pressure might have a positive effect on the lasing properties of TPE1. It could be due to the AIE effect, enhancing the lasing properties when the molecules are more aggregated.

In conclusion, this section reported an initial demonstration of the possibility to use an AIE material for pressure-based sensing. A novel star-shaped oligofluorene tetraphenylethene material called TPE1 presenting AIE properties was tested for lasing applications. A mechanically-flexible all-organic second order DFB laser was made using TPE1 as a gain material. It operates in a single transverse mode, with an average threshold fluence of 60 ± 6 µJ/cm^2 (12 ± 1 kW/cm^2) for an emission close to 517.9 nm. The PCF properties of TPE1 were also tested by studying the influence of pressure on the ASE of a thin film. A linear variation on a given range of the emission wavelength of TPE1 was found when applying different pressures, opening opportunities for development of lasing-based sensors.

6.3. Mechanically-flexible RGB lasers on glass membranes

Multicolour laser sources are particularly attractive in many fields: optoelectronics, reaction control, micrototal analysis systems and sensors [59,274,275]. Gas lasers or solid-state lasers (Ti:Sapphire lasers for example) have been used as multiwavelength laser sources. RGB lasers have been demonstrated with a Pr^{3+}-doped fluoride glass fibre or crystal [276,277], a hollow-cathode He–Cd laser [278] and an Ar–Kr mixed gas laser [279]. However, these systems are often expensive and bulky and cannot be used as integrated devices [24,59,280,281]. Laser diodes can also be used as compact light sources but the integration of several wavelengths has a high cost and it is still difficult to access certain wavelengths like in the green-orange region of the visible [282].

Multicolour inorganic semiconductor lasers are challenging to fabricate, due to the difficulty of growing different gain media on one substrate. OS lasers are a good alternative for tunable lasers as they are easy and quick to fabricate and potentially low-cost as they can be made by using only soft lithography and spin-coating techniques [153]. This simplicity of fabrication also enables various device structures and conformations and flexibility [275], as we have seen in previous chapters. OS can be tailored to cover the whole visible spectrum, allowing selection of wavelengths according to the application [5]. The challenge though is to combine materials so that multi-wavelength emission can be simultaneously obtained, ideally with a single pump source.

In this section, we tackle this challenge and report two types of RGB lasers. Both lasers are encapsulated with polymer and an ultra-thin flexible glass membrane. The first device is a multicolour laser array consisting of three individual lasers (red, green and blue or RGB) juxtaposed on a flexible glass substrate and then encapsulated. The second device is ‘single-chip’ and is made of three lasers stacked on top of each other and emitting simultaneously. In the following, section 6.3.1 explains the design and fabrication process of these two RGB lasers. In section 6.3.1.1, the optical set-up used for their characterisation is detailed. Section 6.3.2 reports the characteristics of a neat red, green and blue laser serving as references to assess the influence of the encapsulation. Finally, section 6.3.3 presents and discusses the experimental results, including spectra and power transfer functions for both device configurations.

6.3.1. Design and fabrication

6.3.1.1. Design of the two RGB lasers pumping set-up

The design of the flexible glass RGB laser is detailed in this section. Figure 6.14 a) represents the structure of the first RGB laser. This structure will be called the “line” configuration in the following. It is formed by three individual lasers made of a gain layer (~180nm-thick for the red laser, ~130 nm for the green laser and ~75 nm for the blue laser) deposited on top of an epoxy grating (~43µm thick). Each laser is assembled manually next to each other onto a 50µm-thick flexible glass substrate. The lasers are pumped by a UV/violet pump laser as described in chapter 2, section 2.5.1. The lasers can be excited individually or simultaneously. For this, the length of the pump stripe is adjusted in order to probe a single laser at a time or to overlap the 3 lasers. Individual lasers were pumped by a stripe having a full width half maximum (FWHM) of 1.1 x 4.4 mm^2. The longer stripe measured 1.8 x 15.3 mm^2. The total thickness of the sample is <150 µm. The gain emitters of the red laser was made of 1,4-diketo-2,3,5,6-tetraphenyl-pyrrolo[3,4-c]pyrrole (linear-c DPP), a monodispersed π-conjugated oligomer. The gain spectrum of DPP spans the 530-600nm region while the absorption peaks at 366 nm [210]. The green emitter is the π–conjugated poly[2,5-bis(2’,5’-bis(2”-ethylhexyloxy)phenyl)-*p*-phenylene vinylene] (BBEHP-PPV). The gain spectrum of BBEHP-PPV is at 490-540nm and it absorbs at 431 nm (Chapter 2) [111,199]. The active element of the blue gain layer is a star-shaped tris(terfluorenyl) based on a truxene core (T3), an oligomer whose main luminescence is around 420-470 nm and its absorption at 375 nm (Chapter 2) [36,198]. Encapsulation is obtained by overcoating with a protective layer of PVA of ~180 nm and a 50µm-thick flexible glass sheet.

The second device structure, as shown in Figure 6.14 b), is formed by the three R, G and B lasers stacked on top of each other (instead of next to each other). In the following, this configuration will be called “stack”. Under optical pumping, each laser layer exhibits simultaneous emission engendering a multi-colour emission. Each individual laser has the same conformation as described for the first RGB structure (organic gain material layer on top of an epoxy grating). Each of them is overcoated with a PVA layer and the whole device is encapsulated with a 50µm-thick flexible glass membrane. The total thickness of the device is <250 µm. These lasers were pumped simultaneously with a stripe having a full width half maximum (FWHM) of 1.1 x 4.4 mm^2.

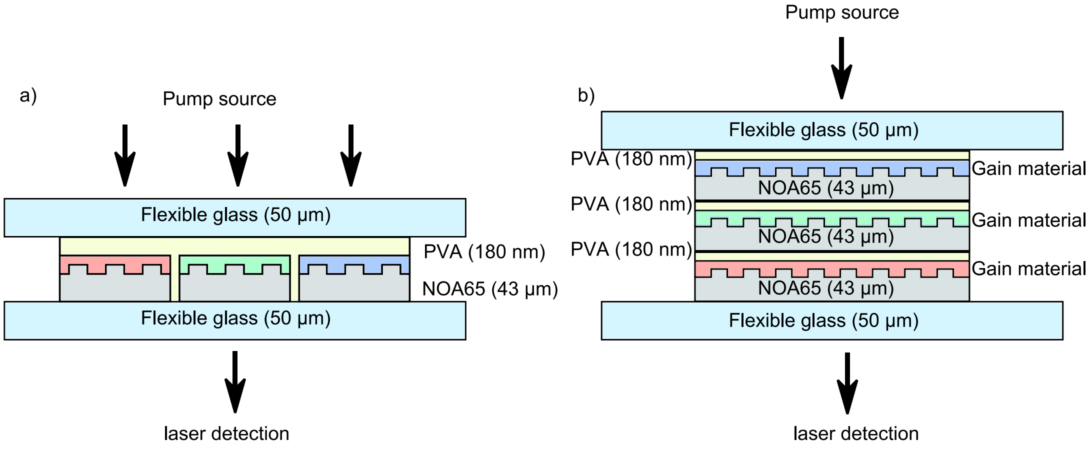

Figure 6.14: Structure of the two RGB devices with a) the "line" design and b) the "stack" design.

6.3.1.2. Fabrication steps

6.3.1.2.1. “Line” conformation device

Each laser constituting the RGB laser were fabricated individually first before being assembled together for the final device. First of all the cavity was fabricated by soft-lithography, reproducing a glass master grating with a UV curable epoxy (NOA65), using the same method as in [153] and in chapter 2, section 2.4.1. An appropriate period is chosen for each master grating: 390 nm for the red emitting material, 350 nm for the green and 276 nm for the blue.

Each gain material was then spin-coated on top of the corresponding grating. DPP was spin-coated at 6000 rpm, BBEHP-PPV at 5000 rpm and T3 at 3200 rpm in order to form a layer that ensures good confinement of the propagating mode within a waveguide structure: ~120 nm for DPP, ~130 nm for BBEHP-PPV and ~75 nm for T3.

Each laser was then cut to form squares of about 0.4 x 0.4 cm^2. A drop of NOA65 (epoxy) was spin-coated at 8000 rpm on top of a 50µm-thick flexible glass membrane and each laser was deposited on the epoxy, followed by a photocuring step under a UV flooding for a total exposure dose of 300 mJ/cm^2. The lasers were overcoated with a 180nm thick layer of PVA, prepared from a 50 mg/mL solution in deionised water and spin-coated at 3200 rpm. A second glass membrane was deposited on top of the PVA layer and sealed to the other glass sheet with NOA65. A final UV dose of 300 mJ/cm^2 was applied. The device was finally annealed in air for three days at 35°C to obtain a good crystalline cohesion of PVA.

6.3.1.2.2. “Stack” configuration device

The preparation of the individual “neat” lasers was the same as described above, for the “line” configuration device. Each laser was then overcoated with a 180nm thick layer of PVA, prepared from a 50 mg/mL solution in deionised water and spin-coated at 3200 rpm.

A drop of NOA65 (epoxy) was spin-coated at 8000 rpm on top of a 50µm-thick flexible glass membrane and the red emitting laser was deposited on the epoxy, and the two others were stacked on top of the red one. A second glass sheet was deposited on top of the blue. The whole device was sealed with NOA65, photo-cured under a UV flooding for a total exposure dose of 300 mJ/cm^2 and finally annealed for three days.

6.3.2. Individual neat laser characteristics

Neat lasers (without encapsulation) were fabricated and used as references for performance comparison, to see the impact of encapsulation. The average threshold energy fluence, F_{th}, of a neat red, green and blue laser was measured. The neat linear-c DPP laser emitted at 603.2 nm and had an average F_{th} of 168.5 µJ/cm^2. The neat BBEHP-PPV laser emitted at 536.9 nm and its average threshold energy fluence, F_{th}, was found to be 239.5 µJ/cm^2 per pulse. Finally, the neat T3 laser had an emission wavelength of 426.3 nm and an average threshold fluence of 70 µJ/cm^2. Spectra and power transfer functions are given in Figure 6.15, for linear-c DPP in Figure 6.15 a), BBEHP-PPV in Figure 6.15 b) and T3 in Figure 6.15 c), respectively.

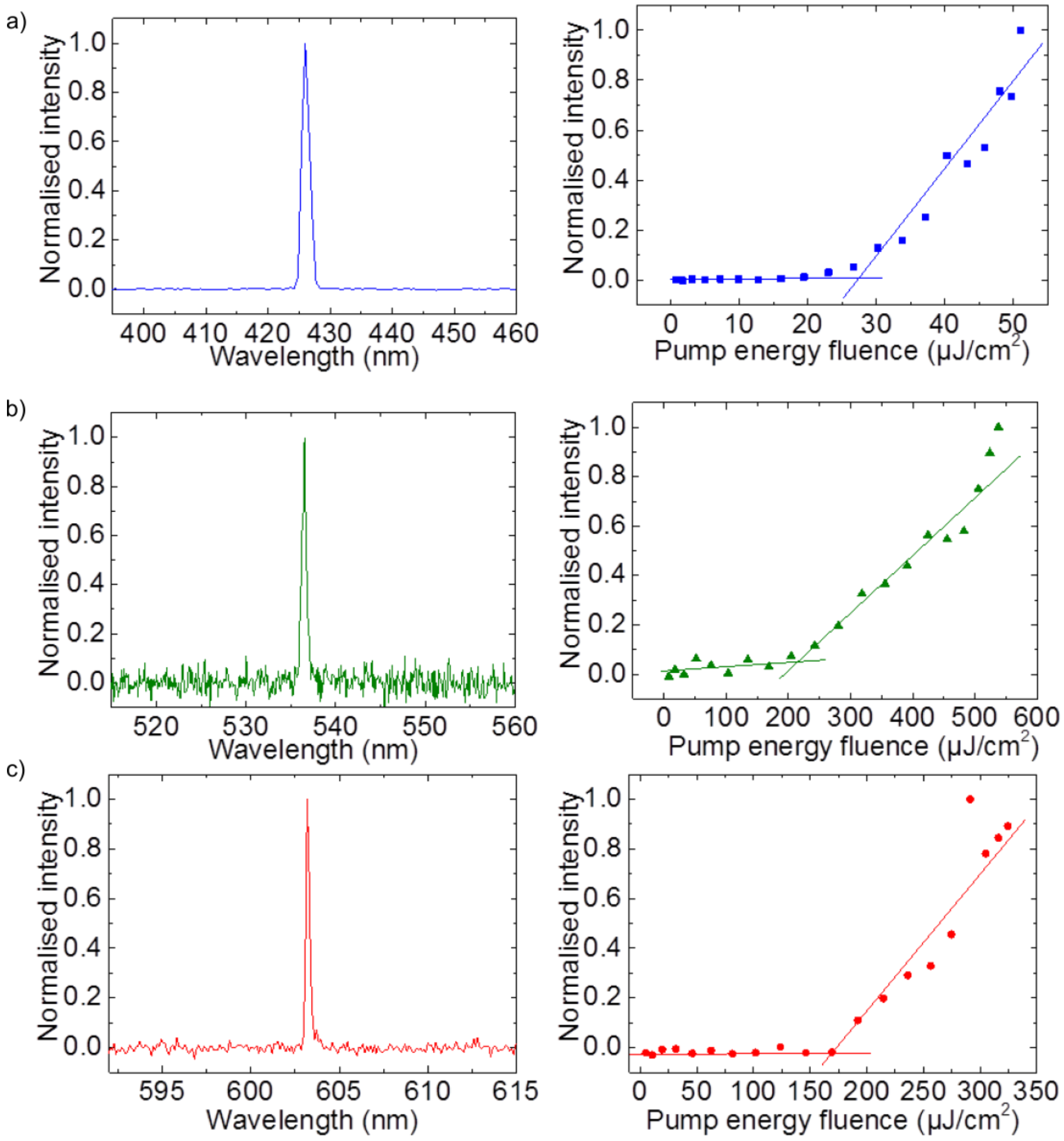

Figure 6.15: Spectra and power transfer functions of a) neat T3 laser, b) neat BBEHP-PPV laser and c) neat linear-c DPP laser.

6.3.3. RGB laser characteristics

6.3.3.1. “Line” configuration device”

The spectrum of the “line” RGB laser is shown in Figure 6.16 a), as well as a picture of the emitted beams. Each output beam is measured independently by spectrometer, at a pump energy fluence of 28 μJ/cm^2. As shown in the picture and the plot of emission spectra, a three-colour laser, with emission wavelengths of 605.4 nm, 537.1 nm and 435.9 nm, is obtained using only one pump source. Results show that the encapsulating layer redshifts the oscillation wavelength when comparing to the equivalent neat laser (603.2 nm, 536.5 nm and 426.3 nm emission). This effect is due to changes in the refractive index profile of the laser structure. As a result of the PVA layer addition, the laser mode is pulled away from the substrate and overlaps more with the gain region leading to an increase in the effective refractive index of the mode (see chapter 3, section 3.4.2).

The threshold fluence of the device were measured and are plotted in Figure 6.16 b). The green emitting laser has the lowest threshold, 11.0 µJ/cm^2, followed by the red laser with an average threshold fluence of 28.2 µJ/cm^2 and the blue laser with an average threshold of 31.6 µJ/cm^2. It is seen that the encapsulation lowers the threshold compared to the equivalent neat lasers, (respectively 168.5 µJ/cm^2, 239.5 µJ/cm^2 and 70 µJ/cm^2), also due to changes in the refractive index profile of the laser structure.

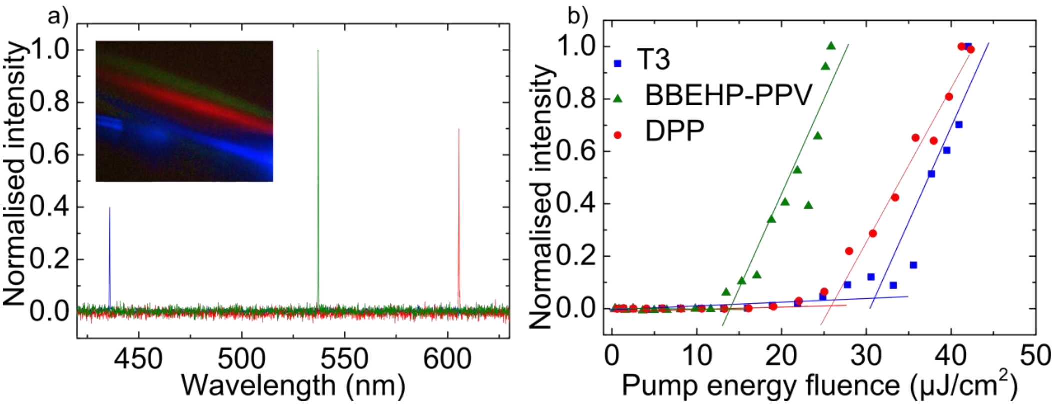

Figure 6.16: a) Spectrum and picture and b) pump energy fluence of the "line" RGB

6.3.3.2. "Stack" configuration device

Figure 6.17 shows the characteristics of the "stack" RGB laser. From Figure 6.17 a) it is seen that the laser emitted simultaneously at three different wavelengths: 435.9 nm, 540.1 nm and 608.3 nm. A shift in wavelength is seen compared to the emission of the neat lasers due to the encapsulation. As seen previously, a red shift in wavelength is engendered by the encapsulation, compared to equivalent neat lasers (603.2 nm, 536.5 nm and 426.3 nm emission). Spectra were recorded at an energy fluence of 54 µJ/cm^2. A picture of the device under optical pumping is shown in the inset of Figure 6.17 a). It is seen that the three beams, red, green and blue emit from the same position on the sample, giving a quasi-white light emission.

The power transfer function of the RGB laser is shown in Figure 6.17 b). The device was pumped through the top of the sample (starting with the blue laser). Once again, thresholds are highly reduced by the encapsulation compared to the neat equivalent devices. The whole device threshold is then 42.1 µJ/cm^2 (when the three lasers emit at the same time). This is an improvement in threshold of ~100 times compared to the result shown by Yamishita *et al.* [275]. However, there is a slight increase in threshold compared to the "line" device due to the configuration of the device as the laser on top of another laser acts as a superstrate.

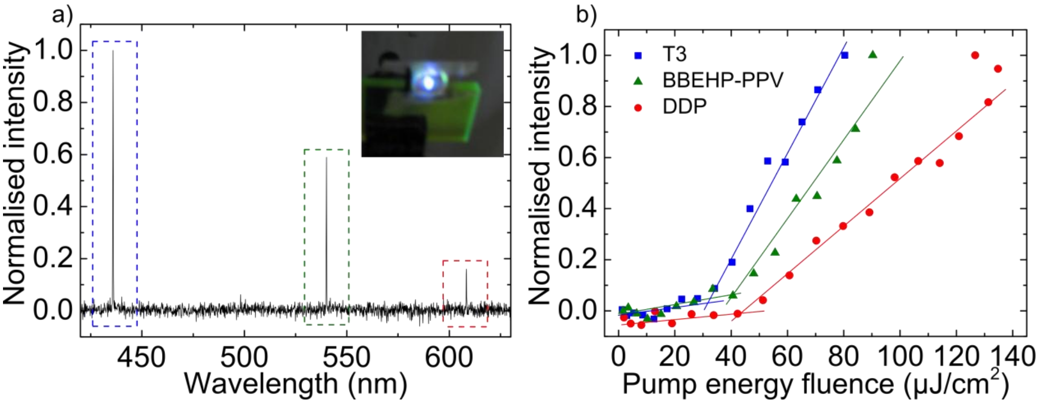

Figure 6.17: a) Spectrum and photograph and b) pump energy fluence of the "stack" RGB laser

In summary, two formats of mechanically-flexible RGB lasers were demonstrated, one consisting of a single-chip quasi-white laser and the other a multicolour laser array. The reported devices were fabricated by combining three individual all-organic DFB lasers entirely made by soft lithography. The complete devices were encapsulated with polymer and a 50µm-thick glass membrane in order to improve the lasing threshold. The first device consists of three lasers placed next to each other on a flexible glass substrate. Each laser can be optically-pumped individually or simultaneously, giving a red, green and blue laser output with an individual threshold of respectively 28.2 µJ/cm^2, 11 µJ/cm^2 and 31.6 µJ/cm^2. The second device has a three layer structure, each layer being an individual red, green and blue laser, emitting at the same time with a lasing threshold of 42.1 µJ/cm^2. These demonstrations offer potential solutions for the development of compact multicolour light sources.

6.4. Conclusion

A new type of star-shaped oligofluorene TPE material (TPE1) was studied as gain material for lasing applications. This gain material presents aggregation induced emission and its mechanofluorochromic properties were tested by studying the effect of the pressure on its amplified spontaneous emission. The ASE wavelength varied linearly as a function of the pressure applied on a film of TPE1 and was reversible. A possible next phase would be to develop a pressure sensor, which monitors for example the ASE wavelength.

Two multicolour lasers have been reported. They were fabricated with three different organic gain media emitting at 3 different wavelengths (red, green and blue). Two configurations were studied, a single-chip RGB laser emitting simultaneously from the same position to create a quasi-white light emission and a device combining the same colours but emitting independently. This opens opportunities for chemical, biological analysis, sensors and many other optoelectronics applications.

This chapter demonstrated that DFB OS lasers offer many possibilities of structures, tunability and configurations as they can be integrated on any substrate, and are simple to fabricate, plastic-like materials offering flexibility and a wide range of wavelengths in the visible.

Part III

Chapter 7

Conclusion and outlook

7.1. Summary

This thesis has focussed on the development of all-organic and hybrid organic/inorganic solution-processed lasers and on advancing their performance in order to increase their applicability. A particular emphasis was placed on mechanically-flexible laser cavities. The gain materials used for most of the devices were organic semiconductors, such as oligomers and conjugated polymers. These types of gain media are very advantageous as they are solution-processable, non-toxic, potentially low-cost and can be tuned easily to emit through the whole visible spectrum. This means they can bring simplicity and flexibility in terms of fabrication of photonic devices: they can be printed onto different substrates using different techniques; they are compatible with conformable/flexible technology and with soft-lithography, etc.

The second type of gain element used in this work was colloidal quantum dots (CQDs). CQDs are attractive nanomaterials and they are also compatible with solution-processing techniques. Their emission wavelength can be tuned over a wide range by changing only their size, by changing their composition or by a combination of both. They are studied here as an alternative to organic semiconductors. They can be processed in the same way as OS but they are potentially more photostable and are possibly not limited to pulsed operation – although current performance of visible CQD lasers do not permit this and do not match that of OS lasers. However, it can be said that this technology is simply not yet as mature. Nevertheless great progress is being made and results of this thesis have contributed to this on-going progress.

All lasers studied were based on DFB resonators. This type of cavity was chosen because its planar fabrication is ideally suited to soft lithography using flexible and transparent plastic materials, because of the potential of the architecture for bio-sensing applications and, importantly, because the lowest lasing thresholds for organic semiconductor lasers are obtained with such cavities (see chapter 1, section 1.4.2).

The first experimental sections of the thesis (chapters 3 and 4) addressed the main challenges to application for optically-pumped organic semiconductor lasers: lowering the lasing threshold, increasing the photostability and changing the pumping implementation for compactness. A blue emitting macromolecule (T3) and a green emitting (and blue absorbing) polymer (BBEHP-PPV) were studied as gain materials. Different approaches were explored to achieve a combination of low emission threshold and high photostability while maintaining mechanical flexibility. These approaches include guest/host nanocomposite format and encapsulation of the gain layer with additional polymers and flexible glass membranes. The performance and capabilities of the organic lasers were significantly improved, as very low thresholds and highly extended photostabilities were demonstrated. The low lasing thresholds allowed solving the problem of bulky and expensive pump sources by replacing them with a gallium nitride laser diode. This combination of achievements is key to real world applications of organic semiconductor lasers by obtaining a low-cost, long-lifetime and compact system.

Chapter 5 reported DFB lasers with colloidal quantum dots as gain media. State-of-the-art threshold for CQD lasers operating in the nanosecond regime and the first demonstration of a laser of any kind on flexible glass (these results predated our polymer/glass work) were achieved and their potential for sensing applications was shown. It was also demonstrated that CQD DFB lasers are suitable for integration on different substrates and can conform to different shapes, according to the applications desired.

The last experimental part (chapter 6) consisted in studying emerging types of organic semiconductors and in assembly of organic semiconductor lasers. This chapter emphasised the variety of possibilities in terms of wavelengths, shapes and assembly of plastic-like lasers, with the demonstration of multicolour RGB lasers excited with a single pump and of a pressure-sensitive laser material.

In conclusion, the work described in this thesis brings solution-processed lasers with mechanically-flexible cavities closer to applications by showing diode-pumped (low-cost and compact) photostable laser operation and also by demonstrating that such lasers enable many configurations, e.g. in terms of emission colours and shapes.

7.2. Future work

7.2.1. Perspectives for solution-processed lasers

Recent advances in OS lasers have brought them closer to applications. However, improvements still need to be achieved in order to overcome the remaining challenges.

The need for compact integrated systems remains one of the main requirements. In this thesis, it has been demonstrated that OS lasers having low threshold can be pumped by laser-diodes. One other way to obtain a compact system and overcome the difficulty of electrically pumping OS lasers is to use an LED as a pump source, which is a solution for a low-cost (cheaper than laser-diodes) and integrated system. Recent papers have reported LED-pumped OS lasers but they require very low threshold as typical commercial InGaN LEDs deliver a power only up to 1 kW/cm^2 in 45 ns pulses [16,283]. Micro-LED pumped OS lasers have also been achieved, opening opportunities for compact integrated lab-on-a-chip devices for bio-sensing and chemo-sensing [82,284,285].

One other challenge is to bring OSLs toward CW lasing. Several research groups are focussing on achieving a CW organic laser. Rabe *et al.* [119] and Lehnhardt *et al.* [167] have investigated semiconductor polymer lasers operating at a repetition rate of several MHz and a pump pulse duration of 400 µs. A recent study by Zhang *et al.* [129] proposed using a three-molecule system that includes a “triplet manager” to help the depopulation of the triplet state of the emitting material.

Concerning CQDs, the main challenge remains the threshold performance. This thesis has demonstrated what we believe to be the lowest thresholds for a CQD laser pumped in the ns regime. However, in order to achieve an integrated and compact system and in the future be able to pump CQD lasers with a laser-diode or an LED, thresholds lower than 450 µJ/cm^2 have to be achieved (about 20 times lower).

Looking at different types of CQDs (for example alloyed dots or different materials from CdSe/ZnS) and encapsulating the lasers could be solutions for reducing the threshold (it has been demonstrated that encapsulation can help by increasing the overlap of the refractive index mode with the gain region).

7.2.2. Bio-sensing

One of the applications for some of the solution-processed lasers presented in this thesis is sensing. These devices can act as evanescent optical sensors to detect minute changes in refractive index at the surface of the laser. The advantages are their planar geometry and the fact that laser oscillation leads to a narrower linewidth than equivalent ‘passive’ sensors, which boosts the sensitivity without trading-off on implementation simplicity. In particular, they are very attractive for medical diagnostics as they offer the possibility for label-free, real-time and non-destructive detection. They have also the potential to be incorporated into compact detection systems (possibly lab-on-chip) for future point-of-care diagnostics. However, the DFB laser sensors based on solution-processed organics that have been developed so far, such as the T3 laser sensors demonstrated by our group (A.-M. Haughey *et al.* [12,231,233]), still present a main challenge for such application: the optical pump source remains bulky, expensive and prevent fabrication of a truly low-cost, compact and portable bio-sensing system.

To address the above point, laser diode pumping using off-the shelf InGaN lasers, as demonstrated in this thesis, is an ideal solution. That way, an integrated, compact and portable system that would use disposable ‘laser capsules’ primed for sensing could be obtained. The blue emitting material (T3) would have to be replaced by a laser material that can be pumped by blue laser diodes, as UV laser diodes remain expensive and have lower power performance. BBEHP-PPV is a candidate material as it was demonstrated in chapter 3 that flexible BBEHP-PPV lasers are suitable for laser diode pumping when coated with PVA, due to their low-operation threshold. We note that flexibility is not a necessary condition for bio-sensing applications but it can facilitate system integration. Additionally, future applications might need conformable or flexible sensors.

Biosensing usually necessitates operation of the laser in a liquid environment. Typically, the first steps to validate a platform for evanescent wave biosensing are: (i) to verify that the laser can indeed operate in a liquid environment and (ii) to assess if it can detect bulk changes in its environment as was done with the CQD laser in chapter 5. Such an experiment was conducted on diode-pumped BBEHP-PPV lasers (overcoated with PVA, see chapter 4). An encapsulated BBEHP-PPV laser was first tested in air and then immersed in toluene (a non-polar solvent, as PVA is water-soluble) in order to detect whether or not a shift in wavelength, indicating a change in refractive index of the superstrate, was obtained. A schematic of the set-up used to carry out this test is shown in Figure 7.1. The laser was immobilised with kapton tape inside a glass cuvette, with the surface of the laser facing into the cuvette. The laser emission was collected through an optical fibre connected to a spectrometer.

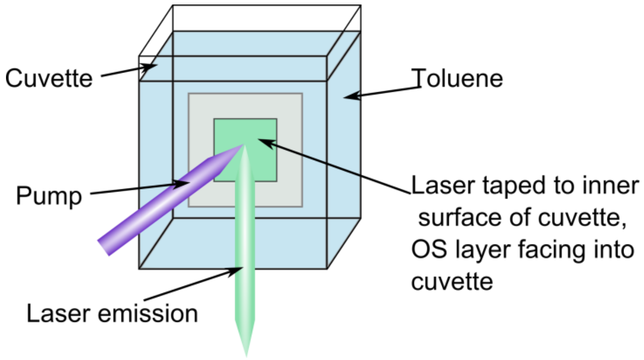

Figure 7.1: Set-up used for testing the potential of laser diode pumped encapsulated BBEHP-PPV laser.

The result is shown in Figure 7.2. In air, the laser emission wavelength was 538.41 nm. Once immersed in toluene, the wavelength was 539.25 nm: a shift of 0.8 nm was obtained. This result therefore shows the potential of laser diode pumped encapsulated BBEHP-PPV laser for bio-sensing applications.

This is only a first step though. The sensitivity of this BBEHP-PPV laser ‘sensor’ is low (1.5 to 2 nm per refractive index unit). Optimisation and further investigations is required: variation of the PVA layer in order to obtain the biggest shift in wavelength and study of the reversibility of this process. An alternative encapsulating layer also needs to be found as PVA is water-soluble and thereby cannot be utilised with biological buffers or blood. Other laser materials suited for InGaN pumping could also be explored.

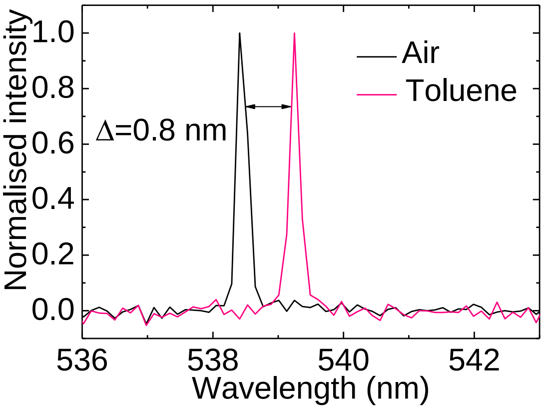

Figure 7.2: Refractive index sensing from a LD pumped BBEHP-PPV/PVA laser.

Bibliography

[1] T. H. Maiman , “Stimulated Optical Radiation in Ruby,” *Nature*, vol. 187, no. 4736, pp. 493–494, 1960.

[2] C. E. Webb and J. D. C. Jones, *Handbook of Laser Technology and Applications: Laser design and laser systems*. CRC Press, 2004.

[3] K. Thyagarajan and A. Ghatak, *Lasers*, 2nd editio. Boston, MA: Springer US, 2011.

[4] A. Miller and D. M. Finlayson, *Laser Sources and Applications*. CRC Press, 1997.

[5] I. D. W. Samuel and G. A. Turnbull, “Organic semiconductor lasers.,” *Chem. Rev.*, vol. 107, no. 4, pp. 1272–95, 2007.

[6] P. Görrn, M. Lehnhardt, W. Kowalsky, T. Riedl, and S. Wagner, “Elastically tunable self-organized organic lasers.,” *Adv. Mater.*, vol. 23, no. 7, pp. 869–72, 2011.

[7] B. Wenger, N. Tétreault, M. E. Welland, and R. H. Friend, “Mechanically tunable conjugated polymer distributed feedback lasers,” *Appl. Phys. Lett.*, vol. 97, no. 19, p. 193303, 2010.

[8] J. Herrnsdorf, B. Guilhabert, Y. Chen, A. Kanibolotsky, A. Mackintosh, R. Pethrick, P. Skabara, E. Gu, N. Laurand, and M. Dawson, “Flexible blue-emitting encapsulated organic semiconductor DFB laser.,” *Opt. Express*, vol. 18, no. 25, pp. 25535–45, 2010.

[9] M. R. Weinberger, G. Langer, A. Pogantsch, A. Haase, E. Zojer, and W. Kern, “Continuously Color-Tunable Rubber Laser,” *Adv. Mater.*, vol. 16, no. 2, pp. 130–133, 2004.

[10] M. D. McGehee and A. J. Heeger, “Semiconducting (Conjugated) Polymers as Materials for Solid-State Lasers,” *Adv. Mater.*, vol. 12, no. 22, pp. 1655–1668, 2000.

[11] N. Tessler, “Lasers Based on Semiconducting Organic Materials,” *Adv. Mater.*, vol. 11, no. 5, pp. 363–370, 1999.

[12] A.-M. Haughey, B. Guilhabert, A. L. Kanibolotsky, P. J. Skabara, M. D. Dawson, G. A. Burley, and N. Laurand, “An oligofluorene truxene based distributed feedback laser for biosensing applications.,” *Biosens. Bioelectron.*, vol. 54, pp. 679–86, 2014.

[13] B. H. Ma, A. K. Jen, and L. R. Dalton, “Polymer-Based Optical Waveguides : Materials , Processing , and Devices ,” *Adv. Mater.*, no. 19, pp. 1339–1365, 2002.

[14] J. Zubia and J. Arrue, “Plastic Optical Fibers: An Introduction to Their Technological Processes and Applications,” *Opt. Fiber Technol.*, vol. 7, no. 2, pp. 101–140, 2001.

[15] C. Pflumm, C. Karnutsch, M. Gerken, and U. Lemmer, “Parametric study of modal gain and threshold power density in electrically pumped single-layer organic optical amplifier and laser diode structures,” *IEEE J. Quantum Electron.*, vol. 41, no. 3, pp. 316–336, 2005.

[16] J. Herrnsdorf, Y. Wang, J. J. D. McKendry, Z. Gong, D. Massoubre, B. Guilhabert, G. Tsiminis, G. A. Turnbull, I. D. W. Samuel, N. Laurand, E. Gu, and M. D. Dawson, “Micro-LED pumped polymer laser: A discussion of future pump sources for organic lasers,” *Laser Photon. Rev.*, vol. 7, no. 6, pp. 1065–1078, 2013.

[17] O. Svelto, *Principles of Lasers*, 5th editio. Boston, MA: Springer US, 2010.

[18] F. Trager, *Springer Handbook of Lasers and Optics*, 2nd Editio. Springer Science & Business Media, 2012.

[19] K. F. Renk, *Basics of Laser Physics*. Berlin, Heidelberg: Springer Berlin Heidelberg, 2012.

[20] F. Hide, M. A. Diaz-Garcia, B. J. Schwartz, M. R. Andersson, Q. Pei, and A. J. Heeger, “Semiconducting Polymers: A New Class of Solid-State Laser Materials,” *Science (80-.).*, vol. 273, no. 5283, pp. 1833–1836, 1996.

[21] Y. Sorek, R. Reisfeld, I. Finkelstein, and S. Ruschin, “Light amplification in a dye-doped glass planar waveguide,” *Appl. Phys. Lett.*, vol. 66, no. 10, p. 1169, 1995.

[22] K. L. Shaklee, “Direct Determination of Optical Gain in Semiconductor Crystals,” *Appl. Phys. Lett.*, vol. 18, no. 11, p. 475, 1971.

[23] P. P. Sorokin and J. R. Lankard, “Stimulated Emission Observed from an Organic Dye, Chloro-aluminum Phthalocyanine,” *IBM J. Res. Dev.*, vol. 10, no. 2, pp. 162–163, 1966.

[24] S. Riechel, U. Lemmer, J. Feldmann, S. Berleb, A. G. Mückl, W. Brütting, a Gombert, and V. Wittwer, “Very compact tunable solid-state laser utilizing a thin-film organic semiconductor.,” *Opt. Lett.*, vol. 26, no. 9, pp. 593–5, 2001.

[25] Y. Oki, S. Miyamoto, M. Tanaka, D. Zuo, and M. Maeda, “Long lifetime and high repetition rate operation from distributed feedback plastic waveguided dye lasers,” *Opt. Commun.*, vol. 214, no. 1–6, pp. 277–283, 2002.

[26] R. Xia, W.-Y. Lai, P. A. Levermore, W. Huang, and D. D. C. Bradley, “Low-Threshold Distributed-Feedback Lasers Based on Pyrene-Cored Starburst Molecules with 1,3,6,8-Attached Oligo(9,9-Dialkylfluorene) Arms,” *Adv. Funct. Mater.*, vol. 19, no. 17, pp. 2844–2850, 2009.

[27] V. Trabadelo, A. Juarros, A. Retolaza, S. Merino, M. G. Ramírez, V. Navarro-Fuster, J. M. Villalvilla, P. G. Boj, J. A. Quintana, and M. A. Díaz-García, “Highly photostable solid-state organic distributed feedback laser fabricated via thermal nanoimprint lithography,” *Microelectron. Eng.*, vol. 87, no. 5–8, pp. 1428–1430, 2010.

[28] A. J. Heeger, “Semiconducting polymers: the Third Generation.,” *Chem. Soc. Rev.*, vol. 39, no. 7, pp. 2354–71, 2010.

[29] C. Chiang, C. Fincher, Y. Park, A. Heeger, H. Shirakawa, E. Louis, S. Gau, and A. MacDiarmid, “Electrical Conductivity in Doped Polyacetylene,” *Phys. Rev. Lett.*, vol. 39, no. 17, pp. 1098–1101, 1977.

[30] N. C. Greenham, I. D. W. Samuel, G. R. Hayes, R. T. Phillips, Y. A. R. R. Kessener, S. C. Moratti, A. B. Holmes, and R. H. Friend, “Measurement of absolute photoluminescence quantum efficiencies in conjugated polymers,” *Chem. Phys. Lett.*, vol. 241, no. 1–2, pp. 89–96, 1995.

[31] A. K. Bansal, A. Ruseckas, P. E. Shaw, and I. D. W. Samuel, “Fluorescence Quenchers in Mixed Phase Polyfluorene Films,” *J. Phys. Chem. C*, vol. 114, no. 41, pp. 17864–17867, Oct. 2010.

[32] N. A. Montgomery, J.-C. Denis, S. Schumacher, A. Ruseckas, P. J. Skabara, A. Kanibolotsky, M. J. Paterson, I. Galbraith, G. A. Turnbull, and I. D. W. Samuel, “Optical excitations in star-shaped fluorene molecules.,” *J. Phys. Chem. A*, vol. 115, no. 14, pp. 2913–9, 2011.

[33] Y. Okamoto, *Organic semiconductors*. Reinhold Pub. Corp., 1964.

[34] W. Brutting, *Physics of Organic semiconductors*, Wiley-VCH. Weinheim, 2012.

[35] R. Xia, G. Heliotis, Y. Hou, and D. D. C. Bradley, “Fluorene-based conjugated polymer optical gain media,” *Org. Electron.*, vol. 4, no. 2–3, pp. 165–177, 2003.

[36] G. Tsiminis, Y. Wang, P. E. Shaw, A. L. Kanibolotsky, I. F. Perepichka, M. D. Dawson, P. J. Skabara, G. A. Turnbull, and I. D. W. Samuel, “Low-

threshold organic laser based on an oligofluorene truxene with low optical losses," *Appl. Phys. Lett.*, vol. 94, no. 24, p. 243304, 2009.

[37] G. Heliotis, R. Xia, G. A. Turnbull, P. Andrew, W. L. Barnes, I. D. W. Samuel, and D. D. C. Bradley, "Emission Characteristics and Performance Comparison of Polyfluorene Lasers with One- and Two-Dimensional Distributed Feedback," *Adv. Funct. Mater.*, vol. 14, no. 1, pp. 91–97, 2004.

[38] G. N. Lewis and M. Kasha, "Phosphorescence and the Triplet State," *J. Am. Chem. Soc.*, vol. 66, no. 12, pp. 2100–2116, 1944.

[39] D. Hertel, S. Setayesh, H. G. Nothofer, U. Scherf, K. Müllen, and H. Bässler, "Phosphorescence in Conjugated Poly(para-phenylene)-Derivatives," *Adv. Mater.*, vol. 13, no. 1, pp. 65–70, 2001.

[40] J. Clark and G. Lanzani, "Organic photonics for communications," *Nat. Photonics*, vol. 4, no. 7, pp. 438–446, 2010.

[41] G. Heliotis, R. Xia, G. A. Turnbull, P. Andrew, W. L. Barnes, I. D. W. Samuel, and D. D. C. Bradley, "Emission Characteristics and Performance Comparison of Polyfluorene Lasers with One- and Two-Dimensional Distributed Feedback," *Adv. Funct. Mater.*, vol. 14, no. 1, pp. 91–97, 2004.

[42] A. Jabłoński, "Über den Mechanismus der Photolumineszenz von Farbstoffphosphoren," *Zeitschrift für Phys.*, vol. 94, no. 1–2, pp. 38–46, 1935.

[43] I. P. Kaminow, H. P. Weber, and E. A. Chandross, "Poly(methyl methacrylate) dye laser with internal diffraction grating resonator," *Appl. Phys. Lett.*, vol. 18, no. 11, p. 497, 1971.

[44] H. Kogelnik, "Stimulated emission in a periodic structure," *Appl. Phys. Lett.*, vol. 18, no. 4, p. 152, 1971.

[45] D. Moses, "High quantum efficiency luminescence from a conducting polymer in solution: A novel polymer laser dye," *Appl. Phys. Lett.*, vol. 60, no. 26, p. 3215, 1992.

[46] N. Tessler, G. J. Denton, and R. H. Friend, "Lasing from conjugated-polymer microcavities," *Nature*, vol. 382, no. 6593, pp. 695–697, 1996.

[47] D. N. Kumar, J. D. Bhawalkar, and P. N. Prasad, "Solid-State Cavity Lasing from Poly(p-Phenylene Vinylene)-Silica Nanocomposite Bulk," *Appl. Opt.*, vol. 37, no. 3, p. 510, 1998.

[48] K. Yamashita, M. Ito, S. Suqimoto, T. Morishita, and K. Oe, "Optically end-pumped plastic waveguide laser with in-line Fabry-Pérot resonator," *Opt. Lett.*, vol. 18, no. 23, pp. 24092–100, 2010.

[49] R. Sastre, V. Martín, L. Garrido, J. L. Chiara, B. Trastoy, O. García, A. Costela, and I. García-Moreno, “Dye-Doped Polyhedral Oligomeric Silsesquioxane (POSS)-Modified Polymeric Matrices for Highly Efficient and Photostable Solid-State Lasers,” *Adv. Funct. Mater.*, vol. 19, no. 20, pp. 3307–3316, 2009.

[50] A. Costela, I. García-Moreno, C. Gómez, O. García, and R. Sastre, “New organic-inorganic hybrid matrices doped with rhodamine 6G as solid-state dye lasers,” *Appl. Phys. B Lasers Opt.*, vol. 75, no. 8, pp. 827–833, Dec. 2002.

[51] A. Schulzgen, C. Spiegelberg, M. M. Morrell, S. B. Mendes, P.-M. Allemand, Y. Kawabe, M. Kuwata-Gonokami, S. Honkanen, M. Fallahi, B. Kippelen, and N. Peyghambarian, “Light amplification and laser emission in conjugated polymers,” *Opt. Eng.*, vol. 37, no. 4, p. 1149, 1998.

[52] S. Frolov, M. Shkunov, Z. Vardeny, and K. Yoshino, “Ring microlasers from conducting polymers,” *Phys. Rev. B*, vol. 56, no. 8, pp. R4363–R4366, 1997.

[53] M. Berggren, A. Dodabalapur, Z. Bao, and R. E. Slusher, “Solid-state droplet laser made from an organic blend with a conjugated polymer emitter,” *Adv. Mater.*, vol. 9, no. 12, pp. 968–971, 1997.

[54] H. Rabbani-Haghighi, S. Forget, S. Chénais, A. Siove, M.-C. Castex, and E. Ishow, “Laser operation in nondoped thin films made of a small-molecule organic red-emitter,” *Appl. Phys. Lett.*, vol. 95, no. 3, p. 033305, 2009.

[55] Q. Song, L. Liu, L. Xu, Y. Wu, and Z. Wang, “Electrical tunable random laser emission from a liquid-crystal infiltrated disordered planar microcavity,” *Opt. Lett.*, vol. 34, no. 3, p. 298, 2009.

[56] V. Bulovi, “Transform-Limited, Narrow-Linewidth Lasing Action in Organic Semiconductor Microcavities,” *Science (80-.).*, vol. 279, no. 5350, pp. 553–555, 1998.

[57] H. Rabbani-Haghighi, S. Forget, S. Chénais, and A. Siove, “Highly efficient, diffraction-limited laser emission from a vertical external-cavity surface-emitting organic laser.,” *Opt. Lett.*, vol. 35, no. 12, pp. 1968–70, 2010.

[58] A. Dodabalapur, M. Berggren, R. E. Slusher, Z. Bao, a. Timko, P. Schiortino, E. Laskowski, H. E. Katz, and O. Nalamasu, “Resonators and materials for organic lasers based on energy transfer,” *IEEE J. Sel. Top. Quantum Electron.*, vol. 4, no. 1, pp. 67–74, 1998.

[59] S. Omi, H. Watanabe, Y. Yang, and Y. Oki, “Development of multicolor DFB dye laser by Transversal Quasi-Mode-Coupling method,” *2009 Conf. Lasers Electro Opt. Pacific Rim Conf. Lasers Electro-Optics*, pp. 1–2, 2009.

[60] L. M. Goldenberg, V. Lisinetskii, Y. Gritsai, J. Stumpe, and S. Schrader, “Second order DFB lasing using reusable grating inscribed in azobenzene-containing material,” *Opt. Mater. Express*, vol. 2, no. 1, p. 11, 2011.

[61] C. Vannahme, F. Maier-Flaig, U. Lemmer, and A. Kristensen, “Single-mode biological distributed feedback laser.,” *Lab Chip*, vol. 13, no. 14, pp. 2675–8, 2013.

[62] T. Spehr, A. Siebert, T. Fuhrmann-Lieker, J. Salbeck, T. Rabe, T. Riedl, H. H. Johannes, W. Kowalsky, J. Wang, T. Weimann, and P. Hinze, “Organic solid-state ultraviolet-laser based on spiro-terphenyl,” *Appl. Phys. Lett.*, vol. 87, no. 16, p. 161103, 2005.

[63] P. Del Carro, A. Camposeo, R. Stabile, E. Mele, L. Persano, R. Cingolani, and D. Pisignano, “Near-infrared imprinted distributed feedback lasers,” *Appl. Phys. Lett.*, vol. 89, no. 20, p. 201105, 2006.

[64] B. H. Wallikewitz, G. O. Nikiforov, H. Sirringhaus, and R. H. Friend, “A nanoimprinted, optically tuneable organic laser,” *Appl. Phys. Lett.*, vol. 100, no. 17, p. 173301, 2012.

[65] S.-B. Lee, J. Yang, S. Moon, J.-H. Lee, K. An, J.-B. Shim, H.-W. Lee, and S. W. Kim, “Chaos-assisted nonresonant optical pumping of quadrupole-deformed microlasers,” *Appl. Phys. Lett.*, vol. 90, no. 4, p. 041106, 2007.

[66] R. Ding, H.-H. Fang, Y. Wang, S.-Y. Lu, X.-L. Zhang, L. Wang, J. Feng, Q.-D. Chen, and H.-B. Sun, “Distributed feedback lasing from thin organic crystal based on active waveguide grating structures,” *Org. Electron.*, vol. 13, no. 9, pp. 1602–1605, 2012.

[67] W. Huang, Z. Diao, Y. Liu, Z. Peng, C. Yang, J. Ma, and L. Xuan, “Distributed feedback polymer laser with an external feedback structure fabricated by holographic polymerization technique,” *Org. Electron.*, vol. 13, no. 11, pp. 2307–2311, 2012.

[68] R. Xia, P. N. Stavrinou, D. D. C. Bradley, and Y. Kim, “Efficient optical gain media comprising binary blends of poly(3-hexylthiophene) and poly(9,9-dioctylfluorene-co-benzothiadiazole),” *J. Appl. Phys.*, vol. 111, no. 12, p. 123107, 2012.

[69] A. Camposeo, P. Del Carro, L. Persano, and D. Pisignano, “Electrically tunable organic distributed feedback lasers embedding nonlinear optical molecules.,” *Adv. Mater.*, vol. 24, no. 35, pp. OP221–5, 2012.

[70] W. Huang, Z. Diao, L. Yao, Z. Cao, Y. Liu, J. Ma, and L. Xuan, “Electrically Tunable Distributed Feedback Laser Emission from Scaffolding Morphologic Holographic Polymer Dispersed Liquid Crystal Grating,” *Appl. Phys. Express*, vol. 6, no. 2, p. 022702, 2013.

[71] C. Vannahme, C. L. C. Smith, M. Brøkner Christiansen, and A. Kristensen, “Emission wavelength of multilayer distributed feedback dye lasers,” *Appl. Phys. Lett.*, vol. 101, no. 15, p. 151123, 2012.

[72] C. L. C. Smith, J. U. Lind, C. H. Nielsen, M. B. Christiansen, T. Buss, N. B. Larsen, and A. Kristensen, “Enhanced transduction of photonic crystal dye lasers for gas sensing via swelling polymer film.,” *Opt. Lett.*, vol. 36, no. 8, pp. 1392–4, 2011.

[73] V. Navarro-Fuster, I. Vragovic, E. M. Calzado, P. G. Boj, J. A. Quintana, J. M. Villalvilla, A. Retolaza, A. Juarros, D. Otaduy, S. Merino, and M. A. Díaz-García, “Film thickness and grating depth variation in organic second-order distributed feedback lasers,” *J. Appl. Phys.*, vol. 112, no. 4, p. 043104, 2012.

[74] L. Shang, L. Liu, and L. Xu, “Highly collimated laser emission from a peanut-shaped microcavity,” *Appl. Phys. Lett.*, vol. 92, no. 7, p. 071111, 2008.

[75] M. G. Ramírez, M. Morales-Vidal, V. Navarro-Fuster, P. G. Boj, J. A. Quintana, J. M. Villalvilla, A. Retolaza, S. Merino, and M. A. Díaz-García, “Improved performance of perylenediimide-based lasers,” *J. Mater. Chem. C*, vol. 1, no. 6, p. 1182, 2013.

[76] E. M. Calzado, J. M. Villalvilla, P. G. Boj, J. A. Quintana, V. Navarro-Fuster, A. Retolaza, S. Merino, and M. A. Díaz-García, “Influence of the excitation area on the thresholds of organic second-order distributed feedback lasers,” *Appl. Phys. Lett.*, vol. 101, no. 22, p. 223303, 2012.

[77] X. Liu, S. Klinkhammer, K. Sudau, N. Mechau, C. Vannahme, J. Kaschke, T. Mappes, M. Wegener, and U. Lemmer, “Ink-Jet-Printed Organic Semiconductor Distributed Feedback Laser,” *Appl. Phys. Express*, vol. 5, no. 7, p. 072101, Jun. 2012.

[78] G. Tsiminis, N. A. Montgomery, A. L. Kanibolotsky, A. Ruseckas, I. F. Perepichka, P. J. Skabara, G. A. Turnbull, and I. D. W. Samuel, “Laser characteristics of a family of benzene-cored star-shaped oligofluorenes,” *Semicond. Sci. Technol.*, vol. 27, no. 9, p. 094005, Sep. 2012.

[79] G. Yang, X. Chen, Y. Wang, and S. Feng, “Lasing characteristic of organic octagonal quasicrystal slabs with single-defect microcavity at low-index contrast,” *Opt. Express*, vol. 21, no. 9, pp. 11457–11464, 2013.

[80] S. Toffanin, S. Kim, S. Cavallini, M. Natali, V. Benfenati, J. J. Amsden, D. L. Kaplan, R. Zamboni, M. Muccini, and F. G. Omenetto, “Low-threshold blue lasing from silk fibroin thin films,” *Appl. Phys. Lett.*, vol. 101, no. 9, p. 091110, 2012.

[81] Z. Xu, Q. Liao, Q. Shi, H. Zhang, J. Yao, and H. Fu, “Low-threshold nanolasers based on slab-nanocrystals of H-aggregated organic semiconductors.,” *Adv. Mater.*, vol. 24, no. 35, pp. OP216–20, 2012.

[82] J. Herrnsdorf, Y. Wang, J. J. D. McKendry, Z. Gong, D. Massoubre, B. Guilhabert, G. Tsiminis, G. a. Turnbull, I. D. W. Samuel, N. Laurand, E. Gu, and M. D. Dawson, “Micro-LED pumped polymer laser: A discussion of future pump sources for organic lasers,” *Laser Photon. Rev.*, vol. 7, no. 6, pp. 1065–1078, 2013.

[83] G. Tsiminis, Y. Wang, A. L. Kanibolotsky, A. R. Inigo, P. J. Skabara, I. D. W. Samuel, and G. A Turnbull, “Nanoimprinted organic semiconductor laser pumped by a light-emitting diode.,” *Adv. Mater.*, vol. 25, no. 20, pp. 2826–30, 2013.

[84] Y. Wang, G. Tsiminis, A. L. Kanibolotsky, P. J. Skabara, I. D. W. Samuel, and G. A. Turnbull, “Nanoimprinted polymer lasers with threshold below 100 W / cm 2 using mixed-order distributed feedback resonators,” *Opt. Express*, vol. 21, no. 12, pp. 9211–9216, 2013.

[85] Z. Diao, S. Deng, W. Huang, L. Xuan, L. Hu, Y. Liu, and J. Ma, “Organic dual-wavelength distributed feedback laser empowered by dye-doped holography,” *J. Mater. Chem.*, vol. 22, no. 44, p. 23331, 2012.

[86] T. Aoki-Matsumoto, H. Mizuno, M. Ichida, H. Ando, T. Hirai, and K. Mizuno, “Room-temperature lasing from fluorene thin-film crystals densely doped with anthracene.,” *Opt. Lett.*, vol. 37, no. 23, pp. 4880–2, 2012.

[87] W. Huang, Y. Liu, L. Hu, Q. Mu, Z. Peng, C. Yang, and L. Xuan, “Second-order distributed feedback polymer laser based on holographic polymer dispersed liquid crystal grating,” *Org. Electron.*, vol. 14, no. 9, pp. 2299–2305, 2013.

[88] H. Mizuno, U. Haku, Y. Marutani, A. Ishizumi, H. Yanagi, F. Sasaki, and S. Hotta, “Single crystals of 5,5’-Bis(4'-methoxybiphenyl-4-yl)-2,2'-bithiophene for organic laser media.,” *Adv. Mater.*, vol. 24, no. 42, pp. 5744–9, 2012.

[89] S. Varghese, S.-J. Yoon, E. M. Calzado, S. Casado, P. G. Boj, M. A. Díaz-García, R. Resel, R. Fischer, B. Milián-Medina, R. Wannemacher, S. Y. Park, and J. Gierschner, “Stimulated resonance Raman scattering and laser oscillation in highly emissive distyrylbenzene-based molecular crystals.,” *Adv. Mater.*, vol. 24, no. 48, pp. 6473–8, 2012.

[90] O. Mhibik, T. Leang, A. Siove, S. Forget, and S. Chénais, “Broadly tunable (440–670 nm) solid-state organic laser with disposable capsules,” *Appl. Phys. Lett.*, vol. 102, no. 4, p. 041112, 2013.

[91] Y. Kawabe, C. Spiegelberg, A. Schülzgen, M. F. Nabor, B. Kippelen, E. A. Mash, P. M. Allemand, M. Kuwata-Gonokami, K. Takeda, and N. Peyghambarian, “Whispering-gallery-mode microring laser using a conjugated polymer,” *Appl. Phys. Lett.*, vol. 72, no. 2, p. 141, 1998.

[92] S. Chen, X. Zhao, Y. Wang, J. Shi, and D. Liu, “White light emission with red-green-blue lasing action in a disordered system of nanoparticles,” *Appl. Phys. Lett.*, vol. 101, no. 12, p. 123508, 2012.

[93] H.-H. Fang, R. Ding, S.-Y. Lu, X.-L. Zhang, J. Feng, Q.-D. Chen, and H.-B. Sun, “Flexible lasers based on the microstructured single-crystalline ultrathin films,” *J. Mater. Chem.*, vol. 22, no. 45, p. 24139, 2012.

[94] Y. Oki, T. Yoshiura, Y. Chisaki, and M. Maeda, “Fabrication of a Distributed-Feedback Dye Laser with a Grating Structure in its Plastic Waveguide,” *Appl. Opt.*, vol. 41, no. 24, p. 5030, 2002.

[95] G. Heliotis, R. Xia, D. D. C. Bradley, G. A. Turnbull, I. D. W. Samuel, P. Andrew, and W. L. Barnes, “Two-dimensional distributed feedback lasers using a broadband, red polyfluorene gain medium,” *J. Appl. Phys.*, vol. 96, no. 12, p. 6959, 2004.

[96] S. Richardson, O. P. M. Gaudin, G. A. Turnbull, and I. D. W. Samuel, “Improved operational lifetime of semiconducting polymer lasers by encapsulation,” *Appl. Phys. Lett.*, vol. 91, no. 26, p. 261104, 2007.

[97] Y. Chen, Z. Li, Z. Zhang, D. Psaltis, and A. Scherer, “Nanoimprinted circular grating distributed feedback dye laser,” *Appl. Phys. Lett.*, vol. 91, no. 5, p. 051109, 2007.

[98] V. Navarro-Fuster, E. M. Calzado, P. G. Boj, J. A. Quintana, J. M. Villalvilla, M. A. Díaz-García, V. Trabadelo, A. Juarros, A. Retolaza, and S. Merino, “Highly photostable organic distributed feedback laser emitting at 573 nm,” *Appl. Phys. Lett.*, vol. 97, no. 17, p. 171104, 2010.

[99] H. Watanabe, H. So, Y. Oki, S. Akine, and T. Omatsu, “Picosecond-Pulse-Pumped Distributed-Feedback Thick-Film Waveguide Blue Laser Using Fluorescent Brightener 135,” *Jpn. J. Appl. Phys.*, vol. 49, no. 7, p. 072105, 2010.

[100] M. Lu, B. T. Cunningham, S.-J. Park, and J. G. Eden, “Vertically emitting, dye-doped polymer laser in the green ($\lambda \sim 536$nm) with a second order distributed feedback grating fabricated by replica molding,” *Opt. Commun.*, vol. 281, no. 11, pp. 3159–3162, 2008.

[101] S. K. H. Wei, S. H. Chen, K. Dolgaleva, S. G. Lukishova, and R. W. Boyd, “Robust organic lasers comprising glassy-cholesteric pentafluorene doped

with a red-emitting oligofluorene," *Appl. Phys. Lett.*, vol. 94, no. 4, p. 041111, 2009.

[102] E. Yariv, S. Schultheiss, T. Saraidarov, and R. Reisfeld, "Efficiency and photostability of dye-doped solid-state lasers in different hosts," *Opt. Mater. (Amst).*, vol. 16, no. 1–2, pp. 29–38, 2001.

[103] O. V. Sakhno, J. Stumpe, and T. N. Smirnova, "Distributed feedback dye laser holographically induced in improved organic–inorganic photocurable nanocomposites," *Appl. Phys. B*, vol. 103, no. 4, pp. 907–916, 2011.

[104] M. G. Ramirez, P. G. Boj, V. Navarro-Fuster, I. Vragovic, J. M. Villalvilla, I. Alonso, V. Trabadelo, S. Merino, and M. a Díaz-García, "Efficient organic distributed feedback lasers with imprinted active films.," *Opt. Express*, vol. 19, no. 23, pp. 22443–54, 2011.

[105] H. Matsuura, M. Fukuda, and H. Sakata, "Threshold reduction induced by silica nanoparticledispersed active layer in diode-pumped microcavity dye laser," *Laser Phys. Lett.*, vol. 6, no. 3, pp. 194–197, 2009.

[106] L. Persano, A. Camposeo, P. Del Carro, P. Solaro, R. Cingolani, P. Boffi, and D. Pisignano, "Rapid prototyping encapsulation for polymer light-emitting lasers," *Appl. Phys. Lett.*, vol. 94, no. 12, p. 123305, 2009.

[107] V. G. Kozlov, V. Bulovic, P. E. Burrows, and S. R. Forrest, "Laser action in organic semiconductor waveguide and," *Nature*, vol. 389, no. September, pp. 362–364, 1997.

[108] R. M. Balachandran, D. P. Pacheco, and N. M. Lawandy, "Laser action in polymeric gain media containing scattering particles.," *Appl. Opt.*, vol. 35, no. 4, pp. 640–3, 1996.

[109] V. G. Kozlov, V. Bulovic, P. E. Burrows, M. Baldo, V. B. Khalfin, G. Parthasarathy, S. R. Forrest, Y. You, and M. E. Thompson, "Study of lasing action based on Förster energy transfer in optically pumped organic semiconductor thin films," *J. Appl. Phys.*, vol. 84, no. 8, p. 4096, 1998.

[110] S. Richardson, "The Fabrication and Lithography of Conjugated Polymer Distributed Feedback Lasers and Development of their Applications," *PhD thesis*, vol. University, 2007.

[111] Y. Chen, J. Herrnsdorf, B. Guilhabert, A. L. Kanibolotsky, A. R. Mackintosh, Y. Wang, R. A. Pethrick, E. Gu, G. A. Turnbull, and P. J. Skabara, "Laser action in a surface-structured free-standing membrane based on a π-conjugated polymer-composite," *Org. Electron.*, vol. 12, no. 1, pp. 62–69, 2011.

[112] R. Gupta, M. Stevenson, and A. J. Heeger, “Low threshold distributed feedback lasers fabricated from blends of conjugated polymers: Reduced losses through Förster transfer,” *J. Appl. Phys.*, vol. 92, no. 9, p. 4874, 2002.

[113] J. R. Lawrence, G. A. Turnbull, and I. D. W. Samuel, “Polymer laser fabricated by a simple micromolding process,” *Appl. Phys. Lett.*, vol. 82, no. 23, p. 4023, 2003.

[114] G. Kranzelbinder, E. Toussaere, J. Zyss, T. Kavc, G. Langer, and W. Kern, “Organic surface emitting laser based on a deep-ultraviolet photopolymer containing thiocyanate groups,” *Appl. Phys. Lett.*, vol. 82, no. 14, p. 2203, 2003.

[115] D. Schneider, T. Rabe, T. Riedl, T. Dobbertin, M. Kröger, E. Becker, H.-H. Johannes, W. Kowalsky, T. Weimann, J. Wang, and P. Hinze, “Organic solid-state lasers based on sexiphenyl as active chromophore,” *J. Appl. Phys.*, vol. 98, no. 4, p. 043104, 2005.

[116] W. Holzer, A. Penzkofer, S. Schrader, and B. Grimm, “Photo-physical and lasing characterisation of a polyparaphenylenevinylene (PPV) neat film,” *Opt. Quantum Electron.*, vol. 37, no. 5, pp. 475–494, 2005.

[117] C. Karnutsch, C. Gýrtner, V. Haug, U. Lemmer, T. Farrell, B. S. Nehls, U. Scherf, J. Wang, T. Weimann, G. Heliotis, C. Pflumm, J. C. DeMello, and D. D. C. Bradley, “Low threshold blue conjugated polymer lasers with first- and second-order distributed feedback,” *Appl. Phys. Lett.*, vol. 89, no. 20, p. 201108, 2006.

[118] T. Riedl, T. Rabe, H.-H. Johannes, W. Kowalsky, J. Wang, T. Weimann, P. Hinze, B. Nehls, T. Farrell, and U. Scherf, “Tunable organic thin-film laser pumped by an inorganic violet diode laser,” *Appl. Phys. Lett.*, vol. 88, no. 24, p. 241116, 2006.

[119] T. Rabe, K. Gerlach, T. Riedl, H.-H. Johannes, W. Kowalsky, J. Niederhofer, W. Gries, J. Wang, T. Weimann, P. Hinze, F. Galbrecht, and U. Scherf, “Quasi-continuous-wave operation of an organic thin-film distributed feedback laser,” *Appl. Phys. Lett.*, vol. 89, no. 8, p. 081115, 2006.

[120] C. Karnutsch, C. Pflumm, G. Heliotis, J. C. DeMello, D. D. C. Bradley, J. Wang, T. Weimann, V. Haug, C. Gärtner, and U. Lemmer, “Improved organic semiconductor lasers based on a mixed-order distributed feedback resonator design,” *Appl. Phys. Lett.*, vol. 90, no. 13, p. 131104, 2007.

[121] J. C. Ribierre, G. Tsiminis, S. Richardson, G. A. Turnbull, I. D. W. Samuel, H. S. Barcena, and P. L. Burn, “Amplified spontaneous emission and lasing properties of bisfluorene-cored dendrimers,” *Appl. Phys. Lett.*, vol. 91, no. 8, p. 081108, 2007.

[122] A. E. Vasdekis, S. A. Moore, A. Ruseckas, T. F. Krauss, I. D. W. Samuel, and G. A. Turnbull, “Silicon based organic semiconductor laser,” *Appl. Phys. Lett.*, vol. 91, no. 5, p. 051124, 2007.

[123] B. K. Yap, R. Xia, M. Campoy-Quiles, P. N. Stavrinou, and D. D. C. Bradley, “Simultaneous optimization of charge-carrier mobility and optical gain in semiconducting polymer films.,” *Nat. Mater.*, vol. 7, no. 5, pp. 376–80, 2008.

[124] Y. Yang, G. A. Turnbull, and I. D. W. Samuel, “Hybrid optoelectronics: A polymer laser pumped by a nitride light-emitting diode,” *Appl. Phys. Lett.*, vol. 92, no. 16, p. 163306, 2008.

[125] N. Tsutsumi and M. Takeuchi, “Ti–sapphire femtosecond pulse pumped laser emission from all-plastic organic waveguide with distributed feedback resonator,” *Opt. Commun.*, vol. 281, no. 8, pp. 2179–2183, 2008.

[126] W.-Y. Lai, R. Xia, Q.-Y. He, P. A. Levermore, W. Huang, and D. D. C. Bradley, “Enhanced Solid-State Luminescence and Low-Threshold Lasing from Starburst Macromolecular Materials,” *Adv. Mater.*, vol. 21, no. 3, pp. 355–360, 2009.

[127] Y. Wang, G. Tsiminis, Y. Yang, A. Ruseckas, A. L. Kanibolotsky, I. F. Perepichka, P. J. Skabara, G. A. Turnbull, and I. D. W. Samuel, “Broadly tunable deep blue laser based on a star-shaped oligofluorene truxene,” *Synth. Met.*, vol. 160, no. 13–14, pp. 1397–1400, 2010.

[128] M. Stroisch, T. Woggon, C. Teiwes-Morin, S. Klinkhammer, K. Forberich, A. Gombert, M. Gerken, and U. Lemmer, “Intermediate high index layer for laser mode tuning in organic semiconductor lasers.,” *Opt. Express*, vol. 18, no. 6, pp. 5890–5, 2010.

[129] Y. Zhang and S. R. Forrest, “Existence of continuous-wave threshold for organic semiconductor lasers,” *Phys. Rev. B*, vol. 84, no. 24, p. 241301, 2011.

[130] G. A. Turnbull, P. Andrew, W. L. Barnes, and I. D. W. Samuel, “Operating characteristics of a semiconducting polymer laser pumped by a microchip laser,” *Appl. Phys. Lett.*, vol. 82, no. 3, p. 313, 2003.

[131] A. E. Vasdekis, G. A. Turnbull, I. D. W. Samuel, P. Andrew, and W. L. Barnes, “Low threshold edge emitting polymer distributed feedback laser based on a square lattice,” *Appl. Phys. Lett.*, vol. 86, no. 16, p. 161102, 2005.

[132] C. Karnutsch, M. Stroisch, M. Punke, U. Lemmer, J. Wang, and T. Weimann, “Laser Diode-Pumped Organic Semiconductor Lasers Utilizing Two-Dimensional Photonic Crystal Resonators,” *IEEE Photonics Technol. Lett.*, vol. 19, no. 10, pp. 741–743, 2007.

[133] H. Sakata, K. Yamashita, H. Takeuchi, and M. Tomiki, “Diode-pumped distributed-feedback dye laser with an organic–inorganic microcavity,” *Appl. Phys. B*, vol. 92, no. 2, pp. 243–246, 2008.

[134] H. Finkelmann, S. T. Kim, A. Muñoz, P. Palffy-Muhoray, and B. Taheri, “Tunable Mirrorless Lasing in Cholesteric Liquid Crystalline Elastomers,” *Adv. Mater.*, vol. 13, no. 14, pp. 1069–1072, 2001.

[135] Y. Huang, Y. Zhou, and S.-T. Wu, “Spatially tunable laser emission in dye-doped photonic liquid crystals,” *Appl. Phys. Lett.*, vol. 88, no. 1, p. 011107, 2006.

[136] E. Yariv and R. Reisfeld, “Laser properties of pyrromethene dyes in sol–gel glasses,” *Opt. Mater. (Amst).*, vol. 13, no. 1, pp. 49–54, 1999.

[137] S. Schultheiss, E. Yariv, R. Reisfeld, and H. D. Breuer, “Solid state dye lasers: Rhodamines in silica–zirconia materials,” *Photochem. Photobiol. Sci.*, vol. 1, no. 5, pp. 320–323, 2002.

[138] S. S. Anufrik, M. F. Koldunov, A. A. Manenkov, and V. V. Tarkovskii, “Lasing efficiency of dyes incorporated into a nanoporous glass-polymer composite,” *J. Appl. Spectrosc.*, vol. 75, no. 5, pp. 714–722, 2008.

[139] A. Costela, “Enhancement of laser properties of pyrromethene 567 dye incorporated into new organic–inorganic hybrid materials,” *Chem. Phys. Lett.*, vol. 369, no. 5–6, pp. 656–661, 2003.

[140] A. Costela, “Highly efficient and stable doped hybrid organic–inorganic materials for solid-state dye lasers,” *Chem. Phys. Lett.*, vol. 387, no. 4–6, pp. 496–501, 2004.

[141] A. Costela, I. García-Moreno, D. del Agua, O. García, and R. Sastre, “Silicon-containing organic matrices as hosts for highly photostable solid-state dye lasers,” *Appl. Phys. Lett.*, vol. 85, no. 12, p. 2160, 2004.

[142] A. Costela, I. GarcÍa-moreno, O. GarcÍa, D. Del Agua, and R. Sastre, “Structural influence of the inorganic network in the laser performance of dye-doped hybrid materials,” *Appl. Phys. B*, vol. 80, no. 6, pp. 749–755, 2005.

[143] I. García-Moreno, A. Costela, A. Cuesta, O. García, D. del Agua, and R. Sastre, “Synthesis, structure, and physical properties of hybrid nanocomposites for solid-state dye lasers.,” *J. Phys. Chem. B*, vol. 109, no. 46, pp. 21618–26, 2005.

[144] I. García-Moreno, F. Amat-Guerri, M. Liras, A. Costela, L. Infantes, R. Sastre, F. López Arbeloa, J. Bañuelos Prieto, and Í. López Arbeloa, “Structural Changes in the BODIPY Dye PM567 Enhancing the Laser Action in Liquid and Solid Media,” *Adv. Funct. Mater.*, vol. 17, no. 16, pp. 3088–3098, 2007.

[145] A. Costela, I. García-Moreno, D. del Agua, O. García, and R. Sastre, “Highly photostable solid-state dye lasers based on silicon-modified organic matrices,” *J. Appl. Phys.*, vol. 101, no. 7, p. 073110, 2007.

[146] A. E. Vasdekis, G. Tsiminis, J.-C. Ribierre, L. O’ Faolain, T. F. Krauss, G. A. Turnbull, and I. D. W. Samuel, “Diode pumped distributed Bragg reflector lasers based on a dye-to-polymer energy transfer blend.,” *Opt. Express*, vol. 14, no. 20, pp. 9211–6, 2006.

[147] A. Argyros, M. A. van Eijkelenborg, S. D. Jackson, and R. P. Mildren, “Microstructured polymer fiber laser,” *Opt. Lett.*, vol. 29, no. 16, p. 1882, 2004.

[148] I. García-Moreno, A. Costela, M. Pintado-Sierra, V. Martín, and R. Sastre, “Enhanced laser action of Perylene-Red doped polymeric materials,” *Opt. Express*, vol. 17, no. 15, p. 12777, 2009.

[149] T. N. Kopylova, G. V. Maier, E. N. Telminov, V. A. Svetlichnyi, and K. M. Degtyarenko, “A double-frequency solid-state laser on organic compounds,” *Russ. Phys. J.*, vol. 52, no. 7, pp. 655–660, 2009.

[150] M. Fukuda and K. Mito, “Laser Oscillation of Energy Transfer Solid-State Dye Laser with a Thin-Film Ring Resonator,” *Jpn. J. Appl. Phys.*, vol. 39, no. Part 1, No. 6A, pp. 3470–3471, 2000.

[151] M. Fukuda, K. Kodama, H. Yamamoto, and K. Mito, “Evaluation of new organic pigments as laser-active media for a solid-state dye laser,” *Dye. Pigment.*, vol. 63, no. 2, pp. 115–125, 2004.

[152] S. Klinkhammer, N. Heussner, K. Huska, T. Bocksrocker, F. Geislhöringer, C. Vannahme, T. Mappes, and U. Lemmer, “Voltage-controlled tuning of an organic semiconductor distributed feedback laser using liquid crystals,” *Appl. Phys. Lett.*, vol. 99, no. 2, p. 023307, 2011.

[153] C. Foucher, B. Guilhabert, A. L. Kanibolotsky, P. J. Skabara, N. Laurand, and M. D. Dawson, “Highly-photostable and mechanically flexible all-organic semiconductor lasers,” *Opt. Mater. Express*, vol. 3, no. 5, p. 584, Apr. 2013.

[154] N. Grassie and G. Scott, *Polymer degradation and stabilisation*. Cambridge: Cambridge University Press, 1985.

[155] L. Cerdán, A. Costela, G. Durán-Sampedro, I. García-Moreno, M. Calle, M. Juan-y-Seva, J. de Abajo, and G. A. Turnbull, “New perylene-doped polymeric thin films for efficient and long-lasting lasers,” *J. Mater. Chem.*, vol. 22, no. 18, p. 8938, 2012.

[156] W. Zhao, T. Cao, and J. M. White, “On the Origin of Green Emission in Polyfluorene Polymers: The Roles of Thermal Oxidation Degradation and Crosslinking,” *Adv. Funct. Mater.*, vol. 14, no. 8, pp. 783–790, 2004.

[157] R. G. Compton, C. H. Bamford, and C. F. H. Tipper, *Degradation of Polymers*, Elsevier A. Elsevier, 1975.

[158] K. Pielichowski and J. Njuguna, *Thermal degradation of polymeric materials*. Shawbury: iSmithers Rapra Publishing, 2005.

[159] N. S. Allen and M. Edge, *Fundamentals of Polymer Degradation and Stabilization*, Illustrate. Springer Science & Business Media, 1992.

[160] S. L. Madorsky, *Thermal Degradation of Organic Polymers*. Interscience Publishers, 1964.

[161] D. C. Wright, *Failure of Polymer Products Due to Photo-oxidation*. iSmithers Rapra Publishing, 2001.

[162] L. Shibryaeva, A. Popov, and G. Zaikov, *Thermal Oxidation of Polymer Blends: The Role of Structure*, Illustrate. CRC Press, 2006.

[163] M. Baldo, R. Holmes, and S. Forrest, “Prospects for electrically pumped organic lasers,” *Phys. Rev. B*, vol. 66, no. 3, p. 035321, 2002.

[164] M. Baldo and S. Forrest, “Interface-limited injection in amorphous organic semiconductors,” *Phys. Rev. B*, vol. 64, no. 8, p. 085201, 2001.

[165] A. P. Kulkarni, C. J. Tonzola, A. Babel, and S. A. Jenekhe, “Electron Transport Materials for Organic Light-Emitting Diodes,” *Chem. Mater.*, vol. 16, no. 23, pp. 4556–4573, 2004.

[166] N. Giebink and S. Forrest, “Temporal response of optically pumped organic semiconductor lasers and its implication for reaching threshold under electrical excitation,” *Phys. Rev. B*, vol. 79, no. 7, p. 073302, 2009.

[167] M. Lehnhardt, T. Riedl, U. Scherf, T. Rabe, and W. Kowalsky, “Spectrally separated optical gain and triplet absorption: Towards continuous wave lasing in organic thin film lasers,” *Org. Electron.*, vol. 12, no. 8, pp. 1346–1351, 2011.

[168] C. B. Murray, C. R. Kagan, and M. G. Bawendi, “Synthesis and characterization of monodisperse nanocrystals and close-packed nanocrystal assemblies,” *Annu. Rev. Mater. Sci.*, vol. 30, no. 1, pp. 545–610, 2000.

[169] V. I. Klimov, “Nanocrystal Quantum Dots from fundamental photophysics to multicolor lasing,” *Los Alamos Sci.*, vol. 28, pp. 214–220, 2003.

[170] C. B. Murray, D. J. Norris, and M. G. Bawendi, “Synthesis and characterization of nearly monodisperse CdE (E = sulfur, selenium, tellurium) semiconductor nanocrystallites,” *J. Am. Chem. Soc.*, vol. 115, no. 19, pp. 8706–8715, 1993.

[171] B. O. Dabbousi, J. Rodriguez-Viejo, F. V. Mikulec, J. R. Heine, H. Mattoussi, R. Ober, K. F. Jensen, and M. G. Bawendi, “(CdSe)ZnS Core−Shell Quantum Dots: Synthesis and Characterization of a Size Series of Highly Luminescent Nanocrystallites,” *J. Phys. Chem. B*, vol. 101, no. 46, pp. 9463–9475, 1997.

[172] M. A. Hines and P. Guyot-Sionnest, “Synthesis and Characterization of Strongly Luminescing ZnS-Capped CdSe Nanocrystals,” *J. Phys. Chem.*, vol. 100, no. 2, pp. 468–471, 1996.

[173] M. Tytus, J. Krasnyj, W. Jacak, A. Chuchmała, W. Donderowicz, and L. Jacak, “Differences between photoluminescence spectra of type-I and type-II quantum dots,” *J. Phys. Conf. Ser.*, vol. 104, p. 012011, 2008.

[174] A. Yakimov, A. Dvurechenskii, A. Nikiforov, A. Bloshkin, A. Nenashev, and V. Volodin, “Electronic states in Ge⁄Si quantum dots with type-II band alignment initiated by space-charge spectroscopy,” *Phys. Rev. B*, vol. 73, no. 11, p. 115333, 2006.

[175] F. Zhang, J. Liu, G. You, C. Zhang, S. E. Mohney, M. J. Park, J. S. Kwak, Y. Wang, D. D. Koleske, and J. Xu, “Nonradiative energy transfer between colloidal quantum dot-phosphors and nanopillar nitride LEDs.,” *Opt. Express*, vol. 20 Suppl 2, no. March, pp. A333–9, 2012.

[176] S. Nizamoglu, T. Ozel, E. Sari, and H. V Demir, “White light generation using CdSe/ZnS core–shell nanocrystals hybridized with InGaN/GaN light emitting diodes,” *Nanotechnology*, vol. 18, no. 6, p. 065709, 2007.

[177] P. V. Kamat, “Quantum Dot Solar Cells. Semiconductor Nanocrystals as Light Harvesters †,” *J. Phys. Chem. C*, vol. 112, no. 48, pp. 18737–18753, 2008.

[178] I. Robel, V. Subramanian, M. Kuno, and P. V Kamat, “Quantum dot solar cells. harvesting light energy with CdSe nanocrystals molecularly linked to mesoscopic TiO2 films.,” *J. Am. Chem. Soc.*, vol. 128, no. 7, pp. 2385–93, 2006.

[179] G. Konstantatos, I. Howard, A. Fischer, S. Hoogland, J. Clifford, E. Klem, L. Levina, and E. H. Sargent, “Ultrasensitive solution-cast quantum dot photodetectors.,” *Nature*, vol. 442, no. 7099, pp. 180–3, 2006.

[180] S. A. McDonald, G. Konstantatos, S. Zhang, P. W. Cyr, E. J. D. Klem, L. Levina, and E. H. Sargent, “Solution-processed PbS quantum dot infrared photodetectors and photovoltaics.,” *Nat. Mater.*, vol. 4, no. 2, pp. 138–42, 2005.

[181] T.-H. Kim, K.-S. Cho, E. K. Lee, S. J. Lee, J. Chae, J. W. Kim, D. H. Kim, J.-Y. Kwon, G. Amaratunga, S. Y. Lee, B. L. Choi, Y. Kuk, J. M. Kim, and K. Kim, "Full-colour quantum dot displays fabricated by transfer printing," *Nat. Photonics*, vol. 5, no. 3, pp. 176–182, 2011.

[182] V. I. Klimov, "Spectral and dynamical properties of multiexcitons in semiconductor nanocrystals.," *Annu. Rev. Phys. Chem.*, vol. 58, pp. 635–73, 2007.

[183] V. I. Klimov, "Optical Gain and Stimulated Emission in Nanocrystal Quantum Dots," *Science (80-.).*, vol. 290, no. 5490, pp. 314–317, 2000.

[184] W. K. Bae, L. A. Padilha, Y.-S. Park, H. McDaniel, I. Robel, J. M. Pietryga, and V. I. Klimov, "Controlled alloying of the core-shell interface in CdSe/CdS quantum dots for suppression of Auger recombination.," *ACS Nano*, vol. 7, no. 4, pp. 3411–9, 2013.

[185] A. V. Malko, A. A. Mikhailovsky, M. A. Petruska, J. A. Hollingsworth, H. Htoon, M. G. Bawendi, and V. I. Klimov, "From amplified spontaneous emission to microring lasing using nanocrystal quantum dot solids," *Appl. Phys. Lett.*, vol. 81, no. 7, p. 1303, 2002.

[186] S. Hoogland, V. Sukhovatkin, I. Howard, S. Cauchi, L. Levina, and E. H. Sargent, "A solution-processed 1.53 mum quantum dot laser with temperature-invariant emission wavelength.," *Opt. Express*, vol. 14, no. 8, pp. 3273–81, Apr. 2006.

[187] J. Schäfer, J. P. Mondia, R. Sharma, Z. H. Lu, a S. Susha, a L. Rogach, and L. J. Wang, "Quantum dot microdrop laser.," *Nano Lett.*, vol. 8, no. 6, pp. 1709–12, 2008.

[188] V. M. Menon, M. Luberto, N. V Valappil, and S. Chatterjee, "Lasing from InGaP quantum dots in a spin-coated flexible microcavity.," *Opt. Express*, vol. 16, no. 24, pp. 19535–40, 2008.

[189] C. Dang, J. Lee, C. Breen, J. S. Steckel, S. Coe-Sullivan, and A. Nurmikko, "Red, green and blue lasing enabled by single-exciton gain in colloidal quantum dot films.," *Nat. Nanotechnol.*, vol. 7, no. 5, pp. 335–9, 2012.

[190] Y. Chen, B. Guilhabert, J. Herrnsdorf, Y. Zhang, A. R. Mackintosh, R. a. Pethrick, E. Gu, N. Laurand, and M. D. Dawson, "Flexible distributed-feedback colloidal quantum dot laser," *Appl. Phys. Lett.*, vol. 99, no. 24, p. 241103, 2011.

[191] F. Todescato, I. Fortunati, S. Gardin, E. Garbin, E. Collini, R. Bozio, J. J. Jasieniak, G. Della Giustina, G. Brusatin, S. Toffanin, and R. Signorini, "Soft-Lithographed Up-Converted Distributed Feedback Visible Lasers Based on

CdSe-CdZnS-ZnS Quantum Dots," *Adv. Funct. Mater.*, vol. 22, no. 2, pp. 337–344, 2012.

[192] V. C. Sundar, H.-J. Eisler, T. Deng, Y. Chan, E. L. Thomas, and M. G. Bawendi, "Soft-Lithographically Embossed, Multilayered Distributed-Feedback Nanocrystal Lasers," *Adv. Mater.*, vol. 16, no. 23–24, pp. 2137–2141, 2004.

[193] A. B. Buckman, *Guided-wave Photonics*, Illustrate. Saunders College, Pub., 1992.

[194] M. D. McGehee, M. A. Díaz-García, F. Hide, R. Gupta, E. K. Miller, D. Moses, and A. J. Heeger, "Semiconducting polymer distributed feedback lasers," *Appl. Phys. Lett.*, vol. 72, no. 13, p. 1536, 1998.

[195] K. Yoshino, S. Tatsuhara, Y. Kawagishi, M. Ozaki, A. A. Zakhidov, and Z. V. Vardeny, "Amplified spontaneous emission and lasing in conducting polymers and fluorescent dyes in opals as photonic crystals," *Appl. Phys. Lett.*, vol. 74, no. 18, p. 2590, 1999.

[196] M. G. Moharam, E. B. Grann, D. A. Pommet, and T. K. Gaylord, "Formulation for stable and efficient implementation of the rigorous coupled-wave analysis of binary gratings," *J. Opt. Soc. Am. A*, vol. 12, no. 5, p. 1068, 1995.

[197] A. L. Kanibolotsky, I. F. Perepichka, and P. J. Skabara, "Star-shaped pi-conjugated oligomers and their applications in organic electronics and photonics.," *Chem. Soc. Rev.*, vol. 39, no. 7, pp. 2695–728, 2010.

[198] A. L. Kanibolotsky, R. Berridge, P. J. Skabara, I. F. Perepichka, D. D. C. Bradley, and M. Koeberg, "Synthesis and properties of monodisperse oligofluorene-functionalized truxenes: highly fluorescent star-shaped architectures.," *J. Am. Chem. Soc.*, vol. 126, no. 42, pp. 13695–702, 2004.

[199] A. Rose, Z. Zhu, C. F. Madigan, T. M. Swager, and V. Bulovic, "Sensitivity gains in chemosensing by lasing action in organic polymers," *Nature*, vol. 434, no. April, pp. 1–4, 2005.

[200] Sigma-Aldrich, "Lumidots: Quantum Dot Nanocrystals." [Online]. Available: http://www.sigmaaldrich.com/materials-science/nanomaterials/lumidots.html.

[201] L. E. Brus, "Electron–electron and electron-hole interactions in small semiconductor crystallites: The size dependence of the lowest excited electronic state," *J. Chem. Phys.*, vol. 80, no. 9, p. 4403, 1984.

[202] J. Luo, Z. Xie, J. W. Y. Lam, L. Cheng, B. Z. Tang, H. Chen, C. Qiu, H. S. Kwok, X. Zhan, Y. Liu, and D. Zhu, "Aggregation-induced emission of 1-

methyl-1,2,3,4,5-pentaphenylsilole," *Chem. Commun.*, vol. 381, no. 18, pp. 1740–1741, 2001.

[203] Y. Hong, J. W. Y. Lam, and B. Z. Tang, "Aggregation-induced emission.," *Chem. Soc. Rev.*, vol. 40, no. 11, pp. 5361–88, 2011.

[204] M. P. Aldred, C. Li, G.-F. Zhang, W.-L. Gong, A. D. Q. Li, Y. Dai, D. Ma, and M.-Q. Zhu, "Fluorescence quenching and enhancement of vitrifiable oligofluorenes end-capped with tetraphenylethene," *J. Mater. Chem.*, vol. 22, no. 15, p. 7515, 2012.

[205] Z. Zhao, J. W. Y. Lam, and B. Z. Tang, "Tetraphenylethene: a versatile AIE building block for the construction of efficient luminescent materials for organic light-emitting diodes," *J. Mater. Chem.*, vol. 22, no. 45, p. 23726, 2012.

[206] Z. Zhu, L. Xu, H. Li, X. Zhou, J. Qin, and C. Yang, "A tetraphenylethene-based zinc complex as a sensitive DNA probe by coordination interaction.," *Chem. Commun. (Camb).*, vol. 50, no. 53, pp. 7060–2, 2014.

[207] Y. Hong, S. Chen, C. W. T. Leung, J. W. Y. Lam, and B. Z. Tang, "Water-soluble tetraphenylethene derivatives as fluorescent 'light-up' probes for nucleic acid detection and their applications in cell imaging.," *Chem. Asian J.*, vol. 8, no. 8, pp. 1806–12, 2013.

[208] R. Hu, J. W. Y. Lam, J. Liu, H. H. Y. Sung, I. D. Williams, Z. Yue, K. S. Wong, M. M. F. Yuen, and B. Z. Tang, "Hyperbranched conjugated poly(tetraphenylethene): synthesis, aggregation-induced emission, fluorescent photopatterning, optical limiting and explosive detection," *Polym. Chem.*, vol. 3, no. 6, p. 1481, 2012.

[209] Z. Zhao, J. W. Y. Lam, and B. Z. Tang, "Tetraphenylethene: a versatile AIE building block for the construction of efficient luminescent materials for organic light-emitting diodes," *J. Mater. Chem.*, vol. 22, no. 45, p. 23726, 2012.

[210] A. L. Kanibolotsky, F. Vilela, J. C. Forgie, S. E. T. Elmasly, P. J. Skabara, K. Zhang, B. Tieke, J. McGurk, C. R. Belton, P. N. Stavrinou, and D. D. C. Bradley, "Well-defined and monodisperse linear and star-shaped quaterfluorene-DPP molecules: the significance of conjugation and dimensionality.," *Adv. Mater.*, vol. 23, no. 18, pp. 2093–7, 2011.

[211] Mantechmaterials, "CP1 data sheet." [Online]. Available: http://www.mantechmaterials.com/products.asp.

[212] L. Cerdán, A. Costela, I. García-Moreno, O. García, R. Sastre, M. Calle, D. Muñoz, and J. de Abajo, "High-Gain Long-Lived Amplified Spontaneous

Emission from Dye-Doped Fluorinated Polyimide Planar Waveguides," *Macromol. Chem. Phys.*, vol. 210, no. 19, pp. 1624–1631, 2009.

[213] O. G. Abdullah and D. R. Saber, "Optical Absorption of Polyvinyl Alcohol Films Doped with Nickel Chloride," *Appl. Mech. Mater.*, vol. 110–116, pp. 177–182, 2011.

[214] J. Gaume, P. Wong-Wah-Chung, A. Rivaton, S. Thérias, and J.-L. Gardette, "Photochemical behavior of PVA as an oxygen-barrier polymer for solar cell encapsulation," *RSC Adv.*, vol. 1, no. 8, p. 1471, 2011.

[215] G. Pritchard, John, *Poly (vinyl alcohol): Basic Properties and Uses*. Macdonald Technical & Scientific, 1970.

[216] J. Brandrup, E. Immergut, and E. Grulke, *Polymer Handbook*, Fourth. John Willey & Sons, 1999.

[217] J. F. Rabek and B. Ranby, "Role of singlet oxygen in photo-oxidative degradation and photostabilization of polymers," *Polym. Eng. Sci.*, vol. 15, no. 1, pp. 40–43, Jan. 1975.

[218] Schott, "AF32." [Online]. Available: www.schott.com.

[219] Sigma-Aldrich, "Toluene data sheet." [Online]. Available: http://www.sigmaaldrich.com/catalog/product/sial/244511?lang=en&region=GB.

[220] Sigma-Aldrich, "Tetrahydrofuran data sheet." [Online]. Available: http://www.sigmaaldrich.com/catalog/product/sial/401757?lang=en&region=GB.

[221] Sigma-Aldrich, "Chloroform data sheet." [Online]. Available: http://www.sigmaaldrich.com/catalog/product/sial/288306?lang=en&region=GB.

[222] Norland, "NOA65 Data sheet." [Online]. Available: http://www.norlandprod.com/adhesives/noa 65.html.

[223] Norland, "NOA85 Data sheet." [Online]. Available: http://www.norlandprod.com/adhesives/NOA85.html.

[224] L. Pang, Y. Shen, K. Tetz, and Y. Fainman, "PMMA quantum dots composites fabricated via use of pre-polymerization.," *Opt. Express*, vol. 13, no. 1, pp. 44–9, 2005.

[225] B. Guilhabert, C. Foucher, A.-M. Haughey, E. Mutlugun, J. Herrnsdorf, H. D. Sun, H. V Demir, and M. D. Dawson, "Nanosecond colloidal quantum dot lasers for sensing," *Opt. Express*, vol. 22, no. 6, pp. 7308–7319, 2014.

[226] Sigma-Aldrich, “PMMA Data sheet.” [Online]. Available: http://www.sigmaaldrich.com/catalog/product/aldrich/182230?lang=en&region=GB.

[227] C. Foucher, B. Guilhabert, N. Laurand, and M. D. Dawson, “Wavelength-tunable colloidal quantum dot laser on ultra-thin flexible glass,” *Appl. Phys. Lett.*, vol. 104, no. 14, p. 141108, 2014.

[228] J. Chilwell and I. Hodgkinson, “Thin-films field-transfer matrix theory of planar multilayer waveguides and reflection from prism-loaded waveguides Jn,” *J. Opt. socity Am. A*, vol. 1, no. 7, pp. 742–753, 1984.

[229] M. Born and E. Wolf, *Principles of Optics*, 7th editio. Cambridge: CUP Archive, 1999.

[230] J. Buseman-Williams, K. D. Frischknecht, M. D. Hubert, A. K. Saafir, and J. D. Tremel, “Flat-plate encapsulation solution for OLED displays using a printed getter,” *J. Soc. Inf. Disp.*, vol. 15, no. 2, pp. 103–112, 2007.

[231] A.-M. Haughey, G. A. Burley, A. L. Kanibolotsky, P. J. Skabara, M. D. Dawson, and N. Laurand, “Organic distributed feedback laser biosensor,” in *2013 IEEE Photonics Conference*, 2013, pp. 161–162.

[232] M. Lu, S. S. Choi, U. Irfan, and B. T. Cunningham, “Plastic distributed feedback laser biosensor,” *Appl. Phys. Lett.*, vol. 93, no. 11, p. 111113, 2008.

[233] A.-M. Haughey, B. Guilhabert, A. L. Kanibolotsky, P. J. Skabara, G. A. Burley, M. D. Dawson, and N. Laurand, “An organic semiconductor laser based on star-shaped truxene-core oligomers for refractive index sensing,” *Sensors Actuators B Chem.*, vol. 185, pp. 132–139, 2013.

[234] M. Lu, S. S. Choi, C. J. Wagner, J. G. Eden, and B. T. Cunningham, “Label free biosensor incorporating a replica-molded, vertically emitting distributed feedback laser,” *Appl. Phys. Lett.*, vol. 92, no. 26, p. 261502, 2008.

[235] P. Lo, J. Ding, J. Hu, Y. Chan, S. Garner, M. He, J. Lin, X. Li, M. Sorensen, J. Li, P. Cimo, and C. Kuo, “29.2: Flexible Glass Substrates for Organic TFT Active Matrix Electrophoretic Displays,” *SID Symp. Dig. Tech. Pap.*, vol. 42, no. 1, pp. 387–388, 2011.

[236] S. Hoehla and S. Garner, “Full color AM-LCDs on flexible glass substrates,” *ITE/SID 17th …*, vol. 8, no. 309, pp. 1689–1692, 2010.

[237] K.-W. Wu, Y. C. Liao, J. W. Shiu, Y. S. Tsai, K. T. Chen, Y. C. Lai, C.-C. Lai, Y.-Z. Lee, S. Garner, J. Lin, X. Li, and P. Cimo, “29.3: Color ChLC E-paper Display with 100 um Flexible Glass Substrates,” *SID Symp. Dig. Tech. Pap.*, vol. 42, no. 1, pp. 389–391, 2011.

[238] R. Mehra, “Application of refractive index mixing rules in binary systems of hexadecane and heptadecane with n -alkanols at different temperatures,” *Indian Acad. Sci.*, vol. 115, no. 2, pp. 147–154, 2003.

[239] A. Higdon, E. H. Ohlsen, and W. B. Stiles, *Mechanics of Materials*. London: Wiley & Sons, 1960, p. 510.

[240] J. M. Gere and B. J. Goodno, *Mechanics of Materials*, SI Edition. 2013, p. 914.

[241] F. P. Beer, E. R. Johnston Jr, J. T. Dewolf, and D. Mazurek, *Mechanics of Materials*, McGraw-Hil. Boston, 2009, p. 617.

[242] R. L. Mott, *Statics and strength of materials*, Prentice H. Boston, 2010, p. 594.

[243] “Coherent.” [Online]. Available: http://www.coherent.com/.

[244] A. Paint, C. H. Hare, and M. T. Section, “The Degradation of Coatings by Ultraviolet Light and Electromagnetic Radiation,” no. May, 1992.

[245] L. Sun, J. J. Choi, D. Stachnik, A. C. Bartnik, B.-R. Hyun, G. G. Malliaras, T. Hanrath, and F. W. Wise, “Bright infrared quantum-dot light-emitting diodes through inter-dot spacing control.,” *Nat. Nanotechnol.*, vol. 7, no. 6, pp. 369–73, 2012.

[246] J. Li and J.-J. Zhu, “Quantum dots for fluorescent biosensing and bio-imaging applications.,” *Analyst*, vol. 138, no. 9, pp. 2506–15, 2013.

[247] M. Segev-Bar and H. Haick, “Flexible sensors based on nanoparticles.,” *ACS Nano*, vol. 7, no. 10, pp. 8366–78, 2013.

[248] R. S. Singh, M. O. Culjat, S. P. Vampola, K. Williams, Z. D. Taylor, H. Lee, W. S. Grundfest, and E. R. Brown, “P3D-6 Simulation, Fabrication, and Characterization of a Novel Flexible, Conformal Ultrasound Transducer Array,” *2007 IEEE Ultrason. Symp. Proc.*, pp. 1824–1827, 2007.

[249] J. Hu, L. Li, H. Lin, P. Zhang, W. Zhou, and Z. Ma, “Flexible integrated photonics: where materials, mechanics and optics meet [Invited],” *Opt. Mater. Express*, vol. 3, no. 9, p. 1313, 2013.

[250] D. Sun, N. Miyatake, and H.-J. Sue, “Transparent PMMA/ZnO nanocomposite films based on colloidal ZnO quantum dots,” *Nanotechnology*, vol. 18, no. 21, p. 215606, 2007.

[251] V. I. Klimov, “Quantization of Multiparticle Auger Rates in Semiconductor Quantum Dots,” *Science (80-.).*, vol. 287, no. 5455, pp. 1011–1013, 2000.

[252] A. W. Fang, B. R. Koch, K.-G. Gan, H. Park, R. Jones, O. Cohen, M. J. Paniccia, D. J. Blumenthal, and J. E. Bowers, “A racetrack mode-locked silicon evanescent laser.,” *Opt. Express*, vol. 16, no. 2, pp. 1393–8, 2008.

[253] M. J. R. Heck, H.-W. Chen, A. W. Fang, B. R. Koch, D. Liang, H. Park, M. N. Sysak, and J. E. Bowers, “Hybrid Silicon Photonics for Optical Interconnects,” *IEEE J. Sel. Top. Quantum Electron.*, vol. 17, no. 2, pp. 333–346, 2011.

[254] R. W. Kelsall, “Hybrid silicon lasers: Rubber stamp for silicon photonics,” *Nat. Photonics*, vol. 6, no. 9, pp. 577–579, 2012.

[255] J. E. Bowers, D. Liang, A. W. Fang, H. Park, R. Jones, and M. J. Paniccia, “Hybrid Silicon Lasers: The Final Frontier to Integrated Computing,” *Opt. Photonics News*, vol. 21, no. 5, p. 28, 2010.

[256] C. Vannahme, M. C. Leung, F. Richter, C. L. C. Smith, P. G. Hermannsson, and A. Kristensen, “Nanoimprinted distributed feedback lasers comprising TiO 2 thin films: Design guidelines for high performance sensing,” *Laser Photon. Rev.*, vol. 7, no. 6, pp. 1036–1042, 2013.

[257] M. Kristensen, A. Krüger, N. Groothoff, J. García-Rupérez, V. Toccafondo, J. García-Castelló, M. Jose Bañuls, S. Peransi-Llopis, and A. Maquieira, “Photonic Crystal Biosensor Chip for Label-Free Detection of Bacteria,” in *Advanced Photonics*, 2011, p. SWB1.

[258] V. Koubová, E. Brynda, L. Karasová, J. Škvor, J. Homola, J. Dostálek, P. Tobiška, and J. Rošický, “Detection of foodborne pathogens using surface plasmon resonance biosensors,” *Sensors Actuators B Chem.*, vol. 74, no. 1–3, pp. 100–105, 2001.

[259] M. Baaske and F. Vollmer, “Optical resonator biosensors: molecular diagnostic and nanoparticle detection on an integrated platform.,” *Chemphyschem*, vol. 13, no. 2, pp. 427–36, 2012.

[260] B. Cunningham, J. Qiu, B. Lin, P. Li, and J. Pepper, “A plastic colorimetric resonant optical biosensor for multiparallel detection of label-free biochemical interactions,” in *Proceedings of IEEE Sensors*, vol. 1, pp. 212–216, 2002.

[261] Y. Yang, G. A. Turnbull, and I. D. W. Samuel, “Sensitive Explosive Vapor Detection with Polyfluorene Lasers,” *Adv. Funct. Mater.*, vol. 20, no. 13, pp. 2093–2097, 2010.

[262] Y. Tan, C. Ge, A. Chu, M. Lu, W. Goldshlag, C. S. Huang, A. Pokhriyal, S. George, and B. T. Cunningham, “Plastic-Based Distributed Feedback Laser Biosensors in Microplate Format,” *IEEE Sens. J.*, vol. 12, no. 5, pp. 1174–1180, 2012.

[263] Y. Dong, J. W. Y. Lam, A. Qin, J. Liu, Z. Li, B. Z. Tang, J. Sun, and H. S. Kwok, “Aggregation-induced emissions of tetraphenylethene derivatives and their utilities as chemical vapor sensors and in organic light-emitting diodes,” *Appl. Phys. Lett.*, vol. 91, no. 1, p. 011111, 2007.

[264] A. Pucci, F. Di Cuia, F. Signori, and G. Ruggeri, “Bis(benzoxazolyl)stilbene excimers as temperature and deformation sensors for biodegradable poly(1,4-butylene succinate) films,” *J. Mater. Chem.*, vol. 17, no. 8, p. 783, 2007.

[265] A. Kishimura, T. Yamashita, K. Yamaguchi, and T. Aida, “Rewritable phosphorescent paper by the control of competing kinetic and thermodynamic self-assembling events,” *Nat Mater*, vol. 4, no. 7, p. 546, 2005.

[266] C. E. Olson, M. J. R. Previte, and J. T. Fourkas, “Efficient and robust multiphoton data storage in molecular glasses and highly crosslinked polymers,” *Nat Mater*, vol. 1, no. 4, 2002.

[267] J. W. Chung, Y. You, H. S. Huh, B.-K. An, S.-J. Yoon, S. H. Kim, S. W. Lee, and S. Y. Park, “Shear- and UV-induced fluorescence switching in stilbenic pi-dimer crystals powered by reversible [2 + 2] cycloaddition.,” *J. Am. Chem. Soc.*, vol. 131, no. 23, pp. 8163–72, Jun. 2009.

[268] Z. Chi, X. Zhang, B. Xu, X. Zhou, C. Ma, Y. Zhang, S. Liu, and J. Xu, “Recent advances in organic mechanofluorochromic materials.,” *Chem. Soc. Rev.*, vol. 41, no. 10, pp. 3878–96, 2012.

[269] L. Bu, M. Sun, D. Zhang, W. Liu, Y. Wang, M. Zheng, S. Xue, and W. Yang, “Solid-state fluorescence properties and reversible piezochromic luminescence of aggregation-induced emission-active 9,10-bis[(9,9-dialkylfluorene-2-yl)vinyl]anthracenes,” *J. Mater. Chem. C*, vol. 1, no. 10, p. 2028, 2013.

[270] S. W. Thomas, G. D. Joly, and T. M. Swager, “Chemical sensors based on amplifying fluorescent conjugated polymers.,” *Chem. Rev.*, vol. 107, no. 4, pp. 1339–86, 2007.

[271] W. Z. Yuan, P. Lu, S. Chen, J. W. Y. Lam, Z. Wang, Y. Liu, H. S. Kwok, Y. Ma, and B. Z. Tang, “Changing the behavior of chromophores from aggregation-caused quenching to aggregation-induced emission: development of highly efficient light emitters in the solid state.,” *Adv. Mater.*, vol. 22, no. 19, pp. 2159–63, 2010.

[272] W. McKeen, Laurence, “Appendix 3: Unit Convertion Tables,” in *Effect of Temperature and other Factors on Plastics and Elastomers*, William An., 2008, p. 776.

[273] H. Bikford, John and S. Nassar, “Torque-Angle Tension Control,” in *Handbook of bolts and bolted joints*, Marcel Dek., 1998, p. 616.

[274] Q. Kou, I. Yesilyurt, and Y. Chen, “Collinear dual-color laser emission from a microfluidic dye laser,” *Appl. Phys. Lett.*, vol. 88, no. 9, p. 091101, 2006.

[275] K. Yamashita, N. Takeuchi, K. Oe, and H. Yanagi, “Simultaneous RGB lasing from a single-chip polymer device.,” *Opt. Lett.*, vol. 35, no. 14, pp. 2451–3, 2010.

[276] F. Cornacchia, A. Di Lieto, M. Tonelli, A. Richter, E. Heumann, and G. Huber, “Efficient visible laser emission of GaN laser diode pumped Pr-doped fluoride scheelite crystals,” *Opt. Express*, vol. 16, no. 20, p. 15932, 2008.

[277] Y. Fujimoto, O. Ishii, and M. Yamazaki, “Multi-colour laser oscillation in Pr3+-doped fluoro-aluminate glass fibre pumped by 442.6 nm GaN-semiconductor laser,” *Electron. Lett.*, vol. 45, no. 25, p. 1301, 2009.

[278] T. Takahashi and Y. Asami, “Hollow-Cathode-Type CW White Light Laser,” vol. 27, pp. 111–114, 1974.

[279] Y. Shin, S. Park, Y. Kim, and J. Lee, “Development of a PC interface board for true color control using an Ar–Kr white-light laser,” *Opt. Laser Technol.*, vol. 38, no. 4–6, pp. 266–271, 2006.

[280] S. M. Giffin, I. T. McKinnie, W. J. Wadsworth, A. D. Woolhouse, G. J. Smith, and T. G. Haskell, “Solid state dye lasers based on 2-hydroxyethyl methacrylate and methyl methacrylate co-polymers,” *Opt. Commun.*, vol. 161, no. 1–3, pp. 163–170, 1999.

[281] Y. Shin, S. Park, Y. Kim, and J. Lee, “Development of a PC interface board for true color control using an Ar–Kr white-light laser,” *Opt. Laser Technol.*, vol. 38, no. 4–6, pp. 266–271, 2006.

[282] M. Kuwata, H. Sugiura, T. Sasagawa, A. Michimori, E. Toide, T. Yanagisawa, S. Yamamoto, Y. Hirano, M. Usui, S. Teramatsu, and J. Someya, “A 65-in. slim (255-mm depth) laser TV with wide-angle projection optical system,” *J. Soc. Inf. Disp.*, vol. 17, no. 11, p. 875, 2009.

[283] Y. Wang, P. O. Morawska, A. L. Kanibolotsky, P. J. Skabara, G. A. Turnbull, and I. D. W. Samuel, “LED pumped polymer laser sensor for explosives,” *Laser Photon. Rev.*, vol. 7, no. 6, pp. L71–L76, 2013.

[284] C. Vannahme, S. Klinkhammer, U. Lemmer, and T. Mappes, “Plastic lab-on-a-chip for fluorescence excitation with integrated organic semiconductor lasers,” *Opt. Express*, vol. 19, no. 9, p. 8179, 2011.

[285] “Hypix.” [Online]. Available: www.hypix.photonics.ac.uk.

List of publications

Journals

[1] C. Foucher, B. Guilhabert, A. L. Kanibolotsky, P. J. Skabara, N. Laurand, and M. D. Dawson, "Highly-photostable and mechanically flexible all-organic semiconductor lasers," *Opt. Mater. Express*, vol. 3, no. 5, p. 584, 2013

[2] B. Guilhabert, C. Foucher, A.-M. Haughey, E. Mutlugun, J. Herrnsdorf, H. D. Sun, H. V Demir, and M. D. Dawson, "Nanosecond colloidal quantum dot lasers for sensing," *Opt. Express*, vol. 22, no. 6, pp. 7308–7319, 2014.

[3] C. Foucher, B. Guilhabert, N. Laurand, and M. D. Dawson, "Wavelength-tunable colloidal quantum dot laser on ultra-thin flexible glass," *Appl. Phys. Lett.*, vol. 104, no. 14, p. 141108, 2014

[4] C. Foucher, B. Guilhabert, J. Hernsdorf, N. Laurand, and M. D. Dawson, "Diode-pumped, mechanically-flexible polymer DFB laser encapsulated by glass membranes," *Opt. Express.*, vol. 22, no. 20, p. 584, 2014

[5] A.-M. Haughey, C. Foucher, B. Guilhabert, A. L. Kanibolotsky, P. J. Skabara, N. Laurand, and M. D. Dawson, "Hybrid organic semiconductor lasers for bio-molecular sensing", *Faraday discussions*, vol. 174, pp. 369-381, 2014

Conferences

[1] C. Foucher, B. Guilhabert, A. L. Kanibolotsky, P.J. Skabara, N. Laurand, M.D. Dawson, “Flexible Polyimide-based Nanocomposite Laser”, EOSAM 2012

[2] C. Foucher, B. Guilhabert, N. Laurand and M.D. Dawson, “Mechanically-flexible colloidal quantum dot lasers on ultra-thin glass”, QD Day 2014

[3] B. Guilhabert, C. Foucher, A.-M. Haughey, E. Mutlugun, J. Herrnsdorf, H. D. Sun, H. V Demir, and M. D. Dawson, CdSe/ZnS Colloidal Quantum Dots for Solution-Processed DFB Laser Sensors and Hybrids with Inorganic Membranes, QD Day 2014

[4] C. Foucher, B. Guilhabert, N. Laurand and M.D. Dawson, Colloidal quantum dot lasers on ultra-thin glass for flexible photonics, SPIE 2014

[5] A.-M. Haughey, C. Foucher, B. Guilhabert, A. L. Kanibolotsky, P. J. Skabara, G. Burley, M. D. Dawson and N. Laurand, Hybrid organic semiconductor lasers for bio-molecular sensing, Faraday Discussions 2014

[6] C. Foucher, B. Guilhabert, J. Herrnsdorf, N. Laurand and M.D. Dawson, Diode-pumped, mechanically-flexible organic lasers fully encapsulated with ultra-thin glass membranes, IPC 2014

[7] B. Guilhabert, C. Foucher, L. McLellan, A.-M. Haughey, Y. Gao, J. Herrnsdorf, E. Mutlugun, H.V. Demir, N. Laurand and M. D. Dawson, Advances in colloidal quantum dot distributed feedback lasers hybridized on glass membranes, IPC 2014